
# Inverse-Bilayer AlN/$(Fe_{90}Co_{10})_{78}Si_{12}B_{10}$ Magnetoelectric Composites

by

Erdem Yarar

A dissertation submitted to
the Faculty of Engineering of Kiel University
in partial fulfillment of the requirement for the degree of
Doctor of Engineering (Dr.-Ing.)
in Materials Science and Engineering

Kiel, 2017

| | |
|---|---|
| 1. Gutachter | Prof. Dr.-Ing. Eckhard Quandt |
| 2. Gutachter | Prof. Dr. Franz Faupel |

| | |
|---|---|
| Datum der mündlichen Prüfung | 23. November 2017 |

# Declaration

I declare that, apart from the counseling of my supervisors, the contents and the form of the following thesis is my own work. I declare that, I have stated all external contributions and recorded their sources. I declare that, this thesis work has not been, partially or completely, submitted to any other university or institute in the context of an examination procedure. I declare that, the following work has been done in compliance with the rules of good scientific practice of the German Research Foundation.

Erdem Yarar
Kiel University

Kiel, 15. December 2017 *(Signature)* .....

*Dedicated to My Mother and Grandmother...*

# Abstract

Non-invasive imaging of brain activity is particularly increasing in importance for the detection of potential pathological activities; e.g., epilepsy. State-of-the-art devices make use of powerful superconducting quantum interference devices (SQUID), which can measure the magnetic fields induced by neural activity; i.e., electric currents. However, the necessity of operating these devices at near absolute-zero temperature (T = 4 K) and in magnetically shielded rooms increase operational costs and nonconformity for continuous patient monitoring. Such limitations necessitate the development of alternative magnetic detection devices.

As of late, magnetoelectric composite sensors are becoming potential candidates for the measurement of low magnetic signals. These sensors constitute of thin film layers sputtered on top of each other and exploit the product property of their constituent materials. Based on the strain transfer between piezoelectric and magnetostrictive layers, magnetoelectric sensors are able to output a polarization in response to an applied external magnetic field. Their sensitivity to magnetic fields in the pT-range, at room temperature and without the need of cooling, represents several advantages including lower running costs, smaller device size and easier applicability.

Aforementioned properties encouraged a wide range of investigations in the last decade, and various sensors with different materials and geometries were investigated. Among these, several sensors of aluminum nitride (AlN) and Fe-based metallic glass alloys; e.g., $(Fe_{90}Co_{10})_{78}Si_{12}B_{10}$ (FeCoSiB), exhibit remarkable results. Sensors performing in the L–T (longitudinal magnetization, transverse polarization) composite mode reportedly reached magnetic detection limits as low as of $1\,\mathrm{pT}/\mathrm{Hz}^{1/2}$. Recently, a limit of detection (LOD) as low as $500\,\mathrm{fT}/\mathrm{Hz}^{1/2}$ is achieved by connecting two PZT/FeCoSiB composite sensors in a

"tuning fork" structure. Other investigations revealed that the deposition of the magnetostrictive layer on a smooth surface improved the $\alpha_{ME}$ coefficient of the magnetoelectric sensors by 30% and the appropriate adjustment of the electrode size enhanced the signal-to-noise ratio (SNR) by 100%. However, neither of these improvements could be implemented to the conventional process flow of AlN/FeCoSiB unimorph sensors, where the high temperature constituent (AlN) had to be deposited as the first layer in order to preserve the soft magnetic properties of the consequent FeCoSiB.

The current work solves these challenges and aims at the fabrication, optimization and characterization of low temperature AlN thin films as well as the development of thin film magnetoelectric sensors based on AlN/FeCoSiB in order to detect $\leq 1\,\mathrm{pT}$ AC magnetic fields. The temperature drawback, which originates mainly from the need of preserving the amorphous structure and the soft-magnetic properties of FeCoSiB, is solved by adopting a new process flow. Following initial research with DC and RF power sources, low temperature AlN fabrication is achieved by establishing a pulsed DC sputtering process, which is afterwards implemented into the production flow of the magnetoelectric sensors. Removal of the temperature limitations allows the realization of new sensor designs where the stack order can be altered in order to maximize the sensor properties. According to this process flow, FeCoSiB can now be deposited as the first layer and AlN, including its seed layer, can be deposited on top of FeCoSiB without any substrate heating. This, in return, improves the piezomagnetic coefficient and conserves the soft-magnetic properties of FeCoSiB. As a result, macroscopic magnetoelectric sensors with an inversed deposition sequence can be produced. Furthermore, optimization of the top electrode dimensions in order to confine the charge collecting area is realized. The most sensitive sensors produce giant magnetoelectric coefficients as high as $7.5\,\mathrm{kV/(cm\cdot Oe)}$ at the mechanical resonance frequency of the sensors. Detection of magnetic fields as low as 400 fT and a LOD in the range of $1\,\mathrm{pT/Hz^{1/2}}$ are achieved when operating at the mechanical resonance of the cantilever sensor and at room temperature.

# Kurzfassung

Die nicht-invasive Bildgebung von Gehirnaktivitäten gewinnt zunehmend an Bedeutung für den Nachweis möglicher pathologischer Aktivitäten, wie z.B. Epilepsie. Hochmoderne Geräte nutzen leistungsstarke supraleitende Quanteninterferenzgeräte (SQUID), welche die durch neuronale Aktivität bzw. elektrische Ströme induzierten Magnetfelder messen können. Die Notwendigkeit, diese Geräte nahe dem absoluten Nullpunkt (T = 4 K) und in magnetisch abgeschirmten Räumen zu betreiben, erhöht jedoch die Betriebskosten und die Unangemessenheit für eine kontinuierliche Patientenüberwachung. Solche Einschränkungen erfordern die Entwicklung alternativer Magnetfeldsensoren.

Seit Kurzem bieten magnetoelektrische Kompositsensoren eine potentielle Alternative zur Messung niedriger magnetischer Signale. Diese Sensoren bestehen aus mehrlagigen Dünnfilmschichten, die übereinander abgeschieden werden und die Produkteigenschaft ihrer Bestandteile ausnutzen. Basierend auf der Dehnungsübertragung zwischen piezoelektrischen und magnetostriktiven Schichten, generieren magnetoelektrische Sensoren in Reaktion auf ein angelegtes externes Magnetfeld eine elektrische Polarisation. Ihre Empfindlichkeit für Magnetfelder im pT-Bereich, bei Raumtemperatur und ohne Kühlung, ist vorteilhaft. Dazu gehören niedrigere Herstellungs- und Betriebskosten, kleinere Gerätegrößen und einfachere Anwendbarkeit.

Die genannten Anforderungen führten im letzten Jahrzehnt zu einem breiten Spektrum von Untersuchungen und der Erforschung verschiedener Sensoren mit unterschiedlichen Kompositsystemen und Geometrien. Besonders verschiedene Sensoren aus Aluminiumnitrid (AlN) und Fe-basierten metallischen Glaslegierungen zeigen bemerkenswerte Ergebnisse wie z.B. $(Fe_{90}Co_{10})_{78}Si_{12}B_{10}$ (FeCoSiB).

Sensoren, die in der L-T- (Längsmagnetisierungs-, Querpolarisations-) Betriebsart arbeiten, erreichten nachweislich niedrige magnetische Detektionsgrenzen im Bereich $1\,\mathrm{pT}/\mathrm{Hz}^{1/2}$. Vor Kurzem wurde eine Detektionsgrenze von $500\,\mathrm{fT}/\mathrm{Hz}^{1/2}$, durch die Verbindung von zwei PZT/FeCoSiB-Kompositsensoren mit einer Stimmgabelstruktur erreicht. Weitere Untersuchungen zeigten, dass die Abscheidung der magnetostriktiven Schicht auf einer glatten Oberfläche den $\alpha_{ME}$ Koeffizienten der magnetoelektrischen Sensoren um 30% verbessert und die entsprechende Optimierung der Elektrodengröße das Signal-Rausch-Verhältnis (SRV) um 100% erhöht. Jedoch konnte keine dieser Verbesserungen in dem herkömmlichen Prozessablauf von AlN/FeCoSiB-unimorph-Sensoren implementiert werden, bei welchem der Hochtemperaturbestandteil (AlN) als erste Schicht abgeschieden werden musste, um die weichmagnetischen Eigenschaften des nachfolgenden FeCoSiB zu erhalten.

Die aktuelle Arbeit löst diese Herausforderungen und behandelt die Fertigung, Optimierung und Charakterisierung von Niedertemperatur AlN Dünnfilmen, darüberhinaus wird die Entwicklung von magnetoelektrischen Sensoren auf Basis von AlN/FeCoSiB gezeigt. Diese Entwicklung soll schlussendlich die Detektion von magnetischen Wechselfeldern $\leq 1\,\mathrm{pT}$ ermöglichen. Die Notwendigkeit die amorphe Struktur und somit weichmagnetische Eigenschaften von FeCoSiB zu erhalten, wird durch den Einsatz eines neuen Niedrigtemperatur Prozessablaufs gelöst. Basierend auf anfänglichen Untersuchungen mit DC- und HF-Sputter prozessen, wird eine Tieftemperatur-AlN-Abscheidung erreicht, indem ein gepulster Gleichstrom-Zerstäubungsprozess, im Prozessablauf der magnetoelektrischen Sensoren implementiert wird. Dieser Prozessablauf ermöglicht die Realisierung neuer Sensortypen, bei denen die Stapelreihenfolge verändert werden kann, um die Sensoreigenschaften zu optimieren. Entsprechend dieses Prozessablaufs kann nun FeCoSiB als erste Schicht abgeschieden werden, und AlN, einschließlich seiner Keimschicht, kann ohne Substraterhitzung auf FeCoSiB aufgebracht werden. Dies verbessert im Gegenzug den piezomagnetischen Koeffizienten und erhält die weichmagnetischen Eigenschaften von FeCoSiB. Als Ergebnis können makroskopische magnetoelektrische Sensoren mit einer umgekehrten Abscheidungssequenz hergestellt werden. Weiterhin wird eine Optimierung der oberen Elektrodenabmessungen zur Begrenzung der Ladungssammelfläche erreicht. Die empfindlichsten Sensoren erzeugen magnetoelektrische Koeffizienten im Bereich $7.5\,\mathrm{kV}/(\mathrm{cm}\cdot\mathrm{Oe})$ in mechanischer Resonanz. Bei Messungen in oder nahe mechanischer Resonanz des Sensors, wird (bei Raumtemperatur) die Detektion von Magnetfeldern im Bereich von $400\,\mathrm{fT}$ sowie eine Detektionsgrenze von $1\,\mathrm{pT}/\mathrm{Hz}^{1/2}$ erreicht.

# Contents

# List of Figures

# List of Tables

# 1 Introduction

## 1.1 Motivation

Technological development often occurs as a combined effort of correlated branches. The needs of a research field often act as a catalysis for another and encourage further research. Monitoring one's environment and its dozens of effects originated from numerous phenomena of the nature, is a fundamental necessity in the modern world. However humans have limited sensing capabilities; most of the electromagnetic spectrum, for instance, is hidden to them as their eye-sight is limited only to several hundred nanometers. The goal to overcome such limitations is what gave birth to the sensor technology; one of the most innovative branches of the $21^{st}$ century.

Sensors are small transducer devices, which monitor/detect environmental changes and produce meaningful signals. They are being utilized in almost all technological applications; either be in science or in industry or even in every day life. With successful miniaturization of sensors, via microelectromechanical systems (MEMS) technology, the global sensor market is expected to grow increasingly. A recent report of market research estimates the global smart sensors market to reach at $ 9.22 billion in 2018 [1]. For instance, an average automobile utilizes 60 – 100 sensors such as motion sensors, air flow sensors, coolant temperature sensors, etc. [2, p.1]. Considering the global size of the automobile industry ($>$ 90 million automobiles in 2015 [3]), estimated amount of the necessary sensors raise up to tens of billions of pieces per year. Indeed, automotive industry is not the only requester of sensors. Additional markets such as consumer electronics, defense industries, communication technologies and health-care are only but a few of them. The latter, in particular, is one of the most sophisticated application fields of the last decade. Medical sensors can be

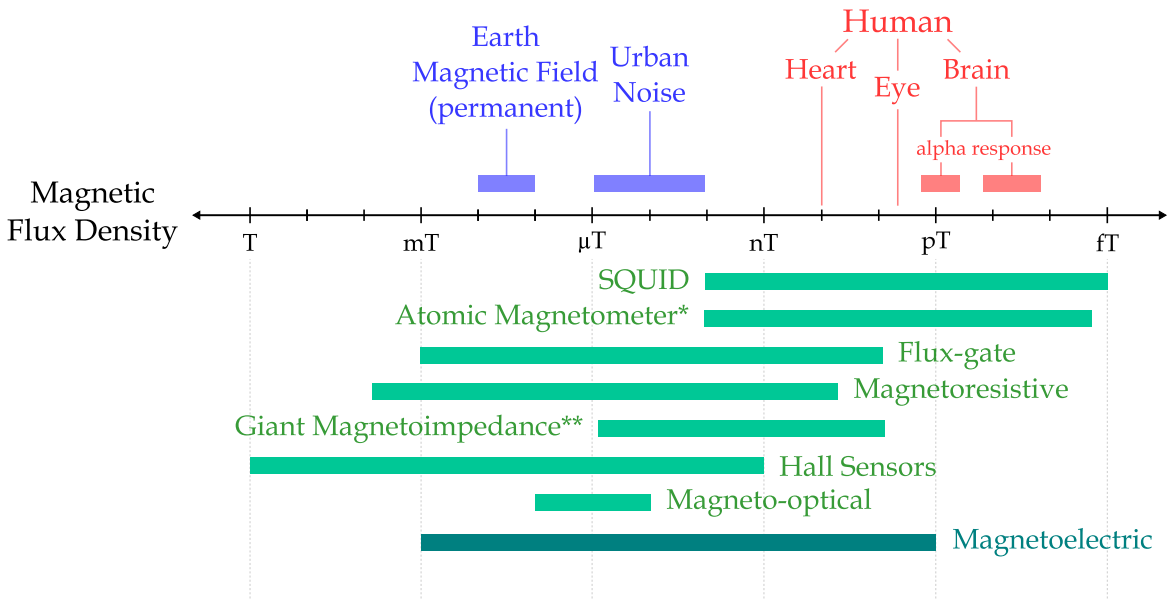


***Figure 1.1:*** *Magnetic induction of enviromental (blue) and biomagnetic fields (red). Devices utilized (green) for the detection of magnetic fields in various application areas. Magnetoelectric sensors are coded as teal. [4, p.71, p.103], *[5, p.489] **[5, p.122, p.123]*

utilized for the measurement of biomagnetic signals; e.g., electric/magnetic signals generated within the human body. Especially the increasing reluctance against invasive procedures further emphasizes the need towards the measurement of biomagnetic signals with little-to-no contact with the patient. There are, of course, conventional non-invasive measurement techniques, which measure potential difference in the human body by surface electrodes. However, these methods suffer from the inhomogeneous conductivity of the human body. Magnetic signals, on the other hand, are free from such restrictions due to the non-magnetic nature of the human body and therefore provide comparably better spatial resolution.

Figure 1.1 depicts the biomagnetic signals of interest for medical applications. Clearly these signals are extremely small, especially with respect to environmental magnetic fields such as the constant earth magnetic field and the urban noise. Unlike the earth magnetic field, the latter can vary depending on the hour of the day, geographical location, the amount of traffic, etc.. Combined, these principal noise sources are up to six orders of magnitude stronger than the biomagnetic signals, among which the human heart and brain produce the strongest and the weakest signals, respectively. It is important to point out, that the signals produced by the human brain differ with respect to the presence of an explicit task; e.g., sensory and/or motor input. The alpha signals, for instance, are generated in the absence of such tasks and are up to two orders of magnitude stronger in comparison to the response signals, which are formed as a reaction to a particular input. Hence, the extremely small magnitude of the biomagnetic

***Table 1.1:*** *Magnetic field sensors and properties. Taken from [6].*

| Magnetic field sensor | Range (mT) | Resolution (T) | Bandwidth (Hz) | Comments |
|---|---|---|---|---|
| Induction coil | $10^{-10}$ ... $10^{6}$ | Variable | $10^{-1}$ ... $10^{6}$ | Can not measure static fields |
| Hall-effect | $10^{-1}$ ... $3 \cdot 10^{4}$ | $10^{-7}$ | DC ... $10^{8}$ | Best for fields above 1T |
| Magnetoresistance | $10^{-3}$ ... 5 | $10^{-8}$ | DC ... $10^{7}$ | Good for mid-range applications |
| Fluxgate | $10^{-4}$ ... 0.5 | $10^{-10}$ | DC ... $2 \cdot 10^{3}$ | General-purpose vector magnetometer |
| Optically pumped | $10^{-2}$ ... 0.1 | $5 \cdot 10^{-12}$ | DC ... 5 | Highest resolution scalar magnetometer |
| SQUID | $10^{-9}$ ... 0.1 | $10^{-13}$ | DC ... 5 | Highest sensitivity magnetometer |

signals necessitates the use of very sensitive magnetic field sensors as well as the reduction of environmental noise contributions below the target signals.

There are numerous devices utilized for the measurement of small magnetic fields or magnetic fields in general. Other than few exceptions, these devices all follow a similar working principle. That is; the detection of the fluctuations in the magnetic moment (of the magnetic material used in the device) when subject to environmental changes such as the magnetic field, temperature, mechanical stress, etc.. While the utilized magnetic material is generally a ferromagnetic alloy, different properties of these materials can be exploited in different devices. In the case of magnetoelectric sensors, for example, the device functionality is based on the magnetoelastic properties of the magnetostrictive/ferromagnetic alloys.

Magnetic sensors can be classified with respect to their sensing range and resolution (see Table 1.1). Currently, the most sensitive sensors for measuring very small magnetic signals are superconducting quantum interference devices (SQUID) and spin exchange relaxation free (SERF) magnetometers [5, p.483]. The latter is a relatively new technology and is not yet fully developed, however SQUIDs are known for several decades and therefore, are incorporated into the most technological biomagnetic measurement techniques; e.g., magnetoencephalography (MEG) and magnetocardiography (MCG) (see Figure 1.2). SQUIDs can measure magnetic field magnitudes as low as several $\mathrm{fT}/\mathrm{Hz}^{1/2}$ with a measurement range of almost 8 orders of magnitude [7][8]. The strength of SQUIDs originate from the principals of superconductivity; a quantum mechanical phenomenon where in certain materials a complete loss of electrical resistance (zero resistance) and the expulsion of magnetic (flux) fields from the interior of the material occur when the material is cooled below a certain (critical) temperature. Hence these devices must be kept around absolute-zero (4 K) temperature via liquid helium cooling at all times. This requirement does not only results in a bulky device but also leads to an extremely expensive one, which roughly costs € 3 million to buy and additionally € 200 thousand per year to maintain [9]. Furthermore, these devices generally operate in magnetically shielded rooms (MSR) since the targeted fields are extremely low. MSRs constitute of several layers of very high permeability soft magnetic materials known

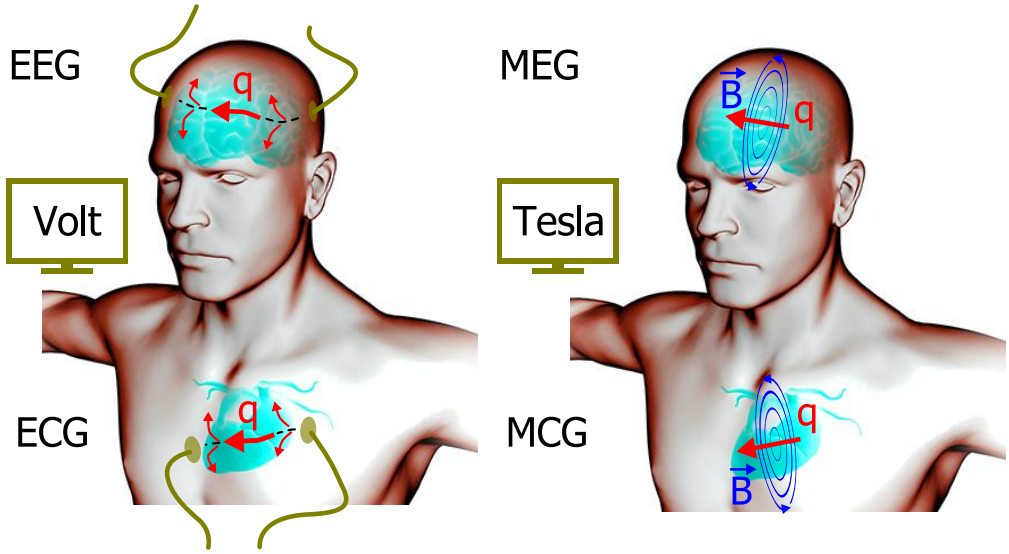


***Figure 1.2:*** *Biosignals and respective monitoring methods depicted on a human body. Signal magnitude is measured in T (for magnetic flux density) and V (for potential difference). Image adapted from [11].*

as the mu-metal[1] and permalloy[2] with several millimeters of thickness, further increasing the costs. Hence despite the undisputed superiority of SQUID-powered measurement techniques, increased costs make it impossible to afford (and/or to sustain) these systems for many countries. Even though these devices are used in many research institutes, the technology proves to be too expensive for widespread medical use [10].

Economically more reasonable options are present as well. Considering medium range sensors, for instance, flux-gate magnetometers are considered as very robust and economical candidates, which can be completely integrated into many modern systems [12]. They are very commercial products despite being bulky in comparison to other alternatives. Unfortunately, they are not suitable for medical applications as the output signal of these devices suffer greatly due to external factors. Another alternative is the magnetoresistive sensors; comparable to flux-gates in application range, these sensors are thin film based and can detect magnetic fields as low as several hundred pT [13]. When measuring at higher fields, sensors exploiting the Lorentz force are utilized. The most well-known sensor of this range are the Hall sensors. These are generally preferred for their successful integration into digital switches with semiconductor elements. Furthermore, they offer passive operation and low power consumption but they have limited frequency range and high costs.

[1] Ni-Fe-Cu-Cr/Mo alloys.
[2] Ni-Fe alloys.

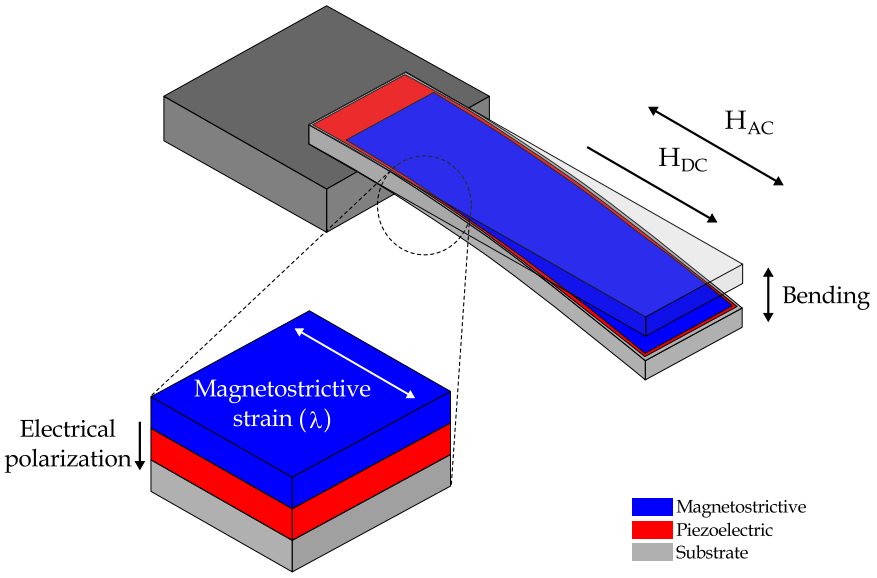


***Figure 1.3:*** *Schematic representation of a conventional AlN/FeCoSiB magnetoelectic sensor and its principle of function. Magnetostrictive material (blue) expands in the presence of an external magnetic field. Induced strain is transferred to a piezoelectric material (red) via mechanical coupling, which deforms the piezoelectric crystal and results in an electric polarization along the material's thickness. FeCoSiB layer acts as the top electrode.*

In summary, it can be said that even though several different devices are able to measure magnetic fields ranging from high T-fields down to pT-fields, they are not strong enough to fulfill health care applications. SQUIDs present the golden standard in magnetic sensing and the sensing of biomagnetic signals in particular, however their elevated costs create the necessity for an affordable device, which can be implemented in every medical institution.

A potential alternative method is the use of magnetoelectric sensors; i.e., composites of magnetostrictive and piezoelectric layers coupled via strain transfer (see Figure 1.3). These sensors have a wide dynamic range and have the potential of detecting biomagnetic signals for greatly reduced costs. The basic principle of operation is as the following; a magnetostrictive material that is subject to an external magnetic field experiences a change in its dimensions; i.e., strain. It is possible to transfer some of this strain to a piezoelectric material via strain coupling, given that both materials are mechanically coupled to each other. In this case, an electric polarization can be induced in the piezoelectric material as a result of the magnetic field induced strain in the magnetostrictive material. Hence, sensors utilizing this relationship would act as a two-ways transducer between magnetic and electric fields, allowing the detection of one another.

In addition to their simple operation principal, magnetoelectric sensors offer numerous ad-

vantages in terms of costs, fabrication, optimization and performance, as well. First of all, magnetoelectric sensors are small in size (ranging from μm to several mm). Application related optimization; e.g., miniaturization, vacuum encapsulation, integration into much complex integrated circuit systems are all possible since they are fully compatible with the state-of-the-art MEMS fabrication techniques. They can be produced on various substrate materials; e.g., silicon, quartz, polymers and shape memory alloys, therefore offering a variety of new possibilities. Unlike SQUIDs, they do not rely on the superconductivity, therefore do not require cooling. This is a very important feature, which reduces the individual sensor dimensions as well as the total device volume and running costs to a great extent. These sensors can perform at room temperature, under atmospheric pressure or in vacuum conditions, hence offering application versatility. The latter is further strengthened by the composite nature of the sensor, which allows the combination of various piezoelectric and magnetostrictive materials in various connectivity schemes. Current state-of-the-art sensors can detect magnetic fields in the range of 1 pT when operated under a suitable bias field and at their mechanical resonance frequency.

The major drawback of MEG is the relatively large distance between the signal source and the detection unit, resulting in a poor signal localization within the brain. Since in MEG, SQUIDs are combined as arrays and placed at some distance from the head, the distance between the signal source and the detector increases, further decreasing the already small signal magnitude. This can be greatly improved using magnetoelectric sensors, since a magnetoelectric sensor-array needs not to be placed in a casing and can be brought to close proximity from the signal source. When all these traits are accounted for, it is fair to say that magnetoelectric sensors offer a potent alternative to most conventional magnetic field detection devices.

## 1.2 Scope of Work

Magnetic field detection capabilities of magnetoelectric sensors currently range up to eleven orders of magnitude, as shown in Figure 1.1. Hence, further extending these capabilities towards higher ($\geqslant 1\,\mu T$) and lower ($\leqslant 1\,pT$) field magnitudes would give a magnetic field sensor, that would outperform its predecessors both technologically and economically.

The current doctoral research aims at the development of magnetic field sensors that use the principals of the magnetoelectric effect for the detection of sub-pT magnetic fields at room temperature and in atmospheric pressure. To that end, realization of a sandwich-type (magnetostrictive–piezoelectric–magnetostrictive), free-standing (partially released from the substrate) and miniaturized (sub-mm dimensions) magnetoelectric composite sensor design has been proposed. A sensor that is less susceptible to external noise sources with diminished substrate clamping and enhanced spatial resolution can be produced by implementing above designated features, respectively. However, this sensor design is not straightforward to realize and requires various improvements/changes with respect to initially developed Si-based magnetoelectric sensors within the framework of the collaborative research center CRC 855 "Magnetoelectric Composites – Future Biomagnetic Interfaces" and PAK 902 "Magnetoelectric Sensors for Medicine". Therefore, the overall research is divided into smaller work packages as follows.

- *Fabrication and optimization of thin film constituents*

  Piezoelectric aluminum nitride (AlN) and magnetostrictive $(Fe_{90}Co_{10})_{78}Si_{12}B_{10}$[1] are chosen as the constituent materials of the intended magnetoelectric composite sensors. FeCoSiB is a soft magnetic material with an amorphous structure and polycrystalline AlN is conventionally fabricated at temperatures that are higher than the crystallization temperature ($> 350\,°C$) of FeCoSiB [14]. In order to overcome this predefined deposition order and to provide design freedom, a low temperature AlN deposition process is developed as the first step. The process is optimized in such a way that it is robust and can deliver stress-compensated thin films, which would otherwise influence the magnetostrictive properties of FeCoSiB. Furthermore, the deposited films provide, comparable if not superior, material properties (microstructural, piezoelectric, dielectric, etc..) in comparison to the state-of-the-art AlN films deposited at conventional magnetron sputtering temperatures ($200\,°C - 400\,°C$) of polycrystalline AlN. Stress

[1] $(Fe_{90}Co_{10})_{78}Si_{12}B_{10}$ will be noted as FeCoSiB from here on.

optimization of the deposited AlN thin films and determining its influence on the relevant properties are organized as a stand-alone master thesis project [15].

- *Sensor designs and fabrication process optimization*

  Si-based miniaturized magnetoelectric sensors were previously investigated [16]. However such research is not present for sandwich-type magnetoelectric composites. Therefore emerging compatibility issues are solved by adopting a consecutive/additive research path, which resulted in the development/optimization of several new sensor concepts. These sensors include inverse-bilayer, sandwich-type and symmetrical sensors. Accordingly, previously utilized methods, such as lift-off techniques, are discarded from the fabrication process and are replaced by a combination of photolithography techniques and wet/dry etching methods. In this way, all constituent layers are fabricated consecutively without breaking vacuum and exposing deposited films to atmospheric conditions. Among the investigated sensors, inverse-bilayer sensors proved to be the most successful and are therefore established as the main focus of this thesis.

- *Miniaturization*

  The final part of the research focus on the realization of miniaturized composites. Due to the extremely small size of the intended free-standing sensors (length $\sim 1.5\,\mathrm{mm}$, width $\sim 300\,\mu\mathrm{m}$), a complete new process flow is adapted and both inverse-bilayer and sandwich-type sensors with sub-mm dimensions are fabricated. With special focus on selective bulk and surface micro machining techniques, structuring of the composite stacks and the release of the cantilever structures from the underlying substrates are realized. Optimized process parameters are determined as a reference for future work and fabricated sensors are investigated with respect to their magnetoelectric properties. This subchapter was organized as a stand-alone master thesis project [17].

# 2 Theory

The following chapter provides a theoretical background for the thesis. It is divided into three main topics with respect to the relevant physical phenomena; piezoelectric effect, magnetostrictive effect and magnetoelectric effect. Each respective topic is organized in such a way that it provides a brief history, necessary background, important materials and material properties as well as a look into the state-of-the-art. Finally, thin film deposition techniques are summarized and magnetron sputtering method utilized in this work is presented.

## 2.1 Piezoelectric Effect and Aluminum Nitride

### 2.1.1 Introduction

Direct piezoelectric effect defines the appearance of an electric polarization ($P$) in response to a mechanical strain ($S$) and/or the deformation ($\varepsilon$) in a crystal in response to an applied electric field ($E$). Even though it was initially observed in the mid-1800s by *C. Linnaeus* and *F. Aepinus*, its actual understanding and discovery is mainly due to the interest put into pyroelectricity by *P.* and *J. Curie* brothers [18, p.2]. They have assumed that a piezoelectric effect would arise in materials with certain crystal asymmetries and have identified the direct piezoelectric effect in single crystal quartz in 1880. In 1881, *G. Lippman* theoretically demonstrated the existence of a converse piezoelectric effect; i.e., the generation of stress when a piezoelectric crystal is subject to an external electric field. 30 years later, *W. Voigt* published his work '*Lehrbuch der Kristallphysik*', where he described 20 natural crystal classes exhibiting piezoelectric properties as well as defining the piezoelectric coefficients

of solid crystals [19, p.816]. Practical applications followed soon after; first *E. Rutherford* developed a passive listening device known as the hydrophone. In 1917, *P. Langevin* fabricated an active ultrasonic transducer; i.e., sonar, using thin quartz crystals sandwiched between steel plates [20]. Today, piezoelectric materials are used in many applications such as energy harvesters, sensors, actuators, etc. [21].

Piezoelectric materials can be divided into two big groups; natural and artificial materials. Initially, there have only been two known piezoelectric materials; quartz and rochelle salt ($KNaC_4H_4O_6 \cdot H_2O$[1]). However, most of the commercially available piezoelectric materials are artificially produced due to much greater properties in comparison to the natural piezoelectrics. With respect to the time of their discovery, some of the most important piezoelectric materials include [18, p.5-15]

- *Perovskite materials*; e.g., barium titanate ($BaTiO_3$) and lead zirconate titanate ($Pb(Zr_x, Ti_{1-x})O_3$, PZT with $0 \leqslant x \leqslant 1$),
- *Complex relaxor ferroelectrics*; e.g., lead magnesium niobate ($[Pb(Mg_{1/3}, Nb_{2/3})O_3]$), lead zinc niobate ($[Pb(Zn_{1/3}, Nb_{2/3})O_3]$) and lead magnesium niobate-lead titanate ($[Pb(Mg_{1/3}, Nb_{2/3})O_3]_{1-x} - [PbTiO_3]_x$, PMN-PT),
- *Single crystal materials*; e.g., lithium niobate ($LiNbO_3$, LN) and tantalate ($LiTaO_3$, LT),
- *Ceramic/polymer composite materials*; e.g., polyvinylidene difluoride (PVDF),
- *Modern perovskite materials*; e.g., bismuth ferrite ($BiFeO_3$) and titanate ($Bi_4Ti_3O_{12}$),
- *Wurtzite-type polycrystalline thin films*; e.g., aluminum nitrite (AlN) and zinc oxide (ZnO).

### 2.1.2 Fundamentals

Certain materials exhibit low conductivity, both in terms of heat and electricity, due to the absence of freely moving charges in their atoms. These materials are defined as insulators [22, p.182]. Dielectric materials, a subgroup of insulators, possess a certain property that leads to an electric polarization within the material. This polarization occurs either spontaneously

[1] Potassium sodium tartrate tetrahydrate.

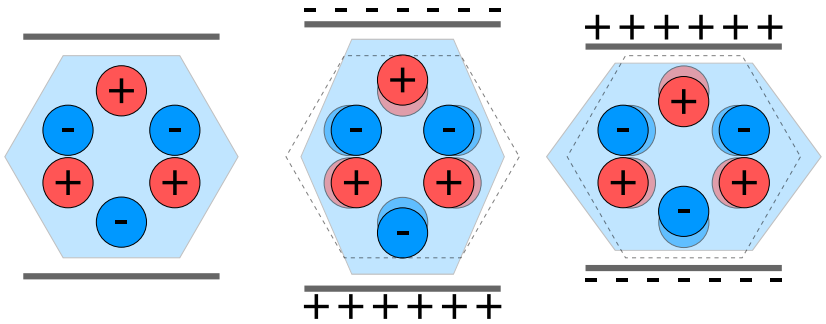

***Figure 2.1:*** *Schematic representation of the direct piezoelectric effect. Strain in the crystal results in a displacement of the charge centers from their initial positions. Consequently dipoles are formed and a polarization is observed. Image adapted from [18, p.8].*

(polar) or strictly when under certain external stimuli (non-polar). The occurrence of the aforementioned phenomena, as a response to an external mechanical stress, is known as the piezoelectric effect [22, p.265]. There are 3 primary contributors to the electric polarization; electronic, ionic and dipole reorientation-related, where the extend of individual contributions are dependent on the frequency of the applied electric field [18, p.2]. In principal, electric polarization is the sum of the electric dipoles and originates from the displacement of the nuclei and the electrons from their initial position as depicted in Figure 2.1.

One essential requirement of the piezoelectric phenomenon is the absence of crystal symmetry, since the separation of charges within a symmetrical crystal would produce zero net polarization. There are 32 classes of crystal materials, among which 11 classes have a center of symmetry (centrosymmetic) and are non-polar. Of the remaining 21 non-centrosymmetrical classes, 20 exhibit piezoelectric effect (see Figure 2.2a) and 10 of them are polar; i.e., exhibit spontaneous polarization [22, p.18].

Spontaneous polarization refers to a permanent polarization present in a material even when absent of an applied electric field or mechanical stress. Materials demonstrating this ability are known as the pyroelectrics. Even though most dielectric materials exhibit a linear relationship between the applied electric field and polarization, this effect vanishes once the external stimuli is removed. A subgroup of pyroelectrics; i.e., ferroelectrics, on the other hand exhibit a non-linear behavior, reach a saturation point when the field strength is increased up to a certain point and retain some of their polarization even if the electric field is removed. A summarized scheme of the mentioned material groups is depicted in Figure 2.2b.

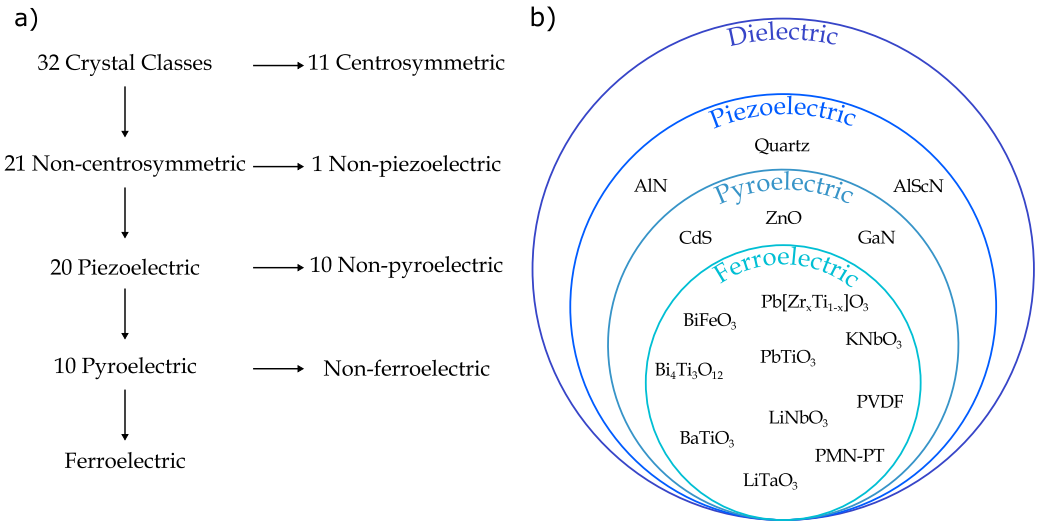


***Figure 2.2:*** *Relationship between crystal classes. a) Crystallographic classification according to crystal centrosymmetry [18, p.4] b) Examples of dielectric materials and the relationship between piezoelectric, pyroelectric and ferroelectric materials.*

### Mathematical Description

Electric polarization ($P$) can be defined as the sum of charge build-up per unit area where it develops

$$P = \frac{Q}{A} \tag{2.1}$$

where, $Q$ is the charge build-up and $A$ is the area.

In piezoelectric materials, this effect is linearly related to the external stress that a crystal is subjected to. Hence the fundamental relationship defining the charge generation within a stressed piezoelectric material can be written as

$$P_i = d_{ijk} \cdot \sigma_{jk} \tag{2.2}$$

where, $P_i$ is the induced polarization, $d_{ijk}$ is the piezoelectric charge coefficient and $\sigma_{jk}$ is the mechanical stress with $i, j, k$ = 1–3 [23, p.116].

Essentially, Equation (2.2) states that the density of generated charge within a piezoelectric material is proportional to the applied external stress and the material's inherent ability to couple the stress to the electric charge. Since piezoelectric effect originates from the cross coupling between elastic (stress ($\sigma$) and strain ($S$)) and dielectric properties (electric charge

density ($q_E$) and electric field ($E$)), tensor relation of the constituent variables are generally given in the form of constitutive equations for direct and converse piezoelectric effects. The relationship is as follows

$$D_i = d_{ijk} \cdot \sigma_{jk} + \varepsilon_{ij}^{\sigma} \cdot E_j \tag{2.3}$$

$$S_{ij} = d_{ijk} \cdot E_k + s_{ijkl}^{E} \cdot \sigma_{kl} \tag{2.4}$$

where, $D_i$ is the electric displacement, $\varepsilon_{ij}^{\sigma}$ is the dielectric permittivity at constant stress, $S_{ij}$ is the mechanical strain and $s_{ijkl}^{E}$ is the elastic compliance at constant electric field [24, p.132].

### Matrix Notation and Piezoelectric Coefficients of Thin Films

Piezoelectric charge coefficient ($d_{ijk}$) is a third-rank tensor due to the linear relationship between the first; i.e., $D$ and $E$, and second-rank tensors; i.e., $\sigma$ and $S$ [24, p. 19]. For the sake of simplicity, it is custom to use the subscripts $\{ijk\}$ as integers from 1 to 3, corresponding to the spatial directions, as shown in Figure 2.3. The notation $d_{31}$, for instance, represents the piezoelectric charge coefficient along the axis 3 when the crystal is subject to an applied stress along the axis 1. Rather than the tensor notation, however, often a matrix notation consisting of a set of replacement indices is utilized. Accordingly, indices $ij$ or $kl$ are replaced by indices $p$ or $q$, where $i$, $j$, $k$ and $l$ have values 1, 2 or 3 and $p$, $q$ have values 1, 2, 3, 4, 5 or 6 (see Table 2.1)

***Table 2.1:*** *Matrix notation of the piezoelectric charge coefficient [25, p. 8].*

| Tensor Notation ($ij$ or $kl$) | Voigt Notation ($p$ or $q$) |
|---|---|
| 11 | 1 |
| 22 | 2 |
| 33 | 3 |
| 23 or 32 | 4 |
| 31 or 13 | 5 |
| 12 or 21 | 6 |

Piezoelectric charge coefficient is also multi-axial, therefore it is possible to have numerous $d$ coefficients for a given piezoelectric material. In principal, the number of independent components of a third-rank tensor can be as high as; $N = 3^3 = 27$. However there are only

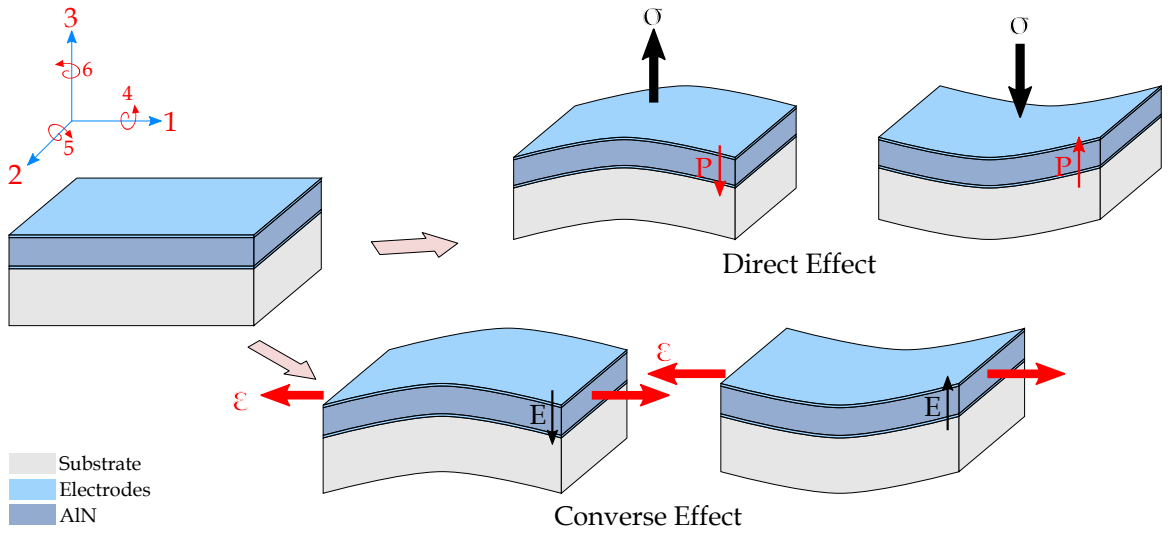


***Figure 2.3:*** *Schematic depiction of the direct and converse piezoelectric effects. Given example is an AlN thin film fabricated on top of a rigid substrate. AlN is sandwiched between two thin metallic layers, which act as the top and bottom electrodes. Input and output quantities are depicted with black and red arrows, respectively. In case of the converse effect, strain manifests in the form of a thickness change strictly along axis 3 due to substrate clamping.*

18 independent components for the piezoelectric tensor, in accordance with the symmetry considerations of stress and strain tensors ($\sigma_{ij} = \sigma_{ji}$ and $S_{ij} = S_{ji}$, respectively).

These independent components can be given in the matrix form as follows

$$d_{ijk} = \begin{pmatrix} 0 & 0 & 0 & 0 & d_{15} & 0 \\ 0 & 0 & 0 & d_{15} & 0 & 0 \\ d_{31} & d_{31} & d_{33} & 0 & 0 & 0 \end{pmatrix}$$

where, $d_{15}$ is the shear piezoelectric coefficient.

Within the scope of this work, the piezoelectric component is strained along its length and the polarization occurs along its thickness. The $d_{ijk}$ piezoelectric coefficients relate the applied electric field with the generated strain and for the current work $d_{31}$ is the relevant coefficient to maximize [26]. However, unlike freely vibrating bodies, piezoelectric films deposited on relatively thick substrates can not freely move in all directions.

Figure 2.3 depicts an exemplary thin film deposited on a substrate. Here, the piezoelectric film is strongly clamped to the substrate and its movement is restrained. Since the boundary conditions utilized for the definition of piezoelectric coefficients initially considered freely vibrating bodies, it is not possible to directly compare bulk properties to the thin film properties. Therefore, it is necessary to define a new set of coefficients. There are two cases to

consider for converse and direct piezoelectric effects.

When a piezoelectric thin film within a composite structure (i.e., strongly clamped to a substrate) is subject to an electric field, in-plane movements along directions 1 and 2 are not allowed hence in-plane strains are equal to zero. Instead, the piezoelectric film can only move along its thickness; i.e., direction 3. Meaning that, as a result of the applied field, in-plane stresses (along 1 and 2) and out-of-plane strain (along 3) would develop. This is the so-called converse effect and it can be formulated as

$$\sigma_{1,2} = -e_{31,f} \cdot E_3 \tag{2.5}$$

$$S_3 = d_{33,f} \cdot E_3 \tag{2.6}$$

where, $\sigma_{1,2}$ are the in-plane stresses, $e_{31,f}$ is the effective transversal piezoelectric coefficient, $E_3$ is the electric field perpendicular to the film plane, $S_3$ is the out-of-plane strain along direction 3 [27].

The conditions change for the direct piezoelectric effect. Here, it is necessary to take into consideration the in-plane strains (along 1 and 2) and out-of-plane stress (along 3) components. In this case, displacement that occurs along direction 3 ($D_3$) equals to

$$D_3 = e_{31,f} \cdot (S_1 + S_2) + d_{33,f} \cdot \sigma_3 \tag{2.7}$$

where, $S_1$ and $S_2$ are the in-plane strains and $\sigma_3$ is the stress along the thickness of the piezoelectric film [28].

Additionally, relevant piezoelectric effective longitudinal ($d_{31,f}$) and transversal ($e_{31,f}$) coefficients can be given from the bulk tensor properties as follows [27][29][30]

$$d_{33,f} = \frac{e_{33}}{c_{33}^E} = d_{33} - \frac{2s_{13}^E}{s_{11}^E + s_{12}^E} \cdot d_{31} \quad \text{with} \quad d_{33,f} < d_{33} \tag{2.8}$$

$$e_{31,f} = \frac{d_{31}}{s_{11}^E + s_{12}^E} = e_{31} - \frac{c_{13}^E}{c_{33}^E} \cdot e_{33} \quad \text{with} \quad |e_{31,f}| > |e_{31}| \tag{2.9}$$

where, $c_{ij}^E$ is the stiffness constant under constant electric field.

### 2.1.3 State-of-the-art: Thin Film Piezoelectric Materials

There are numerous piezoelectric materials utilized in sensor/actuator applications. In particular, ferroelectric materials such as PZT and/or single crystals of PMN-PT distinguish theirselves with their giant piezoelectric coefficients that are several times higher than the conventional piezoelectrics [31]. Thin film piezoelectric materials, on the other hand, are not able to compete with these materials in terms of the piezoelectric coefficient. They are, nevertheless, preferred in many applications due to their orders of magnitude lower dielectric losses and vacuum permittivities.

ZnO, AlN and PZT are often utilized as the piezoelectric constituent within magnetoelectric composite structures. The first two materials have wurtzite crystal structure and are highly piezoelectric along their thickness, hence require preferentially oriented growth. The properties of PZT are dependent on its composition and the highest piezoelectric coefficients are recorded near its near the morphotropic phase boundary[1] (MPB) [33].

These materials offer different advantages/disadvantages over each other considering different applications. Therefore, certain figure of merits (FOM) are evaluated in order to choose the most suitable constituent for a specific application [30][34][35]. In strain-dependent actuator applications, for instance, it is desired to have a high piezoelectric charge coefficient ($d_{ij}$), which relates electric displacement and stress, or strain and electric field [36, p.12]. Considering the sensor applications, on the other hand, it is necessary to have a high piezoelectric voltage coefficient ($g_{ij}$), which is a quantity of the electric field produced per unit mechanical stress applied. The two are related to each other through the permittivity via

$$g_{31} = \frac{d_{31}}{\varepsilon_0 \cdot \varepsilon_{33}} \tag{2.10}$$

where, $\varepsilon_0$ is the vacuum permittivity and $\varepsilon_{33}$ is the relative permittivity.

Basically, both $d$ and $g$ are terms related to the stress as the stimulus. For the current work, however, the external stimulus is strain. Therefore, it is more meaningful to consider another FOM; i.e., $h_{ij}$, which relates strain to the electric field as follows

[1] The term defines the phase transition between the tetragonal and the rhombohedral ferroelectric phases as a result of varying the composition and/or as a result of a mechanical pressure [32].

$$h_{31} = \frac{e_{31,f}}{\varepsilon_0 \cdot \varepsilon_{33}} \tag{2.11}$$

where, $h_{31}$ is the piezoelectric voltage coefficient in a deflected laminated structure [30].

Note that, Equation (2.10) considers freely moving bulk piezoelectric materials whereas Equation (2.11) is related to a thin film piezoelectric material that is strongly clamped to an underlying substrate. Therefore, $e_{31,f}$ is the more relevant coefficient considering the current work.

In resonating structures the effectiveness of energy transformation from electrical to mechanical energy is an important factor to consider. Part of the electrical energy is dissipated and transformed to heat and the dielectric loss angle (tan $\delta$) is involved in this phenomenon [30]. Therefore, it would be misleading to solely consider the voltage coefficient. To that end, another FOM, which would take into consideration the dielectric loss of a given material, is required. Accordingly, dielectric losses and the resulting sensor output can be represented with the following FOM

$$FOM_{piezo} = \frac{e_{31,f}}{\sqrt{\varepsilon_0 \cdot \varepsilon_{33} \cdot tan\delta}} \tag{2.12}$$

where, tan $\delta$ is the dielectric loss tangent [30].

A comparison of thin film piezoelectric materials and important coefficients/FOMs are summarized in Table 2.2. Despite not having the highest piezoelectric coefficients, AlN surpass both ZnO and PZT in terms of the relevant properties. It is advantageous against materials such as PZT and PMN-PT at producing large voltages in response to very small excitation, mainly due to its low vacuum permittivity. Even though, AlN and ZnO exhibit comparable $h_{31}$ values, AlN has a much higher piezoelectric FOM, mainly due to its much smaller tan $\delta$.

There are other requirements for a good piezoelectric material as well. For instance, it is crucial to minimize noise contributions, which in case of piezoelectrics, is generally observed as the pyroelectric noise. When utilizing insulators, high resistivity and dielectric breakdown strength (voltage) are desired. It is important to note that AlN is a highly resistive material ($10^{-10}\,\Omega \cdot \mathrm{cm} - 10^{-14}\,\Omega \cdot \mathrm{cm}$) with a high bandgap (6.2 eV). ZnO and PZT, on the other hand, have rather low bandgaps (3 and 3.4 eV) and are real semiconductors [37].

***Table 2.2:*** *Piezoelectric and dielectric properties of thin film materials used in sensor applications*

| Parameter | Unit | ZnO | PZT | AlN |
|---|---|---|---|---|
| $d_{33,f}$ | $\mathrm{pm/V}$ | 5.9 | 60 ... 130 | 5.1 |
| $e_{31,f}$ | $\mathrm{C/m^2}$ | –1 | –8 ... –12 | –1.3 |
| $\varepsilon_{33}$ | – | 10.9 | 300 ... 1300 | 10.2 |
| $h_{31}$* | $\mathrm{GV/m}$ | –10.3 | –0.7 ... –1.8 | –11.3 |
| $\tan\delta$ (%) | $10^5\,\mathrm{V/m}$ | 1 ... 10 | 1 ... 3 | 0.1 |
| $FOM_{piezo}$** | $10^5\,\mathrm{Pa}^{1/2}$ | 3 ... 10 | 4 ... 8 | 43 |
| References | – | [28][30] | [28][30][38][39] | [28] |

* (see Equation (2.11))
** (see Equation (2.12))
FOM is given in absolute values

Another aspect to consider is the fabrication methods, which usually include temperature treatments during or post fabrication. This necessitates high chemical stability as an important factor to consider. Furthermore, it is also important to keep processing temperatures as low as possible when used in combination with amorphous magnetostrictive alloys that have low Curie temperatures, above which magnetic materials lose their ordering. This is achievable using magnetron sputtering methods, whereas much higher process temperatures are necessary with other techniques. Once the prerequisites are met, they are easily reproducible, giving them an advantage over other piezoelectric materials. Since AlN satisfies the majority of these conditions overall, it is chosen as the piezoelectric constituent in the current work.

### 2.1.4 Aluminum Nitride

AlN is a highly commercialized material due to its superior properties in high frequency acoustic devices. It is fully compatibility with the semiconductor technology. Its most common products include signal processing devices such as the surface acoustic wave (SAW) and bulk acoustic wave (BAW) sensors as well as resonators, RF filters, actuators, energy harvesters, etc. [31].

Unlike ferroelectric piezoelectrics; e.g., PZT, AlN has a linear piezoelectric behavior and does not exhibit spontaneous polarization (Figure 2.4a). PZT, on the other hand, exhibits a non-linear behavior and produces a so-called butterfly loop, as a strain response to an applied electric field (Figure 2.4b). This originates from the domain wall switching of a ferroelectric material [37].

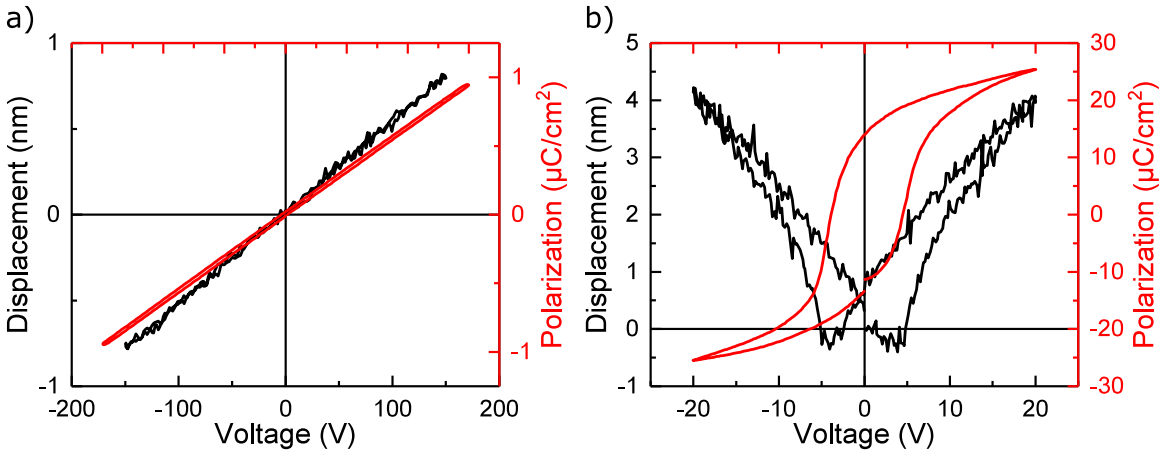


***Figure 2.4:*** *Typical displacement and polarization curves of thin film a) AlN and b) PZT. Investigated samples have 1.6 µm and 1 µm piezoelectric layer thickness, respectively. $d_{33,f}$ coefficient is derived as 5.3 pm/V and 130 pm/V for the samples, respectively.*

AlN is a polar piezoelectric material with a hexagonal wurtzite crystal structure (see Figure 2.5a). Its polar direction is decided during its growth process and can not be changed unlike PZT [21, p.4]. In case of AlN, electric polarization is induced in the AlN crystal resulting in a charge build-up on the material surface only when the material is subject to an external stress. With respect to the sensor design utilized in this work, aforementioned electric polarization shall be maximized along the *c*-axis of the AlN crystal; i.e., perpendicular to the underlying substrate's surface (see Section 2.1.2). Therefore it is essential to have a preferred growth direction during the synthesis of the material.

A closer look into the atomic arrangement within the hexagonal wurtzite structure of AlN is depicted in Figure 2.5b. The theoretical lattice parameters are $a = 3.11\,\text{Å}$ and $c = 4.98\,\text{Å}$, resulting in a near-ideal *c/a* ratio of 1.6 [40]. In theory, thin film AlN can grow in Al– or N–polarity depicted as yellow and blue shadowed tetrahedra, respectively. In practice, however, sputter deposited AlN exhibits N–polarity. Even though the reason for such behavior is not fully understood, one possible explanation can be the ion bombardment during film growth favoring the N-polar formation [41].

A close-up to the N–polar molecular tetrahedra is depicted in Figure 2.5d [42]. The atomic radii of Al and N are reported as 1.25 Å and 0.70 Å, respectively [40]. Here, a single Al atom is surrounded by 4 N atoms and they are connected to each other via covalent bonds. Due to the high difference in terms of electronegativities (1.6 and 3.0, respectively), there is ionic component to the bonding in AlN as well. When AlN crystal is subject to an external stress along its (001) direction, the N–Al–N bond angle seen in the tetrahedra changes; i.e.,

rotation of the bonds and the crystal deforms. In this way, the center of the positive and negative charges displace and gives rise to electric polarization [31].

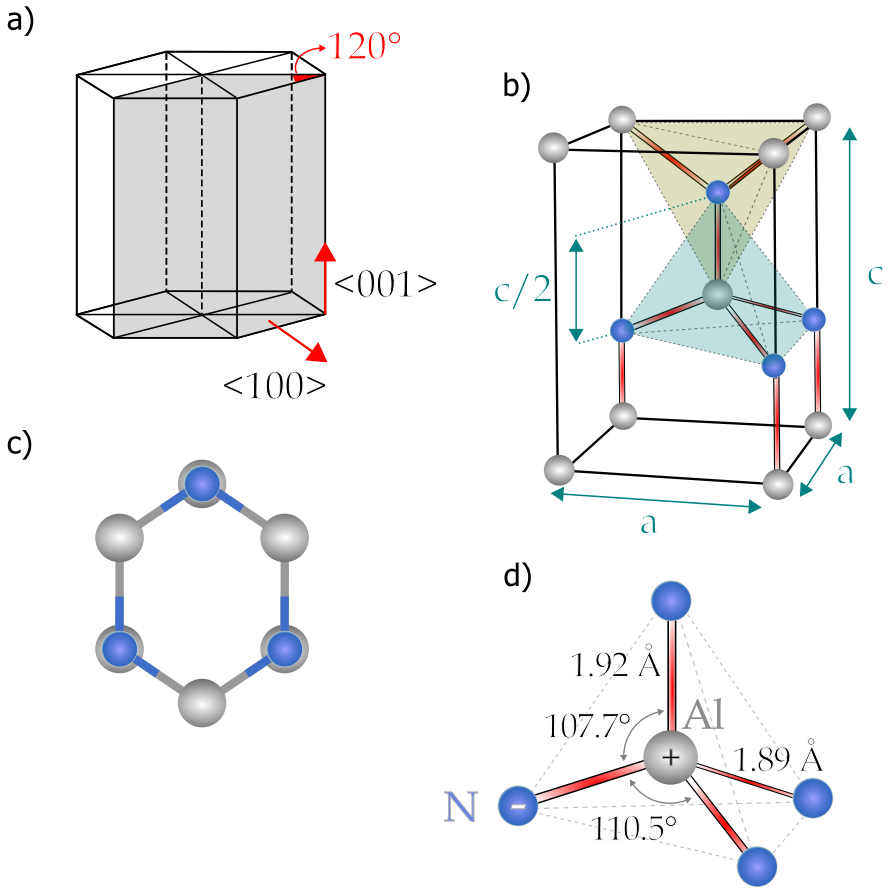


***Figure 2.5:*** *Crystal structure of AlN. a) An exemplary wurtzite hexagonal crystal structure, grey area depicts a (001) prism. Most probable thin film growth directions are shown with red arrows. b) Unit cell of AlN with grey and blue spheres representing N and Al atoms, respectively. The lattice parameters are a = 3.11 Å and c = 4.98 Å, respectively. The shadowed prisms show the tetrahedral molecular geometry for Al–polar (yellow prism) and N–polar (blue prism) AlN crystals. c) Plane view of the hexagonal crystal structure from top and the arrangement of the atoms. d) Close-up to the polar prisms. Angles of a N–polar molecular tetrahedra and lattice lengths are noted. Here, the central Al atom is surrounded by N atoms located at the corners of the tetrahedron. Image adapted from [43].*

## 2.2 Magnetostriction and FeCoSiB

First magnetic material known to men is a mineral called magnetite ($Fe_3O_4$), which is a natural magnet. However the first deliberate use of the magnetism can be related to the $11^{th}$ century, in the form of a magnetic compass invented in China. This magnetic compass; a long lodestone bar would rotate until approximately aligning itself along the north-south axis due to the Earth's magnetic field when allowed to freely float on water. Even though the real understanding of the Earth's magnetic field did not emerge until the end of the $16^{th}$ century, the use of compass nevertheless encouraged navigation and geographic discoveries. The fundamental breakthrough is achieved in 1820 by *H. C. Ørsted*. He discovered that an electric current flowing through a wire would produce a magnetic field and revealed the connection between electricity and magnetism for the first time [44, p.2]. This discovery led to the imminent development of the electromagnets and in the long run made major contributions to the development of the unified electromagnetic theory.

### 2.2.1 Magnetic Materials

Magnetism is a quantum mechanical phenomenon originating from the fundamental properties of the atom and its electrons. Electrons experience two types of rotational motions; i.e., spin and orbit. The former describes an electron's spin around itself and the latter along an orbit stretching around the atom. Both of these rotational movements create magnetic moments, which can interact and couple with each other. This phenomena is known as the spin-orbit coupling [44, p.87].

In simplistic terms, an electron orbiting an atom (and moving along the orbit) is analogous to an electric current flowing through a conducting wire. It has a magnetic dipole moment; i.e., a vector with a direction and a magnitude. Hence the sum of all magnetic dipole moments of all electrons of an atom defines its magnetic dipole moment. Note that in theory all materials are magnetic, but in practice not all materials produce effects that are reasonably large [44, p.12].

The magnetic behavior of different materials under the influence of a magnetic field is given as

$$M = \chi_m \cdot H \tag{2.13}$$

where, $M$ is the magnetization[1], $\chi_m$ is the magnetic (volume) susceptibility and $H$ is the magnetic field strength.

According to Equation (2.13), the magnetic susceptibility is a dimensionless value that can either be positive or negative. The sign of the constant simply relates to the attractive/repulsive nature of the material but tells little about the application relevance of the investigated material. When considering the design of a magnetic sensor, for instance, it is rather necessary to know the amount of magnetization that the material can sustain when under the influence of a magnetic field. Hence another constant; i.e., relative magnetic permeability ($\mu_r$), is often used for the characterization of magnetic materials. Relative permeability gives a material's magnetic permeability ($\mu$) with respect to the permeability of the free space ($\mu_0$). The former relates the external magnetic field strength to the magnetic flux density[2] via

$$B = \mu_0(H+M) = \mu_0(1+\chi_m)H = \mu_0 \cdot \mu_r \cdot H = \mu \cdot H \tag{2.14}$$

where, $B$ is the magnetic flux density [45, p.10].

There are five types of magnetic materials with respect to their magnetic characteristics; dia-, para-, antiferro-, ferri- and ferromagnetic materials.

- *Diamagnetic materials*; e.g., Bi, Cu, He, have negative and small susceptibilities ($\chi_m = 10^{-5}$), hence repulse magnetic fields [45, p.107]. Their permeabilities are lower than 1 [44, p.16]. Even though the effect is extremely small and is not easily observable, diamagnetic materials are often utilized in magnetic levitation.

- *Paramagnetic materials* exhibit positive but small susceptibilities in the range of $\chi_m = 10^{-5} - 10^{-2}$ [45, p.110]. Their permeabilities are greater than 1 [44, p.16]. These materials; e.g., Mg, Al, Na, etc., lack the ability to retain any magnetization in the absence of an external magnetic field. In practice, they are considered non-magnetic since the net sum of all magnetic dipole moments of a paramagnet equal zero.

- *Antiferromagnetic materials* magnetize weakly in the direction of an external field. They exhibit small and positive susceptibilities that are comparable to those of paramagnetic materials [45, p.110]. Their permeabilities are greater than 1 [44, p.16].

[1] The magnetic moment per unit volume.
[2] In the International System of Units (SI).

Materials such as Cr and Mn, certain oxides; e.g., MnO and FeO, as well as certain Fe-based compounds; e.g., FeMn, $Fe_2O_3$ (hematite), etc., belong to this group. Antiferromagnetic materials produce a mixed magnetic ordering, in which neighboring magnetic moments with same magnitudes are aligned in opposing directions with each other; i.e., parallel and anti-parallel [44, p.151].

- *Ferrimagnetic materials*; e.g., $Fe_3O_4$ (magnetite), Zn, etc., exhibit a similar behavior to antiferromagnetic materials; they possess neighboring magnetic moments aligned along opposing directions with each other [45, p. 118]. However since these moments have different magnitudes, magnetic susceptibilities of ferrimagnetic materials are rather high; approximately 3 for $BaFe_{12}O_{19}$ (barium ferrite) for instance [44, p.16].

- *Ferromagnetic materials*; e.g., Fe, Co, Ni, etc., can retain almost perfectly aligned magnetic moments even at the absence of an external magnetic field [46, p.323]. Ferromagnetic materials are the most widely utilized magnets with their very high susceptibilities that are up to $10^6$ higher than paramagnets.

Highest relative permeability value ($\mu_r = 10^6$) belongs to the commercially available ferromagnetic Metglas®2714A alloy [47]; an amorphous metallic glass ribbon fabricated by rapid solidification and consisting of Fe, Ni, Co, B and Si. The magnetic material utilized in this research; i.e., thin film FeCoSiB, is a ferromagnetic material as well. Hence for the remainder of the chapter, the discussion will strictly focus on the ferromagnetic materials and the related theory. Further reading about the uncovered topics can be found in numerous textbooks [44][45][46].

### 2.2.2 Ferromagnetic Materials

Ferromagnetic materials contain small regions with uniformly oriented dipoles known as the magnetic domains [44, p.116] These dipoles, randomly oriented in the paramagnetic state, tend to align along an energetically favorable direction when below the Curie temperature and lead to the formation of a spontaneous magnetization.

Magnetizing/demagnetizing of ferromagnets produce characteristic curves known as the magnetic hysteresis loops. An exemplary hysteresis loop and a close-up to its positive region are shown in Figure 2.6a and Figure 2.6b, respectively. Starting from a non-magnetized state, the material begins to magnetize with the influence of an external magnetic field applied

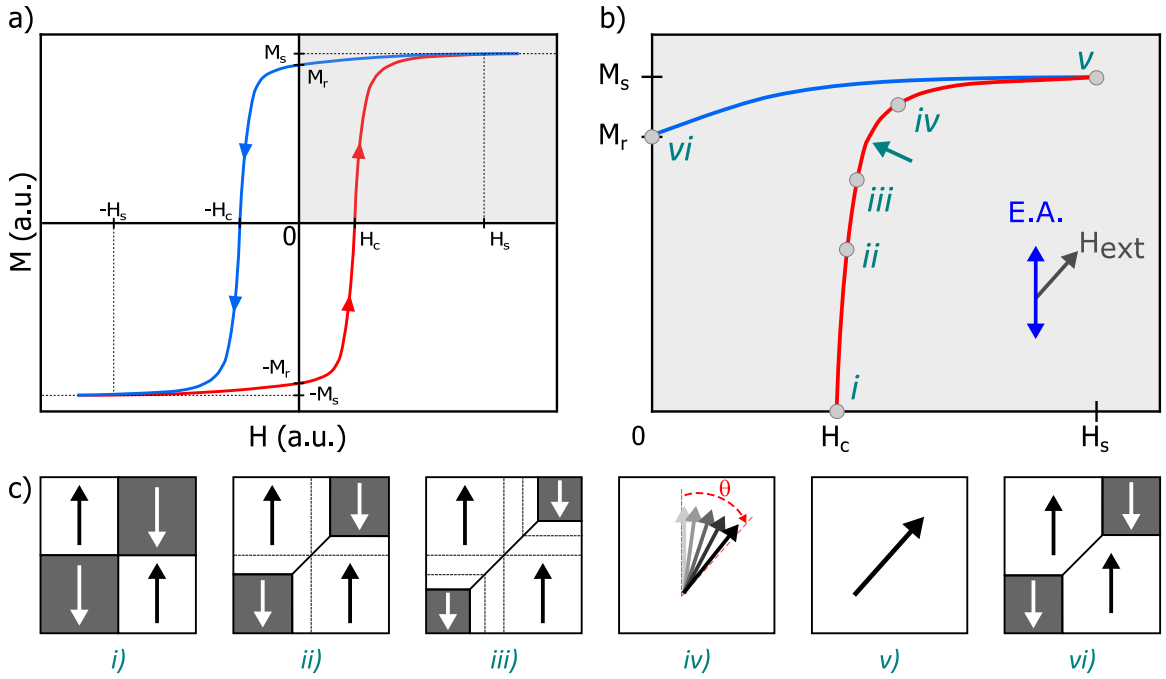


***Figure 2.6:*** *Magnetic properties of an exemplary ferromagnetic material. a) Typical magnetic hysteresis curve as a result of complete magnetization-demagnetization cycles in opposing magnetic field directions. Relevant hysteresis points are marked on the plot. Positive magnetic field - positive magnetization region of the hysteresis loop is highlighted with a gray background color. b) Close-up to the highlighted region. Magnetically easy axis and the direction of the external magnetic field are shown. Note that the easy axis includes two directions that oppose each other. Relevant points of the hysteresis curve are marked with italic roman letters. Accordingly demagnitization (i), increasing magnetization (ii, iii), beginning of magnetization rotation (teal arrow), continued rotation (iv), saturation magnetization (v) and remanent magnetization (vi) points are marked. c) Schematic representation of the respective domain structure at the relevant points. i) Demagnetized state. Magnetization of the individual domains is along the magnetically easy axis. Net magnetization equals zero. ii) Increasing magnetic field starts the domain wall motion. iii) Domain walls are further moved as the magnetic field continues to get stronger. iv) Since all domain walls disappered (at the teal arrow), magnetization starts its rotation towards the external field direction. Magnetization value is less than the saturation value and equals; $M = M_s \cdot cos\theta$, where $\theta$ is the angle between the magnetization and the external field. v) Magnetic saturation, perfectly aligned with the external field. vi) Removal of the external field results in the formation of domains following the energy minimization principle. Spontaneous magnetization is present. Image adapted from [44, p.328].*

along a certain direction. A fully magnetized state ($M_s$) is reached when the magnetic field strength exceeds a certain saturation field strength ($H_s$). Further increase of the magnetic field strength does not influence the magnetization of the material. When the external field is removed, the material retains most of its magnetization. This state is known as the remanent magnetization ($M_r$) state, where a ferromagnetic material forms a permanent magnet. In order to remove this property, it is necessary to apply a magnetic field in a direction that opposes the initial magnetizing field. At an external magnetic field strength that is equal to

the coercitive field strength ($-H_c$), a fully demagnetized state is reached. Further increasing the magnetic field strength along this direction brings the material to its negative saturated state ($-M_s$). Removing the magnetic field results in a remanent magnetization state ($-M_r$) and reversing the field direction and increasing its strength results in the demagnization (at $-H_c$) and saturation of the material once again. Note that the magnetization curve is symmetrical with respect to both magnetization and magnetic field axes; i.e., while the directions of the applied field and the magnetization reverse, their absolute magnitudes stay unchanged. On the other hand, given hysteresis represents a typical hard magnetic material; i.e., a ferromagnet, which would require a large saturation and demagnitizing fields such as permanent magnets. For a FeCoSiB thin film, for instance, these field requirements would shrink to extremely small magnitudes reflecting the soft magnetic nature of the material[1].

The process of magnetization, as schematized in Figure 2.6c, is previously explained by *P. Weiss* [44, p.116]. *Weiss* assumed the magnetization as the conversion from a multi-domain to a single domain state along the direction of an applied external field. Looking into the positive magnetization – positive magnetic field part of the previously investigated hysteresis curve (Figure 2.6b); at the coercive magnetic field (Figure 2.6b -i), magnetic domains are spontaneously magnetized and are aligned along the magnetically easy axis of the material (Figure 2.6c -i). They are separated from each other by domain walls and since neighboring domains are magnetized in opposing directions, they simply cancel each other out in terms of magnetization, hence the net magnetization of the material equals zero. When a magnetic field, which is greater than the coercitive field strength is applied (Figure 2.6b -ii), domains that are energetically favorable begin to grow at the expense of those that are not via domain wall motion (Figure 2.6c -ii). These are demonstrated as arrows that point upwards and downwards, respectively. Further increase of the field strength (Figure 2.6b -iii), prolongs the domain wall motion (Figure 2.6c -iii) until the domain walls are completely moved out. At a strong enough magnetic field strength (teal arrow), all domain walls disappear. After this point, the magnetization responds to further magnetic field increase (Figure 2.6b -iv) simply by rotating and aligning along it (Figure 2.6c -iv). When the material is saturated (Figure 2.6b -v), a single domain state, which is perfectly aligned with the external field is present (Figure 2.6c -v). If the external magnetic field is removed, the material moves to its remanent magnetization state (Figure 2.6b -vi). At this state, the single domain structure is divided into a multi-domain structure with magnetic domains aligned along the magnetically easy axis once more. The magnetization of domains that are along the magnetically easy direction exceeds the magnetization of those that are in the opposing easy direction,

[1] Hysteresis curves of an exemplary soft and hard magnetic material can be seen in Figure 2.10a.

hence a spontaneous magnetization is present (Figure 2.6c -vi). It can be summarized that the magnetization characteristics of a ferromagnet is due to the domain size increase and magnetization rotation in multi-domain and single-domain states, respectively.

### Formation of Magnetic Domains

As discussed, a magnetic material does not retain a fully magnetized single domain state once the external magnetic field is removed. Instead, it tries to establish a certain equilibrium and decreases its energy by forming multiple magnetic domains [48]. The mechanism is schematized considering a ferromagnetic single crystal material in Figure 2.7.

Initially, a uniformly magnetized finite body is in the single domain state. As a result of the magnetization, magnetic poles form at the sample surface and produce another magnetic field known as the demagnetizing field. The latter is a counter-acting field, which decreases the energy of the magnetic material (often called magnetostatic energy) and is proportional to the material's own magnetization via

$$H_d = -N_d \cdot M \tag{2.15}$$

where, $H_d$ is the demagnetizing field and $N_d$ is the demagnetizing factor [44, p.53].

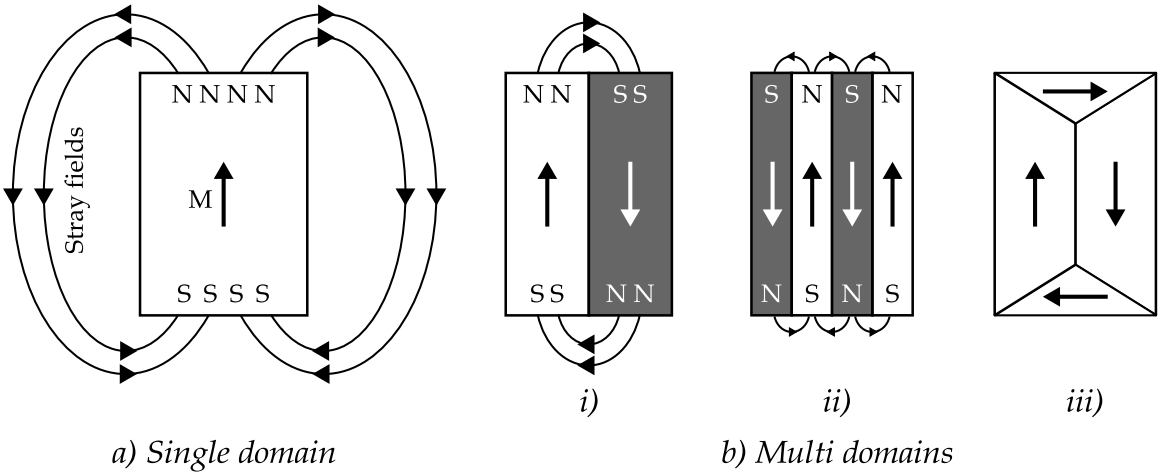


***Figure 2.7:*** *Schematic representation of domain formation. A magnetized sample forms a demagnetizing field that acts against the magnetization. Magnetic energy of the sample diminishes everytime it divides into multiple domains. Image adapted from [46, p.351].*

The energy of the magnetic material is reduced by a half upon formation of a two-domain state as shown in Figure 2.7b -i. Here, the single domain is split into two domains that are magnetized in opposite directions and are separated by magnetic transition zones known as the domain walls [44, p.276]. The distance between north and south poles diminish greatly thus reducing the spatial extent of the demagnetizing field. Domain divisions continue by continuously decreasing the magnetic energy until an equilibrium is reached as shown in Figure 2.7b -iii. Note that at this point, there is no longer any demagnetizing field since the flux circuit is completed within the sample body and consequently the magnetic energy is zero [46, p.352].

### Magnetic Anisotropy

Magnetic anisotropy describes the directional dependency of the magnetic properties. Aforementioned easy magnetization direction, for instance, refers to a specific direction along which alignment of dipoles is much easier in comparison to any other direction. This easy direction, or magnetic anisotropy, can be the result of an intrinsic property or can be induced via different mechanisms [46, p.351]. Most important anisotropies include magnetocrystalline anisotropy, shape anisotropy and stress anisotropy.

*Magnetocrystalline anisotropy* is an intrinsic property, which is related to the crystal lattice of the material in question and suggests that it is easier to magnetize a material along a certain crystallographic direction in comparison to the others. The forces governing the magnetocrystalline anisotropy are related to the interaction of the spin magnetic moment with the crystal lattice; i.e., the spin-orbit coupling [44, p.204]. A single crystal iron, for example, has its magnetically easy/hard directions along the <100> and <111> directions, respectively [46, p.348]. In this case, the external magnetic field strength required to align all of the materials dipoles along the <100> direction is much smaller than <111>. In principal, easy magnetization direction of a material represents the direction of its spontaneous magnetization.

*Stress anisotropy* is an induced property and refers to the alteration of the magnetic properties when under an applied stress [44, p.258]. It is related to the change in the magnetic susceptibility of a magnetostrictive material and is further discussed in Section 2.2.3.

*Shape anisotropy* is another induced property, and is related to the geometrical shape of the magnetized substance. As seen in Figure 2.7, magnetic poles form at the surface of a material

upon magnetization. If no external influence is present, these poles create a demagnetization field of their own. Considering a cantilever shaped sample, as is the case in this work, a much stronger demagnetizing field would form at the poles in comparison to the center region of the specimen [44, p.49]. Hence a much weaker demagnetizing field would be observed, if the magnetization of the sample is along its length (long axis).

### 2.2.3 Magnetostriction

#### Magnetostrictive Effects

Magnetostriction defines the ability of a ferromagnetic materials to change its dimensions when subject to a magnetic field until a saturation point is reached. It was first demonstrated by *J. P. Joule* in 1842 [49]. During the magnetization process (see Figure 2.6), domain boundaries within a ferromagnetic material displace from their initial locations and magnetic dipoles rotate in response to an external magnetic field. As a result, the material undergoes a macroscopic deformation [50]. Additionally, a secondary effect has been discovered in 1865 by *E. Villari*. This effect, known as the magnetoelastic effect, is the inverse magnetostrictive effect and refers to the change of the magnetic susceptibility of a magnetostrictive material when the material is subject to an external stress [51]. Both effects are schematized in Figure 2.8. Other magnetostriction related effects; e.g., Matteucci and Wiedemann effects, are not discussed here but can be found in various textbooks [52, p.37].

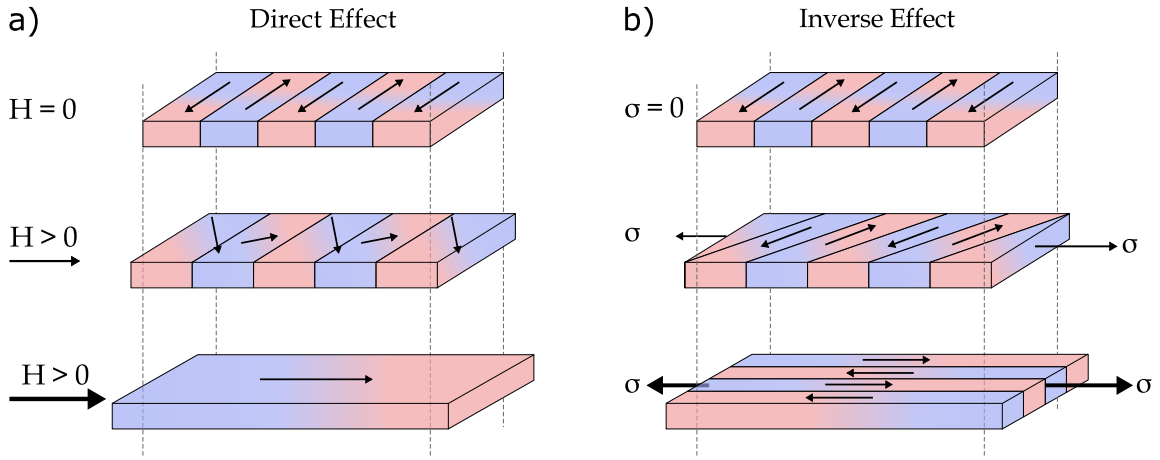


***Figure 2.8:*** *Schematic representation of the a) direct and b) inverse magnetostriction. Each rectangular prism represents a magnetic domain. Red and blue colored areas emphasize opposite poles.*

### Macroscopic Model of Magnetostriction

A simple schematic, describing the mechanism of magnetostriction, is given in Figure 2.9. Here, atoms and their electrons are schematized as black dots surrounded with oval lines, in which black arrows represent the net magnetic moment. Accordingly;

- Above the Curie temperature ($T > T_c$), magnetic sample is in the paramagnetic state, hence it has an initial length of L' (*i*). At this moment, all magnetic dipoles are randomly distributed producing no net magnetization.
- If the material is brought below its $T_c$ and if the material is crystalline, then magnetocrystalline anisotropy dominates and forces a rotation of all dipoles into a semi-ordered alignment (*ii*). A spontaneous magnetization occurs due to the spin-orbit coupling effects and a change in the sample's length is observed ($\Delta L'$). This phenomenon is known as the volume magnetostriction [53]. Note that one would not observe the influence of the magnetocrystalline anisotropy, if the material in question would be an amorphous magnetic material. Instead, a similar length change could be induced as a result of the shape anisotropy.

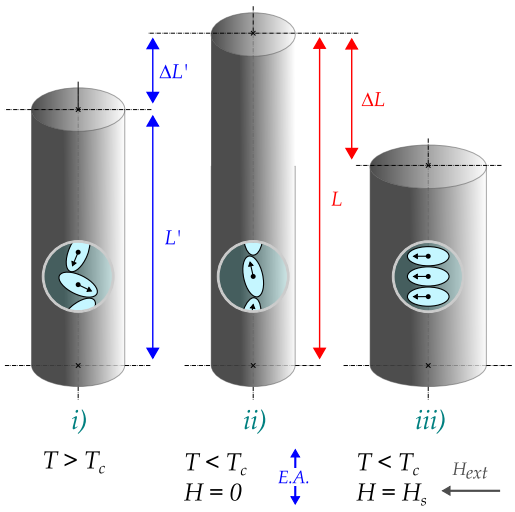


***Figure 2.9:*** *Schematized mechanism of magnetostriction. A ferromagnetic rod and its internal structure are depicted. i) Above $T_c$, there is no magnetic order. All magnetic dipoles (black arrows) of indivudial atoms (black dots) point in random directions. The total net magnetization of the rod equals zero. ii) Below $T_c$, spontaneous magnetization occurs. All spins rotate and align along the magnetic easy axis (depicted with the blue arrow). A certain length change ($\Delta L'$) occurs. iii) An external field is applied along the short axis of the rod. All dipoles rotate in order to align in the same direction. A bigger length change ($\Delta L$) occurs until reaching the magnetic saturation. Note that all dimensional change depictions are exagerated. Adapted from [44, p.257].*

- When a magnetic field along another direction is applied, all dipoles would start to rotate, until the saturation field strength ($H = H_s$) is reached (*iii*). In the given example, the direction of the magnetic field is 90° to the easy axis of the material and the induced strain equals too $\Delta L$.

Hence the magnetostriction of the specimen equals

$$\lambda = \frac{\Delta L}{L} \tag{2.16}$$

where, $\lambda$ is the longitudinal (Joule) magnetostriction, $\Delta L$ is the length change and $L$ is the length of the material in question [44, p.240].

Since Joule magnetostriction is a three-dimensional and anisotropic shape change; not only a longitudinal but also a transversal magnetostriction ($\lambda_t$) occurs, due to volume preservation. The latter equals

$$\lambda_t = -\frac{\lambda_l}{2} \tag{2.17}$$

Note that the magnetostriction can either be positive or negative; suggesting that both an expansion or a shrinkage along the applied magnetic field direction can occur for different materials. The effect is extremely small, however, with a maximum length change ($\lambda_s$) at the saturation magnetization of any given ferromagnet. Highest magnetostriction is observed in Terfenol-D ($Tb_xDy_{1-x}Fe_2$, x$\sim$3), reaching $\lambda_s = 1400 \cdot 10^{-6}$ [54]. It is important to point out that a spontaneous magnetostriction is always present in a ferromagnet when the material is below its Curie temperature ($T < T_c$). However, due to its relatively higher magnitude, the term magnetostriction is often utilized for the saturation magnetostriction.

**Magnetostriction and Piezomagnetic Coefficient**

Magnetostriction is dependent both on the direction and the magnitude of the external magnetic field, therefore follows the magnetization curve. An exemplary magnetostriction curve of a soft magnetic material is shown in Figure 2.10b. Unlike magnetization, magnetostriction does not change sign when the magnetic field direction is reversed by 180°. Therefore, $\lambda_s$ of a ferromagnet is equal at both saturation fields; i.e., $-H_s$ and $H_s$. This is due to the linear

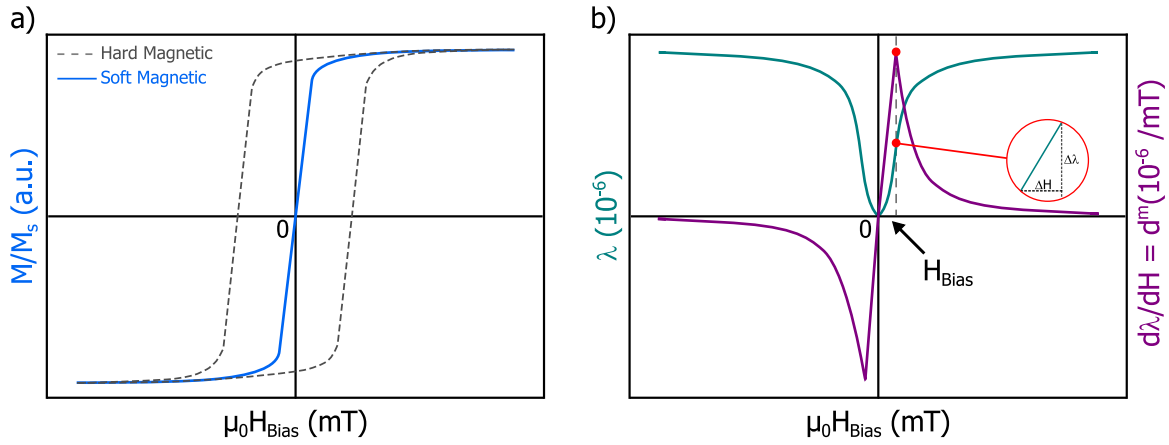


***Figure 2.10:*** *a) Magnetization of a soft ferromagnetic material (blue) in comparison to a hard ferromagnetic material (dashed). The area enclosed by the hysteresis loop is much smaller for a soft magnetic material and is related to the dissipated energy per sample volume. Note that the curve is normalized with respect to the saturation magnetization ($M_s$). b) Magnetostriction and piezomagnetic behavior of an exemplary soft magnetic FeCoSiB thin film. The piezomagnetic coefficient exhibits a maximum where the permeability of the material is the highest. Note that despite the sign change of the magnetic field, the magnetostriction curve is symmetrical with respect to y-axis.*

relationship between the magnetostriction and the square of the magnetization;

$$\lambda = \frac{3}{2}\lambda_{Si} \cdot \left(\frac{M}{M_s}\right)^2 \tag{2.18}$$

where, $\lambda_{Si}$ is the isotropic saturation magnetostriction (of a cubic crystal for instance) and $M = M_s \cdot cos\theta$ with $\theta$ being the angle between the magnetization and the external field.

When considering sensor applications, it is desirable to have a material with a high magnetic susceptibility. Magnetic susceptibility indicates how much a material can magnetize in response to magnetic field, hence reflects to the induced strain per field. The latter is known as the piezomagnetic coefficient and equals to the slope of the magnetostriction curve

$$d_{ij}^m = \frac{\partial \lambda}{\partial H} \tag{2.19}$$

where, $d_{ij}^m$ is the piezomagnetic coefficient.

Piezomagnetic constitutive equations can be written in a similar fashion to the piezoelectric constitutive equations as well [55, p.9]

$$B_i = d_{ij}^m \cdot \sigma + \mu_{ij}^\sigma \cdot H_j \tag{2.20}$$

$$S_{ij} = s_{ij}^H \cdot \sigma + d_{ij}^m \cdot H_j \tag{2.21}$$

where, $B_i$ is the magnetic induction, $\sigma$ is the stress, $\mu_{ij}^\sigma$ is the permeability at constant stress, $S_{ij}$ is the strain and $s_{ij}^H$ is the elastic constant at constant magnetic field.

Exemplary magnetostriction and piezomagnetic curves of the amorphous magnetostrictive alloy utilized in this work; i.e., FeCoSiB, are given in Figure 2.10b. Note that the material is extremely soft magnetic, hence exhibits almost no hysteresis unlike hard magnetic material. The derivative of the magnetostrictive curve (purple) with respect to the external magnetic field exhibits a maximum where the slope of the magnetostriction curve (teal) is the highest, but decays when the material reaches its magnetic saturation. Hence the magnetic field magnitude where the material has the highest piezomagnetic coefficient defines its working point. Therefore, magnetostrictive materials are subject to a DC bias field in order to bring them to their working point in a magnetoelectric sensor concept. Further discussion of this topic will be presented in Section 2.3.4.

### 2.2.4 State-of-the-art: Magnetostrictive Materials

Considering their use in magnetoelectric composites, magnetostrictive materials that satisfy necessary material properties are limited. Most important parameters to consider include the magnetic permeability, remanent magnetization magnitude, coercive magnetic field strength, saturation magnetostriction magnitude, piezomagnetic coefficient ($d_{33}^m$), Curie temperature and electromechanical coupling coefficient ($k_{33}$) [68][56]. A summary of the most important magnetostrictive materials is given in Table 2.3

***Table 2.3:*** *Material properties of relevant magnetostrictive materials utilized in magnetoelectric composites*

| Material / Parameter | Structure | $\mu_r$ | $\lambda_s$ ($10^{-6}$) | $d_{33}^m$ ($10^{-6}$/Oe) | $k_{33}$ | $T_c$ (°C) | Ref. |
|---|---|---|---|---|---|---|---|
| $NiFe_2O_4$ (*NFO*) | PC | 20 | -26 | $\sim 0.06$ | - | 535 | [56][57] |
| $TbFe_2$ (*Terfenol*) | PC | - | $> 1000$ | 0.1 | - | 423 | [58] |
| *$Tb_{0.4}Fe_{0.6}/Fe_{0.5}Co_{0.5}$ | ML | - | 30 | 0.1 - 0.4 | - | 140/980 | [59][60] |
| $Tb_xDy_{1-x}Fe_2$ (*Terfenol-D*) | SC | 6 ... 10 | 900 ... 1620 | $\sim 1.2$ | 0.44 | 380 | [56][61][62] |
| FeGa (*Galfenol*) | PC | 20 | -2100 | $\sim 0.3$ | - | - | [56][63][64] |
| *FeGaB | A | 400 | 70 | 7 | - | - | [65][66] |
| FeBSiC (*Metglas 2605SA1/SC*) | A | $> 40000$ | 27/60 | $\sim 4$ | 0.37 | 370 | [56][62][63][67] |

*Except $Tb_{0.4}Fe_{0.6}/Fe_{0.5}Co_{0.5}$ and FeGaB, all properties belong to bulk materials.
Material structures; SC: single crystal, PC: polycrystal, A: amorphous and ML: multilayers of amorphous TbFe and crystalline FeCo.

Among these materials, FeBSiC and FeGaB come forward with their extremely high permeabilities and piezomagnetic coefficients. On the other hand, they have very small magnetostrictions in comparison to materials such as $TbFe_2$, $TbDyFe_2$ and FeGa. Despite their extremely high magnetostrictions, however, materials such as $TbDyFe_2$ lack in terms of $d_{33}^m$ hence require very large magnetic fields to flip the direction of the magnetization. This necessitates the application of relatively high DC bias fields; e.g., 450 Oe for $TbDyFe_2$ [69]. This is more than an order of magnitude higher in comparison to what is necessary for FeBSiC and FeGaB [63][65].

### 2.2.5 Thin Film FeCoSiB

Aforementioned FeBSiC refers to relatively thick ($10\,\mu m - 35\,\mu m$) layers, which are functionalized in the form of macroscopic sensors bonded by epoxy resin. They are produced via melt spinning; i.e., fast cooling from very high temperatures [70, p.1725]. Magnetostrictive materials used in this work, on the other hand, are thin films ($1\,\mu m - 3\,\mu m$) of FeCoSiB alloy fabricated using magnetron sputtering. Similar to the metallic glasses, chosen alloy target contains large amounts of Fe and Co in order to provide the necessary magnetic properties whereas Si and B are the glass-forming constituents [71]. In contradiction to the thick layers, thin films of FeCoSiB are deposited at low temperatures; i.e., $< 100\,^{\circ}C$, either with [72] or without [73] the presence of a bias field ($\sim$100 Oe) during deposition.

Since these thin films are deposited on thick substrates, they are not able to freely move. Therefore, it is more reliable to evaluate the magnetostrictive properties of these films using the magnetoelastic coefficient ($b$) instead of the magnetostriction. Magnetoelastic coefficient[1] is related to the magnetostriction via

$$\lambda = -b\left(\frac{1+\nu_f}{E_f}\right) \tag{2.22}$$

where $E_f$ and $\nu_f$ are the Young's modulus and the Poisson's ratio of the film, respectively [74]

Previous research demonstrated that, these films exhibit a magnetoelastic coefficient as high as $b = 10$ MPa at saturation, following a post deposition magnetic annealing process [72].

[1] The determination of $b$ is discussed in Section 3.3.4.

## 2.3 Magnetoelectric Effect and Composite Sensors

### 2.3.1 Introduction

The magnetoelectric effect describes the appearance of an electric polarization ($P$) in response to an applied magnetic field ($H$) or the change in magnetization ($M$) in response to an applied electric field ($E$) [75]. The very first prediction of the magnetoelectric effect belongs to *P. Curie* during his work on the crystallographic symmetry. According to *P. Curie*, the conditions of symmetry showed that a body with asymmetric molecules would get dielectrically polarized when placed in a magnetic field and magnetically polarized when placed in an electric field [76]. Half a century later, *I. E. Dzyaloshinskii* further investigated the asymmetry argument and correctly predicted that there was a linear reciprocal interaction between the local electric field (in a medium) and its magnetization, as well as between the local magnetic field (in a medium) and its electric polarization [77]. His prediction was experimentally confirmed by *D. N. Astrov*, who induced magnetization in an antiferromagnetic $Cr_2O_3$ single-phase compound by applying an electric field at various temperatures [78]. Experimentally proven existence of the magnetoelectric effect led to further investigation on additional single-phase materials; e.g., $Ti_2O_3$, $GaFeO_3$, $Mn_3B_7O_{13}I$, $LiCoPO_4$, $LiNiPO_4$, etc. [79]. However, utilization of the magnetoelectric effect did not prove to be easy due to very low effect magnitude and near zero Curie temperatures of the investigated materials. *O'Dell et al.* previously offered that a high magnetoelectric effect could only be achieved in a material which combines high electric and magnetic susceptibilities [80]. The only known single-phase material adequate to this description is epitaxially grown $BiFeO_3$, which shows a magnetoelectric coefficient ($\alpha$)[1] that is an order of magnitude higher in comparison to other single-phase materials [81]. In 1972, *J. van Suchtelen* proposed the composite effect [82][83]. The very first artificial magnetoelectric material was fabricated by unidirectional solidification of an eutectic composite of $BaTiO_3$ (BTO) and $CoFe_2O_4$ (CFO). Observed magnetoelectric voltage coefficients ($\alpha_{ME}$)[2] were as high as $130\,\mathrm{mV/(cm\cdot Oe)}$, representing an approximately two orders of magnitude improvement compared to the intrinsic magnetoelectric effect. This discovery encouraged the pursue of the previously unattainable applications via use of composites instead of single phase magnetoelectric materials [79].

[1] The magnetoelectric voltage coefficient, $\alpha$, is given in $\mathrm{V/Oe}$.
[2] The magnetoelectric coefficient, $\alpha_{ME}$, is given in $\mathrm{V/(cm\cdot Oe)}$.

### 2.3.2 Fundamentals

Magnetoeletric effect offers the possibility to manipulate electric and magnetic orders through each other. Previous research mainly focus on two material groups, which were identified as major source for large magnetoeletric coupling; i.e., multiferroic and composite materials (see Figure 2.11a).

#### Magnetoelectric Effect in Multiferroic Materials

Multiferroic materials are ferroic order materials, which combine two or more ferroic properties; i.e., spontaneous magnetization (Co, Fe, Ni, etc.), polarization ($BaTiO_3$, $PbTiO_3$) and deformation (NiTi alloys), in the same single phase [84]. There are several cross-coupling phenomena involving the ferroic order parameters, as shown in Figure 2.11b. In particular, cross-coupling between magnetic/electric fields and their respective products (polarization/magnetization) give rise to the magnetoelectric effect. Simply put, magnetoelectric effect enables the control of dielectric polarization by a magnetic field and the manipulation of magnetization by an electric field [68]. Accordingly, the linear relationship between these parameters; i.e., direct and converse magnetoelectric effects, can be written as

$$\Delta P = \alpha_H \Delta H \tag{2.23}$$

$$\mu_0 \Delta M = \alpha_E \Delta E \tag{2.24}$$

where, $P$ is the electric polarization, $H$ is the magnetic field, $\alpha_H$ and $\alpha_E$ are the magnetoelectric coupling coefficients between electric and magnetic fields, $\mu_0$ is the vacuum magnetic permeability, $M$ is the magnetization and $E$ is the electric field [68].

The interactions shown in Figure 2.11b can be better understood via the Landau theory of phase transitions, where the expansion of the free energy of a material can be written as [79]

$$\begin{aligned} F(\vec{E},\vec{H}) = F_0 - P_i^S E_i - M_i^S H_i - \frac{1}{2}\varepsilon_0 \varepsilon_{ij} E_i E_j - \frac{1}{2}\mu_0 \mu_{ij} H_i H_j \\ - \alpha_{ij} E_i H_j - \frac{1}{2}\beta_{ijk} E_i H_j H_k - \frac{1}{2}\gamma_{ijk} H_i E_j E_k - \ldots \end{aligned} \tag{2.25}$$

where, $F_0$ is the initial free energy.

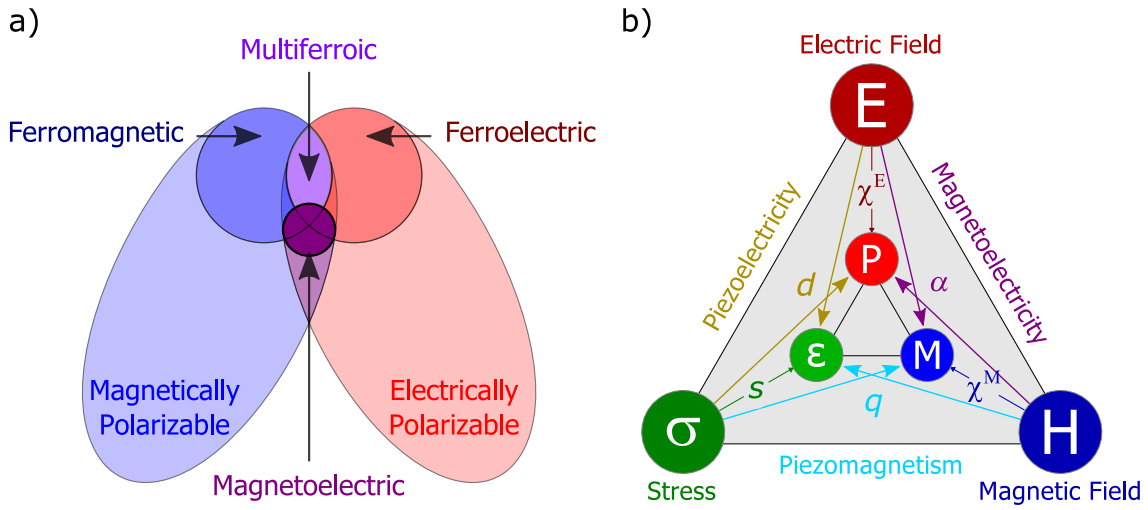


***Figure 2.11:*** *a) Relationship between multiferroic and magnetoelectric materials. Image adapted from [85]. b) Schematic depiction of the coupling mechanisms with respect to the expansion of the free energy described within the Landau theory of phase transition [86]. The applied fields and the stress tensor (E, H, σ) produce electric polarization, magnetization and strain (P, M, ε), respectively. Electrostatic, magnetostatic and elastic energies in materials are represented with electrical susceptibility ($\chi^E$), magnetic susceptibility ($\chi^H$) and the elastic tensor (s). The remaining terms represent the linear magnetoelectric (α), piezomagnetic (q) and piezoelectric (d) effects [23][75].*

Differentiation of Equation (2.25) produces the terms for polarization and magnetization

$$\begin{aligned} P_i(\vec{E},\vec{H}) &= -\frac{\partial F}{\partial E_i} \\ &= P_i^S + \varepsilon_0 \varepsilon_{ij} E_j + \alpha_{ij} H_j + \frac{1}{2}\beta_{ijk} H_j H_k + \gamma_{ijk} H_i E_j - \ldots \end{aligned} \tag{2.26}$$

$$\begin{aligned} M_i(\vec{E},\vec{H}) &= -\frac{\partial F}{\partial H_i} \\ &= M_i^S + \mu_0 \mu_{ij} H_j + \alpha_{ij} E_i + \beta_{ijk} E_i H_j + \frac{1}{2}\gamma_{ijk} E_j E_k - \ldots \end{aligned} \tag{2.27}$$

where, $P_i^S$ and $M_i^S$ are the spontaneous electric polarization and magnetization, respectively. Electric and magnetic susceptibilities are denoted with $\varepsilon$ and $\mu$, respectively. $\beta_{ijk}$ and $\gamma_{ijk}$ are the higher-order magnetoelectric effects. Finally, $\alpha$ is the magnetoelectric voltage coefficient, which represents the induction of polarization by a magnetic field ($ME_H$) or magnetization by an electric field ($ME_E$).

This last effect is designated as the linear magnetoelectric effect or simply the magnetoelectric effect. It can be deducted from Equation (2.26) and Equation (2.27), that a multiferroic

material can be electrically (and/or magnetically) polarized by an applied magnetic (and/or electric) field by means of the magnetoelectric effect. The magnitude of the magnetoelectric effect is limited by the microscopic mechanisms that drives it [87];

$$\alpha_{ij}^2 < \kappa_{ii}^E \chi_{jj}^M \tag{2.28}$$

where, $\kappa^E$ and $\chi^M$ are electric and magnetic susceptibilities, respectively [88].

**Magnetoelectric Effect in Composites**

Unlike the first group, composite materials do not possess inherent magnetoelectric properties but the magnetoelectric effect appears as the product property of physically separated magnetostrictive and piezoelectric phases [86]. Magnetoelectric coupling in composite systems can be mediated in three distinctive ways; through (*i*) strain, (*ii*) charge carrier and (*iii*) spin exchange [89][90][91]. The initial method, strain-mediated magnetoelectric coupling, has been the point of interest in the recent years, as is in this work.

Considering a simple composite system, where piezoelectric (*phase 1*) and ferromagnetic (*phase 2*) materials are mechanically attached to each other. If such a system is placed under an applied magnetic field, the latter material would change its shape and produce a strain, as its magnetization aligns itself along the direction of the external field. The generated strain would then be transferred to the piezoelectric phase, since both phases are elastically coupled with each other. This coupling would shift the dipoles (within the piezoelectric phase) from their initial position, producing a net polarization that can be observed as an electrical signal. Above described strain-mediated coupling of intrinsically non-magnetoelectric materials is known as the composite magnetoelectric effect [79].

In principal, composite magnetoelectric effect is a product property in the form of

$$\left.\begin{array}{ll} \textit{Phase}\,1: & A \longrightarrow B \\ \textit{Phase}\,2: & B \longrightarrow C \end{array}\right\} A \longrightarrow C \tag{2.29}$$

where, one phase exhibits the property $A \longrightarrow B$ and the other $B \longrightarrow C$. These properties

***Table 2.4:*** *List of well-known piezoelectric and magnetostrictive materials used as constituents of magnetoelectric composites. Table taken from [68].*

| Piezoelectric Phase | Magnetostrictive Phase |
|---|---|
| **Lead-based:** | **Metals:** |
| $Pb(Zr,Ti)O_3$ (PZT) | Fe, Co, Ni |
| $Pb(Mg_{1/3}Nb_{2/3})O_3 - PbTiO_3$ (PMN-PT) | **Alloys:** |
| $Pb(Zn_{1/3}Nb_{2/3})O_3 - PbTiO_3$ (PZN-PT) | FeNi-based |
| $Pb(Mg_{1/3}Nb_{2/3})_y(Zr_xTi_{1-x})_{1-y}O_3$ (PMN-PZT) | FeCo-based |
| $Pb(In_{1/2}Nb_{1/2})O_3 - Pb(Mg_{1/3}Nb_{2/3})O_3$ | CoNi-based |
| $-PbTiO_3$ (PIN-PMN-PT) | |
| **Lead-free:** | $Ni_2MnGa$ |
| $BaTiO_3$ (BTO)-based | Permendur (FeCoV) |
| $(K_{0.5}Na_{0.5})NbO_3$ (KNN)-based | Galfenol (FeGa), FeGaB |
| $Na_{0.5}Bi_{0.5}TiO_3$ (NBT)-based | Samfenol |
| **Others:** | Terfenol-D ($Tb_{1-x}Dy_xFe_2$) |
| AlN | Fe-based metallic glasses (FeBSi, FeBSiC, FeCoB) |
| ZnO | FeCoSi, FeCoSiB, FeCuNbSiB |
| $(Sr,Ba)Nb_2O_5$ | **Ceramics:** |
| $Ba_{1-x}Sr_xTiO_3$ (BSTO) | $Fe_3O_4$ |
| $Bi_{1-x}Sr_xTiO_3$ (BST) | $Zn_{0.1}Fe_{2.9}O_4$ (ZFO) |
| $La_3Ga_{5.5}SiO_{14}$ (LGS) | $La_xSr_yMnO_3$ (LSMO) |
| $La_3Ga_{5.5}Ta_{0.5}O_{14}$ (LGT) | $La_xCa_yMnO_3$ (LCMO) |
| Polyurethane (PU) | Ferrites or doped Ferrites (e.g., $NiFe_2O_4$ (NFO), |
| Polyvinylidene difluoride (PVDF) | $CoFe_2O_4$ (CFO), Li ferrite, Cu ferrite, Mn ferrite |

combined suggests that the application of variable A (or B) results in the effect B (or A), respectively. Hence the composite exhibits a new property $A \longrightarrow C$ that appears as the product property of variables $A$ and $B$. Practically, composite magnetoelectric effect depicted in Equation (2.29) translates into the cross interaction of the magnetostrictive and piezoelectric effects and can be summarized as

$$\begin{aligned} ME_H &= \frac{magnetic}{mechanic} \times \frac{mechanic}{electric} \\ ME_E &= \frac{electric}{mechanic} \times \frac{mechanic}{magnetic} \end{aligned} \tag{2.30}$$

where, $ME_H$ and $ME_E$ represent direct and converse couplings, ${}^{magnetic}/_{mechanic}$ and ${}^{mechanic}/_{electric}$ define magnetostrictive and piezoelectric effects, respectively [92].

Basic principal to achieve a high magnetoelectric effect is to combine materials with high piezoelectric and magnetostrictive properties with good interfacial coupling between the two. Accordingly, numerous material combinations have been investigated. PZT-based ceramics have been the number one choice among piezoelectric materials, due to their high piezoelectric coefficients and easy processing. On the magnetic side, materials such as $TbDyFe_2$

[93] and $Fe_{81}B_{13.5}Si_{3.5}C_2$ (Metglas) [67] are subject to much attention due to their high magnetostriction and permeability, respectively. A list of the well-known piezoelectric and magnetostrictive materials used as components of magnetoelectric composites are given in Table 2.4.

### Connectivity

The magnitude of the composite magnetoelectric response and the efficiency of the strain transfer depend mainly on the quality of the phase connectivity and the interfacial bonding between the constituents [68]. Mechanical bonding is evaluated through the coupling factor and it varies with respect to the connectivity scheme of the composite. The influence can be better understood from the formula expressing the magnetoelectric coefficient of a composite

$$\alpha_{ME} = \frac{\partial P}{\partial H} = d^p \cdot k_c \cdot d^m \tag{2.31}$$

with

$$d^p = \frac{\partial P}{\partial S} \qquad \text{and} \qquad d^m = \frac{\partial S}{\partial H} \tag{2.32}$$

where, $\alpha_{ME}$ is the magnetoelectric coefficient, $k_c$ is the coupling factor; i.e., quality of the strain transfer between two phases ($0 \leq k_c \leq 1$), $d^p$ and $d^m$ are the piezoelectric and piezomagnetic coefficients, respectively [94].

Clearly, a low coupling is not desirable, since effective strain transfer is one of the most important, if not the most important, variable from the application point of view of the magnetoelectric composites.

Connectivity defines different composite geometries and can be given by the ratio $(n+3)!/3!n!$ where $n$ represents the number of phases in the composite. Hence there are 10 possible connectivity schemes for two-phase composite systems. Most common connectivity schemes utilized in bulk composites include; (0-3) type particulate composites, (1-3) type fiber/rod composites and (2-2) type laminate composites where the numbers (0 to 3) denote the connectivity of each phase within the composite [95] (see Figure 2.12). Initial composites utilized the (0-3) type connectivity; i.e., a composite consisting of single-phase magnetic par-

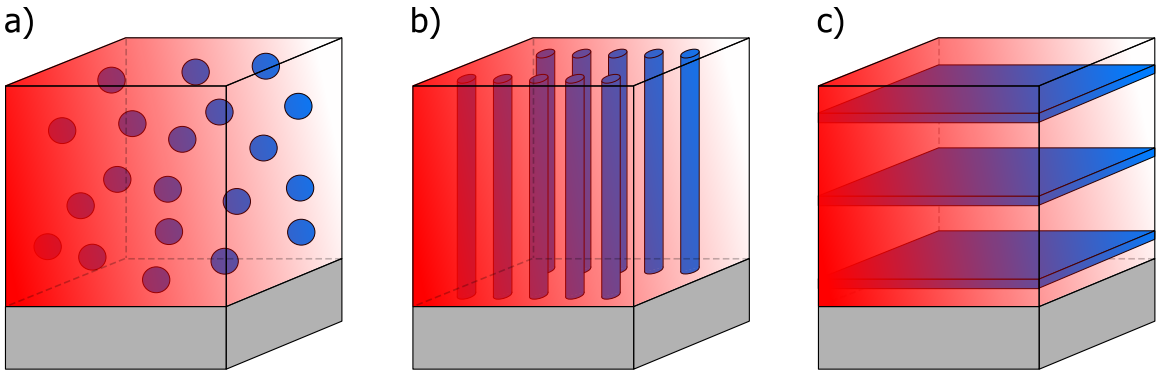


***Figure 2.12:*** *Schematic illustration of common connectivity schemes: a) 0-3 particulate composite, b) 1-3 fiber/rod composite, c) 2-2 laminate composite. The color code is as follows; red represents the piezoelectric phase, blue represents the magnetostrictive phase and grey represents the substrate on which the composite is fabricated. Image adapted from [95].*

ticles (0) embedded in a piezoelectric matrix (3) [83]. However, this type of connectivity offered limited coupling resulting in a greatly reduced magnetoelectric coefficient, generally one to two orders of magnitude below $1\,\mathrm{V}/(\mathrm{cm}\cdot\mathrm{Oe})$ [94]. Even though they are easier to process, they suffer from interdiffusion of phases during sintering, mechanical defects such as pores and high dielectric losses [79].

### Bulk 2-2 Laminate Composites

A connectivity scheme, which solves the coupling problem as well as structural problems, is the (2-2) laminate (horizontal) system. Laminate composites using this connectivity consist of simple bilayers or multilayer structures, where the piezoelectric and magnetostrictive layers are alternated on top of each other, usually in the form of sandwich structures. The first demonstration of a sandwich structure was presented by *Ryu et al.*, achieving a giant magnetoelectric voltage coefficient of $4.7\,\mathrm{V}/(\mathrm{cm}\cdot\mathrm{Oe})$ using a PZT/$TbDyFe_2$ trilayer disc [96][97]. Further examples of such laminates can be found in [61][96][98] .

These laminate composites exhibit various working modes of operation with respect to the direction of polarization and magnetization of the constituents. Fundamental working modes include T-T (transverse magnetization and transverse polarization), L-T (longitudinal magnetization and transverse polarization), L-L (longitudinal magnetization and longitudinal polarization) and T-L (transverse magnetization and longitudinal polarization) (see Figure 2.13). A late addition is the reworked version of the L-L mode; the so-called push-pull mode [99].

A direct relation between the operation mode and the magnitude of the magnetoelectric effect

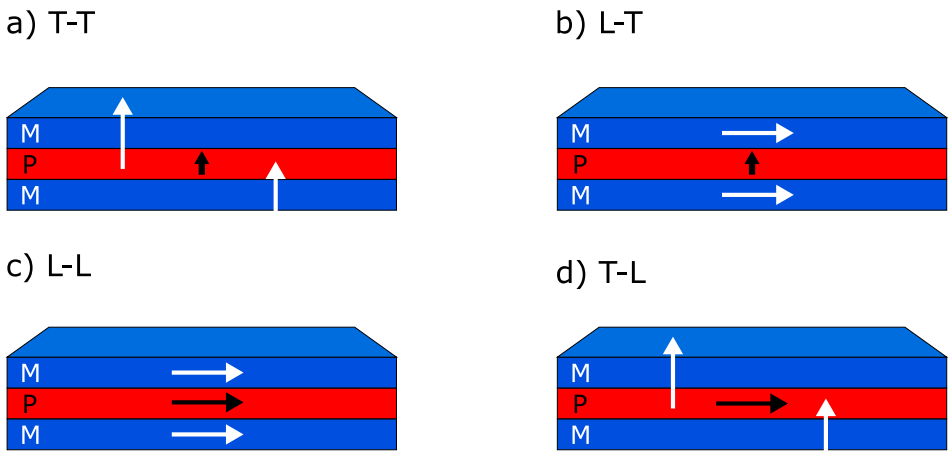


***Figure 2.13:*** *Fundamental operation modes of laminate structures; a) T-T (transverse magnetization and transverse polarization), b) L-T (longitudinal magnetization and transverse polarization), c) L-L (longitudinal magnetization and longitudinal polarization), d) T-L (transverse magnetization and longitudinal polarization). Blue and red colors represent magnetostrictive and piezoelectric components, respectively. White and black arrows represent respective magnetization and polarization directions. Image adapted from [100].*

was previously demonstrated and respective transverse/longitudinal magnetoelectric coefficients were formulated as

$$\alpha_{E_{31}} = \frac{\partial E_3}{\partial H_1} = \frac{-2d_{31}^p q_{11}^m v^m}{(s_{11}^m + s_{12}^m)\varepsilon_{33}^{T,P} v^p + (s_{11}^p + s_{12}^p)\varepsilon_{33}^{T,P} v^m - 2(d_{31}^p)^2 v_m} \tag{2.33}$$

$$\alpha_{E_{33}} = \frac{\partial E_3}{\partial H_3} = \frac{-2d_{31}^p q_{13}^m v^m}{(s_{11}^m + s_{12}^m)\varepsilon_{33}^{T,P} v^p + (s_{11}^p + s_{12}^p)\varepsilon_{33}^{T,P} v^m - 2(d_{31}^p)^2 v_m} \tag{2.34}$$

where, $d_{31}^p$ is the piezoelectric coefficient, $v^m$, $v^p$, $s_{11}^m$, $s_{12}^m$, $s_{11}^p$ and $s_{12}^p$ are volumes and elastic compliances for the magnetostrictive and piezoelectric phases, $q_{11}$ is the piezomagnetic coefficient of the magnetostrictive phase and finally $\varepsilon_{33}^{T,P}$ is the permittivity of the piezoelectric phase [56][57].

Accordingly, the highest magnetoelectric coefficient was obtained from the L-L and push-pull operation modes in Terfenol-D/PZT/Terfenol-D and Terfenol-D/PMN-PT/Terfenol-D laminates. This anisotropic behavior of the magnetoelectric coefficient can be explained by the directional dependency of the piezoelectric effect and the influence of the electrode spacing. Above mentioned ferroelectric materials are poled in order to maximize their piezoelectric properties in one direction; i.e., longitudinal or transversal. However, both materials

exhibit much larger dielectric displacements along the longitudinal direction (length) compared to the transversal (thickness) direction, hence the respective piezoelectric coefficients differ. Despite obtained high magnetoelectric coefficients, this method is not easily applicable to the current work where the piezoelectric film thickness never exceeds several microns. In this work, piezoelectric phase acts as a parallel-plate capacitor and is sandwiched between two conductive layers; i.e., electrodes. In order to utilize longitudinal polarization, one has to implement electrodes on the side-faces of the piezoelectric layer. However, this is very difficult considering the methods utilized in this work. Furthermore, such a configuration would suffer from short-circuiting problems due to the fact that FeCoSiB is a conductive material.

### 2.3.3 Thin Film (2-2) Laminate Composites

Horizontal composites discussed so far are all macroscopic heterostructures that are generally fabricated by epoxy bonding of individual layers followed by an appropriate curing step at $80\,^{\circ}\mathrm{C} - 100\,^{\circ}\mathrm{C}$ [101]. In other words, epoxy acts as the transfer layer between the piezoelectric and magnetostrictive constituents. Hence the coupling in such composites, despite being higher than other connectivity schemes, is not optimal neither. Even though, there have been recent optimization efforts concerning the laminating processes [102], the use of epoxy is generally a disadvantage. Epoxy is much softer than the piezoelectric/magnetostrictive constituents of the composite structure and even the thinnest epoxy layer can absorb most of the generated strain, which in return can greatly diminish the amount of the transferred strain between phases. Additionally, such a method is not compatible with the fabrication methods that are utilized within this work, mainly due to temperature limitations. Therefore from the application point of view, it is always preferable to have a thin film based magnetoelectric composite [103].

A suitable alternative is the thin film deposition technology [104]. It offers a superior interfacial adhesion and strongest coupling between phases. Furthermore, it allows the fabrication of high quality films ranging from a few nanometers up to several micrometers in thickness. One of the early examples is the inspiring work of *Zheng et al.* by pulsed lased deposition (PLD) [105]. Fabricated specimen were epitaxial, self-assembled hexagonal arrays of $CoFe_2O_4$ nanopillars embedded in a $BaTiO_3$ matrix, which showed a strong coupling of electric and magnetic parameters through the heteroepitaxy of the two lattices. Afterwards, *Greve et al.* reported sputter deposited (2-2) thin film composites with a giant magneto-

electric coefficient as high as $737\,\mathrm{V}/(\mathrm{cm}\cdot\mathrm{Oe})$ [106]. Additional methods include physical vapor deposition, chemical vapor deposition, chemical solution deposition, molecular beam epitaxy and several others [68]. All these methods can be applied for the fabrication of both single phase and composite structures, under various conditions and on numerous substrates; e.g., Si, quartz, etc. Hence the compatibility with MEMS technology brings ease of processing, where more complicated sensor structures; e.g., partially released composites and/or multilayer composites can be produced. The main focus for the remainder of this work will rather be given to the horizontal multilayer heterostructures fabricated by magnetron sputtering method. Nevertheless, interested parties can look into the referenced review paper for reports on single phase thin film materials [86].

### 2.3.4 Working Principle of Thin Film Magnetoelectric Composites

#### Influence of the Magnetic Bias Field

An exemplary AlN/FeCoSiB magnetoelectric composite sensor produced on a thick non-piezoelectric substrate is shown in Figure 2.14a. At the initial case, there is no external magnetic field applied. When the composite is subject to an external magnetic DC field, the magnetostrictive phase starts to change its shape and shifts the magnetostriction curve. Accordingly, the linear coupling between the magnetic polarization and the mechanical strain; i.e., piezomagnetic curve ($d^m = {}^{\partial\lambda}/_{\partial H}$) shifts as well. At some particular external magnetic field magnitude, the slope of the magnetostriction curve (Figure 2.14b) reaches its maximum value. This specific point coincides with the highest peak of the piezomagnetic (Figure 2.14b) and magnetoelectric (Figure 2.14c) curves, where the latter is simply due to elastic coupling. The field necessary to induce enough magnetization, so that the slope of the magnetostrictive curve reaches its maximum, was previously defined as the external bias field ($H_{Bias}$).

This correlation can be explained with the following coupling relation

$$\alpha_{ME} = \left|\frac{\partial T}{\partial S}\times\frac{\partial D}{\partial T}\times\frac{\partial E}{\partial D}\right|\times\frac{\partial S}{\partial H} \tag{2.35}$$

where, $T$ is the mechanical stress, $S$ is the mechanical strain, $D$ is the electric displacement, $E$ is the electric field and $H$ is the magnetic field. The first part of the equation is related with

the piezoelectric component, thus not relevant here. Therefore the relation can be simplified to

$$\alpha_{ME} \propto d^m = \frac{\partial S}{\partial H} = \frac{\partial \lambda}{\partial H} \tag{2.36}$$

where, $\lambda$ is the magnetostriction [107].

Equation (2.36) proves the afore discussed influence of the magnetic material and the elastic coupling between phases on the magnetoelectric coefficient. Figure 2.14b and Figure 2.14c depict how $\lambda$, $d^m$ and $\alpha_{ME}$ behave under the influence of the magnetic DC field. The working point is defined with respect to the magnetostrictive properties of the magnetic component, since it exhibits a maxima at a specific DC magnetic field under off-resonance condition [68].

Equation (2.36) further depicts the dependency of the magnetoelectric coefficient on the magnetostrictive phase. Similarly, necessary bias field magnitude is also dependent on the permeability of the utilized magnetostrictive phase. In other words, it is material specific. Even though the application of a bias field leads to a huge effect increase, this property is probably the biggest drawback of the magnetoelectric composites, since the composite effect is very small in the absence of it. Bias field requirements of different magnetostrictive materials can be seen in Table 2.5.

**Influence of the Mechanical Resonance**

Application of an external DC magnetic field is not the only way to enhance the magnetoelectric effect. *Tilley et al.* demonstrated that an improvement of the magnetoelectric response can be observed when the modulation frequency of the applied field coincides with magnetic, electrical or mechanical eigenmodes of the magnetoelectric system [79][108]. Considering thin film magnetoelectric composites fabricated on thick substrates, magnetoelectric effect can be enhanced orders of magnitude when the frequency of the modulation AC magnetic field ($f_{\mathrm{AC}}$) matches the natural resonance frequency ($f_{\mathrm{res}}$) of the composite structure [109]. Note that the modulation field shall be applied alongside and in the same direction as the DC bias field. This behavior presents both an advantage and a disadvantage from the application point of view. Despite the enhanced sensing capabilities near the resonance frequency, this dependency limits the use of the magnetoelectric sensors to a specific frequency bandwidth,

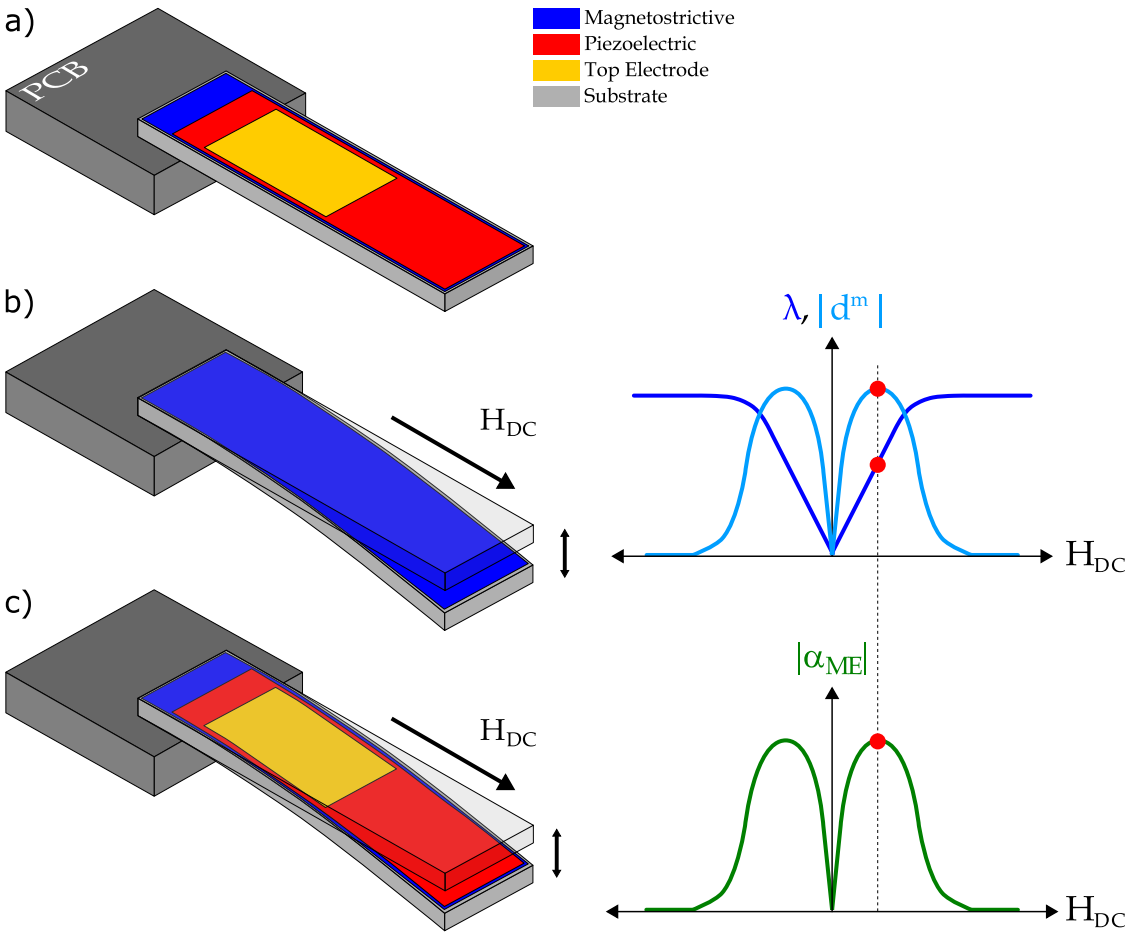


***Figure 2.14:*** *Magnetoelectric behavior as a function of DC magnetic field. a) Exemplary FeCoSiB/AlN magnetoelectric composite sensor and relevant constituents. b) Magnetoelectric composite sensor under the influence of external magnetic field. At the initial state, there is no applied external magnetic field. In presence of an external magnetic field, magnetostriction (dark blue) increases and bends the composite downwards. $\lambda$ and $d^m$ are the magnetostriction and the piezomagnetic coefficients (light blue), respectively. $d^m$, which equals to the derivative of the magnetostriction curve with respect to applied magnetic field, reaches its maximum peak where the slope of the magnetostriction curve is at maximum (red dots). Maximum magnetoelectric coefficient ($\alpha_{ME}$, green) follows the same behavior as well. This material specific magnetic field is defined as the bias field; i.e., $H_{DC} = H_{Bias}$. Note that AlN is a linear piezoelectric material Section 2.1.4.*

which can not cover wide ranges (see Figure 2.15).

Resonating systems can have multiple resonance frequencies and modes. Initially investigated magnetoelectric composites, where a piezoelectric layer is sandwiched between two magnetostrictive layers for instance, operated in the expansion mode and possessed natural frequencies as high as several kHz (see Figure 2.15a). First longitudinal frequency ($f^L$) of such a composite can be given as

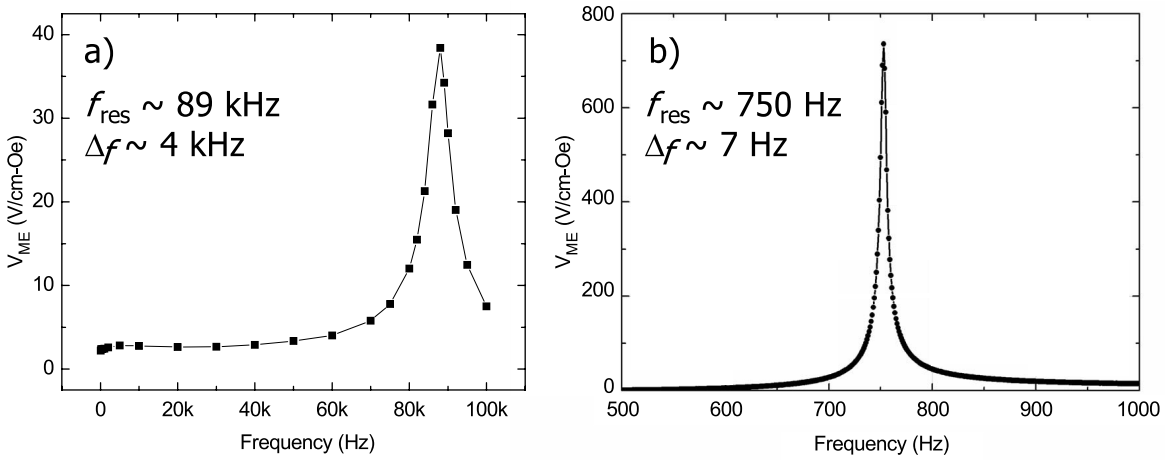


***Figure 2.15:*** *Influence of the mechanical resonance on the magnetoelectric voltage coefficient. a) Resonance enhancement in the exemplary sandwich-type laminate. $f_{res} \sim 89\,kHz$ and $H_{DC} = 55\,mT$ Image adapted from [56]. b) Resonance enhancement in an exemplary bilayer laminate. $f_{res} \sim 750\,Hz$ and $H_{DC} = 0.6\,mT$ Image adapted from [106].*

$$f^L = \frac{1}{2l\sqrt{\rho s_{11}}} \tag{2.37}$$

where, $l$ is the length, $\rho$ is the average density and $s_{11}$ the elastic compliance of the laminates [56][110].

However it is not advantageous to work at these frequencies since sensors operating at high frequency suffer from the Eddy currents; i.e., currents induced in a magnetic material according to the Faraday's law of induction [44, p.409]. Eddy currents circulate in the magnetic material and produce a high amount of power loss due to heating ($I^2 \cdot R_{loss}$), which in return deteriorates the sensing abilities. Since $f^L$ is inversely proportional to the composite length, decreasing it below 1 kHz, for instance, would result in a two orders of magnitude extension in the composite length [56]. Clearly, this is not an applicable solution.

Therefore an alternative method is adopted in order to reduce the resonance frequency. That is the use of bilayer systems, rather than sandwich structures and engaging the bending vibration mode arising from the lack of structural symmetry [109][110][111]. In this case, the resonance movement is dominated by the underlying thick substrate and the magnetoelectric effect is further enhanced by the quality factor ($Q = {}^{f_{res}}/_{\Delta_f}$) [112]. *Petrov et al.* previously investigated acoustic mode frequencies as well as different vibrational options of a bilayer composite, which include free-to-vibrate at both ends, fixed at both ends and fixed at one end configurations [113]. This model concluded, that there occurred an enhancement in the

magnetoelectric coupling at the lowest bending resonance of a composite with one end fixed and one end free to vibrate structures. These composites demonstrated magnetoelectric voltage coefficients slightly below $1\,\mathrm{kV/(cm\cdot Oe)}$ [106]. Resonating systems experience certain losses; i.e., damping, from cycle to cycle. Recently, several $\mathrm{kV/(cm\cdot Oe)}$ magnetoelectric voltage coefficients were reached by reducing the damping, either via substrate thinning [72] and/or under vacuum operation [114].

Figure 2.15b depicts the resonance enhancement of the magnetoelectric effect in an exemplary thin film magnetoelectric composite fabricated on a Si substrate. In this case, the resonance frequency of the first bending mode can be given as

$$f_n = \frac{1}{4\pi}\frac{\lambda_n^2}{L^2}\sqrt{\frac{E_{eff}\cdot h^3}{3\left(\sum_n \rho_n \cdot h_n\right)}} \tag{2.38}$$

with

$$E_{eff} = \frac{E_s}{1-\nu_s} \tag{2.39}$$

where, $n$ is the mode order, $\lambda_n$ is a dimensionless parameter, $L$ and $h$ are the length and the thickness of the cantilever, $\rho$ is the density of the individual materials, $E_{eff}$ is the effective Young's modulus of the substrate with $E_s$ and $\nu_s$ being the Young's modulus and the Poisson's ratio of the substrate [115].

It is important to note that even though thin film composite systems are far superior in terms of the magnetoelectric voltage coefficient, their bandwidth is greatly limited to several Hz.

### Influence of the Quality Factor

The relationship between the quality factor and the sensor output can be investigated through a simple model of a damped mechanical oscillator [116]. According to this model, the frequency dependent output magnitude of the mechanical oscillator ($G(f)$) equals

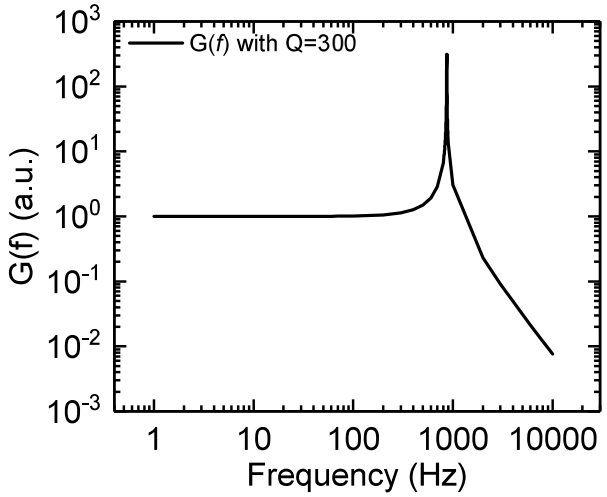


***Figure 2.16:*** *Frequency dependent output magnitude and the influence of the quality factor [116]. Quality factor is considered as Q = 300.*

$$G(f) = \frac{1}{\sqrt{\left(1-\left(\frac{f}{f_{res}}\right)^2\right)^2 + \left(\frac{f}{f_{res}\cdot Q}\right)^2}} \tag{2.40}$$

where, $Q$ is the quality factor and $f_{res}$ is the resonance frequency.

Figure 2.16 depicts the calculated $G(f)$ for an exemplary mechanical oscillator with $Q = 300$. At the resonance frequency, the output magnitude of the mechanical oscillator is enhanced by the quality factor since $G(f) = Q$. However, this enhancement does not take into account any loss mechanism; i.e., displacement noise density.

### Influence of the Electrode Size

In magnetoelectric sensors, increasing the volume of the magnetostrictive material improves the SNR [117]. In conventional thin film bilayer sensors, FeCoSiB is deposited as the top layer and therefore functions as the top electrode [72]. This results in top electrodes that stretch across the whole cantilever length, leading to a large sensor capacitance. The latter is beneficial, since it improves the voltage gain of the charge amplifier. However, the strain and the bending stress in a magnetoelectric resonant sensor, which is clamped at one end and operating at the first-bending mode, are maximum near the bending point of the sensor and gradually decrease as the electrode length extents away from that point [118]. This behavior can be seen in Figure 2.17a and b for the strain and the stress, respectively. Therefore despite

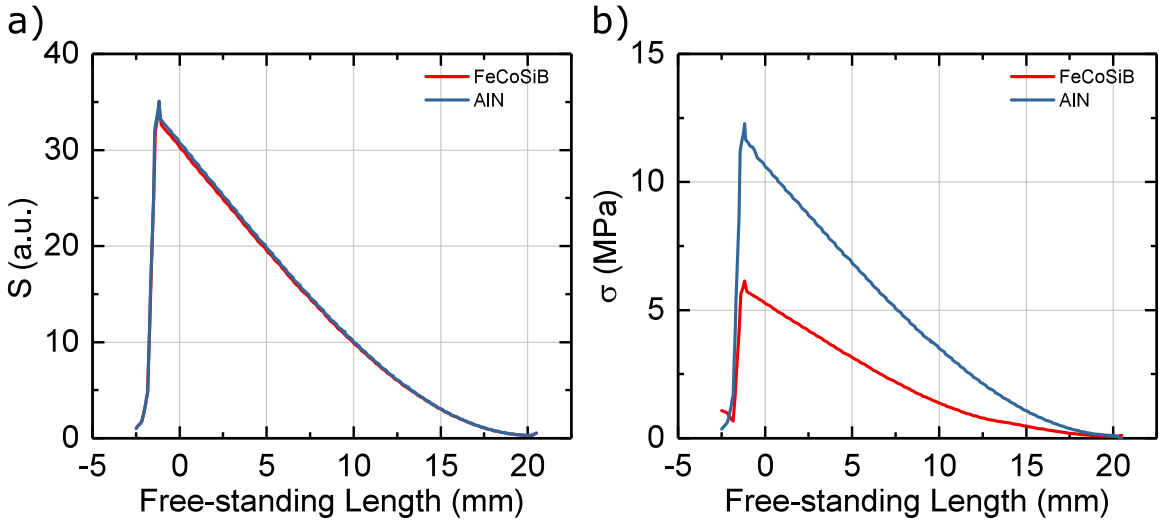


***Figure 2.17:*** *Modeled a) strain and b) stress distributionof individual constituent layers in a resonating magnetoelectric sensor as a function of the electrode length. For all modeling, Q = 300.*

the increased gain, overall sensor properties deteriorate for larger top electrodes.

This problem can be solved by changing the sensor stack configuration into an inverse-bilayer order; i.e., substrate/FeCoSiB/AlN/electrode. In this way, the top electrode dimensions can be optimized in a way that it is confined where the bending is highest and the charge generation can be maximized [103].

### 2.3.5 State-of-the-art: Magnetoelectric Sensors

It was discussed that several bulk and thin film based magnetoelectric composites exhibit high magnetoelectric effect under various working conditions. Composites exhibiting the direct magnetoelectric effect are utilized in many application fields such as magnetic sensors, current sensors, transformers, gyrators, energy harvesters and memory devices [68]. There are numerous review papers and books, which summarize thoroughly all the current and prospect applications of all the devices based on the direct and converse magnetoelectric effects [119].

Magnetic field sensing of AC and/or DC magnetic fields is the topic of interest of the current work. Magnetoelectric composites aiming at these applications are required to address and fulfill several goals; i.e., operating at low frequencies, having a high sensitivity and the detection of very low magnetic fields in room temperature and to ensure a wide bandwidth. In biomedical applications, for instance, these goals range between $10^{-2}$ Hz to $10^{3}$

Hz for frequency, $\mathrm{pT}/\mathrm{Hz}^{1/2}$ to $\mathrm{fT}/\mathrm{Hz}^{1/2}$ for magnetic detection limit and $0.1\,\mathrm{Hz} - 100\,\mathrm{Hz}$ for bandwidth, respectively. To that end, various research groups adapted different constituents (bulk and thin film) combined in various ways (epoxy bonding and thin film deposition) and build numerous sensors (resonant and non-resonant) of different geometries (bimorph and sandwich). Considering all of these, state-of-the-art magnetoelectric composites and their important parameters are summarized in Table 2.5.

Presented composites are classified in terms of their components and their thicknesses. The first group includes composites with thick magnetostrictive layers, which are generally combined with piezoelectric components via epoxy bonding. In this approach, it is possible to implement a variety of commercially available piezoelectric materials; e.g., PMN-PT, PZT, PVDF in combination with highly magnetostrictive materials; e.g., Terfenol-D, Metglas, etc.. Individual components can be magnetized and polarized in various directions in order to obtain different operational modes. However, as is previously discussed, the use of epoxy decreases the coupling in these composites hence the magnetoelectric coefficient values do not reach $\mathrm{kV}/(\mathrm{cm}\cdot\mathrm{Oe})$ range. Nevertheless, they present great sensing capabilities both in- and off-resonance applications.

The second group includes thin-film based composites that are generally fabricated via sputter deposition of individual constituents on top of each other. Ensuring a great coupling between the magnetostrictive and piezoelectric layers, this type of composites possess the disadvantage of strong clamping by the thick Si substrate, on which they are deposited. On the other hand, their suitability for MEMS technology allows the use of various lithography and etching processes to thin down or completely remove the underlying substrate. These composites exhibit the highest magnetoelectric voltage coefficients as well as the lowest limit of detection (LOD) values. Furthermore, they are easily miniaturized and can form sensor-arrays that can be used for non-invasive brain imaging.

***Table 2.5:*** *State-of-the-art magnetoelectric composites and important properties.*

| **Magnetoelectric Composites** | | | | | | | | |
|---|---|---|---|---|---|---|---|---|
| Magnetoelectric Composites | Speciality | Dimensions (mm) | $t_{substrate}$ (µm) | $H_{DC}$ (Oe) | $\alpha_{ME}$ (V/(cm·Oe)) | LOD (pT/Hz$^{1/2}$) | $f_{res}$ (kHz) | Ref. |
| **Thick-film based:** | | | | | | | | |
| Terfenol-D / PMN-PT | L-T | $6 \times 2.5$ | – | 400 | 2.2 | $\sim 40$ | 1 | [120] |
| Terfenol-D / PMN-PT | Push-Pull | $15 \times 6$ | – | 500 | 30.8 | $\sim 1$ | 77.5 | [61] |
| FeGa / PMN-PT | L-L | $14 \times 6$ | – | 750 | 36.2 (1) | $\sim 2$ (0.01) | 91 (1) | [69] |
| ($TbCo_2$/FeCo) / AlN | L-T Bilayer | $18 \times 5$ | – | 9 | 30 (4) | – | 35 | [121] |
| Terfenol-D / PZT | Symmetric Bimorph | $16 \times 6$ | – | – | 70 | – | 34 | [56] |
| **Thick-film and Metglas®based:** | | | | | | | | |
| Metglas® / PVDF | L-T Sandwich | – | $t_{total} < 100$ | 8 | 238 (7.2) | $< 10$ | 50 (1) | [100] |
| Metglas® / PVDF | L-T Bilayer | – | $t_{total} < 100$ | 8 | 310 | – | 50 | [100] |
| Metglas® / PZT | (2-1) Sandwich | – | – | 4 | 500 (22) | – | 22 (1) | [98] |
| Metglas® / PMN-PT | Push-Pull | – | – | 8 | 52 | 5.1 | (1) | [102] |
| Metglas® / PZT | Self Biased | – | – | – | 380 (12) | – (30) | 33.7 (1) | [122] |
| **Thin-film based:** | *all L-T mode* | | *all Si substrate* | | | | | |
| FeCoSiB / AlN | Trenched | $20 \times 2$ | 140 | 6 | 737 (3.1) | – | 0.75 (0.1) | [72] |
| FeCoSiB / AlN | Trenched | $25 \times 3$ | 130 | 6 | 1800 | – | 0.33 | [106] |
| FeCoSiB / AlN | Encapsulated | $0.9 \times 0.2$ | $SiO_x - 7$ | -26 | 1900 | 27 | 7.1 | [123] |
| FeCoSiB / AlN | Self Biased | $25 \times 3$ | 650 | – | 96.7 | 10 | 1.26 | [124] |
| FeCoSiB / PZT | Sol-Gel PZT | $25 \times 2$ | 300 | 4 | 200 | 2.6 | 0.98 | [34] |
| FeCoSiB / AlN | in Vacuum | $25 \times 3$ | 90 | 10 | 20000 | – | 0.15 | [114] |
| | – | $1 \times 0.2$ | $SiO_x - 6$ | 18 | 12000 | 300 | 4.7 | [114] |
| FeCoSiB / AlN | Self Biased | $23.3 \times 2.3$ | 300 | – | 860 | 8 (180) | 1 (0.01) | [125] |
| FeCoSiB / PZT | Tuning Fork | $25 \times 2$ | 350 | – | 3400 | 0.5 | 0.96 | [126] |
| FeCoSiB / AlN | Inverse-Bilayer | $25.2 \times 2.2$ | 300 | $\pm 2.1$ | 5000 | 0.4 | 0.87 | [73] |

Values given in paranthesis represent off-resonance measurements. In macroscopic samples, the biggest dimensions are provided.

## 2.4 Thin Film Fabrication

Thin films can be fabricated using various methods, which can be considered within two big groups; chemical and physical deposition techniques [127, p.171].

- *Chemical vapor deposition (CVD)* techniques include; spin coating [128], chemical solution deposition [129], metal organic CVD [130], plasma enhanced CVD [131] and atomic layer deposition [132], etc..
- *Physical vapor deposition (PVD)* techniques include; sputtering [133, p.181], pulsed laser deposition [134, p.4] and molecular beam epitaxy [135], etc..

In this work, sputtering is the method of choice for the fabrication of all thin films due to its relative simplicity, high and uniform film quality even at low process temperatures and its full integration into MEMS processing. Therefore other techniques will not be discussed here. Nevertheless, further reading concerning other thin film fabrication methods can be found in textbooks such as [136] and [137].

### 2.4.1 Sputtering

Sputtering is a physical vapor deposition technique, where a target material is eroded and its atoms are deposited onto a substrate in the form of a thin film. It is used both in industrial and scientific applications due to its many advantages such as the target material variety, relatively low process temperatures, resulting high film quality, reproducibility, high deposition rates, large processing areas, etc.. Sputtering offers versatility and ease of processing since it allows the deposition of both metallic and isolating compound films onto different substrate materials. Furthermore, modern devices using this method can be equipped with multiple target materials at once and realize the fabrication of multilayer composite materials.

Figure 2.18a depicts a conventional sputtering setup designed in the parallel-plate configuration, where a DC excitation is utilized. Given setup consists of a target material (cathode) and a substrate (anode) separated with a distance ($L$). They are placed in a vacuum chamber and the chamber is filled with an inert gas. Argon (Ar) is the most commonly chosen gas due to its high molecular weight, which increases the sputter yield of the target atoms. The substrate is usually grounded but can also be connected to a RF generator in order to apply an additional (RF) bias voltage.

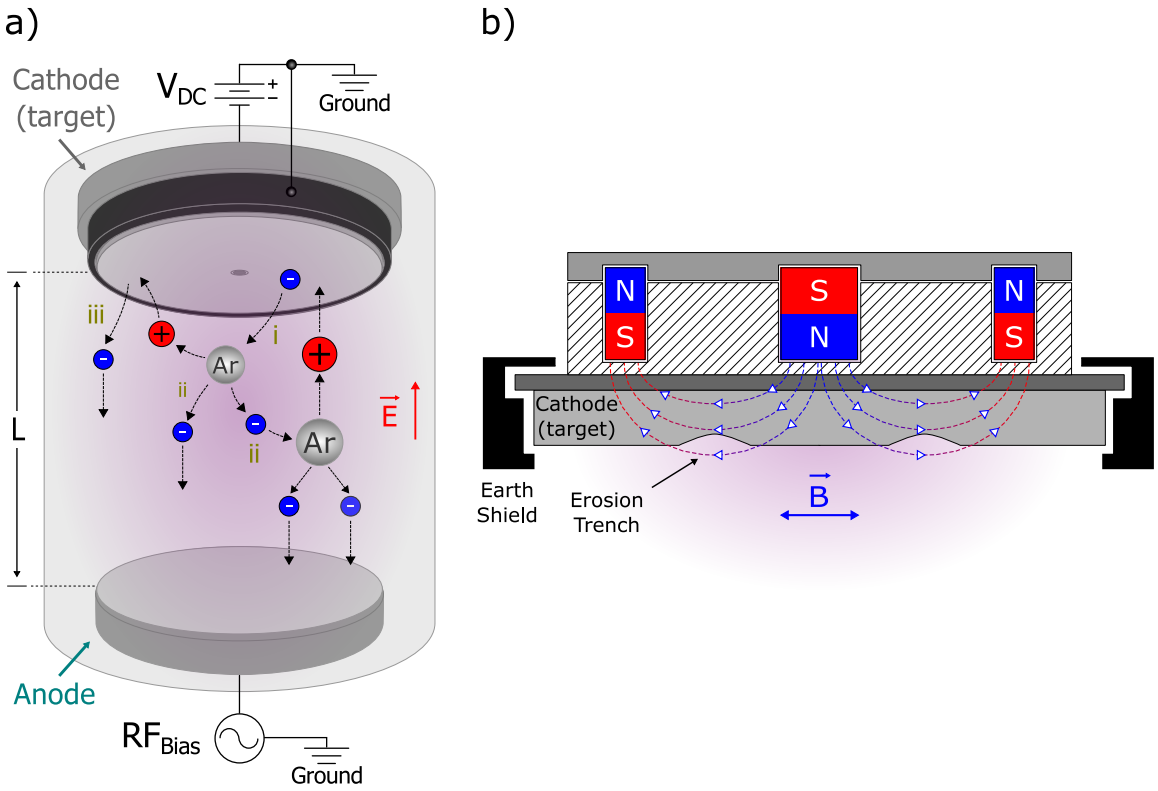


***Figure 2.18:*** *Basics of sputtering. a) Schematic depicting a parallel-plate DC-glow discharge setup in a vacuum chamber containing an anode and a cathode that are separated with a distance L and occupied by Ar plasma. Cathode is connected to a DC power source and is grounded. The dark-space shield around the cathode (black) is grounded as well. Anode is connected to a RF generator and is grounded. A magnetron ring is present behind the cathode. Ionization phenomenon and current flow in a plasma is depicted: i) initiating electron, ii) electron-impact ionization and iii) ion bombardment-induced secondary electron emission. Blue, red and gray circles are electrons, positive Ar ions and Ar atoms/molecules, respectively. b) Close-up to the planar magnetron structure and the behavior of the magnetic fields. Images adapted from a) [137, p.471] and b) [137, p.482].*

The principle of operation is as follows; when a negative potential is applied to the cathode, free electrons present in the chamber are accelerated by the emerging electric field ($\vec{E}$). As the energetic free electrons collide with Ar atoms present in the chamber, Ar atoms become both excited and ionized. The latter leads to the generation of positive Ar ions ($Ar^+$) as well as more secondary electrons through the following reaction

$$Ar + e^- \rightarrow Ar^+ + 2e^- \tag{2.41}$$

When a high enough sputter pressure is provided, Ar ions in the plasma go through consecutive collisions and the plasma density increases. As a result of the potential difference between the cathode and the positive plasma, these ions accelerate towards the target and initi-

ate the sputtering process. Sputtering process defines the knocking-out of target atoms and/or ionized clusters by the bombarding ions as a result of momentum transfer [136, p.319]. Therefore, it is necessary that the momentum transfer is energetic enough to overcome the surface binding energy of the most-weakly-bound target atom [136, p.321]. When the sputtering of the target material is succeeded, the ejected atoms and/or clusters travel through the plasma and condense on the substrate, where an homogeneous film growth occurs.

### 2.4.2 Magnetron Sputtering

Despite its simplicity conventional sputtering has an inherent weakness, that is its dependency to energy; typical DC glow discharge plasma operates at pressures in the range of $0.03\,\text{mbar} - 3\,\text{mbar}$ and at potentials ($V_0$) of approximately between $1\,\text{kV} - 2\,\text{kV}$ [137, p.472]. Thin films deposited at such relatively higher pressures often suffer from impurities and degraded film quality. Moreover, the fundamentals of the method makes it impossible to operate below the given pressure range since in that case the number of collisions an electron experiences (before it escapes to the anode) is too small and the deposition rates are extremely low.

Often a magnetron system, which creates magnetic trapping fields close to the target surface, is installed behind the target in order to overcome this limitation [138, p.223]. An exemplary planar magnetron structure and its influence is depicted in Figure 2.18b. Here, electrons that are already accelerated towards the target by the electric field are caught by the trapping magnetic fields and curve into the magnetic orbits as a result of the Lorentz force acting on them [137, p.382]. The Lorentz force is described as the combined force acting on a charged particle; e.g., electron, which is in electric and magnetic fields. Hence the total force equals

$$F = F_E + F_B = q_e E + q_e v \times B \tag{2.42}$$

where, $F$ is the combined force, $q_e$ is the electron charge, $v$ is the electron velocity, $E$ and $B$ are the electric and magnetic fields, respectively [138, p.156].

In this manner, electrons are forced to hit the target surface several times before they can escape to the anode. This interaction results in a much higher sputter yield as more atoms are ejected from the target. It further increases the ionization rate due to an enhanced generation rate of secondary electrons [139, p.559]. Furthermore, when operating at low process

pressures, energetic particles bombarding the target material retain most of their energy due to reduced number of collisions in the plasma. This is very beneficial for the quality of the deposited films and its effect will be discussed in the following chapters (Section 4.1.3). On the other hand, an enhanced sputter yield, where the magnetic field lines are stronger, leads to heterogeneous material erosion. In any case, the use of magnetron systems successfully improves the pressure limitations of the DC sputtering process by an order of magnitude down to $10^{-3}$ mbar and allows the fabrication of higher quality thin films.

### 2.4.3 Reactive Magnetron Sputtering

AlN thin films can be fabricated from a pure Al target via reactive sputtering method. Reactive sputtering allows the deposition of compound materials by adding a reactive gas into the process chamber during the sputtering process. The process is complex in nature and can be easily influenced by individual variables such as the process parameters, substrate material, gas composition, etc.. A comprehensive theoretical model and in-depth analysis of the reactive sputtering in general was previously presented by *Berg et al.* [140]. Nevertheless, a short summary of the typical process behavior during a reactive deposition process will be presented here as well.

When a metal target is sputtered in an inert gas atmosphere, interactions occur at the target and substrate's surfaces. When an additional reactive gas is introduced into the process chamber, however, the reactive gas interacts with all non-passivized surfaces. As a result, compound formation occurs not only on the substrate surface but also on the chamber walls as well as on the target itself. This phenomenon is known as the target poisoning [141]. As the target gets covered with the insulating compound, a charge accumulation starts to occur on the target's surface. This leads to the formation of a secondary voltage between the target material and the surface, which eventually equals the applied cathode voltage. Unless addressed, compound formation on the target surface leads to eventual plasma failure.

Target poisoning is inevitable during reactive sputtering but it can be reduced and/or prevented to a great extent using RF and pulsed DC (PDC) power sources (see Section 2.4.4). The rate at which the target gets poisoned is dependent on the reactive gas flow hence it is also possible to optimize it to an extent. Additionally, the amount of reactive gas present during the process establishes an hysteric behavior with three different deposition modes [136, p.341][142]. These modes produce films with different stoichiometry and are known as the metallic, transition and compound modes as given in Figure 2.19.

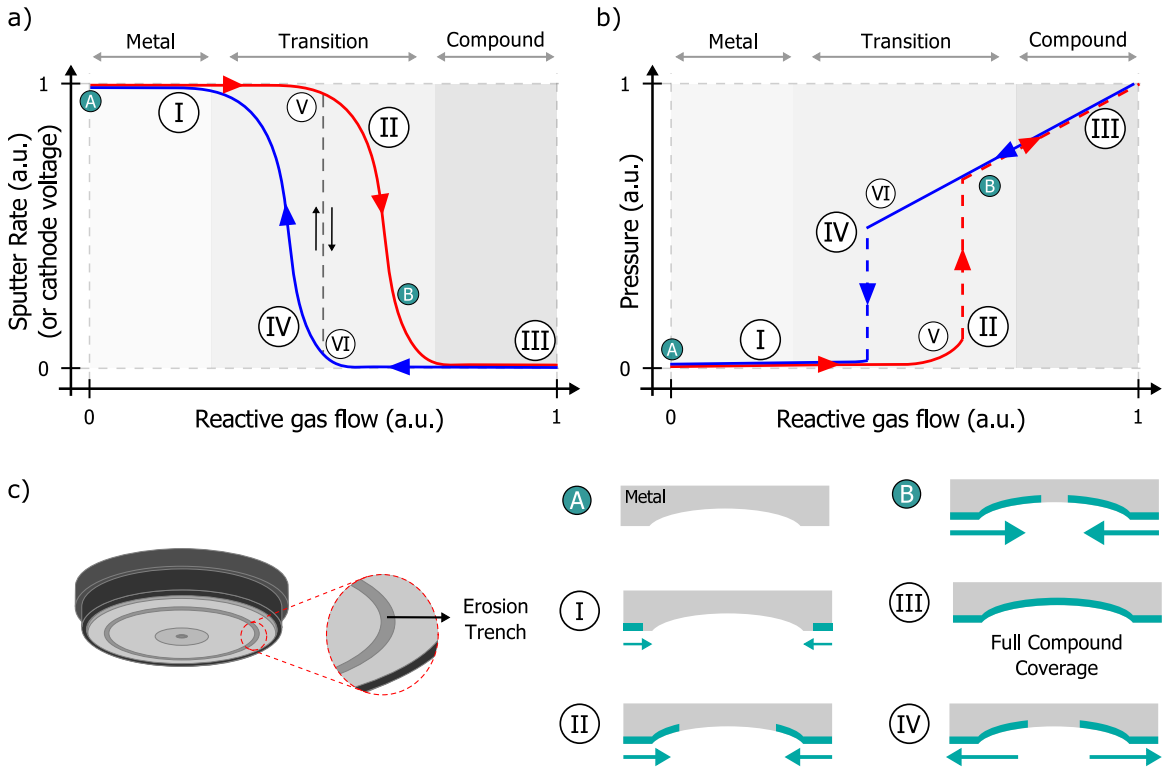


***Figure 2.19:*** *Target poisoning and different deposition modes during reactive sputtering. Influence of the reactive gas over sputter rate is depicted. The hysteric relationship between the reactive gas flow and a) the sputter rate b) partial gas pressure. The hysteresis loops are divided into 3 zones. Image adapted from [137, p.480][138, p.218]. c) Influence of the erosion trench on target sputtering. While the majority of the target is being covered by the compound, erosion trench initially delays compound formation due to enhanced material erosion. Extensive reactive gas presence eventually leads to full target coverage. Decrease of the gas flow leads to compound decrease, starting from the erosion trench as well.*

Accordingly, when a plasma is ignited in the presence of an inert gas, the process is basically the conventional sputtering of a metallic target with a high sputter yield (*A*). As the reactive gas flow increases (*I*), reactions on non-passivized surfaces of the chamber begin. While the compound formation proceeds on the target surface, the presence of a magnetron system results in an intense material removal around the erosion trench delays the compound formation on this area (see Figure 2.19c). When a certain reactive gas flow is reached (*II*), the sputter yield of the target material drops below the compound formation rate (gas adsorption) on the target surface. In other words, compound formation on the target surface becomes faster than its erosion. The target poisoning starts and the process experiences a remarkable decrease in the sputter yield as the compound formation begins to invade the erosion trench area as well[1]. Process becomes unstable, as slight variations of the reactive gas flow further decreases the sputter yield (*B*). The process is now in the compound mode

[1]Note that AlN is an insulating material

and the target surface is completely covered with the compound material (*III*). As long as a voltage can be established on the cathode, the plasma stays on and the sputtering process continues with near-zero deposition yield. However there is no longer sputtering, but instead a continuous compound formation on the target surface until finally the target surface is completely covered. As the conductivity on the surface is completely lost, the discharge voltage experiences a huge drop. Keeping the reactive gas flow at this high rate leads to an eventual plasma death and the process stops completely. At this point, the plasma can not be lit again unless the compound on the target surface is removed through mechanical or chemical cleaning.

For the sake of discussion, consider that the plasma is still on and the gas flow is slowly decreasing. In order to initiate target poisoning reversal, it would be necessary to decrease the gas flow down to the point (*IV*), where the sputter yield is once more above the gas adsorption rate. At this point, enough compound would be removed from the erosion trench and sputtering from the target surface would restart. Note that the gas flow at (*IV*) does not coincide with (*II*), since the partial pressure for (*II*) and (*IV*) are substantially different [136, p.341]. Continued decrease of the reactive gas flow would eventually push the process into the metal zone, where the compound formation nearly stops.

It is preferable to establish a working point, where a high deposition rate is kept in addition to the desired stoichiometry. According to the hysteresis loop, (*V*) and (*VI*) would be the possible working points for most applications. However, due to the instability of the transition zone, it is safer to approach to the process from a higher gas flow rate and work at (*VI*) rather than at (*V*) since while working at (*V*), the process can easily shift to a much lower sputter yield point such as (*B*). Hence, a working point in the transition zone, but close to (*VI*) shall be established for optimal stoichiometry/sputter rate ratio as well as process control.

### 2.4.4 Pulsed DC Sputtering

Poisoning of a metallic target occurs due to compound formation on the target surface and the erosion trench. It is possible to limit such effect by periodically reversing the potential applied to the target, a practice which inherently occurs during RF sputtering. However, RF generators operate at predefined frequencies of 13.56 MHz, leaving no room for optimization. At this high operating frequency, sign reversal of the applied voltage occurs approximately at every 70 ns, resulting in very short sputtering periods. As a result, deposition rates diminish and process times increase. Even though RF sputtering delays and/or pre-

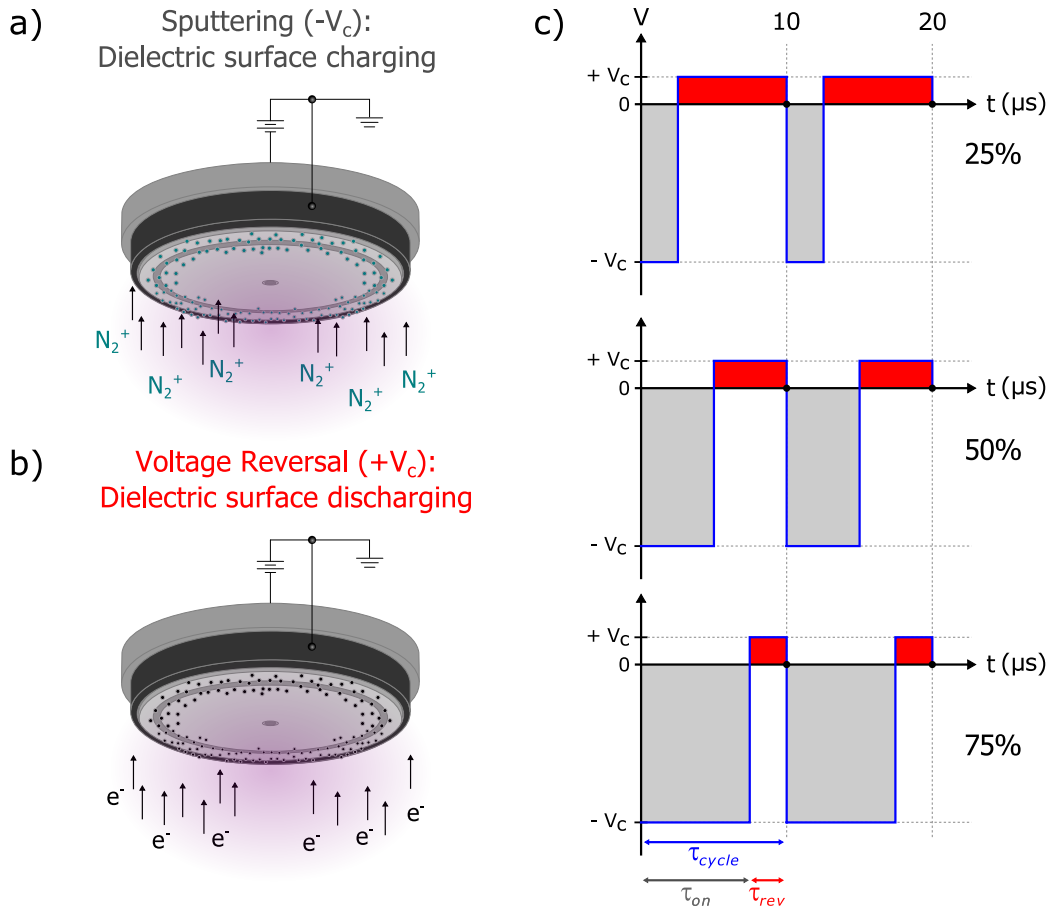


***Figure 2.20:*** *Operation modes of an exemplary PDC deposition system. The system is schematized as a target (cathode) connected to a PDC power source containing an internal switching box; i.e., pulsing unit. The pulsing unit offers two operation modes; a) sputtering mode and b) voltage-reversal mode. In the sputtering mode, nitrogen ions bombard the target as a result of the applied negative voltage and compound formation occurs on the target's surface. When the voltage is reversed, electrons are accelerated towards the target. Achieved electron bombardment removes any compound formation from the surface. c) Voltage sign and magnitude of the two modes can be seen for various duty cycles. Gray areas refer to the sputtering voltage and red areas refer to the reverse-voltage.*

vents compound formation, a more viable alternative is found in the form of PDC sputtering. PDC sputtering is often preferred over RF sputtering since this method allows the reversal of the cathode voltage with a wide optimization window. Typical pulsing frequencies of a PDC generator can range between 5 kHz – 350 kHz allowing pulse reversals in the range of 1 µs – 10 µs [143].

Basic working principle is as follows; when a negative voltage is applied to the cathode, compound formation starts on the target surface leading to a charge build-up (Figure 2.20a). When the cathode voltage is reversed, free electrons in the plasma are accelerated towards

the cathode due to the potential difference (Figure 2.20b). This results in the dispersion of the build-up charge and the removal of the surface compound [144]. The combination of the sputtering and reversal periods form a pulsing cycle. The fraction of the on-time over a complete cycle defines the duty cycle of the generator

$$Duty\ Cycle = \frac{\tau_{on}}{\tau_{on} + \tau_{rev}} \tag{2.43}$$

where, $\tau_{on}$ and $\tau_{rev}$ are the time length of on and reverse-parts, respectively.

Figure 2.20c depicts the voltage change over time for 3 exemplary depositions completed at 100 kHz with different duty cycles; 25, 50 and 75%. Here, gray zones depict the on-time; i.e., the sputtering part of a cycle. Zones colored as red represent the reverse-time; i.e., the cleaning part of a cycle. Note that the magnitude of the applied voltage differs for positive and negative values. This type of PDC generator, where the magnitude and the on-time of the pulses vary, is defined as an asymmetric PDC generator [145].

### 2.4.5 Nucleation and Growth of Sputter Deposited Thin Films

All materials have a structural order, either short or range, depending on how much energy their atoms possess during the fabrication process. With respect to the microstructure, it is possible to divide material classes into three subgroups; i.e., amorphous, single crystalline and polycrystalline. Considering the magnetron sputtering process, for instance, once the

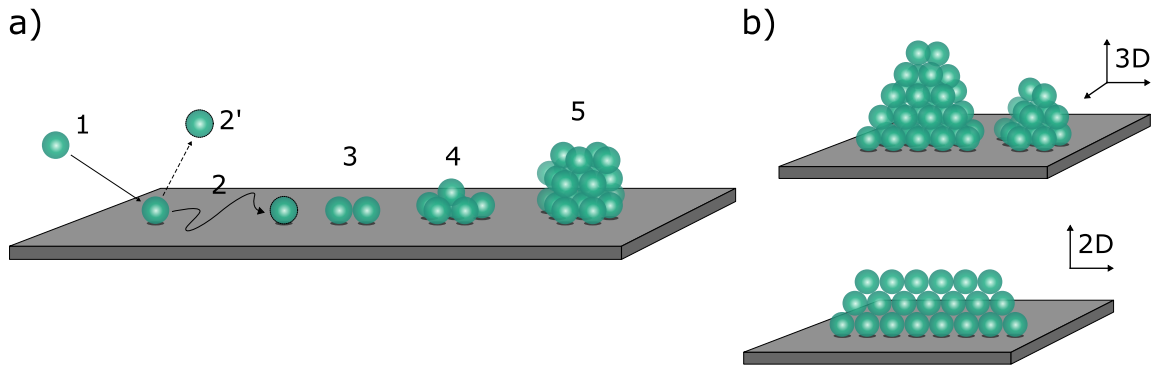


***Figure 2.21:*** *a) Schematic representation of the nucleation process. Depicted individual steps are; 1) adsorption, 2) surface diffusion, 2') desorption, 3) meta-stable cluster formation, 4) stable cluster formation and nucleation, 5) microstructure formation. b) Thin film growth modes; Volmer-Weber (3D islands) and Frank-Van der Merwe (2D layers). Note that Stranski-Krastanov (mixed growth) mode is not depicted. Image adapted from [138, p.360].*

sputtered particles reach the substrate surface, they move along it via surface diffusion until they find an energetically favorable position where they can form stable clusters and finally nucleate (see Figure 2.21a). In order to form stable clusters, nuclei shall overcome a certain local energy barrier, reach a critical size and unite with each other [146]. Mentioned energy barrier is the energy sum of various interfaces; i.e., substrate-vapor, film-substrate and film-vapor [138, p.46]. Those unable to overcome the aforementioned barrier would be desorbed (ejected) from the surface.

After a successful nucleation, the microstructure formation and the film growth steps follow. These steps have three basic growth modes; (*i*) Volmer-Weber (island), (*ii*) Frank-Van der Merwe (layer) and (*iii*) Stranski-Krastanov (mixed) as summarized in Figure 2.21b [138, p.358]. Island growth is commonly observed for metal and semiconductor materials deposited on oxide substrates. Here, the energy on the substrate's surface is very high, hence sputtered atoms are strongly bound to each other rather than to the substrate. Fabricated films end up having an uneven growth due to slow diffusion and stabilized clusters exhibit 3D islands. Unlike island growth, layered growth benefits from a much better adhesion to the substrate surface. In this case, deposited atoms grow as 2D layers on top of each other. Highest quality of crystalline films are obtained in this mode. The final mode is the mixture of the two where initially, layer-by-layer growth and then 3D island formation is observed. It is a common mode and is generally observed in metal-metal and metal-semiconductor composites.

**Structure Zone Model**

Depending on the process parameters, sputter deposition of thin films result in various microstructures and film properties. These properties are related into a structural zone model (SZM) defined by *J. A. Thornton* [147]. SZM describes the microstructural properties of a deposited film with respect to the homologous temperature ($T_{substrate}/T_{melting}$) and the partial gas pressure ($P_{Ar}$) during fabrication as seen in Figure 2.22a. In this model, 4 different film morphology can be observed.

- *Zone 1* (green): It is a low temperature; i.e., low energy zone where film growth through shadowing processes occur. Shadowing describes the case where grain growth is faster on some directions compared to the others. It is observed between $T_s/T_m < 0.1$ and 0.4 at low and high pressures, respectively. Here incoming atoms reach the substrate surface from random directions. There is a general lack of surface mobility,

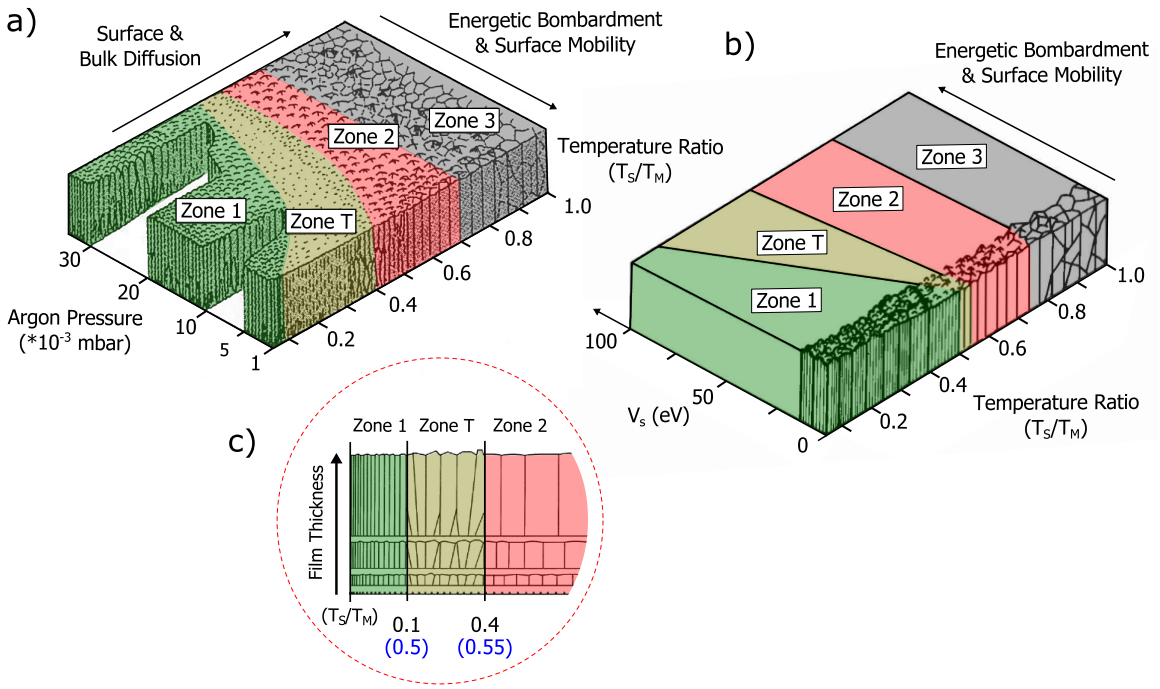


***Figure 2.22:*** *a) Structure zone model of Thornton et al. and b) Revised SZM by Messier et al. Image shows the different zones, where deposited films exhibit different microstructure. c) Close-up to the microsturucture with respect to film thickness. Homologous temperature values given in black and blue fonts belong to the case a and b, respectively. Images adapted from [148][149][150] and manually colored.*

hence grown films exhibit fibrous structures with voids and high porosity. In summary, a poorly crystalline structure is achieved.

- *Zone T* (yellow): This is the transition zone between Zone 1 and 2, which emerges with decreasing pressure. It is observed between $0.1 < {}^{T_s}/_{T_m} < 0.4$ and $0.4 < {}^{T_s}/_{T_m} < 0.5$ for low and high pressures, respectively. Void density is slightly reduced compared to Zone 1. Zone T contains densely (not fully) packed fibrous grains, where a competitive texture is present.

- *Zone 2* (red): This zone contains fully dense and columnar grain structure due to high surface diffusion. It is observed between $0.4 < {}^{T_s}/_{T_m} < 0.7$. Nucleated grains are oriented and they grow through the whole film thickness. Since voids are filled as a result of the surface diffusion, number of defects is greatly diminished.

- *Zone 3* (black): It is the highest temperature zone, way above the recrystallization temperatures of the spoken material. It is observed between $0.6 < {}^{T_s}/_{T_m} < 1$. Recrystallization results in randomly oriented grains that are no longer columnar. Therefore smaller grains vanish and larger grains form.

Temperature and pressure are considered as very influential parameters. The former is considered largely responsible for the surface diffusion phenomenon and the latter for the transportation of the sputtered atoms to the substrate's surface. Therefore, the pressure variable of the SZM can be considered as the kinetic energy of the incoming particles in the gas phase. Since the energy of these particles is inversely proportional to the process pressure, low pressures (and high homologous temperature) would result in higher energetic bombardment and greater surface mobility.

Following the empirical model of *J. A. Thornton*, *Messier et al.* revised the SZM with the consideration that $V_s$ induced mobility was more influential than the process pressure [150]. In this model, gas pressure is replaced by the floating substrate potential and the physical structure; i.e., microstructure, and its evolution under the influence of energetic particle bombardment that results from floating substrate bias is investigated. In this case, a much wider Zone 1 is observed, different from the Thornton model, a linear boundary-zone between Zone 1 and Zone T is approximated, as depicted in Figure 2.22b.

### 2.4.6 Fabrication of AlN Thin Films

AlN thin films can be fabricated using various methods including sputtering [151], pulsed laser deposition [152], ion beam deposition [153], molecular beam epitaxy [154], plasma enhanced CVD [155] and metal organic chemical vapor deposition [156]. Both quality and texture of the fabricated films, as well as the fabrication conditions such as process temperature, process gases and underlying substrate, can show variations with respect to the used method.

It was previously mentioned that, magnetron sputtering is the chosen method for the fabrication of thin films in this work. Using magnetron sputtering, fabrication of AlN thin films can either be realized from pure metallic targets in a reactive plasma (as is here) or from a compound target in an inert plasma. The former is generally preferred due to the stoichiometric freedom it offers, but requires a good understanding of the process in order to ensure high quality film deposition. AlN deposition from an Al target and involved particles are rather different than conventional sputtering of metallic targets (see Figure 2.23). Here, molecular $N_2$ becomes reactive through collisions with energetic particles. It dissociates into neutral $N$ and charged $N^+$, $N^-$ and $N_2^+$ [157]. If a high enough reactive gas flow is provided, positively charged ions accelerate towards the Al target where they form AlN (see Figure 2.19). As a result of the sputtering process, not only AlN molecules but also atomic nitrogen arrives to

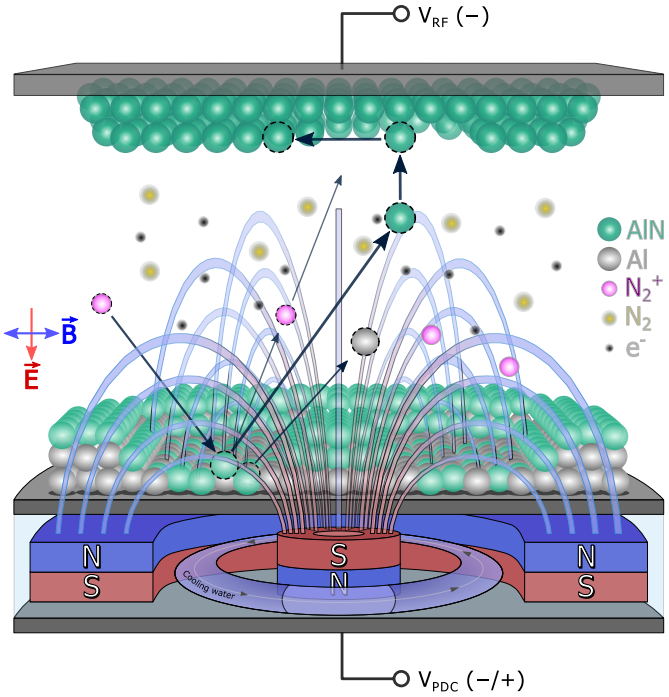


***Figure 2.23:*** *Reactive magnetron deposition of aluminum nitride from an aluminum target using pure reactive gas. Species involved in the process are shown with individual color code. Electrical and magnetic field directions are shown. Note that the anode is connected to a PDC generator, as is the set-up utilized in this work. Image adapted from [158].*

the growing film's surface from the target [21, p.11].

### Preferential Growth of AlN Thin Films

All thin films are made of grains, deposition parameters influence the grain growth and the grain growth dictates structural and electrical properties. Polycrystalline materials can be grown along different crystallographic directions according to the intended application's requirements. For SAW sensors, for instance, it is necessary to ensure <100> oriented AlN growth in order to maximize the piezoelectric activity along the film surface [159]. For the desired magnetoelectric sensor concept, on the other hand, it is imperative to obtain maximum piezoelectric response along the *c*-axis of AlN; i.e., <001> direction that is perpendicular to the substrate's surface. This is challenging since magnetron sputtering of thin film AlN is generally conducted far from the thermodynamic equilibrium; i.e., at low temperatures ($< 750\,^{\circ}\mathrm{C}$). Unlike chemical vapor deposited epitaxial[1] films; sputtered AlN films

[1] Epitaxial growth refers to the case where a crystalline thin film grows on a crystalline surface by adopting the crystal order of the latter [137, p.221].

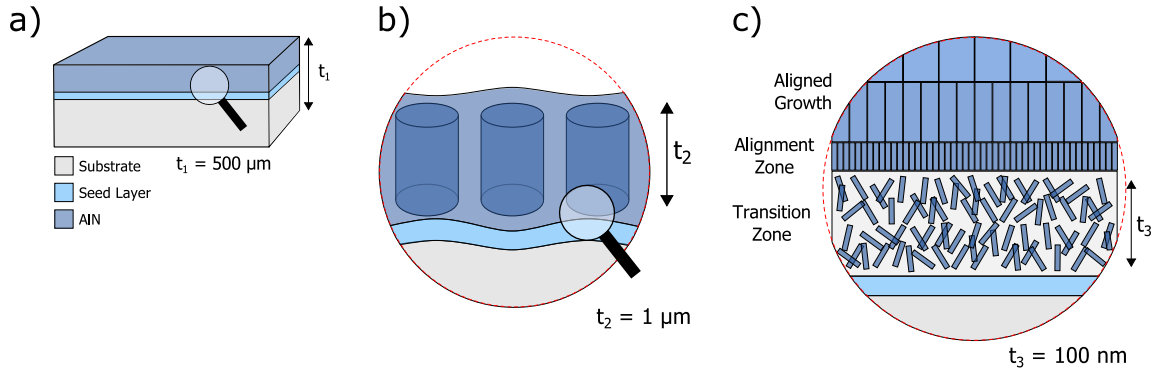


***Figure 2.24:*** *AlN nucleation and growth. a) Exemplary AlN film deposited on a seed layer covered substrate. b) Close-up to the microstructure of AlN. Oriented columnar structure is depicted. c) Schematized crystal growth of AlN. AlN nucleates on the seed layer's surface with a number of different growth directions. In the initial transition zone (t <100 nm), crystals of different orientations compete with each other. Energetically favored growth direction gains advantage and continues growing at the expense of the other directions forming an alignment zone. This alignment is preserved for the rest of the film growth, given that the deposition parameters are kept constant.*

are polycrystalline. Polycrystalline AlN films typically grow in the Volmer-Weber growth mode [160], where a number of microstructures with various orientations nucleate and initially grow together due to the lack of energy at the surface. During the early stages of the film growth ($t < 100\,\text{nm}$), grains of different orientations compete with each other. Grains nucleating along the energetically favored directions grow much faster than the misaligned grains and the latter group is consumed in the process [161]. This leads to an enhanced microstructural order, where all but one growth direction vanish. After the alignment zone, the orientation of the growing film is maintained as long as the process continues with constant parameters (Figure 2.24). It is often seen that in AlN films, for instance, the preferred orientation results from the competitive growth of (100) and (001) planes [162]. Such competitive growth usually results in diverse properties; e.g., orientation, grain size, morphology, etc., for the same film and eventually deteriorates piezoelectric properties.

Numerous reports discussing preferential AlN growth with respect to various process parameters; e.g., gas composition [107][163][164], seed layer material [165][166][167], process pressure [157][168][169], substrate temperature and bias [157][170][171] etc., can be found in the literature. No matter the investigated parameter, all previous literature agree that the preferential growth direction depends on the amount of kinetic energy transferred to the growing film.

This is in good agreement with a widely accepted thermodynamic model, which correlates the growth rate on different families of planes to the energy supplied to the adatoms

[172][173] [174][175][176][177][178]. Accordingly, when enough energy is brought to the growing film's surface, <001> oriented growth dominates. Otherwise, growing crystals start to tilt away from the <001> direction and other preferred orientations are observed to a point where <001> oriented crystals completely vanish. Influence of the mentioned factors and underlying mechanisms will not be discussed here in detail. Instead, necessary discussion will be presented within the results chapter in Section 4.1.3.

A summary of the possible AlN growth directions and respective peak intensities recorded via powder diffraction is provided in the Appendix (see Table A.1).

# 3 Experimental

The following chapter summarizes the experimental methods utilized in this work. The chapter is structured in a way that all fabrication and characterization methods are covered in detail. Both the technological background and the application specific parameters are presented. Additionally, utilized models are defined as well. Furthermore, a detailed process flow of an exemplary magnetoelectric sensor is presented.

## 3.1 Magnetoelectric Sensor Fabrication: State-of-the-art

Due to the constituent materials' specific properties, the fabrication of conventional-bilayer magnetoelectric sensors (substrate/AlN/FeCoSiB) follows a predefined process flow [72] [123]. Accordingly, a seed layer for AlN; e.g., Mo, Pt, etc., is deposited using a lift-off process as the first step. In the next step, AlN deposition in a reactive atmosphere is completed at temperatures as high as $200\,^{\circ}\mathrm{C} - 400\,^{\circ}\mathrm{C}$. A hard mask material such as Cr/Au, Ti/Pt or Mo is deposited on top of the AlN. Structuring of the hard mask is achieved with another lift-off process. Then AlN is brought to a desired geometry by wet chemical etching in an appropriate solution. Despite the presence of numerous media [179, p.118], the following are generally used due to their high etch rates;

- Aqueous *phosphoric acid solution* (PWS) at $80\,^{\circ}\mathrm{C} - 90\,^{\circ}\mathrm{C}$ with $\sim$90 nm/min etch rate,
- *Tetramethylammonium hydroxide* (TMAH) at $82\,^{\circ}\mathrm{C}$ with $\sim$8 µm/min etch rate,
- *Hydrofluoric acid* (HF) based buffered oxide etch (BOE) at room temperature with $\sim$4.5 nm/min etch rate.

Afterwards the hard mask material is removed with an appropriate method (without attacking the underlying AlN), generally using another wet etchant. Magnetostrictive film, which also acts as the top electrode material, is deposited and structured via additional lift-off processes, as well.

Even though the described fabrication process is well established, it does not provide optimal conditions. Every single lift-off or wet etching process requires an individual photolithography step, where an appropriate photoresist is applied, illuminated, developed and then stripped. Therefore, the surfaces on which thin film layers are deposited, are never intact. In fact, thin films are always grown on surfaces that are previously treated. This is especially problematic in cases where the utilized photoresist is subject to high energy physical etching methods; e.g., ion beam etching. In this case, the residual resist removal from the surface requires treatment with stronger compounds at high temperatures (80 °C) for several hours. However, such compounds can corrode the magnetostrictive material and deteriorate its magnetic properties. As a result, removal of the photoresist becomes almost impossible without using further physical etching methods such as plasma etching. These techniques, however, remove layers from the topmost material surface without selectivity and increase the surface roughness.

## 3.2 Magnetoelectric Sensor Fabrication

In order to prevent aforementioned problems, lift-off processing is completely removed from the current work. Instead, an inverse-bilayer sensor design and appropriate processing methods are adopted. In this way, all thin films are sputtered consecutively without exposing nucleation surfaces to non-vacuum conditions. Deposited films are then structured using standard photolithography techniques and a variety of wet/dry etching methods However since all surfaces except the one to be etched is protected at all times, remaining layers are never exposed to etchants. A schematized summary of the inverse-bilayer and conventional-bilayer type sensor fabrication is given in Figure 3.1 and the detailed explanations of individual steps are presented in the following sections.

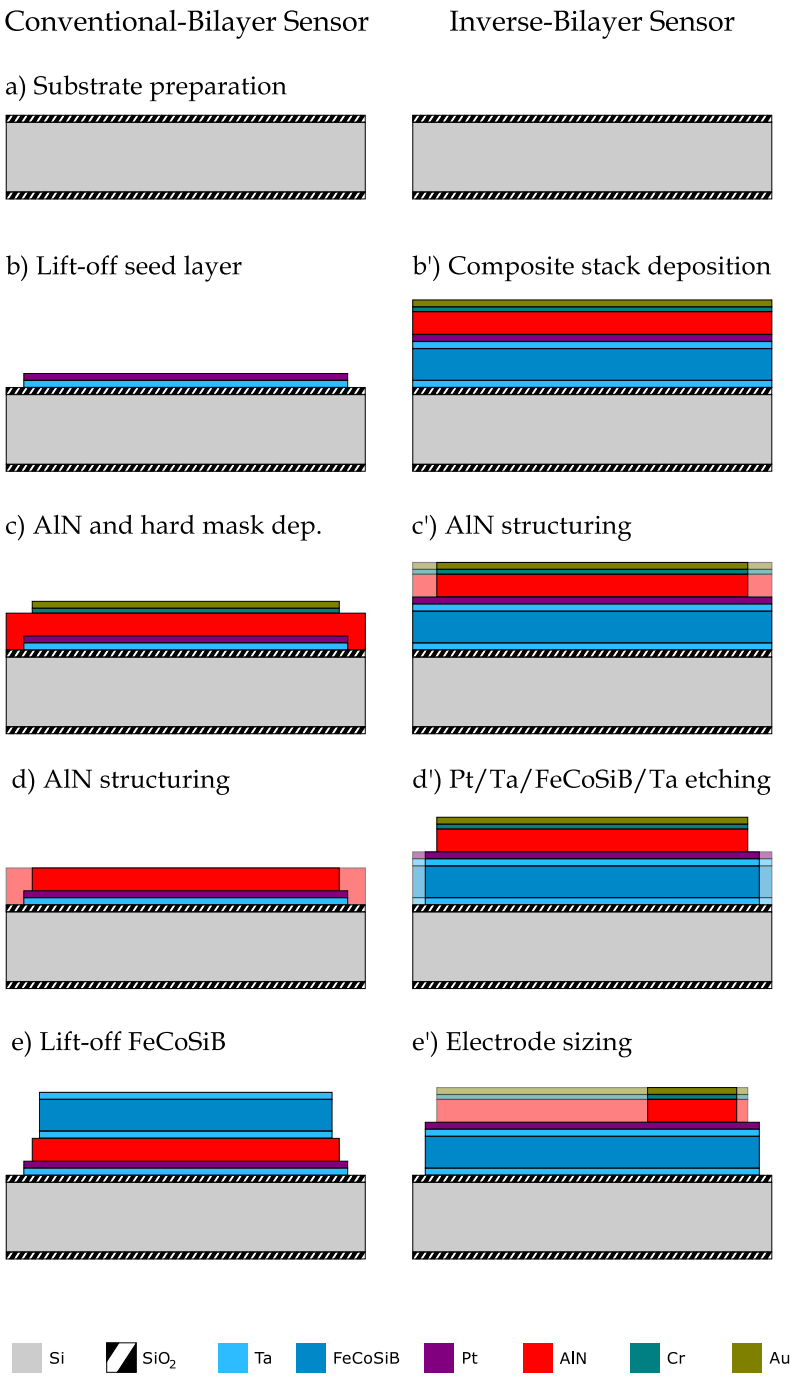


***Figure 3.1:*** *Fabrication of conventional-bilayer and inverse-bilayer magnetoelectric composite sensors. Individual steps include a) substrate preparation, b) seed layer deposition via lift-off, b') deposition of the composite stack, c) deposition of the AlN and an appropriate hard mask material, c') etching of the top electrode and structuring of the piezoelectric layer, d) structuring of AlN via wet chemistry and removal of the hard mask, d') etching of the remaining layers via IBE, e) deposition of the FeCoSiB layer via lift-off and e') scaling of the top electrode. The color code of the involved films are given below. Areas with lighter opacity represent the etched materials. Note that the top magnetostrictive layer acts as the top electrode for conventional-bilayer sensors. However, an additional Au/Cr gold layer is depicted for the sake of comparability during relevant studies.*

### 3.2.1 Thin Film Deposition

All processing begin with an initial substrate preparation step, where commercially available $4''$ wafers are cleaned and then cut into smaller chips by a semi-automated dicing saw (see Figure 3.1a). The chip size is chosen as $25\,\text{mm} \cdot 30\,\text{mm}$ for all sensors. Cleaning of the substrates is a three step process; where substrates are first dipped into acetone filled containers and subjected to ultrasonic vibrations in order to remove any organic residues, then flushed with isopropyl-alcohol and DI water in order to remove excess acetone and finally baked several minutes on an heating plate above the evaporation temperature of the aforementioned substances. Prepared substrates are then taken to the sputtering device; a Von Ardenne CS 730S magnetron cluster system, which allows the consecutive deposition from various target materials. In particular, the deposition of metallic adhesion and electrode layers (Ta, Cr, Pt and Au), as well as magnetostrictive and piezoelectric functional layers (FeCoSiB and AlN) were completed in this manner. Constituent layer order of the sensors may vary. For instance, conventional-bilayer stacks include a layer ordering of Ta/Pt/AlN/Ta/FeCoSiB/Cr/Au, whereas inverse-bilayer stack deposition order is as Ta/FeCoSiB/Ta/Pt/AlN/Cr/Au. Note that, a plasma etching step[1] is included into the process flows in order to remove the initial several nm of the underlying layers and to improve the texture quality of the deposited films.

Sputtering of AlN with optimized parameters is completed with a sputtering power of 1.5 kW. Reactive gas flow and the process pressure are optimized as 10 sccm and $2 \cdot 10^{-6}$ bar, respectively. Each AlN layer is preceded with a $100\,\text{nm} - 150\,\text{nm}$ thick Pt layer, in order to facilitate preferential AlN growth along the *c*-axis. The adhesion of the Pt seed layer is promoted by an underlying 30 nm thick Ta layer. Note that, both layers as well as AlN deposition conditions can be altered or their thicknesses can be varied in order to fulfill the requirements of

***Table 3.1:*** *Fabricated thin films and respective sputtering parameters.*

| Target Material | Power Generator | Power Density ($W/inch^2$) | Gas Flow ($sccm$) | Pressure ($bar$) |
|---|---|---|---|---|
| Ta | DC | $\sim 4$ | $Ar$, 30 | $4 \cdot 10^{-6}$ |
| Pt | DC | $\sim 8$ | $Ar$, 25 | $8 \cdot 10^{-6}$ |
| Cr | DC | $\sim 4$ | $Ar$, 25 | $4 \cdot 10^{-6}$ |
| Au | DC | $\sim 4$ | $Ar$, 25 | $6 \cdot 10^{-6}$ |
| FeCoSiB | RF | $\sim 4$ | $Ar$, 40 | $6 \cdot 10^{-6}$ |
| AlN | PDC | $\sim 30$ | $N_2$, 10 | $2 \cdot 10^{-6}$ |

[1] 100 W RF power, 30 sccm Ar flow and $6 \cdot 10^{-6}$ bar process pressure.

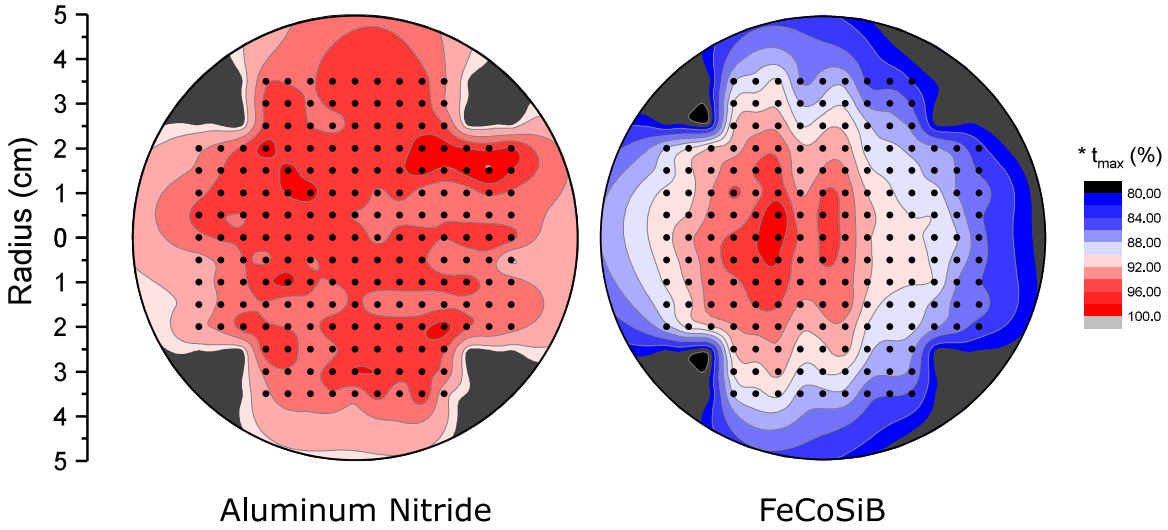


***Figure 3.2:*** *Film thickness distribution of AlN and FeCoSiB across 4″ wafers. Represented samples are characterized after 1.6 µm AlN and 3 µm thick FeCoSiB depositions, respectively. Color scale shows the thickness distribution as a percentage of the total thickness. Data points are shown as black circles. Color code scale represents the percentage film thickness with respect to the maximum film thickness.*

various sensor applications or to optimize residual film stress of the composite stacks. Suggested optimization steps were introduced during the cooperative works within the CRC 855 and PAK 902, such as the fabrication of magnetoelectric exchange-biased [125] and delta-E effect sensors [180], for instance.

For electrical and dielectrical characterizations, an additional top electrode of 90 nm thick Au is utilized. The adhesion of the Au film is promoted with a 10 nm thick Cr layer, which also acts as a hard mask during the wet structuring of AlN. Respective sputtering parameters of all constituent materials are summarized in Table 3.1.

Figure 3.2 depicts the thickness distribution of AlN and FeCoSiB film across 4″ wafers. Here, 1.6 µm AlN and 3 µm thick FeCoSiB covered wafers are represented. Using the deposition parameters summarized in Table 3.1, an extremely homogeneous AlN deposition is achieved. The thickness distribution across the wafer area is as high as $96.3\% \pm 1.4\%$ and the thickness difference between the center and the edge of the wafer is less than 5%. Even though both AlN and FeCoSiB targets are 8″ wide, a distinct thickness distribution is observed for the latter. The deposition exhibits a thickness distribution as high as $90.9\% \pm 3.9\%$, however unlike the AlN case, highest thickness is not achieved at the center of the wafer. FeCoSiB deposition is completed with a higher gas flow and pressure then AlN, hence the mean free path (MFP) of sputtered FeCoSiB is lower in comparison to the Al. In

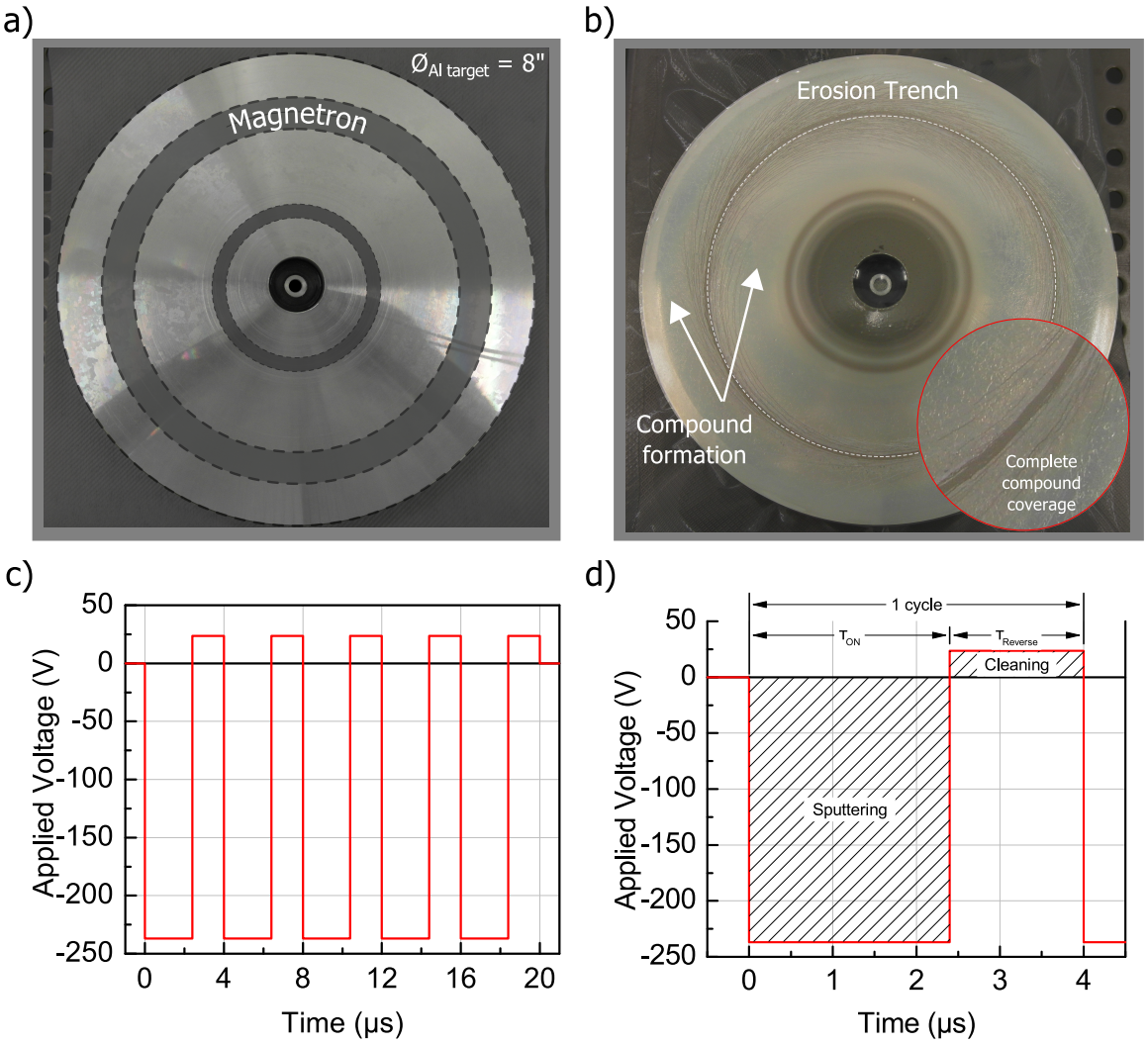


***Figure 3.3:*** *Target poisoning and its prevention. a) Initial target state; clean Al surface. Location of the magnetron is projected onto the target with dark grey coloring. Note that magnetron is a two-ring setup. b) Poisoned target. The surface is covered with AlN. Extreme compound formation along the magnetron rings is observed. c) Asymmetric-bipolar pulsing with an exemplary 250 kHz pulsing frequency. d) Close-up to a pulsing cycle of 4 µs. During the "on time", the sputtering of the Al target occurs. During the "reverse time", the applied voltage is reversed in order to clean the target surface. The magnitude of the reverse pulse equals to* $\left| {}^{1}/_{10} \right|$ *of the main pulse.*

that case, it is possible that some of the sputtered FeCoSiB is deposited on the chamber walls. Another possible reason can be the influence of the magnetic field created by the magnetron ring. However, the main reason is unclear at this point since no additional investigation was done.

As was previously discussed (see Section 2.4.3), the reactive sputtering of AlN is not a straightforward process unlike the DC magnetron sputtering of metallic layers. As a result of the reactive process nature, compound formation occurs on the target's surface as well (see

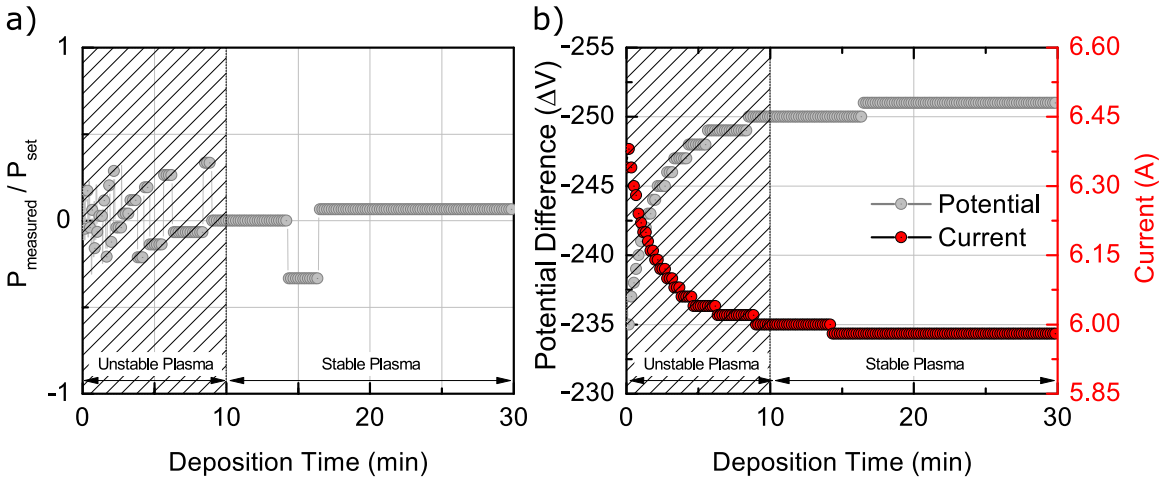


***Figure 3.4:*** *Properties of AlN deposition process. a) Discrepancy of the set power with respect to the deposition time. Set power is almost constantly delivered to the target after the initial 10 min of process time. b) Change in the voltage potential and the plasma current with respect to the deposition time. The process pressure is automatically regulated with a butterfly valve with respect to increasing plasma resistance. The process completely stabilizes after 10 min of deposition time.*

Figure 3.3a and b). This prevents reproducibility since sputtering from a compound covered target produces thin films of different stoichiometry. Furthermore, it leads to the formation of short/hard arcs, which inhibits the final film quality. Hence, it is necessary to establish an effective arc prevention/reduction method and to condition the target prior to each AlN deposition. The latter brings the target to an initial condition, which is used as the starting point for constant and reproducible film quality. Conditioning of the Al target is completed in two steps; first in pure Ar atmosphere[1] and then at the actual sputtering conditions.

Prevention of arc formation, on the other hand, is achieved by periodically pulsing the target voltage. In this work, the target is pulsed at a frequency of 250 kHz with a reverse period of 40%, which translates into a 1.6 µs cleaning period after a 2.4 µs deposition period[2]. The pulsing of the target voltage and consecutive deposition/cleaning parts of a cycle are depicted in Figure 3.3c and d. These pulsing parameters are optimized in order to minimize/prevent compound coverage at the erosion trench and the resulting arc formation. However, it is possible to adjust them in order to trade between sputtering rate and the target poisoning.

In order to regulate the generator, power is chosen as a constant (with less than $\pm$ 0.5% variation) input parameter (see Figure 3.4a). Plasma related properties such as the potential difference between the target and the substrate holder as well as the plasma current were

[1] 200 W DC power, 30 sccm Ar flow and $6 \cdot 10^{-3}$ mbar process pressure.

[2] An asymmetric bipolar PDC power supply[181] was integrated into the sputtering tool after initial investigations with RF and DC generators.

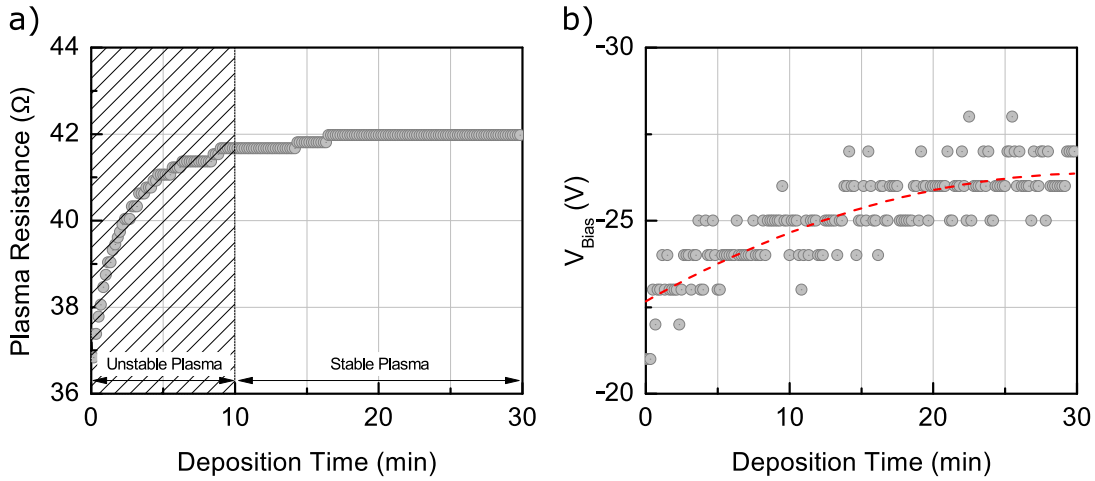


***Figure 3.5:*** *Plasma behavior during AlN deposition. a) Constant increase of the plasma resistance during the initial 10 min. b) Influence of the plasma on the self-bias measured at the substrate holder. Dashed line is a simple guide for the eyes.*

recorded from the generator output data. The former, for instance, increases during the process as seen in Figure 3.4b. The reason for this behavior is explained by *Dubois and Muralt*; when processing in high nitrogen concentration, the ionization probabilities decrease since some energy is lost to the motion of nitrogen molecules [172]. The optimal working conditions of a reactive process were previously described in Section 2.4.3. It can be argued that the optimal working condition is reached at the end of the initial 10 min. At this point, the target surface is covered with compound but the erosion trench is not. As a result, the voltage difference is firmly established and the unstable deposition period is over.

It is important to point out that AlN deposition is completed at pressure conditions as low as $0.9 \cdot 10^{-3}$ mbar $- 6 \cdot 10^{-3}$ mbar. This further decreases the aforementioned ionization probability, hence increases the plasma resistance. Suggested phenomenon can be observed from Figure 3.5a, where the change in the plasma resistance is depicted with respect to the process time. Figure 3.5b exhibits the change in the self-bias developed at the anode (substrate holder). Self-bias is influenced by all sputtering parameters and is often enhanced by applying additional RF bias. It is especially practical for the optimization of the residual film stress [182]. Here, on the other hand, its increase reflects the change of the plasma properties since all influential parameters; e.g., gas composition, cathode power, gas pressure, etc., are kept constant.

### 3.2.2 Structuring of Thin Films

***Photolithography:*** Photolithography is a pattern transfer method that is utilized both in industrial and scientific applications. The technique allows the realization of extremely fine and complex topographies for single and/or multilayered thin films [127, p.14]. It involves a number of process steps as depicted in Figure 3.6.

Here, a thin film deposited on a substrate is coated with a positive photoresist layer. Meanwhile the sample is spin-rotated with a speed of 2000 rpm – 4000 rpm in order to obtain an even resist distribution across the whole surface (*a*). Rotation speed is inversely proportional to the resist thickness and is therefore an important parameter to consider [127, p.3]. High speed rotation leads to the evaporation of the resist's solvent constituent to an extend. However, it is often the case that a resist baking step is necessary in order to evaporate the rest of the solvent (*b*). Baking time and temperature vary with respect to the utilized resist's type and viscosity but baking temperatures of $\sim$100 °C and times of $\sim$1 min are commonly observed for positive resists [127, p.6]. Next step is the pattern transfer from a masking structure onto the photoresist by means of ultraviolet (UV) illumination (*c*). UV illumination results in a chemical reaction on the photoresist's exposed surfaces, enhancing the solubility with respect to the unexposed surfaces (in case of positive resist). Then the sample is treated with an appropriate developer, which transforms the latent image created during the exposure into a visible one (*d*). The latter is achieved as the previously exposed photoresist surfaces dissolve and leave behind the unexposed features. The sample is then hard baked in order to remove any residual solvent and to increase the hardness of the undissolved resist. Once the resist is hard enough, it is suitable for wet/dry etching processes during which it acts as a masking layer (*e*). When the thin film structuring is completed, exposed photoresist is removed by an appropriate stripper (*f*).

As shown in Figure 3.1, several etching steps are necessary for the structuring of the sensors. Each etching process has a dedicated mask pattern (see Appendix, Figure A.1), which is imprinted on the photo resist covered sample via UV illumination. During the processing of inverse-bilayer sensors, Au, Cr and AlN layers are etched away by means of wet chemistry (see Figure 3.1c'). Relatively thin layers of Au and Cr are individually etched in respective etch solutions.

***Gold etching***: Etching of Au thin films is achieved using a potassium iodide and iodine mixture[1] in water. Common mixing ratio is $KI : I_2 : H_2O = 4\,g : 1\,g : 40\,ml$. The etchant

[1] TechniEtch ACI2.

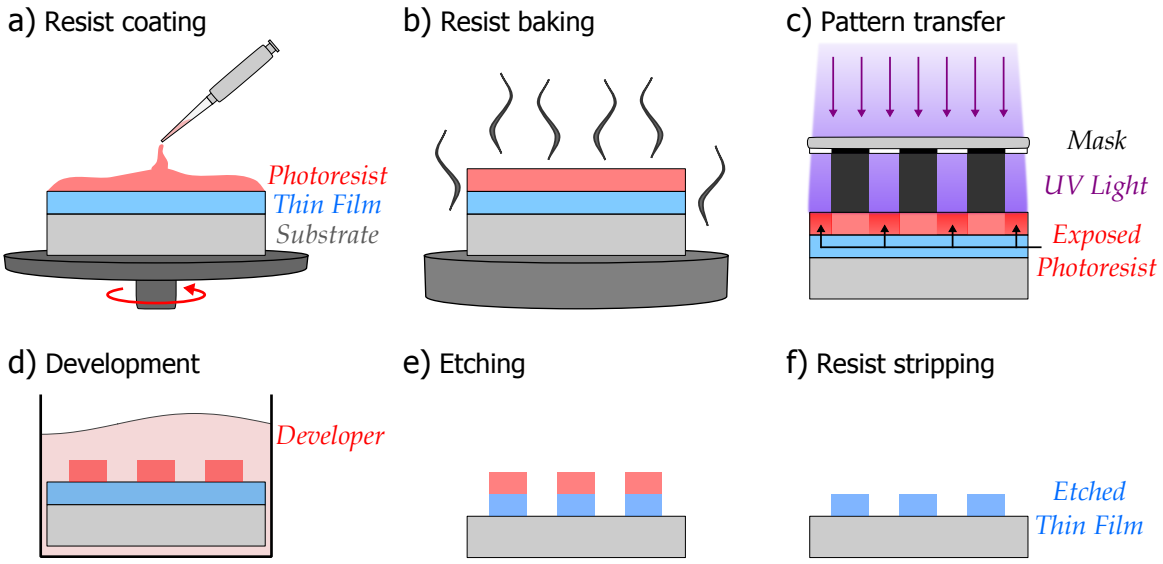


***Figure 3.6:*** *Photolithography process with a positive resist. a) Resist coating on a spin coater, b) resist baking in order to evaporate the solvent, c) latent image generation via UV-light exposure, d) dissolvement of the exposed resist in a developer, e) etching of the sample, f) stripping of the exposed photoresist. Image adapted from [127, p.2].*

is often mildly agitated in order to enhance and homogenize the process. With respect to the agitation, the etch rate of gold might vary between $0.5\,\mu m/min - 1\,\mu m/min$ at room temperature. The transformation of Au into gold iodide (AuI) is given as

$$2Au + I_2 \longrightarrow 2AuI \tag{3.1}$$

***Chromium etching*:** Cr adhesion layers are removed at room temperature using commercially available ceric ammonium nitrate (CAN) and perchloric acid[1] mixture in water with a mixing ratio of $Ce(NH_4)_2(NO_3)_6 : HClO_4 : H_2O = 10.9\% : 4.25\% : 84.85\%$. The etch mechanism is as follows

$$Cr + 3Ce(NH_4)_2(NO_3)_6 \longrightarrow 3Cr(NO_3)_3 + 3Ce(NH_4)_2(NO_3)_5 \tag{3.2}$$

The etch rate can be as high as $\sim$30 nm/min depending on the agitation level. This particular etch solution shows very high selectivity against AlN, hence Cr is often utilized as an AlN hard mask. Noble metals such as Au and Pt are not attacked neither, however the mixture is a very strong etchant against FeCoSiB. Therefore, a positive resist[2] is often used as the

[1] TechniEtch Chrome ETCH N°1.
[2] Microchemicals AZ6632.

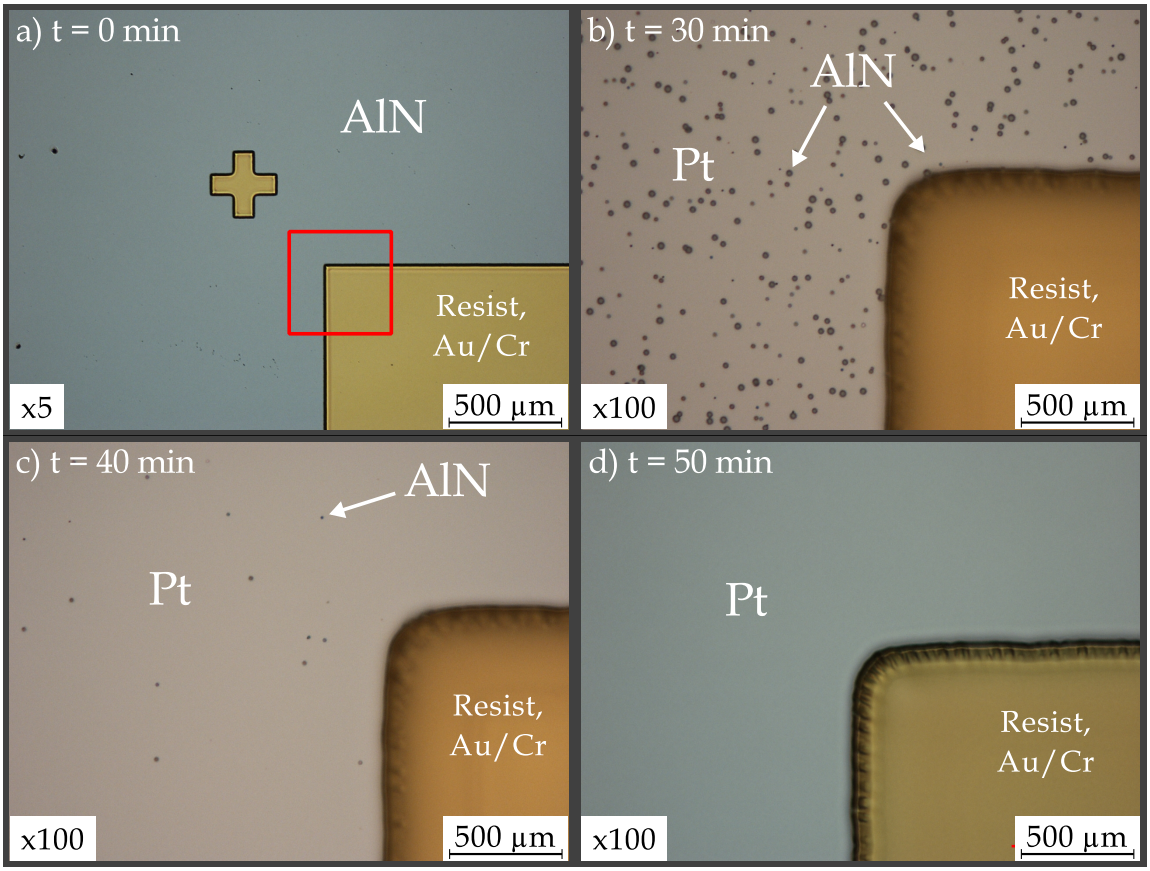


***Figure 3.7:*** *Microscope images of a sample surface during the wet etching process of AlN. a) Areas to be protected from the etchant are covered with a positive resist. Close-up to the marked area (red rectangle) b) after 30 min of etching, c) after 40 min of etching and d) after 50 min of etching. The underlying surface is Pt, observed residual particles are AlN. At the end of 50 min, all residual AlN particles are removed from the Pt surface.*

masking layer for both Au and Cr etching.

***Aluminum nitride etching*:** Commercially available phosphoric acid ($H_3PO_4$) solution[1] is utilized for the etching of AlN thin films. A combination of thin Cr/Au films and $3\,\mu m - 4\,\mu m$ thick layer of positive resist is used as the masking layer. No additional etch-stopper layers are required, since phosphoric acid is highly selective and would not attack other constituent materials. An etch rate of $\sim 53$ nm/min is observed with mild agitation at 82 °C. Faster etch rates via PWS or TMAH have been previously reported [35]. These etchants were not utilized in this work, however, due to the relatively thin AlN thicknesses and easier control of the phosphoric acid in comparison to the much stronger PWS and TMAH. Note that such etchants can be preferred for the etching of thicker films ($\geq 5\,\mu m$). Dry etching options are also investigated for the structuring of AlN. However wet etching in a $H_3PO_4$ solution proved

[1] ROTH ortho-Phosphorsäure 85%.

to be advantageous in terms of process time and economy, hence is adopted as the standard structuring method of AlN. As shown in Figure 3.7b, phosphoric acid reacts with AlN and removes the majority of the layer in ∼30 min. By the end of 50 min, complete removal of residual AlN (2 µm thick) particles is achieved and the underlying Pt is accessed.

At this point, the function of Cr/Au layers as the hard mask is completed. Therefore they are sized down to smaller dimensions and are further utilized as the top electrode of the magnetoelectric sensors (see Figure 3.1e').

***Ion beam etching (IBE)*:** Etching of Pt, Ta and FeCoSiB thin films (see Figure 3.1d') is achieved with an Ionfab® 300 IBE device from Oxford Instruments [183]. Unlike chemical etching, dry etching methods are based on the physical interaction between charged particles and the thin film, hence this process is not selective. The technique is suitable for various material types; e.g., metals, magnetic alloys, oxides, nitrides, etc.. Therefore it was possible to use IBE for the removal of all three layers consecutively during a single process until the underlying $SiO_2$ was reached.

The working principle is as follows; the process chamber is evacuated to a high vacuum ($P_{base} \leq 1 \cdot 10^{-7}$ mbar) and then is filled with Ar gas. As a RF power generator ignites the plasma, Ar ions are generated via electron bombardment and are driven through an accelerating grid that is negatively biased in order to form an ion beam. The sample surface is subject to interactions with energetic ions, however process areas can be limited using photolithography methods. When the energy of the striking ions is high enough to knock target surface atoms, etching is achieved.

The following process parameters were used in all processes; $1 \cdot 10^{-4}$ mbar process pressure and 500 W RF power. A relatively high beam current at 350 mA, which results in an ∼9 nm/min etching rate was chosen. Re-deposition issues, that are often observed during IBE processing, were avoided by using a neutralizer driven at 400 mA current. Over heating of the samples was prevented by cooling the sample holder's back surface by He gas that was supplied at 8 Torr pressure. IBE delivers very uniform etch profiles as a result of its rotating and tilting stage. Here, the sample stage was 30° tilted with respect to the incoming beam. The rotation speed of the substrate was chosen as 8 rpm.

The Ionfab® 300 device employs secondary ion mass spectroscopy (SIMS); a technique that evaluates the mass and the charge of the secondary ions ejected from the etched sample. Therefore it allows accurate control of the etch process as well as the exact etch depth

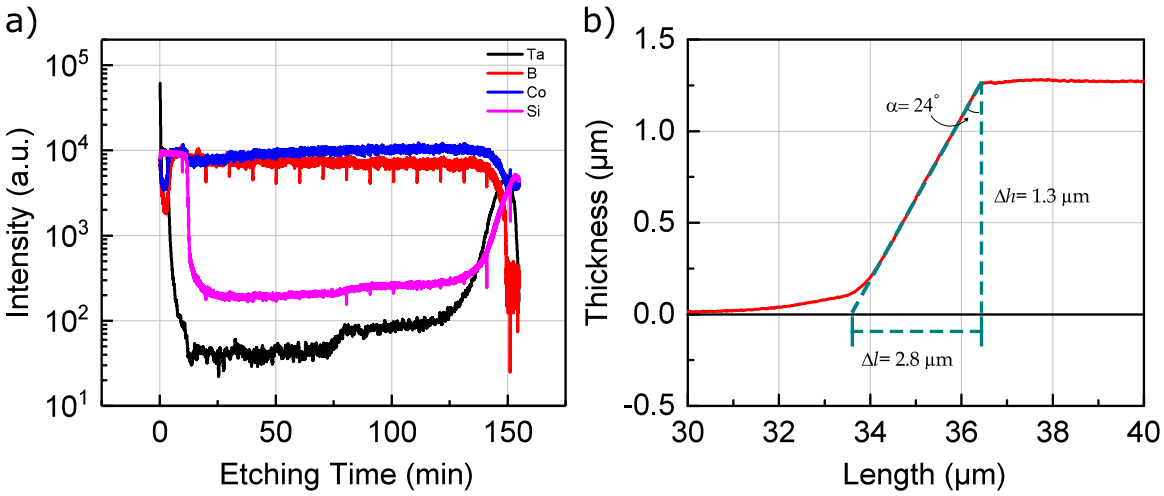


***Figure 3.8:*** *Ion beam etching of composite stacks. a) SIMS recording during an examplary IBE process of Pt/Ta/FeCoSiB/Ta layer stack. The signals from Ta, B and Co elements are plotted with respect to the etching time. Note that the down-time of the processing is not included in the plot. b) Exemplary etch profile after the photoresist is stripped.*

[184]. An exemplary SIMS recording, with a FeCoSiB thickness of ∼1.8 µm, is given in Figure 3.8a. Normally, an IBE process includes several etching/cooling cycles. Therefore, SIMS profiles depict the down-time where there is no signal detected from the sample due to the closed chamber shutter. These steps are omitted in the given figure. Instead, the whole process is depicted as a single etch step. As shown, the initial Ta layer is thinner in comparison to the secondary Ta layer due to the fact that the initial layer has previously been subject to plasma etching (prior to Pt deposition). Since Ta layer is extremely thin (∼10 nm), B and Co signals from the underlying FeCoSiB can be detected as well. The former is quickly removed from the surface and the signal of the other two increases. After this point Ta layer lays too deep for SIMS to detect, hence observed signals shall be considered as background noise. At approximately 1.7 µm etch depth (125. min), SIMS is able to detect the Ta signal as a result of the greatly diminished FeCoSiB thickness. At 1.8 µm etch depth, FeCoSiB layer is almost completely removed. Resulting step profile for an exemplary 1.3 µm thick sample is shown in Figure 3.8b. The process produces an etch profile of 24° and an etch step ($\Delta l$) of 2.8 µm, which is approximately twice as large as the sample thickness.

The IBE process finalizes the sensor fabrication steps and the final cantilevers are ready for magnetic optimization.

### 3.2.3 Field Annealing

Anisotropic properties of magnetostriction are previously discussed in Section 2.2.3. In its amorphous state, FeCoSiB does not exhibit a magnetocrystalline anisotropy. Therefore an in-plane anisotropy has to be induced into the thin film via magnetic annealing [104]. The process is completed below its Curie temperature and in a vacuum chamber operating under high-vacuum conditions as depicted in Figure 3.9a [185]. Accordingly, FeCoSiB samples are heated up to 250 °C and an external magnetic field as high as 2 kOe is applied along the short cantilever axis. The magnetic annealing is applied for 30 min and then the heating is turned-off while maintaining the magnetic field constant. As a result of the annealing, magnetically easy and hard axes are induced in the sample. The resulting influence can be seen in Figure 3.9b, where exemplary magnetostrictive curves of a sample before and after magnetic annealing are depicted. Dashed lines represent the initial measurements prior to magnetic annealing. Here, red and blue curves are recorded when the magnetically easy direction of the samples are aligned at 90° and 180° to the applied external field direction, respectively.

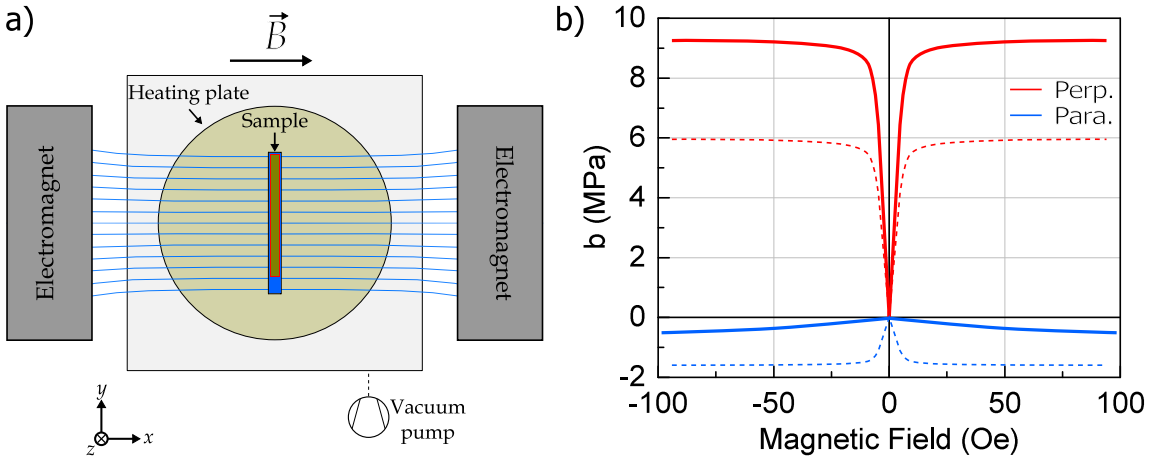


***Figure 3.9:*** *Field annealing of FeCoSiB. a) Schematic depiction of the magnetic annealing setup. Process completed in a vacuum chamber and at 250 °C. Heated samples are under a constant 2 kOe magnetic field for 30 min. Field is present during the cooling period as well. b) Influence of the magnetic annealing on the magnetostriction curves. Dashed and full lines represent the non-annealed and annealed samples, respectively. The measurement is done twice; once when the easy axis of the cantilever is perpendicular to the external magnetic field and once when parallel.*

## 3.3 Characterization Methods

It is often the case that, several substrates are processed together during the fabrication of a sensor. Not all of these substrates are completely structured into sensors but are prepared in order to investigate different properties of the constituent layers. Most important properties to characterize include microstructural properties of AlN and FeCoSiB, residual stress of individual thin films and composite stacks, dielectric and piezoelectric properties of AlN, magnetostrictive properties of FeCoSiB, etc.. To that end, numerous characterization methods were used and in the following section technological background and application parameters of these methods are presented.

### 3.3.1 Microstructural Properties

***X-ray Diffractometer (XRD)***: Crystallographic properties of the deposited films were investigated by a Seifert XRD-3000 PTS device as seen in Figure 3.10. The device consists of a X-ray tube containing a Cu anode material, Goebel mirrors, a goniometer which can be manipulated in 4 different axes and a detector. The working principle is as follows; $K_\alpha$ radiations of a Cu anode material[1] are generated in the X-ray tube. Since they contain multiple incident angles, they are directed to the Goebel mirrors; i.e., X-ray reflectors. Goebel mirrors produce highly intensified beams and generate parallel beams by refocusing the main beam into parallel paths. These beams are driven through divergent slits, which block X-rays with high divergence before they hit the specimen. The specimen to be investigated is mounted onto the goniometer's dedicated holder. As X-rays hit the specimen, they penetrate the lattice and interact with atoms of the target material [137, p.247]. They get diffracted by the target atoms and scatter into various directions. If a certain condition, where the incident and scattered beam angles ($\Theta$) are equal, is fulfilled than a constructive interference of the beam is achieved. All scattered beams are captured and counted by a point detector, which is connected to a software that can generate characteristic plots known as X-ray diffractograms.

Aforementioned condition is known as the Bragg's diffraction law [187] and is schematized in Figure 3.11. It forms the fundamental measurement principle of X-ray techniques. In cases, where the Bragg's diffraction law is fulfilled, path length of the incoming beams that hit atoms residing in neighboring lattice planes differ by $S$. Considering the reflection of the beam, path length difference between the beams equals $2S$. Hence it can be deduced

[1] $\lambda_{Cu} = 1.54056\,\text{Å}$ [186].

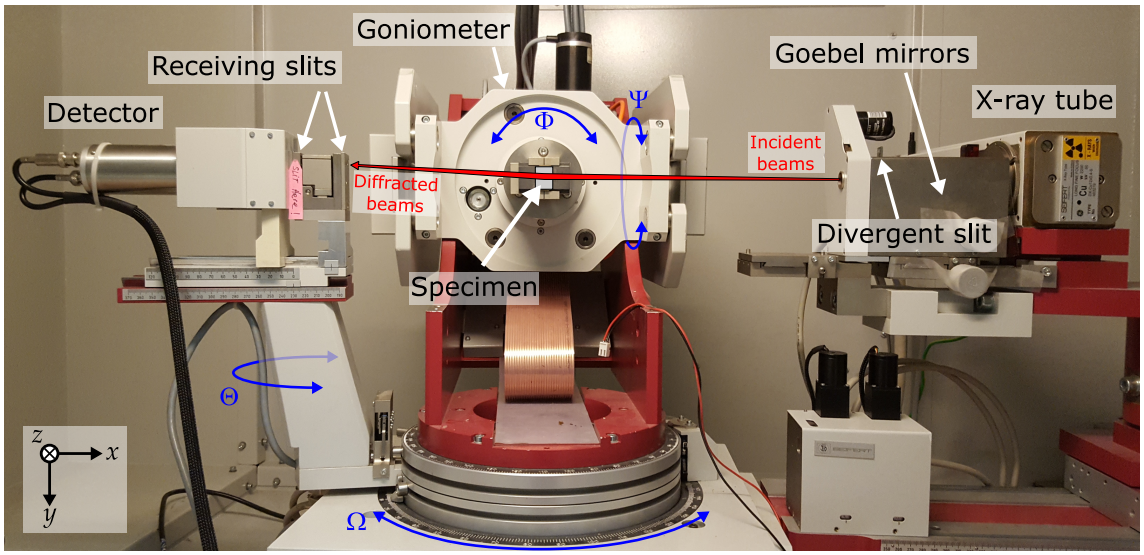


***Figure 3.10:*** *Seifert XRD-3000 PTS device. The diffractometer constitute of a X-ray tube, Goebel mirrors to intensify and refocus the generated X-rays into parallel paths, divergent slits to limit X-rays before they interact with the specimen, a goniometer to carry and to manipulate the specimen in different axes, receiving-end slits to condition the diffracted X-rays and a detector to count and record the quantity of X-rays scattered by the specimen. 4 different rotation axis of the goniometer; i.e.,* $\Omega$*,* $\Theta$*,* $\Phi$ *and* $\Psi$*, are shown with blue arrows.*

from Figure 3.11 that $S = d_{hkl} \cdot sin\Theta$ and $2S = 4\lambda$. Accordingly, Bragg's condition can be summarized as

$$2d_{hkl} \cdot sin\Theta = n\lambda \tag{3.3}$$

where, $d_{hkl}$ is the lattice spacing between neighboring planes, $\Theta$ is the incident and scattering angles, $\lambda$ is the wavelength of the incident beam, $n$ is an integer and $h$, $k$, $l$ are the Miller indices.

Note that the former is given with

$$d_{hkl} = \frac{a}{\sqrt{h^2 + k^2 + l^2}} \tag{3.4}$$

where, $a$ is the lattice spacing of the cubic crystal.

Two measurement modes were used in this work; i.e., the Bragg-Bretano scan and the rocking curve scan. The former is also known as the $\Theta - 2\Theta$ scan and measures the degree of

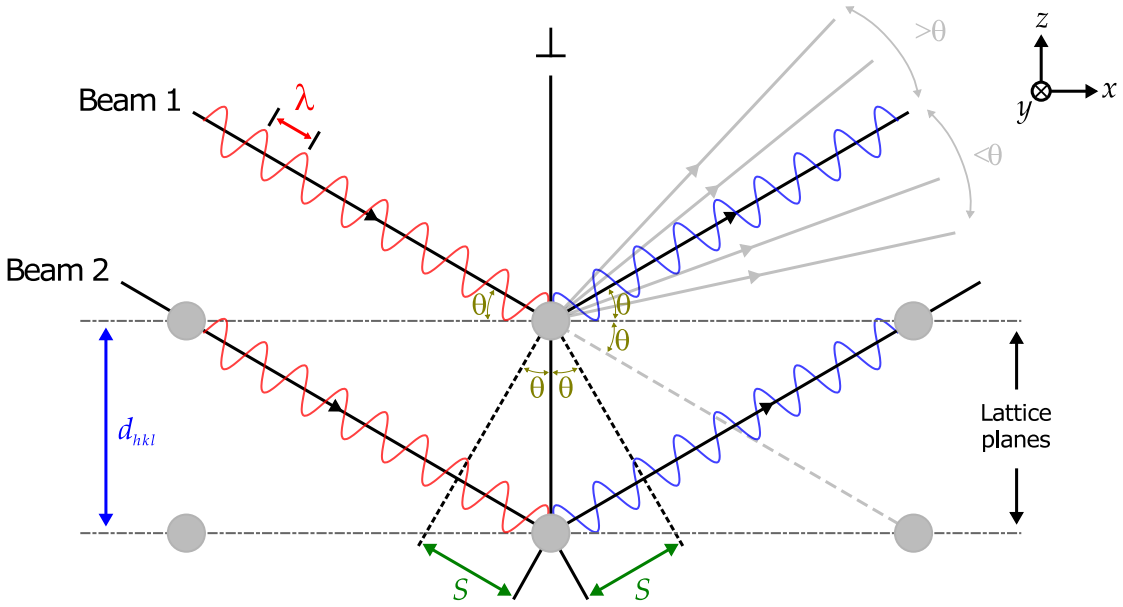


***Figure 3.11:*** *Schematic depiction of Bragg's diffraction law and constructive interference. A thin film specimen laying along the x-axis, two identical beams; i.e., with same wavelength ($\lambda$) and phase, hit neighboring lattice planes of the specimen and scatter in all directions. Parallel beams, scattered by different atoms, traverse additional path-lengths, which equal $2d_{hkl} \cdot sin\Theta$. When the Bragg's condition is fulfilled, the incoming and diffracted beam angles are equal. In this case additional path-length traversed by the beam is a multiple of the incoming beam's wavelength by an integer ($n\lambda$). Image adapted from [137, p.248].*

preferential orientation (texture level) in polycrystalline films [137, p.565]. Considering Figure 3.10, where the specimen surface lays in the $x-y$ plane, $\Theta-2\Theta$ scan is performed by rotating the goniometer in $\Omega$ and $\Theta$ axes. During the scan, the X-ray detector is constantly kept at a $2\Theta$ angle with respect to the incident beam. Generated diffractograms show maximum peaks at characteristic $2\Theta$ angles, which belong to particular atomic planes of crystallites of the investigated specimen. Intensity of the measured peaks is a qualitative measure of the degree of texturing for that specific crystallite. It is also possible to deduce the size of the crystal grains from the width of the aforementioned peaks at half of the maximum intensity; i.e., FWHM, and the modified Scherrer Formula

$$ln\beta = ln\left(\frac{\kappa \cdot \lambda}{\tau}\right) + ln\left(\frac{1}{cos\Theta}\right) \tag{3.5}$$

where, $\beta$ is the FWHM at the $2\Theta$ angle (radians), $\kappa$ is the shape factor ranging between 0.62 – 2.08 (usually taken as $\kappa = 0.89$), $\lambda$ is the wavelength of the XRD radiation (nm), $\tau$ is the mean grain size (nm) and $\Theta$ is the half diffraction angle of crystalline orientation peak ( $^\circ$ or

radians) [188].

After determining the crystallites present in a specimen, it is often the case that rocking curve scans are performed. Rocking curve scans are done by fixing the detector at the previously determined 2Θ angle and by tilting the specimen along the Ω-axis. These measurements produce plots, where the peak intensity decreases as the specimen is further tilted from the initial position until the disappearance of the intensity. Hence, rocking curves allow a way to deduce the crystalline perfection [137, p.565]. Generally, rocking curve measurements are used for epitaxial films but here they were utilized in combination with pole figures in order to confirm high texture quality of the deposited films. After applying a Gaussian fit to the generated rocking curve plot, it is possible to deduce the FWHM using

$$FWHM_{RC} = 2\sqrt{2ln2} \cdot \sigma \tag{3.6}$$

where, $\sigma$ is the standard deviation related to the width of the curve.

***Transmission Electron Microscopy (TEM)***: Further investigations of the fabricated films were completed with TEM. TEM is an analysis technique, which utilizes electron beams in order to obtain atomic level information on the microstructure; i.e., grain structure, precipitates, dislocations, crystal quality, etc.. Here, thin lamellae of AlN were prepared by focused ion beam (FIB) milling[1] with an FEI Helios Nanolab system. Structural investigations were performed using a FEI Tecnai F30 G2 STwin operated at 300 kV (field emission gun, spherical aberration coefficient CS = 1.2 mm). Selected area electron diffractions (SAED) were carried out via apertures limiting the illuminated area of the thin films circularly to diameters up to 250 nm and 850 nm. The evaluation of all high resolution (HR)TEM micrographs, Fast Fourier Transforms (FFTs) and SAED patterns was executed with the program Digital Micrograph 3.6.1 (Gatan, Inc.) (DM). Contrast enhancement for HRTEM micrographs was enabled using the HRTEM filter plug-in for DM [189]. Chemical characterization of the deposited AlN films were done using energy-dispersive X-ray spectroscopy (EDX). EDX is a localized chemical analysis method, which collects information from X-rays emitted from a solid specimen upon interaction with an electron beam [190, p.18]. In this work, EDX was performed by an EDAX Si-Li drift detector integrated into the TEM device.

***Atomic Force Microscopy (AFM)***: AFM is a high resolution scanning probe microscopy

[1]Thin lamellae were prepared by Dr. rer. nat. Christiane Zamponi from the chair for Inorganic Functional Materials (Prof. Dr.-Ing. Eckhard Quandt) of the Kiel University.

technique, which can resolute surface features below 1 nm [191]. It consists of a cantilever with a sharp tip, which scans the surface of the specimen, a laser directed onto the cantilever and a photo-diode. As the cantilever interacts with the specimen's surface and displaces, so does the reflection of the laser on the photo-diode. As a result, three dimensional (3D) topography of the investigated surface is determined. AFM creates the surface topography along the $z$-axis via raster scanning; i.e., taking consecutive scans along the $x$-axis within a given scan length along the $y$-axis [137, p.562]. Lateral resolution; i.e., resolution along the $z$-axis, is dependent on the stylus radius. There are three imaging modes of AFM; contact, tapping and non-contact. In this work, an Autoprobe CP AFM from Thermo Microscopes was used in the tapping mode for the investigation of the fabricated films.

***Magneto-optic Kerr Microscopy (MOKE)***: MOKE is a magnetic imaging technique that is used to characterize the magnetization on a magnetic materials's surface [192]. The method relies on the interactions between the magnetization within a sample and the polarized light shined upon it. Upon reflection from the sample's surface or transmission through it, the polarization characteristics of the light changes with respect to the incident beam. In this work, MOKE was used in the order to investigate conventional-bilayer magnetoelectric composites[1] .

### 3.3.2 Piezoelectric and Dielectric Properties

Piezoelectric thin films can not be characterized similar to bulk materials since their displacement is governed by the strong clamping onto the underlying thick substrates. In this case conventional methods do not properly define the piezoelectric coefficients, hence it is necessary to have new measurement methods and appropriate piezoelectric coefficients. Over the last years, two new measurement methods have been developed for the characterization of thin film piezoelectrics; the double beam laser interferometry and the 4-point-bending method. These methods can determine the effective longitudinal ($d_{33,f}$) (see Equation (2.8)) and transversal ($e_{31,f}$) (see Equation (2.9)) piezoelectric coefficients, which are the directly measurable piezoelectric coefficients of the fabricated AlN thin films [29]. In this work, $d_{33,f}$ and $e_{31,f}$ coefficients were determined using aixDBLI [193] and aix4PB [194] devices of the aixACCT Systems, respectively.

***Double Beam Laser Interferometer (DBLI)***: The first measurement device; i.e., aixDBLI,

[1]MOKE investigations are completed by M.Sc. Matic Klug from the chair of Nanoscale Magnetic Materials (Prof. Dr.-Ing. Jeffrey McCord) of the Kiel University.

is shown in Figure 3.12.

Basic measurement principle relies on the differential measurement of both top and bottom surfaces of a specimen; i.e., a piezoelectric thin film deposited onto a substrate. Accordingly, a single intensity stabilized HeNe laser[1] beam is reflected towards and driven through a $\lambda/2$ wave plate with the help of mirrors ($M_1$ and $M_2$) and then is split into two individual beams by a polarizing beam splitter (PBS); i.e., the measurement beam and the reference beam. The measurement beam (blue) is directed to both surfaces of the sample; it hits the top surface after passing through a $\lambda/4$ wave plate with the help of a mirror ($M_3$). Upon being reflected back from the top surface, it is driven to the back surface of the sample with the help of a beam splitter and another mirror ($M_4$). The polished bottom surface of the sample reflects the beam back, which is then directed to the photo diode with the help of additional mirrors ($M_5$ and $M_6$). The reference beam (white), on the other hand, is driven through a $\lambda/4$ wave plate, hits the reference mirror and is then reflected back towards the beam splitter. It also follows the same path to the back side of the sample and is directed to the photo-diode in a similar manner as the measurement beam. The whole system is encapsulated preventing parasitic beam reflections and reducing acoustical disturbances as well as air flow effects.

When a voltage is applied across the thickness of the piezoelectric sample, its thickness changes. Considering a piezoelectric thin film deposited on a Si substrate, the thickness change would disturb and change the optical path length of the measurement beam relative to the reference beam. As a result of the path length change, the interference pattern detected by the photo diode would change as well. Due to the difference in the intensity change of the interference patterns captured by the photo-diode, the DBLI device can determine the linear expansion of the piezoelectric film with extreme precision ($\leq 1\,\text{pm}$). Even though several characteristic properties can be measured, DBLI was mainly used in order to determine the effective longitudinal piezoelectric coefficient as given in Equation (2.8).

***4-Point-Bending Setup***: Determination of the effective transversal piezoelectric coefficient ($e_{31,f}$) relies on a customized mechanical 4-point-bending setup as shown in Figure 3.13a. Unlike the DBLI, 4-point-bending device measures the current response of a piezoelectric material upon mechanical bending. It consists of a single-point vibrometer, a laser that is directed towards the sample with a mirror, a sample holder and a piezoelectric actuator to prestress the sample. In this method, a cantilever shaped sample is fixed between 4 cylindrical supports, where the separation between the top support pair ($l_2$) is twice as much as the bottom support pair ($l_1$) (see Figure 3.13b). During the measurement, the sample is subject

[1] $\lambda = 632.8\,\text{nm}$.

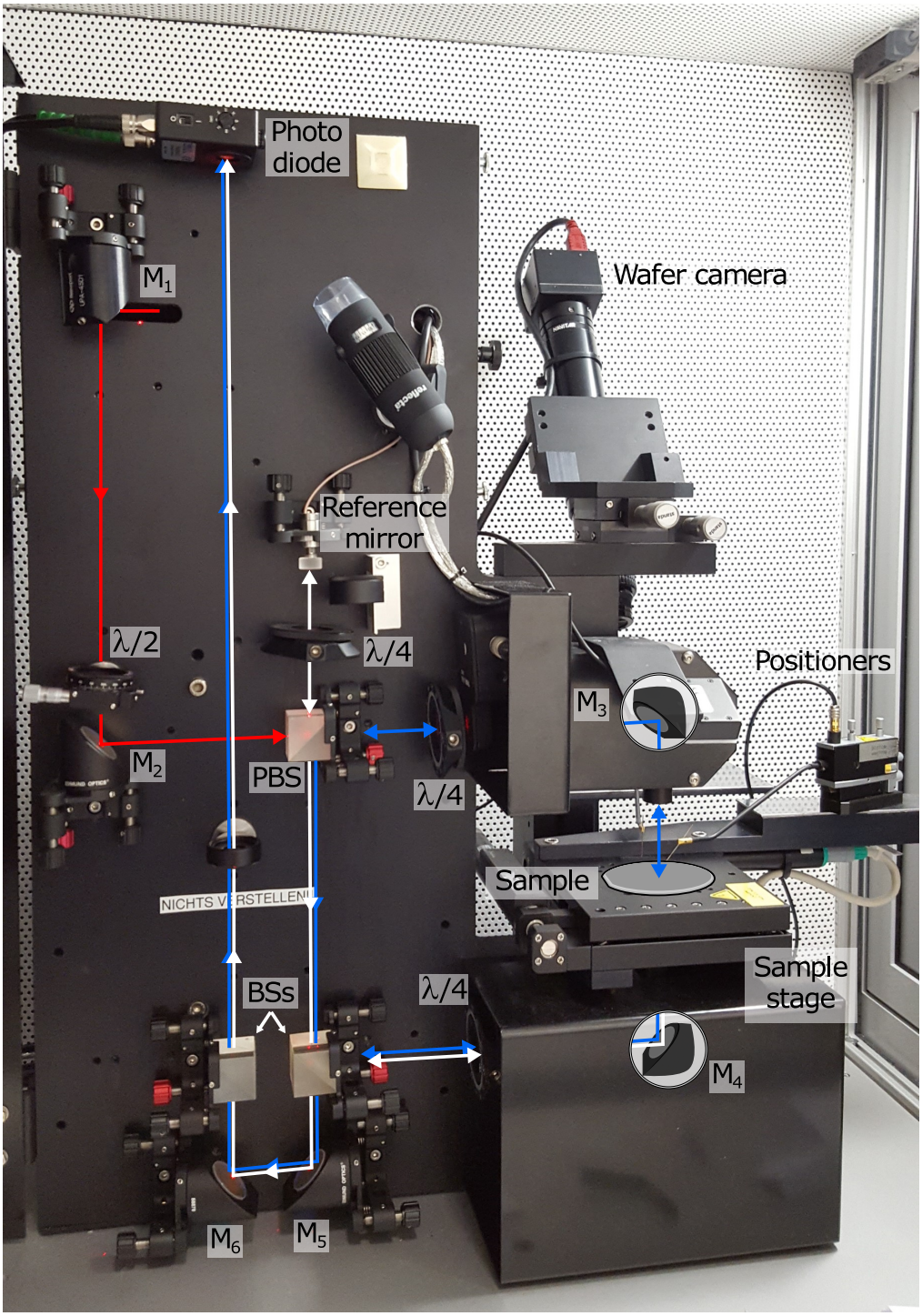


***Figure 3.12:*** *aixDBLI semi automatic DBLI. The measurement chamber consists of a HeNe laser, beam splitters, several mirrors to guide individual beams, wave-plates to alter the wavelength of the beams and a photo diode. Initial (red), reference (white) and measurement beam (blue) paths are shown. Upon subject to voltage, piezoelectric thin film undergoes a thickness change which in turn alters the optical path length and the interference pattern of the measurement beam.*

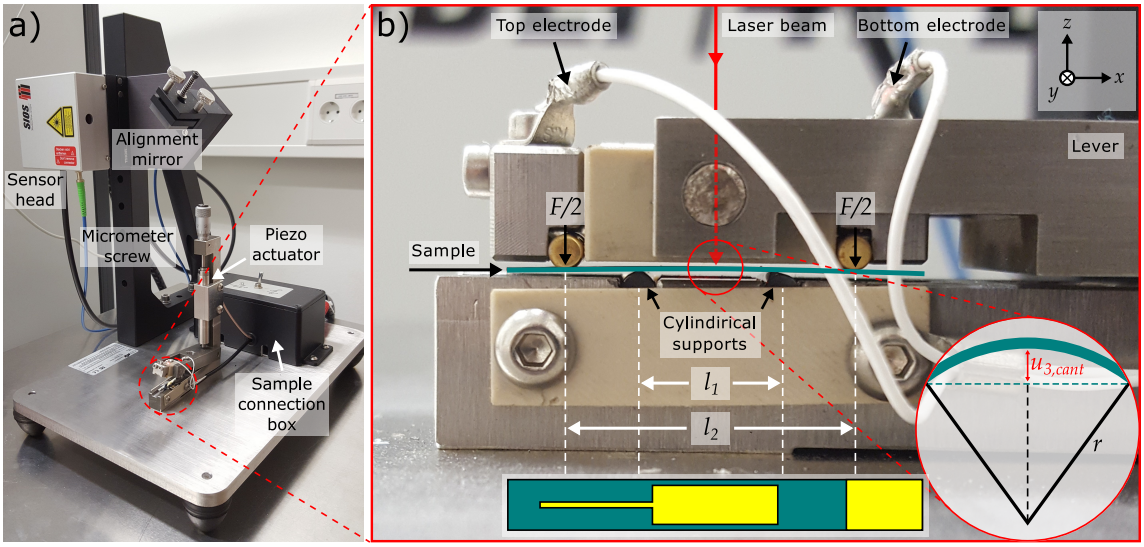


***Figure 3.13:*** *aix4PB measurement system. a) Sample holder with 4-point-bending configuration. b) Close-up to the sample holder; relevant constituents as well as the sample geometry are shown. Sample produce a constant bending moment when mechanical force is exerted onto it. Resulting out-of-plane displacement is detected by the laser vibrometer and the transversal piezoelectric coefficient is calculated by the dedicated software.*

to a constant mechanical force ($F$) that is evenly distributed between the two top supports ($F/2$), which also act as top and bottom electrode contacts. Applied force results in a constant bending moment ($M$) on the sample, hence an homogeneous stress and strain distribution is achieved between the inner supports where the actual piezoelectric film is deposited. Generated strain; i.e., an out-of-plane thickness change of the cantilever ($u_{3,cant}$) is detected by the laser vibrometer. Finally, the effective transversal piezoelectric coefficient is determined with respect to Equation (2.9) from the induced electrical charge. The specific cantilever geometry, which is a prerequisite of the method, was adopted from *Prume et al.* [195].

***Inductance-Capacitance-Resistance (LCR) meter***: Piezoelectric thin films fabricated in this work are sandwiched between two metallic electrodes, therefore operate in a plate capacitor geometry. Unlike DC polarization conditions, where a constant relative permittivity ($\varepsilon_r$) is present, piezoelectric AlN in a magnetoelectric sensor configuration is always under AC conditions. Under AC conditions, the movement of atoms/molecules of a dielectric result in dielectric losses. Practically all dielectric mediums, other than the vacuum, experience a certain amount of energy loss when an electric charge flows through. This energy loss is known as the dissipated energy and is often observed in the form of heat [30]. The importance of dielectric losses in this work is related to the SNR of the piezoelectric material and the magnetoelectric sensors [196]. The former is inversely proportional to the frequency dependent

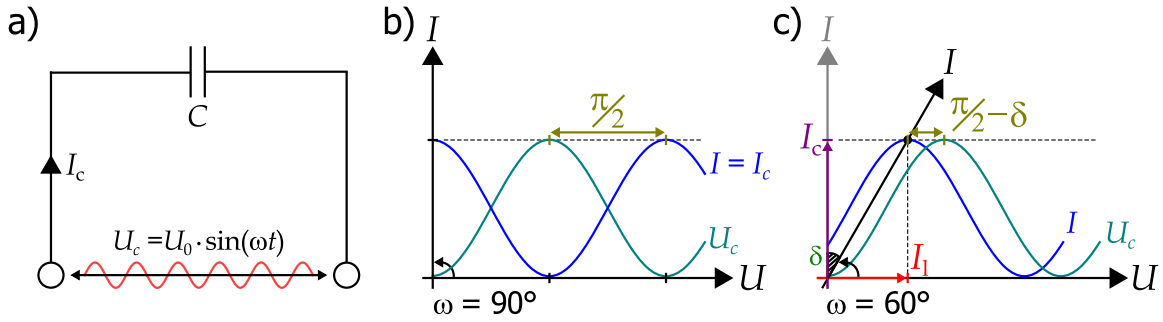


***Figure 3.14:*** *a) Circuit depicting a perfect capacitor with an applied AC voltage. Capacitance and the current are given as C and $I_c$, respectively. b) Phasor diagram and the behavior of the voltage/current for a perfect capacitor. Angular frequency w and a constant phase difference of $\pi/2$ radian (= 90°) are maintained. c) Phasor diagram for a real capacitor. Current has two components one of which ($I_l$) leads to power losses and shift the phase difference by $\delta$. Image adapted from [22, p.61-64].*

dissipation factor; i.e., loss tangent ($\tan\delta$), as shown in Equation (2.12).

An exemplary circuit containing a perfect capacitor with capacitance ($C$) and an AC voltage source is schematized in Figure 3.14a. The alternating voltage in the circuit ($U_c$) can be described as

$$U_c = U_0 \cdot sin(\omega t) \tag{3.7}$$

where, $U_0$ is the peak voltage and $\omega$ is the angular frequency with $\omega = 2\pi f$.

The phasor diagram of the same capacitor is depicted in Figure 3.14b. In this case, where there are no dielectric losses, the current ($I = I_c$) is 90° out-of-phase with the voltage ($U_c$) and equals

$$\begin{aligned} I_c &= C \cdot \dot{U} \\ I_c &= C \cdot U_0 \cdot \omega \cdot cos(\omega t) \end{aligned} \tag{3.8}$$

Accordingly time averaged dissipated power can be given as

$$\bar{P} = \frac{1}{T} \int_0^T (U_c \cdot I_c) dt = 0 \tag{3.9}$$

where, the time period $T = {}^{1}/_{f}$ [22, p.61].

The phasor diagram of an exemplary real capacitor is shown in Figure 3.14c. In the given example, the current ($I$) is 60° out-of-phase with the voltage ($U_c$) and its minimum no longer coincides with the peak voltage. It constitutes of two components; the first component is identical to the ideal case; i.e., the non-lossy (capacitive) component ($I_c$). The second component is the lossy component ($I_l$) and is in-phase with the voltage ($U$). In this case, the time averaged power loss can be given as follows

$$\begin{aligned} \bar{P} &= \frac{1}{T}\int_0^T (U_c \cdot I)dt = \frac{1}{T}\int_0^T \Big\{\Big(U_0 \cdot sin(\omega t)\Big) \cdot \Big(I_0 \cdot cos(\omega t - \delta)\Big)\Big\}dt \\ \bar{P} &= \frac{1}{2}\Big(U_0 \cdot I_0 \cdot sin\delta\Big) \end{aligned} \tag{3.10}$$

By replacing $I_0 = {}^{I_C}/_{cos\delta}$ and Equation (3.8) in Equation (3.10), the power loss equals

$$\bar{P} = \frac{1}{2}\Big(U_0^2 \cdot \omega \cdot C \cdot tan\delta\Big) \tag{3.11}$$

Equation (3.11) shows that the dissipated power is linearly dependent on the aforementioned $\tan\delta$. Hence it is desired to have a dissipation factor as low as possible. A Sourcetronics ST2819A Precision LCR meter [197] was utilized for the determination of the dissipation factor. The device applies a voltage across the thickness of the sample at a given frequency and measures the parallel capacitance ($C_p$) and resistance ($R_p$) of the circuit. It then calculates the dissipation factor from

$$tan\delta = (\omega \cdot C_p \cdot R_p)^{-1} \tag{3.12}$$

For the sake of uniformity, the applied voltage was kept as $1\,\mathrm{V_{rms}}$ and the frequency was varied between $1\,\mathrm{kHz} - 10\,\mathrm{kHz}$ for all measurements. Custom made electrode pins were attached to the device in order to access top and bottom electrodes of the samples to be characterized. The capacitance of the cables were compensated prior to measurements and each measurement was recorded using a customized MATLAB program. Furthermore, a model to predict power losses with respect to $\tan\delta$ and capacitance was also prepared (see Section A.2 in the Appendix).

### 3.3.3 Residual Film Stress

Since thin films deposited on rigid substrates can not freely expand, they can not release stress. Therefore almost all thin films contain stress; either generated internally during film nucleation or induced due to external stimuli such as temperature [127, p.264]. The former is commonly observed in case of multilayered thin film composites where non-epitaxial crystal nucleation/growth occurs. Since internal stresses originally arise from the non-equilibrium nature of the deposition processes, the latter can be manipulated as an optimization tool as well. Especially when dealing with film deposition techniques, growth stresses can be greatly optimized by adjusting process parameters; e.g., pressure, temperature, substrate bias etc..

The total stress in a thin film $\sigma_{tot}$ can be given as

$$\sigma_{tot} = \sigma_{int} + \sigma_{th} + \sigma_{ext} \tag{3.13}$$

where, $\sigma_{int}$ is intrinsic stress induced during growth, $\sigma_{th}$ is the thermally induced stress and $\sigma_{ext}$ is the externally induced stress; i.e., plastic deformation, thermal annealing, etc. [127, p.263].

Residual stress is not desired in a sensor structure since stress anisotropy might influence the performance. It is often the case, however, that such stresses endure processing and freeze

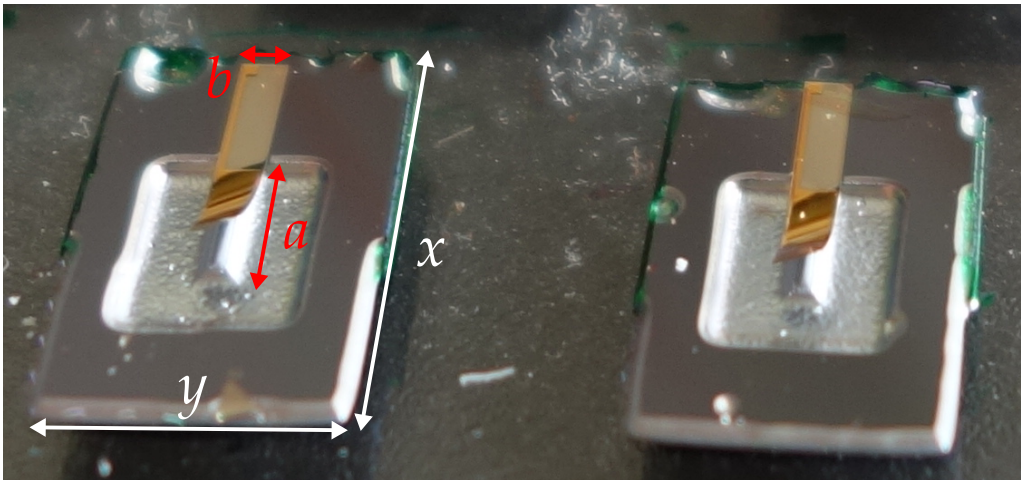


***Figure 3.15:*** *Wrapage of stressed cantilevers upon release from the underlying substrate. In this case, thin films are bent vertically and/or torsionally. Sample dimensions are; x = 11 mm, y = 7 mm, a = 3 mm and b = 1 mm.*

in the films as residual stress. This is especially problematic as it leads to film wraparound when released from the substrate. An exemplary case is seen in Figure 3.15. Shown sensors are completely released from the underlying substrate material via surface micromachining. Upon release, however, they are bent vertically and torsionally with the influence of the residual tensile stress ($\sigma > 0$). Such sensors, which are under the influence of large residual stresses, can not be used for the intended sensing purposes. Hence stress optimization is considered as one of the important tasks of this work.

Stress optimization can either address $\sigma_{tot}$ or focus on the individual components. In this work, main interest is given to $\sigma_{int}$, since it is the dominant stress contributor. One approach can be the introduction of additional thin film layers with opposite stress sign to decrease $\sigma_{int}$ [35]. Aforementioned thermally induced external stresses generally originate from inhomogeneous thermal expansion coefficients of different films. They are often observed during growth processes at high temperatures or during post-deposition annealing processes. Note that, thermal annealing is often utilized as a tool to release stress via atomic rearrangement however that is not the condition here.

***Biaxial Stress in Thin Films:*** An exemplary thin film is depicted in Figure 3.16a. Considering the film is not clamped onto a substrate and can freely move in all directions, the stress-strain relation along different axes can be given by the generalized Hooke's Law

$$\begin{aligned} \varepsilon_x &= \frac{1}{E}\Big(\sigma_x - \nu(\sigma_y + \sigma_z)\Big) \\ \varepsilon_y &= \frac{1}{E}\Big(\sigma_y - \nu(\sigma_z + \sigma_x)\Big) \\ \varepsilon_z &= \frac{1}{E}\Big(\sigma_z - \nu(\sigma_x + \sigma_y)\Big) \end{aligned} \tag{3.14}$$

where, $\varepsilon$ is the strain, $E$ is the Young's modulus, $\sigma$ is the stress and $\nu$ is the Poisson's ratio of the film; i.e., ratio of transverse strain to longitudinal strain[1] [198, p.201].

According to Equation (3.14), strain in one direction would result in strain along other directions as well. However this is not valid for a thin film that is rigidly clamped on a thick substrate as seen in Figure 3.16b. In this case the thin film can only expand/contract on $x$– and $y$–directions by bending the substrate vertically (along $z$–axis). Since the film can

[1] Volume of a sample is conserved when $\nu = 0.5$.

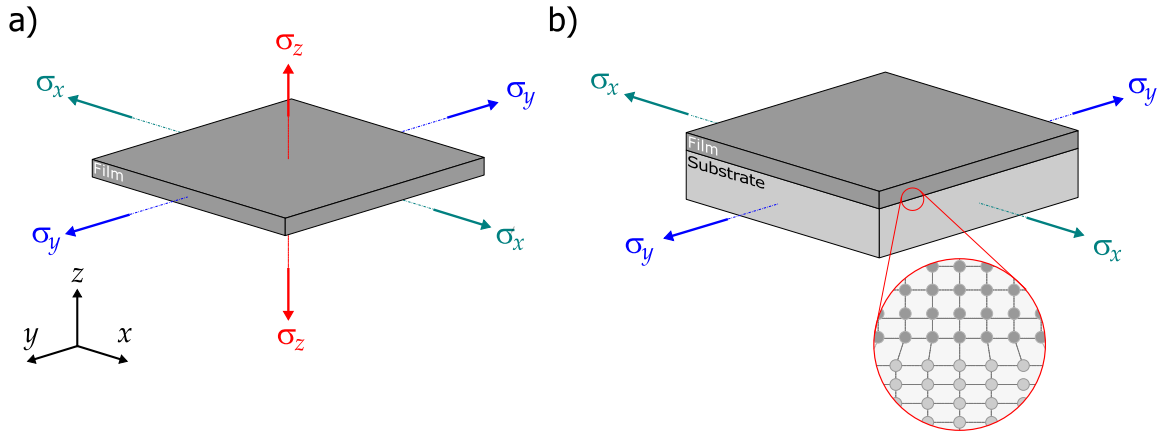


***Figure 3.16:*** *Strain as a result of stress. a) Uniaxial stresses acting on a freely expanding film. Stress/strain relationship can be given by the generalized Hooke's Law. b) Biaxial stresses acting on a thin film deposited on a thick substrate. Thin film's movement is hindered by the substrate. Note that no stress occurs along the z-direction. The zoom-in depicts the lattice mismatch between the film and the substrate as the source of stress for this specific case.*

freely move along the vertical direction, bending of the substrate would not induce stress; i.e., $\sigma_z = 0$. Considering Equation (3.14) and assuming an isotropic case, where strain/stress along $x$– and $y$–directions are identical, stress can be written as

$$\sigma = \frac{E}{1-\nu} \cdot \varepsilon \tag{3.15}$$

where, $E/1-\nu$ is the biaxial modulus of the film.

***Calculation of Residual Stress:*** There are numerous ways to characterize film stress [199]. In this work, both residual stress of individual thin films and that of composite stacks were determined via curvature measurement method and consecutive use of the Stoney equation. In this method, the curvature of a cantilever is measured before and after film deposition by a profilometer[1]. Deposited film induces a deformation; i.e., bending, and the curvature of the cantilever changes. Characterized deformation is then related to the film stress ($\sigma_f$) through the Stoney equation, which contains material properties of the film and the substrate

$$\sigma_f = \left(\frac{E_s}{1-\nu_s}\right)\left(\frac{1}{6R} \cdot \frac{{t_s}^2}{t_f}\right) \tag{3.16}$$

where, the first term is the biaxial modulus of the substrate, $R$ is the radius of curvature, $t_s$ is

[1] Ambios Technology XP-2 profilometer device [200].

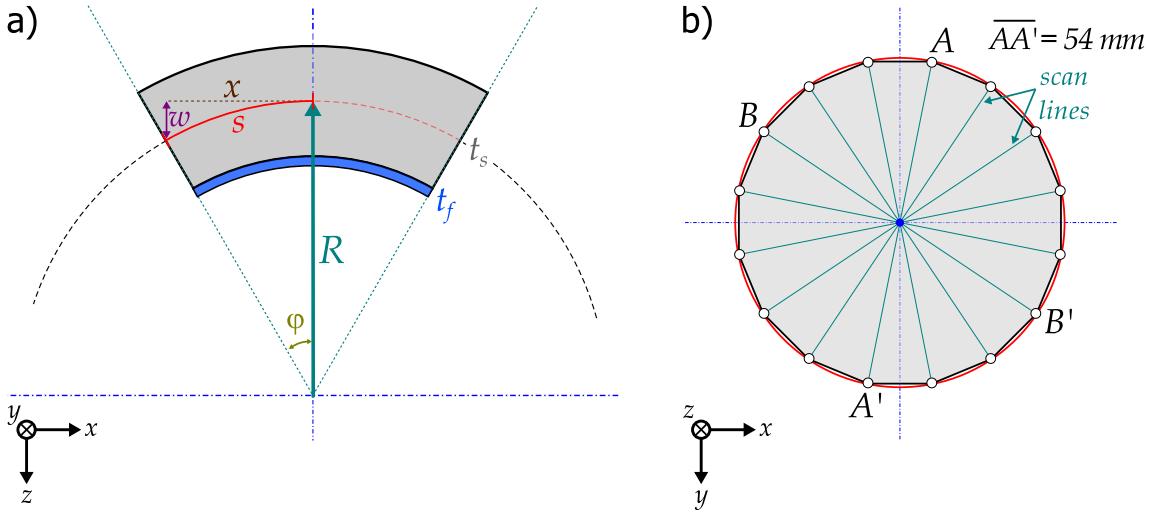


***Figure 3.17:*** *Curvature measurement for residual film stress analysis. a) Curvature of a sample under tensile stress. Radius of the stress induced curvature (R) can be derived from the displacement in the z-direction (w) and the angle of the curvature (φ). b) Hexadecagon-shaped stress samples (grey). Keeping the center point constant (blue dot) 8 measurement lines are defined. Length of individual measurement lines (green lines) equals 54 mm. Respective circumscribed circle is given in red.*

the substrate thickness and $t_f$ is the film thickness [201].

Simple schematic of a bent cantilever is depicted in Figure 3.17a. Assuming an isotropic deformation, the shape of the surface curvature can be treated as an arc. Considering the displacement in $z$-direction as a continuous function along the length of the substrate, $w = f(x)$, then radius of curvature ($R$) at any point can be given as

$$R(x) = \frac{ds}{d\varphi} = \frac{\sqrt{dx^2 + dw^2}}{\left(\left(\arctan(w')\right)'\right)dx} = \frac{\left(1 + (w')^2\right)^{3/2} dx}{w'' dx} \tag{3.17}$$

where, $w$ is the displacement in the $z$-direction and $s$ is the length of the arc corresponding to the angle $\varphi$. First and second derivative of $w$ equal $w' = {}^{dw}/_{dx}$ and $w'' = {}^{d^2w}/_{dx^2}$, respectively.

The common practice in this method is to use disc-shaped substrates [127, p.265]. However, use of a polygon provides more accurate measurements when conducting multiple measurements per sample. Therefore, hexadecagon-shaped substrates were prepared (see Figure 3.17b). In this way, it was possible to establish multiple scan lines; e.g., AA', BB', etc., that pass through the center point of the substrate.

### 3.3.4 Magnetic Properties

***DC Magnetic Properties***: DC magnetic properties of FeCoSiB thin films were investigated via a LakeShore VSM 7400 vibrating sample magnetometer (VSM) [202]. In this method, the sample to be characterized is magnetized with a uniform DC magnetic field (Figure 3.18a), which induces a magnetic dipole moment in the sample [203]. Upon magnetization, the sample is vibrated perpendicularly with the help of a transducer assembly, which converts an AC signal into a sinusoidal motion with a frequency $f$. This influences the amount of magnetic flux lines interacting with the pickup coils mounted on the pole pieces (Figure 3.18b), hence the resulting signal [44, p.68]. The former can be calculated from the Faraday's law of induction

$$\varepsilon(t) = -N\frac{d\Phi_B}{dt} \tag{3.18}$$

where, $\varepsilon$ is the electromotive force (voltage), $N$ is the number of wire turns in the coil, $\Phi_B$ is the magnetic flux [44, p.39]. The former; i.e., the voltage induced in the pick up coils, is proportional to the magnetic moment of the sample.

Prior to the measurement, VSM is calibrated with a magnetic standard of known magnetic properties [204]. It is important that the sample to be characterized has the same dimensions as the standard material. Furthermore, the initial position of the sample has to be at the center of the 4 coil arrangement in order to maximize the induced voltage.

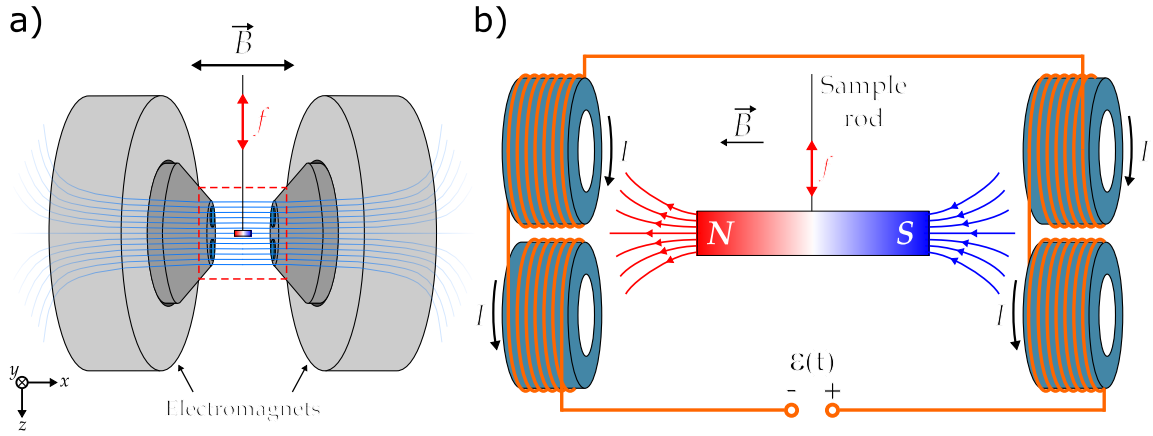


***Figure 3.18:*** *Simplified depiction of a LakeShore VSM 7400 device. a) Most important constituents of the setup include a pair of electromagnets, a vibrating sample holder rod and pick-up coils. b) A close-up to the dashed area. Sample's position with respect to the 4 pick-up air coils and the series connection scheme of the coils are seen. Image adapted from [202].*

***Magnetostrictive Properties***: Magnetostrictive properties of the FeCoSiB thin films are characterized using a custom measurement setup based on the principle of cantilever deflection method [205]. The setup consists of a HeNe laser [206], a duolateral position sensitive device (PSD) containing a light sensitive chip[1], a pair of electromagnets and a vibration damping table placed in a light/acoustic shielding casing (Figure 3.19a).

The measurement principle is as the follows; samples to be characterized; i.e., magnetostrictive films deposited on cantilever shaped Si substrates, are individually mounted on a non-magnetic sample holder, where one end of the cantilever is rigidly clamped (Figure 3.19b). A laser beam is then directed towards the tip of the sample where it produces an angle ($\alpha$) with the substrate's normal ($\perp_1$) and gets reflected towards the PSD. PSD includes a p-i-n diode, which exhibits a change in its local resistance when interacted with the laser beam. If an external DC magnetic field is applied, the magnetostrictive film elongates and/or contracts following Equation (2.16). Due to the underlying substrate, both the film and the substrate bend. The bending produce a certain angle ($\theta$) at the substrate's clamping point and a displacement ($D$) at its tip (Figure 3.19c). Accordingly, the angle between the incoming beam and the substrate's normal ($\perp_2$) amounts to $\beta = \alpha + \theta$ and the light spot on the PSD displaces to a different point (from I to II), changing the current detected by its electrodes. The output voltage of the PSD can finally be related to the displacement on the PSD by using a calibration factor

$$h = U \cdot k \tag{3.19}$$

where, $h$ is the displacement on the PSD, $U$ is the output voltage of the PSD and $k$ is the calibration factor.

Considering the geometry of the measurement setup (Figure 3.19c), the following relation can be written

$$\begin{aligned} 2\alpha + \phi &= 2\beta \\ 2\alpha + \phi &= 2\alpha + 2\theta \\ \phi &= 2\theta \end{aligned} \tag{3.20}$$

[1] Sensitive area dimensions: 10 mm · 10 mm.

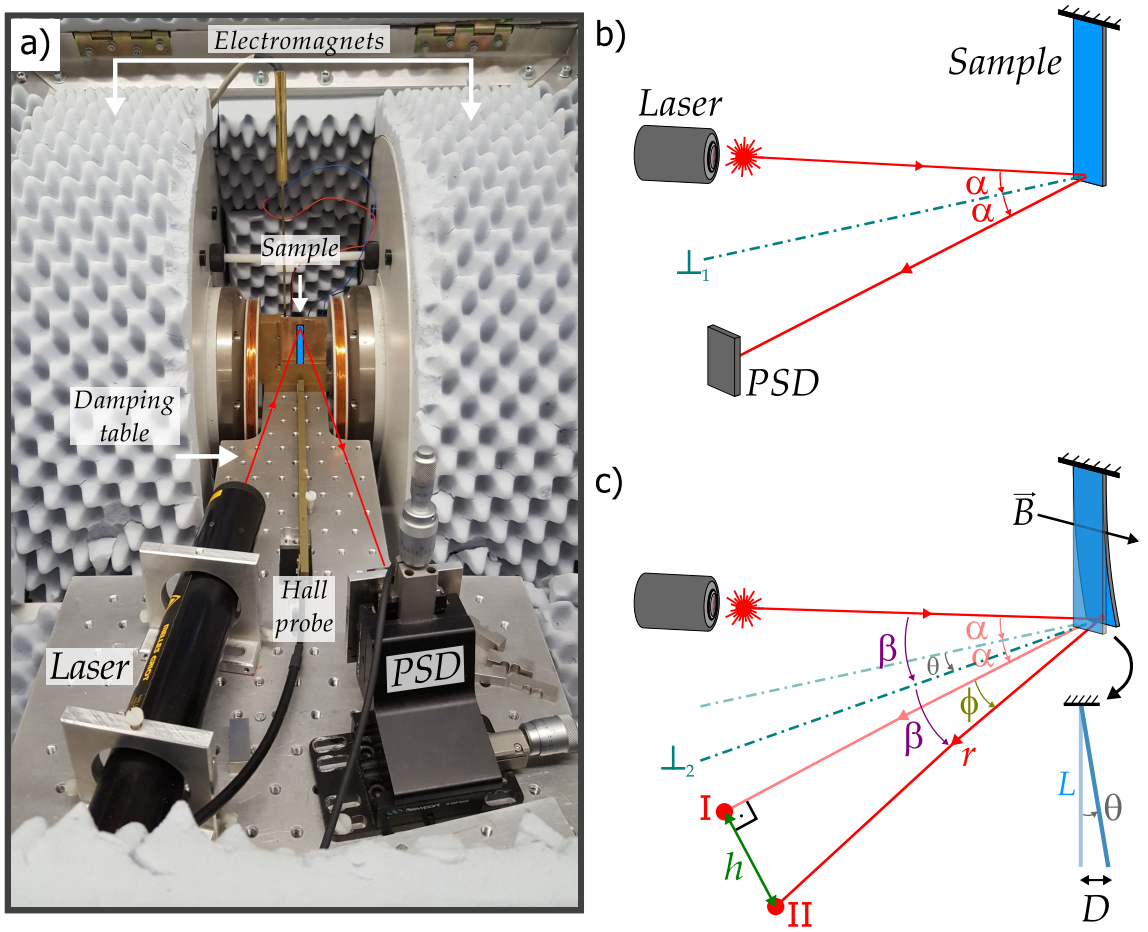


***Figure 3.19:*** *Custom-build magnetostriction measurement setup. a) The measurement principle relies on the cantilever deflection method, where the reflection of a laser beam detected by PSD varies with respect to the applied magnetic field and the consequent sample bending. Laser-sample-PSD interaction b) in the absence and c) in the presence of a magnetic field. Displacement of the laser reflection on the PSD (from I to II) is geometrically related to the cantilever's tip displacement.*

Furthermore,

$$tan\theta = \frac{D}{L}$$
$$tan2\theta = \frac{h}{r} \tag{3.21}$$

where, $r$ is the distance between the tip of the cantilever and the PSD.

Combining Equation (3.20) and Equation (3.21), the displacement of the cantilever tip can be related to beam displacement on the PSD with

$$D = \frac{h \cdot L}{2r} \tag{3.22}$$

Equation (3.22) summarizes the geometrical aspect of the magnetostrictive characterization setup. Since the displacement of the tip is dependent on the mechanical properties of both the film and the substrate, it is possible to relate Equation (3.22) to the magnetoelastic coefficient ($b$) via [74].

$$b^{\gamma,2} = \frac{1}{3}\Big(\frac{D_{\parallel} - D_{\perp}}{L^2}\Big)\Big(\frac{E_s}{1+\nu_s}\Big)\Big(\frac{t_s^2}{t_f}\Big) \tag{3.23}$$

where, $D_{\parallel}$ and $D_{\perp}$ are the displacement when applying a magnetic field along the magnetically easy axis of the film and perpendicular to it, respectively. $E_s$ is the Young's modulus ($E_s = 169\,\text{GPa}$) and $\nu_s$ is the Poisson's ratio ($\nu_s = 0.064$) along the <110> direction of the Si substrate. $t_s$ and $t_f$ are the thickness of the substrate and the film, respectively [207].

Finally, the saturation magnetostriction coefficient is calculated by

$$\begin{aligned}
\lambda_s &= \frac{2}{3}\lambda^{\gamma,2} \\
\lambda_s &= \frac{2}{3}b^{\gamma,2}\Big(\frac{-(1+\nu_f)}{E_f}\Big) \\
\lambda_s &= -\frac{2}{9}\Big(\frac{D_{\parallel} - D_{\perp}}{L^2}\Big)\Big(\frac{E_s}{E_f}\Big)\Big(\frac{t_s^2}{t_f}\Big)\Big(\frac{1+\nu_f}{1+\nu_s}\Big)
\end{aligned} \tag{3.24}$$

where, $\lambda_s$ is the saturation magnetostriction. Full derivation of the aforementioned coefficients can be found in [74].

### 3.3.5 Magnetoelectric Properties

Magnetoelectric properties of the fabricated sensors were characterized using a custom measurement setup as seen in Figure 3.20a [185]. The setup consists of a pair of 20 cm long cylindrical coils inserted into each other. They are used to apply the DC bias field and the

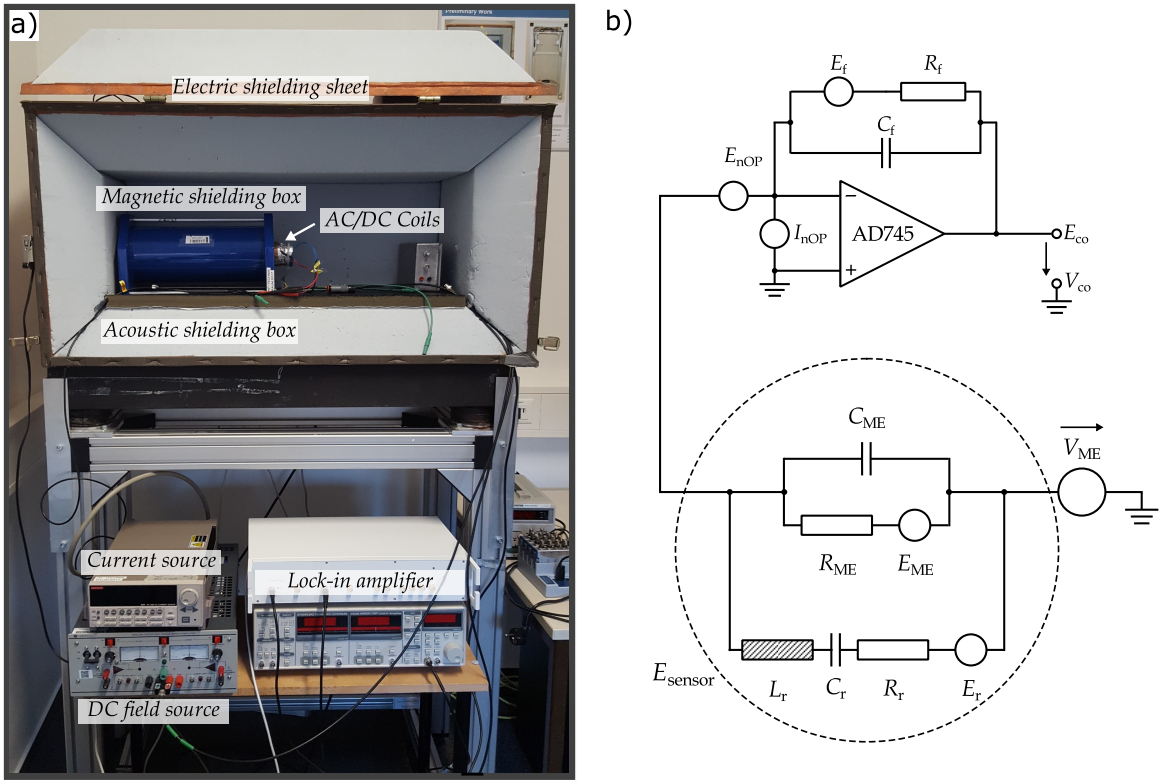


***Figure 3.20:*** *Custom-build magnetoelectric characterization setup and electrical noise equivalent circuit of the magnetoelectric sensor and the detection circuit. Here, $L_r$, $C_r$, $R_r$ and $E_r$ are inductance, capacitance, resistance and thermal-mechanical noise at the resonance, respectively. $R_{ME}$, $E_{ME}$ and $C_{ME}$ are the frequency dependent parallel magnetoelectric resistance, thermal-electrical noise of the piezoelectric phase and the capacitance of the plate capacitor, respectively. $R_f$, $E_f$ and $C_f$ are feedback resistor, the thermal-electrical noise of the feedback resistor and the capacitance of the feedback capacitor, respectively. $E_{nOP}$ and $I_{nOP}$ are the operational amplifiers voltage and current noise, respectively. $E_{sensor}$ and $E_{co}$ are the intrinsic sensor noise and the overall noise at the charge amplifiers output, respectively. Image adapted from [211].*

AC signal field, respectively. Magnetic bias field is controlled with a DC power supply[1] and the AC coil is driven with a current source[2]. Sensors to be characterized are centered in the coils with a custom made sample holder and are placed in a magnetically shielding mu-metal cylinder[3], which is located in an acoustic- and vibration-shielded box.

### Noise Models

Initially, a noise model defined by *Jahns et al.* was used for the characterization of the magnetoelectric sensors [117]. This model takes into consideration the combined intrinsic

[1] KEPCO BOP20-10ML [208].
[2] Keithley 6221 [209].
[3] Aaronia ZG1 [210].

noise of the sensor and the noise from the detection unit; i.e., the charge amplifier.

Intrinsic noise of the sensor originates from the pyroelectric properties of AlN and is known as the Johnson-Nyquist noise [212][213]. Noise from the detection unit, on the other hand, includes contributions from the feedback resistor ($R_f$) as well as the operational amplifier. Even though the chosen model performs accurate estimation over a wide frequency range, it omits the increased noise at the actual mechanical resonance frequency. Therefore a complementary model was used in order to confirm the validity of the measurements (see Figure 3.20b). The second model focuses on the thermal-mechanical noise at the first bending mode of a resonant sensor, hence exhibits a very accurate estimation of the actual measurement noise at the working conditions of the sensor [211].

*Signal Enhancement*: When working with sensors of small capacitance, the output signal is often enhanced by using a charge-preamplifier [117]. Accordingly, sensors to be characterized were connected to a custom-built charge-preamplifier[1] during all measurements. Since the voltage gain of the charge amplifier is dependent on the capacitance ratio between the sensor and the feedback capacitor ($G_c = {}^{C_{ME}}/_{C_f}$), the actual voltage output of the sensor is determined by extracting the gain factor from the measured voltage output

$$V_{co} = \frac{V_{ME}}{G_c} \tag{3.25}$$

where, $V_{co}$ and $V_{ME}$ are the actual and measured voltage outputs, respectively.

Using the aforementioned setup, numerous investigations[2] were conducted in order to characterize the magnetoelectric sensors and to determine the following fundamental properties.

***Resonance frequency***: Resonance frequency of a cantilever ($f_{res}$) can be estimated from Equation (2.38). It is often the case, however, that the calculated and measured frequency values differ due to inaccurate manual clamping of the cantilevers onto the PCBs[3]. Therefore, the resonance frequency of individual sensors are determined while the sample mounted on a PCB is subjected to DC and AC magnetic fields. An exemplary frequency sweep is shown in Figure 2.15b. The frequency, where the magnetoelectric response; i.e., voltage output of the sensor, reaches its maximum marks the mechanical resonance frequency of the

[1] Analog Devices AD 745 [214] with $C_f = 10\,\text{pF}$ and $R_f = 5\,\text{G}\Omega$.

[2] Magneoelectric investigations are completed by M.Sc. Sebastian Salzer and Dr.-Ing. Alexander Teplyuk from the chair of Microwave Engineering (Prof. Dr.-Ing. Michael Höft) of the Kiel University.

[3] PCB stands for printed circuit board.

sensor. Note that the thick underlying substrate dominates the movement of the whole cantilever, hence the resonance enhancement of the output voltage can be related to the quality factor of the Si cantilever, as was previously mentioned in Section 2.3.4.

***Working point and sensor sensitivity*:** Working point of a magnetoelectric sensor refers to the external magnetic field magnitude ($H_{Bias}$ in Oe), where the piezomagnetic coefficient of the sensor reaches its maximum (see Figure 2.14b). It is proportional to the first derivative of the magnetostrictive strain with respect to the external magnetic field, hence depends on the material properties of the magnetostrictive layer. The working point of the magnetostrictive layer is generally determined by VSM and magnetostriction measurements. However it might show variations as a result of stress related effects in a composite sensor stack. Therefore, the working points of the fabricated sensors were determined at the actual resonance frequency and while the sensors were subject to an AC driving field. An exemplary bias sweep is shown in Figure 2.14c. Accordingly, the magnetic field magnitude, where the magnetoelectric response of the sensor (in resonance) is at its maximum marks the working point of the sensor. Aforementioned magnetoelectric response is known as the sensitivity of the sensor ($\alpha_{ME}$ in $\mathrm{V}/(\mathrm{cm}\cdot\mathrm{Oe})$). It is often normalized with respect to the piezoelectric constituent thickness in order to obtain a comparable value with respect to the literature data.

***Voltage noise density*:** Voltage noise density (in $\mathrm{V}/\mathrm{Hz}^{1/2}$) refers to the noise behavior of the whole detection unit with respect to frequency. In this characterization, voltage noise density of the whole detection unit was measured using a SR785 low-frequency signal analyzer with an equivalent noise bandwidth (ENBW) of 1 Hz [215]. Furthermore, the bias field was supplied by a pair of batteries instead of a DC power supply, in order to prevent noise from switching the power supply. A typical frequency range of $10^{-1}\,\mathrm{Hz} - 10^{5}\,\mathrm{Hz}$ was investigated for all sensors. The electrical noise equivalent circuit of the magnetoelectric sensor and the detection circuit are schematized in Figure 3.20b.

***Sensor Resolution and LOD*:** Resolution of a magnetoelectric sensor (in T) refers to the minimum magnetic field it can detect. In this work, it was determined by measuring the magnetoelectric output voltage with respect to the decreasing magnetic AC field with a SR830 lock-in amplifier. Magnetoelectric sensors produce a linear relationship between the magnetic field and the output voltage up to a point where the background noise overcomes the signal; i.e., SNR = 1. The magnetic field magnitude at this point is known as the minimum detectable field or the LOD of the sensor (in $\mathrm{T}/\mathrm{Hz}^{1/2}$). LOD of a magnetoelectric sensor at its resonance frequency can be estimated using

$$LOD = \frac{E_{co}}{\alpha_{ME} \cdot t_{piezo}} \tag{3.26}$$

where, the $E_{co}$ and $\alpha_{ME}$ magnitudes are taken from the voltage noise density and sensitivity measurements, respectively.

$E_{co}$ is the total noise voltage density at the output of the charge amplifier and yields

$$E_{co}^2 = E_{co,EnOP}^2 + E_{co,InOP}^2 + E_{co,ERF}^2 + E_{co,Esensor}^2 \tag{3.27}$$

where, $E_{co,EnOP}$ and $E_{co,InOP}$ are the voltage and current noise contributions of the amplifiers, $E_{co,ERF}$ is the contribution of the feedback resistor and finally $E_{co,Esensor}$ is the contribution of the sensor. $E_{co,Esensor}$ is the intrinsic noise of the sensor and includes both the pyroelectrical noise ($E_{ME}$) and the thermal-mechanical noise ($E_r$) of the sensor. The latter is the dominant noise source at the first bending resonance frequency of the sensor.

SNR of a magnetoelectric sensor is given as

$$SNR = \frac{|V_{co}|^2}{|E_{co}|^2} \tag{3.28}$$

where, $V_{co}$ is the magnetoelectric voltage coefficient at the output of the charge amplifier and equals to

$$V_{co} = \alpha_{ME} \cdot t_{piezo} \cdot H_{AC} \tag{3.29}$$

where, $\alpha_{ME}$ is the magnetoelectric coefficient as shown in Equation (2.36), $t_{piezo}$ is the thickness of the piezoelectric layer and $H_{AC}$ is the magnitude of the applied AC field.

Combining Equation (2.36) and Equation (3.29), $V_{co}$ equals to

$$V_{co} = \frac{d_{31}}{\varepsilon_0 \cdot \varepsilon_{r,33}} \cdot k_c \cdot d_{33}^m \cdot t_{piezo} \cdot H_{AC} \tag{3.30}$$

for L-T laminate composites used in this work.

It is important to emphasize that, the term LOD refers to the value that is the resolution of the sensor with respect to the ENBW of the measurement device. While the latter equals 1 Hz for SR785 signal analyzer, it is only 78 mHz for the SR830 lock-in amplifier [216]. State-of-the-art magnetoelectric sensors are almost always characterized with lock-in amplifiers due to their noise rejection capabilities [217]. The difference of the ENBW, however, is often not mentioned in the literature (see Table 2.5). Nevertheless, it is considered necessary to point out here for the integrity of the current work.

### 3.3.6 Finite-Element Method Modeling

According to *Bala et al.*[118], voltage generation on the surface of a one-end-fixed cantilever sensor is not homogeneous along its length. Instead, it is much higher in close proximity to the clamping point. In order to estimate the suggested improvement of a confined electrode (see Section 2.3.4), a finite-element method (FEM) model was prepared via Comsol Multi-physics software[1]. Optimal electrode size delivering the maximum voltage output and the highest SNR was determined via theoretical and experimental results. Detailed information on the utilized FEM can be found in the previously published data [218].

The small signal behavior of the magnetoelectric sensors with varied electrode lengths were calculated using a two dimensional (2D) FEM model where linear material equations and an in plane-stress boundary condition (along the width direction). Bottom and top electrodes

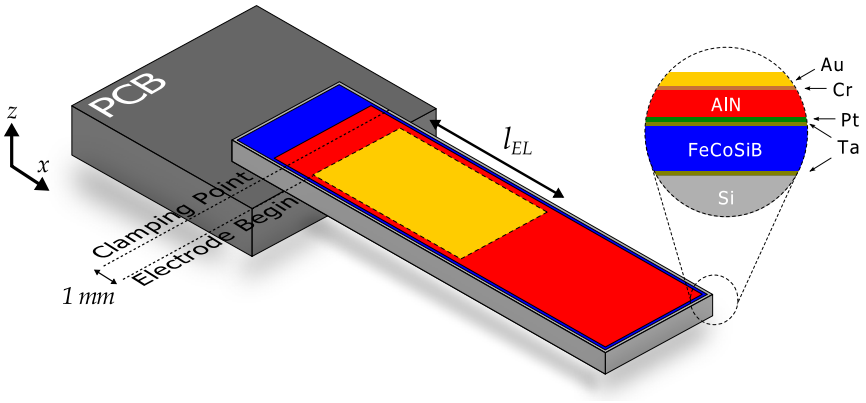


***Figure 3.21:*** *Schematic of the modeled/fabricated inverse-bilayer magnetoelectric sensors. The model comprise of a 1.6 µm thick AlN, 3 µm thick FeCoSiB and 300 µm thick Si. The cantilever is 2 mm wide with a free-standing length of 22 mm. Top electrode size ($l_{EL}$) is varied.*

[1]Modeling of the inverse-bilayer magnetoelectric sensors are realized by Dr.-Ing. Jascha Lukas Gugat from the chair for Integrated Systems and Photonics (Prof. Dr. Martina Gerken) of the Kiel University.

were set to an electric potential of 0 V as the electrical boundary condition while considering the short-circuit (SC) operation. With this configuration, total induced electric charge density on the top electrode was calculated. The resonant SC magnetoelectric coefficient can be given as

$$\alpha_{ME_{SC}} = \frac{Q}{t_{PE}} \cdot \frac{\int_0^a \int_0^b D_z \cdot dA_{EL}}{H_{AC} \cdot C_f} \tag{3.31}$$

where, $Q$ is the quality factor, $t_{PE}$ is the thickness of the piezoelectric layer, $a$ and $b$ are the maximum length and width of the electrode area, $D_z$ is the $z$-component of the electric flux density, $A_{EL}$ is the top electrode area, $H_{AC}$ is the applied external magnetic field magnitude and $C_f$ is the amplifier's feedback capacitance.

Constant values of the resonance frequency as $f_{res} = 854\,\text{Hz}$, quality factor of $Q = 300$, feedback capacitance of $C_f = 10\,\text{pF}$, free-standing length of 22 mm and an electrode width of 1.4 mm were used for all calculations. Electrode length was varied from 0.25 mm up to 15 mm. Thickness of AlN, FeCoSiB and the Si substrate were considered as 1.6 µm, 3 µm and 300 µm, respectively (see Figure 3.21). In addition to the prepared model, actual inverse-bilayer sensors with varied top electrode sizes were fabricated and characterized. The results of both modeled and fabricated sensors are summarized and discussed in Section 4.2.2.

# 4 Results and Discussion

Characteristic properties of AlN thin films and prerequisites for highly piezoelectric films are discussed in the previous chapters. In summary; sputter deposited thin film AlN is a polycrystalline material, containing various crystallographic growth orientations especially when fabricated out of the thermodynamic equilibrium. It is often the case, that one of these growth directions dominates as the preferential growth direction, depending on the energy brought to the growth surface. However, the piezoelectric coefficient of AlN is greatly reduced in the presence of multiple growth directions. Since AlN acts in a plate-capacitor arrangement within the ME sensor geometry utilized in this work, it is an important task to fabricate films which possess a single growth direction along the <001> direction. In addition to the preferential growth, it is also essential that fabricated films contain a high texture quality and good piezoelectric/dielectric properties. However, the lack of substrate heating of the utilized process leads to an energy deficiency on the growth surface, in comparison to conventional processes completed at higher temperatures. Many sources point out that this deficiency can be compensated via ion bombardment of the growing film. Hence, it is necessary to optimize various process variables in such a way that the necessary ion bombardment is achieved.

To that end, the influence of several factors including sputtering parameters, substrate treatment, seed layer, etc., were systematically investigated. As a rule of thumb, all parameters other than the investigated parameter were kept constant during these experiments. The results of the mentioned investigations are presented in the first part of the following chapter. Obtained results were then utilized in order to establish a standard process flow for the fabrication of *c*-axis textured and highly piezoelectric AlN thin films. Note that, extreme variations of the sputtering parameters; e.g., very high or very low process pressure, often

result in plasma failure and are therefore avoided.

In the second part, investigations completed on magnetoelectric sensors are summarized. These include the microstructural properties of the constituent layers, DC magnetic and magnetostrictive properties of the magnetostrictive layer as well as the magnetoelectric properties of the fabricated sensors. From the latter, the overall performance and the application range of these sensors were evaluated. Furthermore, influence of various factors such as the top electrode dimensions, surface roughness and residual film stress was investigated.

## 4.1 Properties of Aluminum Nitride Thin Films

### 4.1.1 Influence of the Gas Composition

Basic principles of sputtering were previously explained in Section 2.4.1. Considering the influence of the sputtering gas composition on the film stoichiometry, the first investigations aim to determine optimal sputtering atmosphere. To that end, numerous AlN samples were deposited on identical substrates[1] in varied gas composition (see Table 4.1). The gas composition was adjusted by keeping the reactive gas flow ($\Phi_{N_2}$) constant and decreasing the inert gas flow ($\Phi_{Ar}$), thus changing the ratio of the reactive gas over the total gas.

***Table 4.1:*** *Gas flow ratios utilized for the determination of gas composition influence on AlN thin film properties.*

| Sample | $\Phi_{N_2}$ (sccm) | $\Phi_{Ar}$ (sccm) | $\Phi_{N_2}/\Phi_{Total}$ (%) |
|---|---|---|---|
| I | 10 | 10 | 50 |
| II | 10 | 5 | 66 |
| III | 10 | 0 | 100 |

***Microstructural Properties***: XRD diffractograms of the fabricated samples are presented in Figure 4.1a. Two AlN reflections; i.e., main reflection at $2\Theta = 36.1^\circ$ and a secondary reflection at $2\Theta = 37.9^\circ$, belonging to (002)-AlN and (101)-AlN respectively, are present for all samples. *Ruh and Zangvil* argues that <101> orientation is a more probable growth direction compared to <001> orientation [219]. However, relatively stronger signal intensity of the (002) reflection suggests a textured growth along the preferential direction. Considering the presence of a secondary reflection, on the other hand, it is clear that the sample is polycrystalline and contains multiple nucleation sites of different orientations on the AlN-Pt

[1] Si (300 µm) / $SiO_2$ (1.5 µm) / Ta (15 nm) / Pt (140 nm).

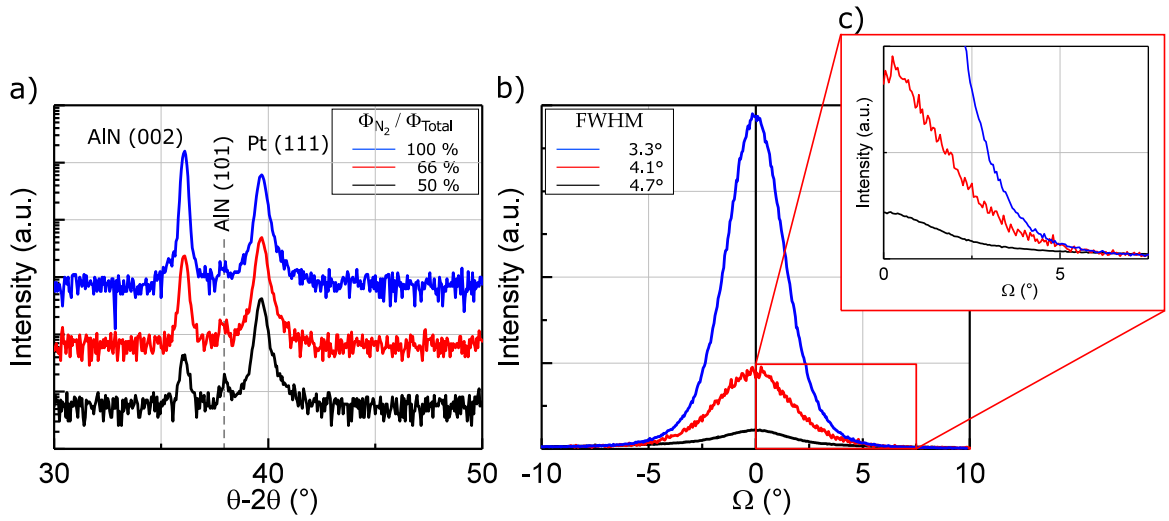


***Figure 4.1:*** *Influence of the sputtering gas composition on AlN thin film microstructure. a) XRD diffractograms depict two growth directions. Despite polycrystallinity, <001> is the preferential growth direction. b) Rocking curve measurements. A decrease of the FWHM with respect to decreasing Ar flow is observed. c) Close-up to the base region of the rocking curves. A higher degree of nitridification occurs in $\Phi_{N_2}$ rich atmospheres, the base shape of the curve shrinks and the curve gets sharper. Note that the intensity values of each plot is normalized with respect to individual film thickness.*

interface. Furthermore, a strong increase of the (002) peak intensity is observed in response to decreasing $\Phi_{Ar}$. This is an indication for higher texture quality of the films deposited in a relatively more reactive atmosphere. Nevertheless, the secondary reflection is preserved independent of the sputtering atmosphere and film thickness.

The (002) texture quality is evaluated from the rocking curve measurements completed at $2\Theta = 36.1^\circ$, as shown in Figure 4.1b. A decrease in the rocking curve width with respect to decreasing $\Phi_{Ar}$ is observed. Accordingly, sample produced with (1:1) gas ratio results in a FWHM of $4.7^\circ$. FWHM shrinks to $4.1^\circ$ and $3.3^\circ$, for samples produced in (2:1) and (1:0) gas ratios, respectively. This corresponds to a 12% improvement as $\Phi_{Ar}$ is halved and then another 20% as it is completely removed from the process chamber.

A close-up to the rocking curves is presented in Figure 4.1c. All three samples have an identical base shape and generate the first signals at approximately $\Omega = 5^\circ$. However the sample deposited absent of Ar (Sample III) displays a much steeper slope compared to the other two samples. Considering the fact that a perfect crystal would produce a very sharp peak in the rocking curve measurements and investigated samples all have comparable film thicknesses, it can be assumed that the much sharper curve observed from Sample III indicates a higher texture quality, with lower dislocation density and misorientations. Clearly, all

samples are fabricated well above stoichiometric prerequisites hence the increase of reactive gas concentration only influences the texture quality. Even processing in a 100% reactive gas atmosphere does not prevent the nucleation of multiple growth directions, but on the other hand, removal of the Ar improves the main (002) peak by a large margin. At this point, the sharper peak and the improved FWHM suggest that a higher nitrification of the non-passivized surfaces occur as the inert gas flow decreases.

***Discussion***

Observed influence of the gas composition is related to the chemical species present in the plasma and their interaction with the target atoms. When the plasma is ignited, positive ions present in the plasma are attracted towards the Al target and undergo elastic collisions with the target's surface atoms. Upon impact, impinging particles transfer their energy to the target atoms and the formed compound molecules following the laws of momentum and energy conservation. The energy transferred from the positive ions is known as the recoil energy and can be given as;

$$T_m = \left( \frac{4 m_i m_t}{(m_i + m_t)^2} \right) \cdot E_i \tag{4.1}$$

where, $T_m$ is the transferred energy, $m_i$ and $m_t$ are the ion and target atom/molecule masses and $E_i$ is the kinetic energy of the impinging ions [133, p.19].

For a (1:1) gas ratio, for instance, aforementioned species include Ar, molecular $N_2$, the positive ions $Ar^+$ and $N_2^+$ and finally sputtered Al atoms/AlN molecules [220]. Considering the mass of Al and the gas ions[1], for instance, the magnitude of the first term in Equation (4.1) is almost equal for both $Ar^+$ and $N_2^+$. Depending on the amount of energy brought by the ions, several surface effects can occur;

- *Reflection* of the ions from the target surface while retaining most of their energy,
- *Penetration* of the ions into the target surface while transferring all their energy,
- *Sputtering* of the target material as a result of the received energy.

According to *Eckstein and Biersack*, if the target material has a higher mass than the impinging particles ($m_t > m_i$), the number of reflected ions as well as their retained energy $E_r$

[1] Al: $A_r = 26.981\ u$, Ar: $A_r = 39.948\ u$ and $N_2$: $A_r = 28.013\ u$[221].

increases [222]. If the opposite is true ($m_t < m_i$), then the amount of the reflected ions decreases since reflected ions lose their energy as they penetrate deeper into the target surface. Therefore, it can be assumed that the sputtering of the target material is mainly achieved by the Ar ions while processing in a Ar + $N_2$ gas mixture. That is simply because Ar ions can penetrate deeper into the Al target and knock surface atoms out with relative ease compared to the $N_2^+$. Nitrogen ions, on the other hand, have a limited contribution to the sputtering process due to their low mass. Instead, the majority of the impinging nitrogen would get reflected back from the target's surface, with most of their energy retained. As they reach to the growing film surface, the retained energy would then contribute to the surface adatom mobility and enhance the (002) texture quality. This assumption agrees both with the measured deposition rates and the texture improvement of the deposited films. The former decreases from 65 nm/ min to 58 nm/ min and finally to 53 nm/ min with respect to decreasing Ar flow. Furthermore, the (002) peak intensity increases accordingly.

One could also argue, that the observed change of the deposition rate is due to the increased MFP when Ar is removed from the chamber. MFP defines the average distance that molecules travel between two consecutive collisions [137, p.23] and is given by

$$\tilde{l} = \frac{k_B \cdot T}{\sqrt{2} \cdot \pi \cdot P \cdot d_m^2} \tag{4.2}$$

with

$$k_B = \frac{R}{N_A} \tag{4.3}$$

where, $\tilde{l}$ is the mean free path, $k_B$ is the Boltzmann constant, $T$ is the temperature, $P$ is the pressure, $d_m$ is the molecular diameter[1], $R$ is the ideal gas constant and $N_A$ is the Avogadro constant [137, p.24].

Hence the MFP relates with the energy delivered onto the growing film surface through the kinetic energy of the plasma particles as well as the amount of the present molecules. Therefore, under constant pressure conditions, as is here, a higher total gas amount will result in a relatively diminished MFP. In case of a lower MFP, sputtered target atoms and compound molecules would experience more collisions during their flight towards the substrate and

[1] Molecular diameter of nitrogen molecule equals 364 pm [223, p.2013].

***Table 4.2:*** *Plasma properties under different gas compositions.*

| Sample | $\lvert\Delta_V\rvert$ $(V)$ | Current $(A)$ | Resistance $(\Omega)$ | $\lvert V_{Bias}\rvert$ $(V)$ |
|---|---|---|---|---|
| I | 230 (*245*) | 6.52 (*6.12*) | 35 (*40*) | 16 (*21*) |
| II | 232 (*246*) | 6.46 (*6.10*) | 36 (*40*) | 17 (*22*) |
| III | 237 (*250*) | 6.34 (*6.00*) | 37 (*42*) | 19 (*24*) |

Values are manually extracted from the generator at the end of 1 min (upright) and 30 min (in parenthesis) processing.

often deposit onto the chamber walls instead. Furthermore, when Ar is removed from the chamber the plasma resistance increases due to the decreased amount of positive ions (see Table 4.2). This necessitates a higher voltage to be applied to the target. In this case, a higher potential difference between the plasma and the substrate holder is established as well. Hence the remaining nitrogen ions would have an enhanced acceleration both towards the target and the substrate holder.

On the other hand, one shall consider the nitrification process, as well. Given diffractograms exhibit an increased (002)-AlN texture quality and signal intensity with decreasing Ar but the (101)-AlN peak stays constant. It can be speculated that when Ar is removed from the chamber, even though there are less sputtered target material, there is a higher nitrification (compound formation) rate since more nitrogen occupies the chamber and interacts with the target. Furthermore it is also possible, that there is not enough nitrogen ions present in the chamber to nitrite all the sputtered/surface Al at (1:1) and (2:1) ratios, however this possibility is not proven here.

Gas composition influence the grain shape and size, as well. AFM investigations depict the evolution of the surface properties with respect to sputtering gas composition as seen in Figure 4.2. In all compositions, the surface is covered with rather large polygonal features. The large grains seen in the presence of Ar overlap the circular grains (see Figure 4.2f). Feature dimensions up to $250\,\text{nm} \times 250\,\text{nm}$ can be observed. The average RMS roughness range between 8 nm and 9 nm. The height difference between the highest peak and the lowest point varies between 85 nm to 115 nm. With the decrease of Ar, on the other hand, uniformly circular grains begin to appear below the polygone-type features.

In summary, the observed influence of the process gas composition shall be considered as a combined effect. Absent of Ar, reflected nitrogen particles retain most of their energy and contribute to the AlN texture quality. Lack of Ar gas in the plasma decreases the overall sputter rate but on the other hand improves the total nitrification of the sputtered as well as

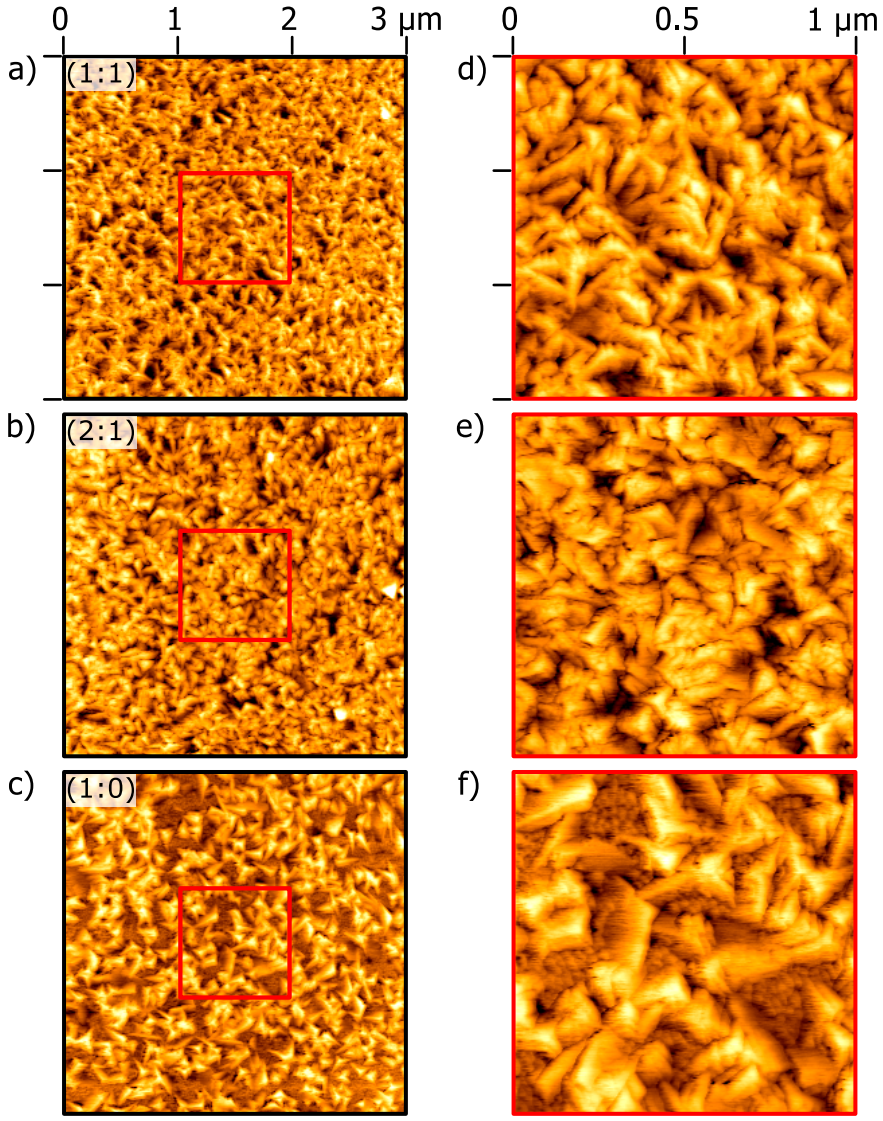


***Figure 4.2:*** *AFM investigations of AlN films deposited in different gas compositions. Tapping mode. Images size 3 µm × 3 µm for a–c and 1 µm × 1 µm for d–f. Average RMS roughness 8 nm and peak-to-valley difference of ∼100 nm.*

the surface Al atoms. AFM images exhibit two distinct features, which can be correlated with the different AlN orientations (see Figure 4.1). Circular grains are observed as the texture quality of (002) AlN increases.

### 4.1.2 Influence of the Seed Layer

The underlying seed layer; i.e., nucleation layer, is considered as one of the most influential elements for the fabrication of high quality AlN thin films [167][224][225]. Various textured

metallic seed layers; e.g., Au, Ag, Al, Ta, Ti, Mo, Pt, etc., can be used to a certain success in order to encourage a <001> oriented growth of AlN. Among these materials, AlN deposited on Pt and Mo exhibit the highest reported effective piezoelectric coefficients [35][172][226]. On the other hand, Pt offers favorable properties in terms of fabrication and processing such as resistance to the utilized wet etch solutions for instance. More importantly, there is an epitaxial orientational relationship between <111> oriented Pt and AlN, which promote the columnar and <001> oriented growth of AlN [157]. Actually, Pt is often deposited on pre-heated substrates (at 300 °C) and/or is subject to post-deposition annealing (at 550 °C) in order to improve the <111> orientation [35]. However, such process temperatures are well above the desired conditions of this work and can introduce thermal residual stress as well. Considering these, the fabrication of Pt was realized absent of substrate heating or post deposition annealing. It is clear from Figure 4.1, that the established deposition conditions already result in a <001> preferred AlN growth. However, the conditions necessary for the realization of a single growth direction are not present. In that regard, the modification of the Pt surface properties, hence modification of the AlN nucleation conditions are interesting topics to the current work.

***Microstructural Properties***: Figure 4.3a compares XRD diffractograms of AlN films deposited on Pt covered substrates. One of the samples was subject to plasma treatment prior to AlN deposition (see parameters in Section 3.2.1). The $\Theta - 2\Theta$ scans show that the non-treated sample retains both (002) and (101) reflections of AlN at $2\Theta = 36.1\,^{\circ}$ and $2\Theta = 37.9\,^{\circ}$, respectively. On the other hand, the plasma treated sample contains only the (002) reflection. The evaluation of the texture quality can be seen from the rocking curve measurements given in Figure 4.3b and c. AlN sample deposited on the plasma treated Pt exhibits an approximately 50% narrower FWHM. Furthermore, the shape of the curves are distinctively different. A sharper peak with a much smaller base width is obtained after the plasma treatment. Since all other parameters are kept constant during processing, the disappearance of the (101)-AlN reflection as well as the improvement of the FWHM are direct consequences of the plasma treatment of the nucleation surface.

***Discussion***

During plasma etching, plasma particles are accelerated towards the substrate by applying a negative bias voltage to the substrate holder and the Pt surface is modified through ion bombardment [137, p.407]. It is possible that such modification of the surface results in a higher amount of nucleation sites, which favor <001> oriented grains, or a lower amount of nucleation sites, which favor <101> oriented grains or enhance the shadowing effect (see

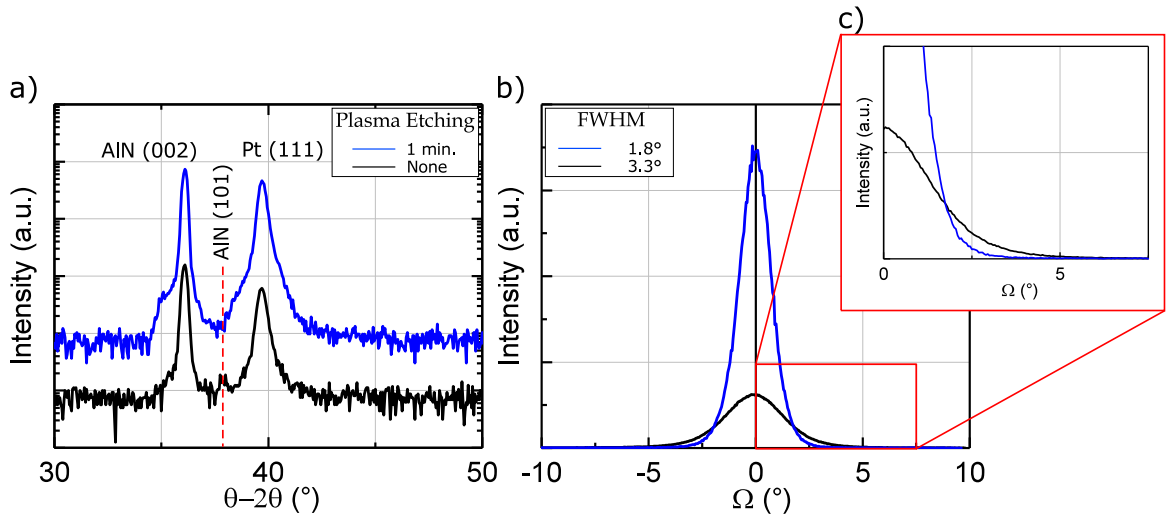


***Figure 4.3:*** *Influence of the seed layer and plasma treatment on AlN thin film microstructure. a) XRD diffractogram of the AlN films (1.75 µm thick) deposited on plasma-treated Pt (blue) depicts a single preferential growth direction while the non-treated case (black) retains an additional (101) peak. b) Rocking curve measurements at $2\Theta = 36.1°$. FWHM improves greatly as a result of plasma treatment of the seed layer. The base width is narrowed and the peak is sharpened. All plots are normalized with respect to individual film thickness.*

Figure 2.24). The latter is often observed in Zone 1 growth processes as discussed in Section 2.4.5. In fact, it was determined by profilometer measurements that a 1 min plasma etching process removed 3 nm – 5 nm; i.e., several atomic layers, from the Pt surface. This suggests that the top most layers of the Pt seed layer were removed due to bombardment by highly energetic Ar ions. It is possible that due to the bombardment, atomic bonds in the Pt structure are severed and high energy nucleation sites are generated. In this case, the plasma treated sample would have an increased local defect density on the surface in comparison to the untreated sample.

The influence of the shadowing effects, however, is rather hard to observe using conventional methods. Therefore, complementary TEM investigations[1] were conducted on a 100 nm thick AlN film deposited in pure nitrogen atmosphere and on a plasma treated Pt seed layer. TEM bright field image of the 100 nm thick cross-section prepared by FIB milling is seen in Figure 4.4. A detailed inspection of the corresponding SAED[2] is presented in the inset. Despite the observation of a textured growth along the *c*-axis, slight elongation of the (002) reflections was emphasized as well. This is due to the different crystal structure and lattice width; i.e., interfacial difference between Pt and AlN[3]. A possible result of this difference would

[1] TEM investigations are completed by Dr.-Ing. Dipl. Phys. Viktor Hrkac from the chair for Synthesis and Real Structure (Prof. Dr. Lorenz Kienle) of the Kiel University.

[2] Diameter of the analyzed circular area: 250 nm.

[3] Lattice constants, $Pt = 3.92$ Å [227] and $a_{AlN} = 3.11$ Å, see Figure 2.5.

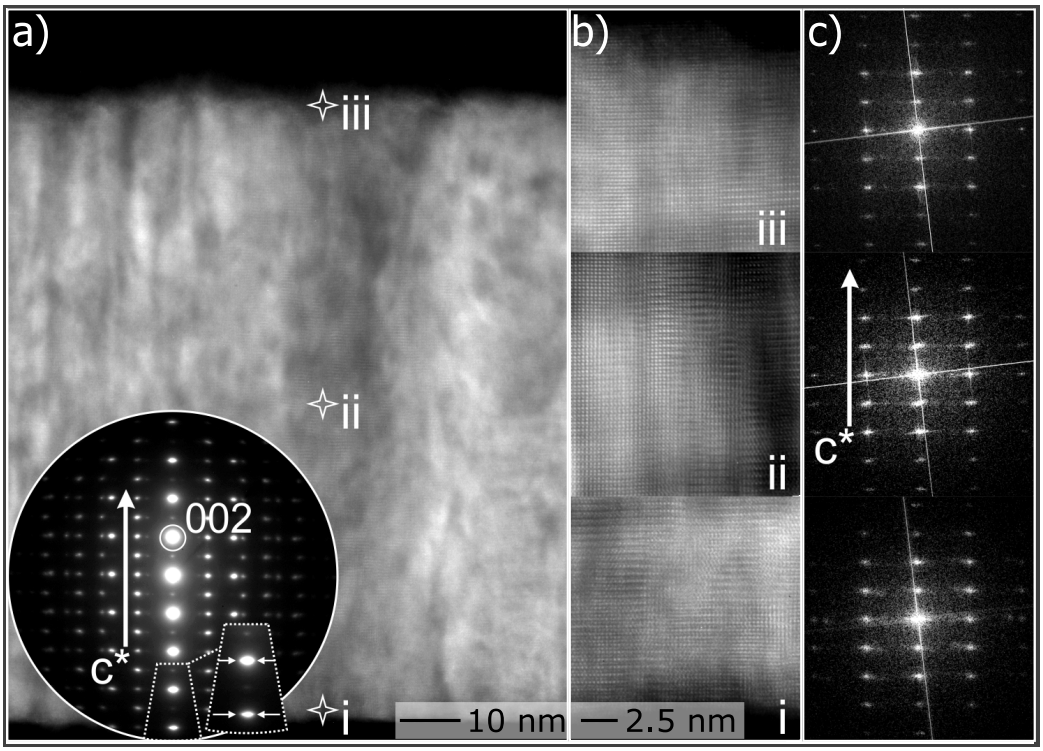


***Figure 4.4:*** *TEM study on a 100 nm thick AlN sample deposited on plasma treated Pt. a) TEM bright field image with SAED pattern as inset and a magnified view pointing out an elongation of the (002) reflections. The crosses (i, ii, iii) mark the positions of; b) recorded HRTEM micrographs and the accompanied c) FFT patterns. The white arrows mark the growing direction along c-axis (or the corresponding reciprocal c*).*

be residual thin film stress [137, p.279]. A series of HRTEM micrographs and their associated FFT patters were recorded parallel to the *c*-axis as seen in Figure 4.4b and c. It is clear, that a well defined *c*-axis oriented AlN growth starts directly at the joined Pt-AlN interface. The orientation integrity is preserved through the thickness of the sample, validating an identical structure along the entire size of the column. This is a remarkable observation, since it was previously reported that polycrystalline AlN films possessed a transition zone of randomly oriented crystallites as thick as 500 nm [161]. It was also reported that a self-adjusting system, despite an initial competitive growth between different orientations, was present for AlN [21, p.20]. This self-adjusting system required a minimum thickness of 30 nm as a prerequisite of the perfect material growth. Completed investigations, however, do not suggest such a transition zone for the AlN films fabricated in this work. It is not possible to determine/suggest any shadowing effects, neither. HRTEM micrographs neither exhibit tilted grains at the Pt-AlN interface (see Figure 4.4b -i) nor vanishing grains at any point (see Figure 4.4b -ii and -iii). AlN nucleates and grows along the *c*-axis without any secondary orientation. The preferential growth direction does not require a certain minimum

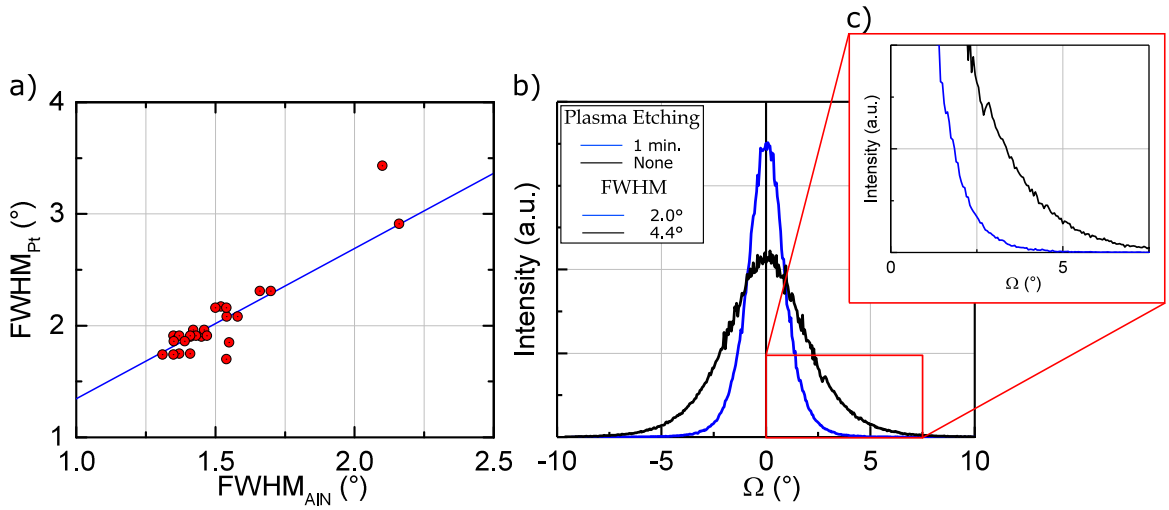


***Figure 4.5:*** *Influence of plasma treatment on the microstructure properties. a) Relationship between $FWHM_{Pt}$ and $FWHM_{AlN}$ values. Blue line represents the averaged $FWHM_{Pt}$ and $FWHM_{AlN}$ ratio for each sample and is simply a guide for the eye. b) Rocking curve measurements at $2\Theta = 39.7°$. $FWHM_{Pt}$ improves from 4.4° to 2° upon plasma treatment. c) The base shape difference suggests different nucleation conditions for the samples. Upon plasma treatment, the base width is narrowed and the peak is sharpened.*

film thickness, but exhibits a heteroepitaxial AlN nucleation on the Pt surface, that is similar to what was observed for high temperature AlN films [228].

The influence of the Pt texture quality on the texture quality of AlN was investigated, as well. The results are summarized in Figure 4.5a. A clear interaction between the texture qualities can be concluded from the FWHM values and how they are related. For instance, $FWHM_{AlN}$ values above 2° are recorded when the films are deposited on Pt with poor texture quality ($FWHM_{Pt} > 3°$). However, improving the Pt texture quality ($FWHM_{Pt} < 2°$) improves $FWHM_{AlN}$ values as well. In this case, FWHM values as low as 1.3° are reached. Note that the improvement of the Pt texture quality is achieved after plasma treating both the Pt and the underlying Ta layers prior to consecutive depositions.

The influence of the plasma treatment on the Pt rocking curve shape can be observed in Figure 4.5b. Upon plasma treating both the Ta and Pt layers, the $FWHM_{Pt}$ decreases approximately 50%. Similar to the AlN case, plasma treatment of the Ta might have modified the surface in a way that a higher amount of nucleation surfaces favoring the nucleation of <111> oriented Pt grains are obtained. Change of the rocking curve's base shape further suggests distinct nucleation processes for the plasma treated and non-treated samples, as can be seen from Figure 4.5c. This is an interesting result since all the samples are always kept in vacuum along consecutive depositions. Therefore the possibility of surface oxidation is

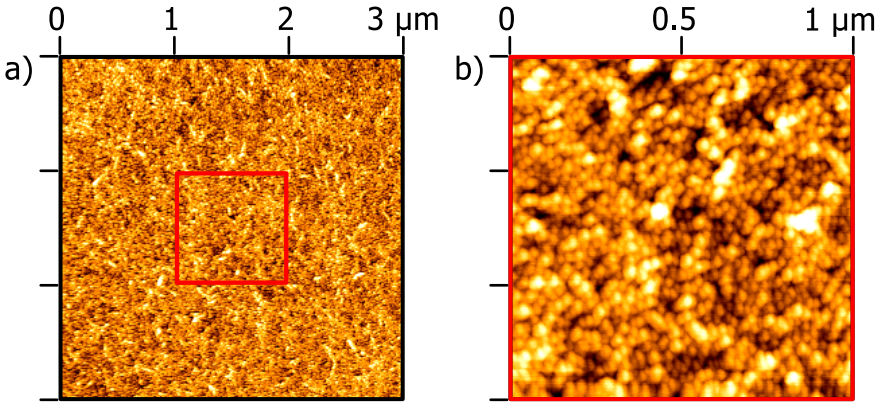


***Figure 4.6:*** *AFM study on a 1.7 µm thick AlN sample deposited on plasma treated Pt in pure nitrogen plasma. Tapping mode. Images size a) 3 µm × 3 µm and b) 1 µm × 1 µm. Average RMS roughness is observed as 1.4 nm and 1.2 nm. Peak-to-valley difference is found as 14 nm and 11 nm.*

minimum for AlN. Since Pt is chemically inert, it would not be affected even if the vacuum would be broken. However, it is possible that there are some residual particles stuck to the target surface or some resputtering from the chamber walls which influence the nucleation surface. In summary, it was observed that film growth of individual layers did all benefit from the removal of the first couple of nanometers off the nucleation surface.

Finally, surface properties of a highly textured AlN thin film was investigated with AFM (see Figure 4.6). Investigated area depicts uniformly shaped and distributed circular grains. The average (RMS) roughness extracted from the large and small area scans are as low as 1.4 nm and 1.2 nm, respectively. The distance between the highest peak and the minimum valley is down to 14 nm and 11 nm, respectively. These findings suggest an extremely dense structure and smooth thin film surface.

### 4.1.3 Influence of the Process Pressure

Pressure is one of the key parameters, which allow the tailoring of the deposited film properties such as the texture quality, residual film stress, piezoelectric properties, etc.. In order to characterize the stress properties of AlN thin films, a set of samples were prepared under varied pressure conditions.

***Microstructural Properties***: Figure 4.7a depicts the recorded XRD diffractograms of the investigated samples. As a result of the previously optimized process parameters, <001> orientation presents itself as the only growth direction. Observed shoulders at $2\Theta = 35.1^\circ$

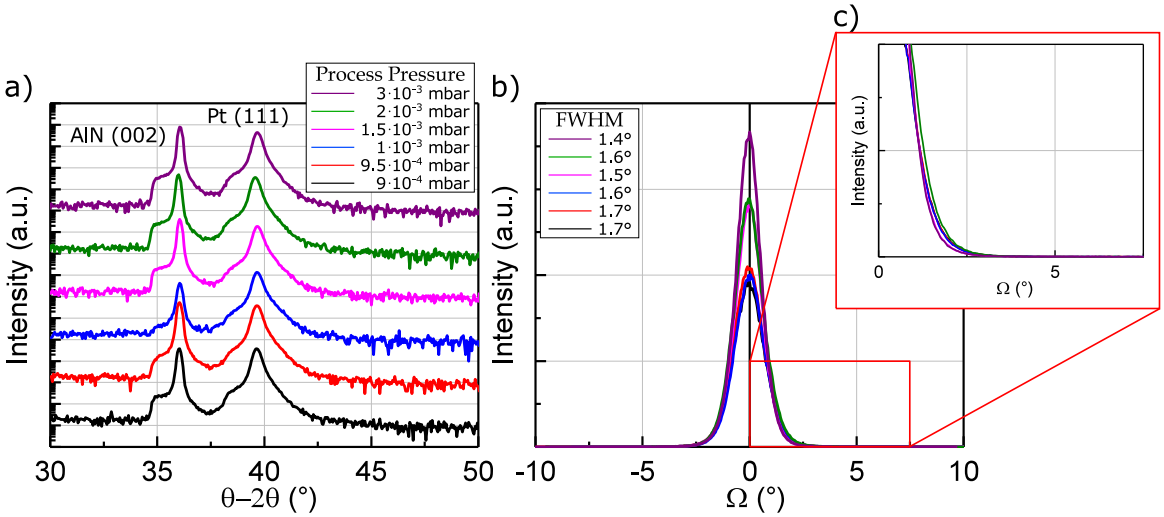


***Figure 4.7:*** *Influence of the process pressure. Investigated sample stacks include Si (300 µm) / $SiO_2$ (1.5 µm) / Ta (15 nm) / Pt (150 nm) / AlN (1.5 µm) a) XRD diffractograms of the investigated samples. (002)-AlN and (111)-Pt reflections are observed. No secondary AlN orientations are present. b) Texture quality of AlN in terms of FWHM recorded at 2Θ = 36.1°. FWHM exhibit minimal improvement with respect to increasing pressure. Base shape remains almost identical.*

and $2\Theta = 38^\circ$ do not belong to the AlN peaks. The difference in the signal intensity can be an artifact since all samples have similar film thicknesses, however, it is not very significant. Rocking curve measurements depict a high texture quality for all samples independent of the process pressure. Considering the whole investigated pressure range, however, the total variation of the FWHM is as high as 20% (see Figure 4.7b and c).

### *Discussion*

A higher FWHM resulting at low process pressure can be attributed to the influence of the extra energy brought to the surface by the bombarding particles. It is important to point out that additional energy may act counter-productively and damage the AlN surface by re-sputtering the surface atoms similar to a plasma etching process. This might be a potential reason for slightly higher FWHM as the pressure decreases. On the other hand, it was previously reported that processing at relatively high pressures could result in mixed growth orientations [168]. This was not the case here, probably due to the chosen pressure range not being large enough. It is also possible that the nucleation/growth direction of AlN is not established solely by the process pressure but as a result of the combined influence of several factors. If one assumes that there is a certain energy threshold for the nucleation of <001> oriented grains, then it can be suggested that the combination of the chosen deposition parameters, seed layer material and its surface treatment already overcome this requirement.

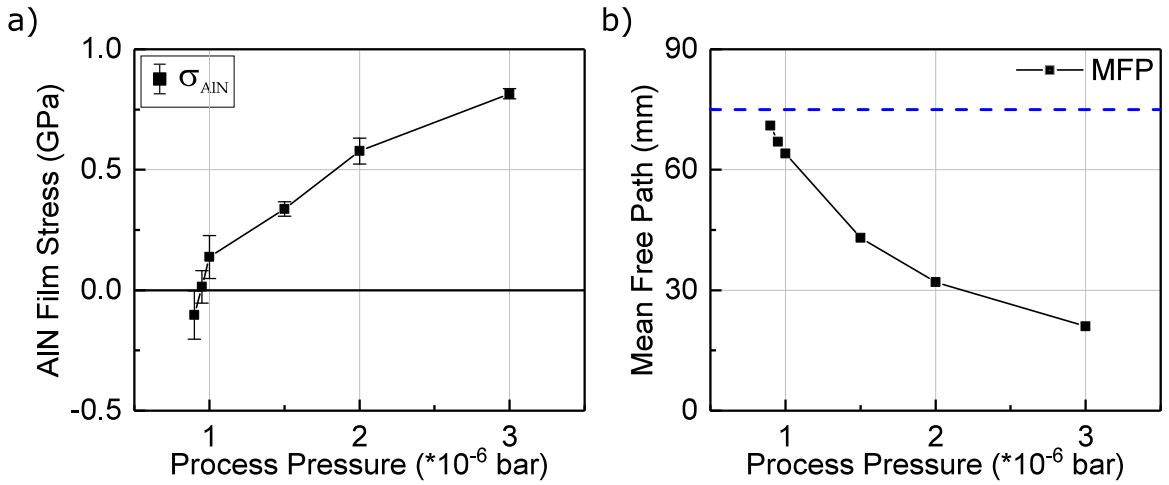


***Figure 4.8:*** *Influence of the process pressure on film stress and mean free path. Investigated specimen stacks include Si (300 µm) / $SiO_2$ (1.5 µm) / Ta (15 nm) / Pt (150 nm) / AlN (1.5 µm) a) Change in the residual film stress as a result of varied pressure and the consequent transition od the stress sign. b) Inverse relation between the process pressure and the MFP of the ions. Blue dashed line represents the target-to-substrate distance. Number of investigated samples is 7 for each investigated pressure. Each sample is measured for a minimum of 3 times.*

***Residual Film Stress Properties***: Energy brought to the growing film surface can influence the residual film stress. Accordingly, in-plane residual stress of AlN films were investigated as a function of process pressure as given in Figure 4.8a. Residual stress of AlN films depict a transition from tensile to compressive stress as the pressure decreases. The transition occurs just below $1 \cdot 10^{-6}$ bar with the current conditions (gas flow, power, etc.). Observed behavior is in well agreement with the previously published data on the stress behavior with respect to process pressure (see [148][229]).

The residual stress constituents were previously given in Equation (3.13). In this work, deposition of individual layers are completed on nominally non-heated substrates. Nevertheless, temperature at the sample's surface would increase during the deposition process due to the ion bombardment. Therefore there is a stress contribution (to an extent) as a result of the different thermal expansion coefficients of the constituent films. Investigated samples are not annealed or subjected to any deformation, hence there are not any externally induced stress contributions. On the other hand, lattice mismatch between consecutive layers is generally a major contributor of residual thin film stress. However, thickness of the AlN films in the current investigation was $\sim$1.5 µm, hence too thick to be influenced by the lattice mismatch. This leaves behind the ion bombardment as the major responsible of stress.

***Discussion***

Ion bombardment describes the phenomenon where ions formed in the plasma are accelerated towards the substrate holder [160]. Hence it is a mechanism, which is directly responsible of the kinetic energy delivered to the growing film surface [172]. It is one of the three influential factors that are known to increase the adatom mobility on the film surface. The other two factors are the substrate temperature and the process gas pressure. Ion bombardment itself is the sum of ion-assisted and atom-assisted growth mechanisms.

***Ion-assisted growth mechanism*:** The first mechanism is the ion-assisted growth mechanism, which describes an energy transfer to the growing film surface as a result of the ion bombardment. Therefore it depends on the positively charged species involved in the process; i.e., $N^+$ and $N_2^+$ (see Section 2.4.6). During film deposition, these positively charged ions bombard the growing film surface as a result of the potential difference between the plasma and the substrate holder. It is further enhanced when a negative bias is applied to the substrate and/or when the pulsed DC generator is at its positive pulse of the cycle. The latter is called self-biasing and is highly influential in the early stages of the AlN growth process. However, its influence decays over time with increasing film thickness due to the fact that AlN is an insulator material.

***Atom-assisted growth mechanism*:** Atom-assisted mechanism describes the enhancement of the film crystallinity via the energy carried by the sputtered target species, instead of the ions. It was previously defined by *Iriarte et al.* in analogy with the ion-assisted growth mechanism [160]. Since the energy distribution of the sputtered atoms exhibit a maximum at around half the surface binding energy of the sputtered material [133, p.14], the average energy of the sputtered atoms is sufficiently high to promote the surface diffusion and film densification. This energy is dependent on the process pressure and the target-to-substrate distance, as well. If the MFP of the target atoms/compound molecules, which are dependent on the process pressure, is much shorter than the target-to-substrate distance, then many collisions will occur and the arrival angle distribution of the sputtered species will broaden. But if the process pressure is low enough, then sputtered particles will retain most of their energy as they arrive to the growing film surface. On the other hand, at high pressures the atoms are mostly thermalized before they reach to the film's surface and the atom-assisted growth mechanism is suppressed [160]. This points out one of the advantages of using a magnetron sputtering setup, which allows film deposition at low pressures.

Furthermore, process pressure is influential on the growth mechanisms via the MFP and the

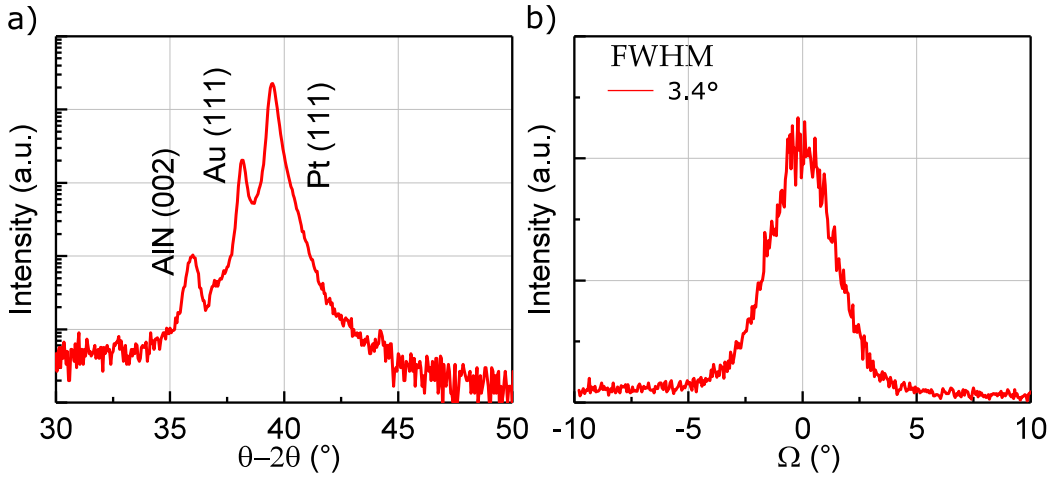


***Figure 4.9:*** *Microstructural properties of a 30 nm thick AlN thin film. a) XRD diffractogram of a 30 nm thick AlN sample deposited on a Pt seed layer. b) FWHM is found as 3.4° from the applied Gaussian fit.*

two are inversely proportional (see Equation (4.2)). The MFP of a nitrogen molecule in the current case[1] is plotted with respect to process pressure as seen in Figure 4.8b. For instance, at $1 \cdot 10^{-6}$ bar a single nitrogen ion would collide with another nitrogen ion at every 64 mm. At $3 \cdot 10^{-6}$ bar, on the other hand, the collisions would occur as often as at every 20 mm. In this case, a big energy difference is created, considering the fact that the target-to-substrate distance is only 75 mm (blue line). As a result, it is possible to induce a wide range of residual stress onto the deposited AlN films using process pressure as an optimization tool.

### 4.1.4 Influence of the Film Thickness

Another parameter of interest is the AlN film thickness and its influence on the film properties. To that end, a number of samples with varied thickness (30 nm - 2 µm) were prepared. First investigations aim at the determination of minimum necessary film thickness that provides textured AlN.

Figure 4.9a depicts the XRD diffractogram of a 30 nm thick film, thinnest AlN sample of the current work. The main (002)-AlN peak is found at $2\Theta = 36°$. Additional reflections found at $2\Theta = 38.2°$ and $39.5°$ belong to top and bottom electrode materials, respectively. Remarkably, a <001> oriented film growth, without secondary AlN peaks, is confirmed for the investigated sample. The rocking curve width of the AlN peak is as low as 3.4° as seen in Figure 4.9b. This further strengthens the previously given argument; that a transition zone

[1] In vacuum and at room temperature.

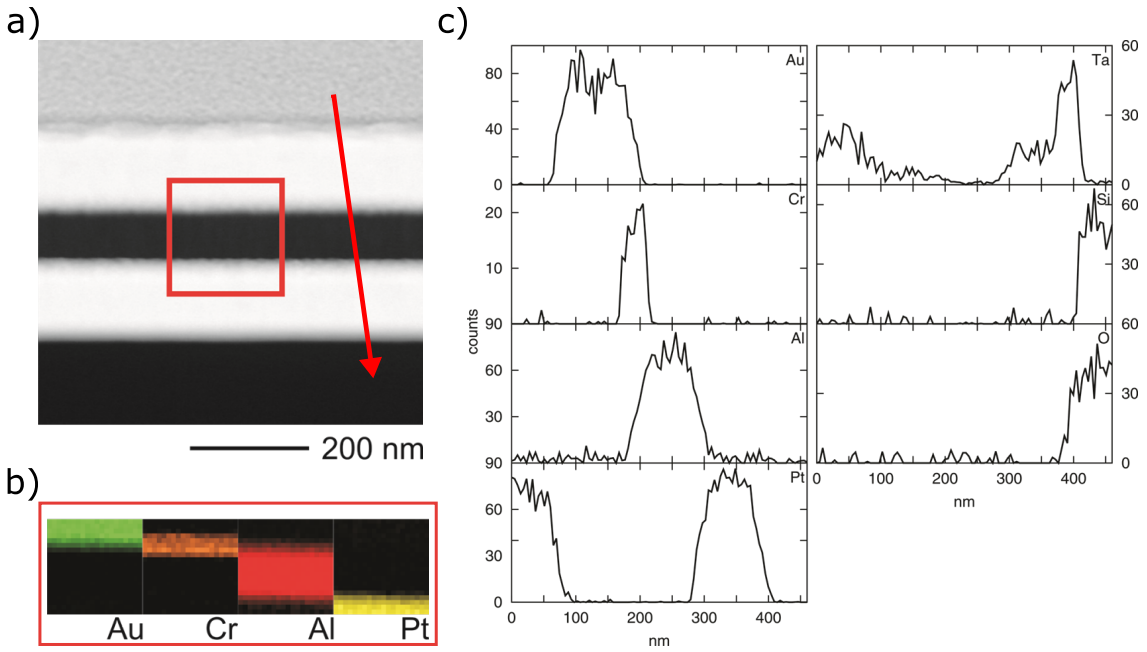


***Figure 4.10:*** *Chemical analysis of a 100 nm thick specimen. (a) Area investigated via STEM-EDX is marked with a red square. (b) Chemical mapping and detected elements within the investigated area. (c) Line scan along the thickness of the sample and detected respective signals. Thickness of individual layers can be read from the x-axes. The sample was prepared on a Si / $SiO_2$ / Ta / Pt stack, with the latter plasma treated.*

of randomly oriented crystallites is not present in the fabricated AlN films. Growth along the <001> direction starts directly at the Pt-AlN interface, due to perfect local epitaxy between Pt and AlN at the optimized process parameters. It can be assumed that at 30 nm thickness, there is not enough time for misaligned grains to be consumed by fast growing grains. Even though it is unlikely, one can always argue that there might be a transition zone, which occurs in the first 10 nm – 20 nm, for instance. In this case, a much faster mechanism than previously observed must be present [161].

***Composition Properties***: The chemical integrity of the deposited AlN films is highly important, as well. AlN films, which do not satisfy the stoichiometry conditions are not suitable for the current work. Especially the presence of oxygen is reported detrimental when above 1 at.% [230]. In order to validate the chemical integrity of the AlN films, a 100 nm thick AlN FIB sample was investigated using STEM-EDX. The chemical mapping of a selected area is shown in Figure 4.10b. A clear separation between the detected elements; i.e., Au, Cr, Al and Pt, is observed. This suggests that no diffusion took place during the deposition of consecutive layers. The findings of a complementary line scan, ranging from the specimen's surface until the underlying Si substrate, exhibit similar results (see Figure 4.10c). Looking

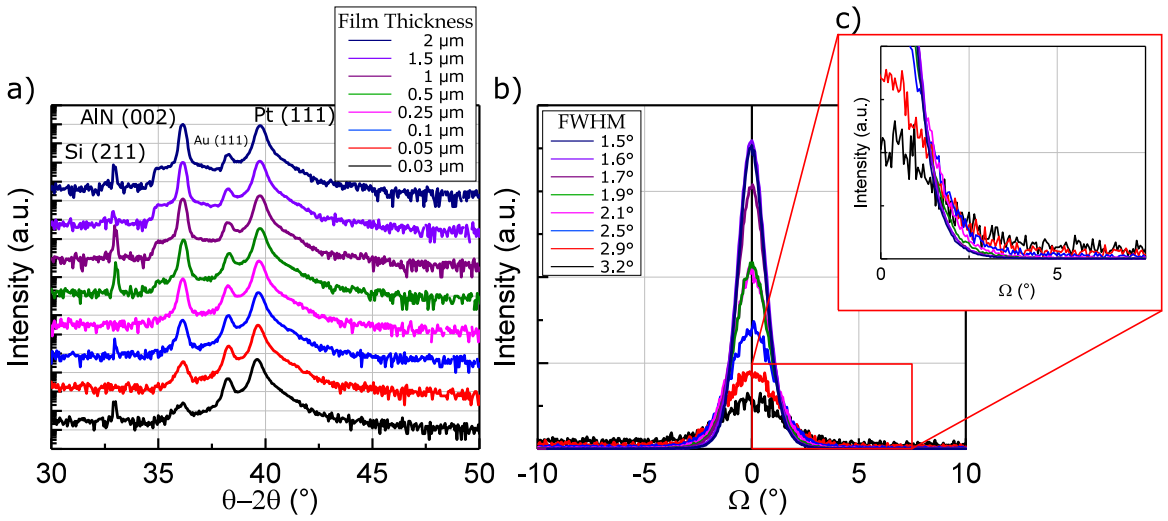


***Figure 4.11:*** *Microstructural properties of AlN films with varied thickness. a) XRD diffractograms exhibit the main AlN peaks of individual samples at 2Θ = 36.1°. (211)-Si reflection is observed at 2Θ = 33.04°. Additional reflections belong to the top and bottom electrode materials. b) Rocking curve measurements. FWHM calculated from the applied Gaussian fits exhibit an improvement as the film thickness increase. c) A similar base shape is present for all samples. Increased thickness leads to a decreased width.*

at the line scan, detected oxygen signals belong only to the thermal oxide layer of the Si substrate. Furthermore, chemical distribution of Al and N was determined as $49.79 \pm 0.98$ and $50.21 \pm 0.98$ at.%, respectively. Hence not only the preferential growth and the structural integrity but also the chemical structure of the deposited films are confirmed.

***Microstructural Properties***: Figure 4.11a shows the XRD diffractograms of the AlN samples with thickness varied between 30 nm and 2 µm. The main (002)-AlN peaks are found between $2\Theta = 36.1° - 36.2°$. Additional reflections are present at $2\Theta = 33°, 38.2°$ and $39.7°$ belonging to (211)-Si, (111)-Au and (111)-Pt, respectively. Independent of the film thickness, an (002) oriented preferential growth is confirmed for all samples. The rocking curve width of the main AlN peaks are plotted in Figure 4.11b. There is an apparent improvement of the texture quality in the form of decreasing rocking curve width as the thickness increases. FWHM decreases from $3.2°$ at 30 nm down to $1.5°$ at 2 µm. Close-up to the rocking curve base is given in Figure 4.11c. At very low thickness, measurement signals are deteriorated due to the limited material volume, nevertheless a similar base shape with steady width decrease can be deduced from the plots. This is expected since all samples nucleate at identical conditions and film thickness has no influence on the nucleation of grains.

The relationship between process time (film thickness) and FWHM is summarized in Figure 4.12a. Furthermore, the evolution of the self-induced bias voltage is demonstrated as

well[1]. There is an apparent improvement of the texture quality with respect to increasing self induced-bias, which amounts to 25 V at the end of an exemplary 38 min long deposition.

***Discussion***

Self-induced bias is formed as a result of the potential difference between the plasma and the substrate holder. The increase in the potential difference, therefore, suggests that either the plasma becomes more positively charged or the substrate holder becomes less conductive due to increasing AlN thickness. Figure 3.5a shows that the plasma become rather more resistant as the processing time increases. Hence the potential difference observed shall be the result of the increasing film thickness on the substrate holder and the chamber walls. As the surfaces are covered with thicker AlN, which is an insulator, a higher amount of potential is necessary across the target in order to sustain the sputtering process. Consequently the potential differences between target-substrate holder and plasma-substrate holder increase.

In summary, the growing film is bombarded by increasingly energetic particles and if there really is not a transition zone, as suggested, than the improvement of the texture quality at higher AlN thickness shall be related to the higher amount of energy brought to the surface as a result of longer process time. However, the same argument is not valid for the thinnest films.

Within the investigated thickness range, longer deposition time results in a higher texture quality but the improvement rate decays over time. Considering the slope of the FWHM curve in Figure 4.12a, it is obvious that a high improvement occurs in the first 250 nm thickness, but then the improvement slows down as the thickness increases. The reason for the high texture improvement at very small thickness can not be due to the energetic particle bombardment, since the thinnest sample, for instance, was subject to sputtering for approximately half a minute. In other words, the process time was simply not long enough for the ion bombardment to be influential. The presence of large dislocation densities observed in the first 100 nm was previously offered as a possible reason [165]. However, this seems unlikely in this work.

A more reasonable explanation can be found from the grain growth process and grain coarsening. Using the XRD diffractograms and the modified Scherrer formula (see Equation (3.5)), the size of the crystal grains were estimated. According to Figure 4.12b, crystallite size increases with respect to film thickness only up to a certain point where a saturation is reached.

[1]The deposition rate of AlN with the optimized parameters at $2 \cdot 10^{-6}$ bar pressure equals approximately 52 nm/ min.

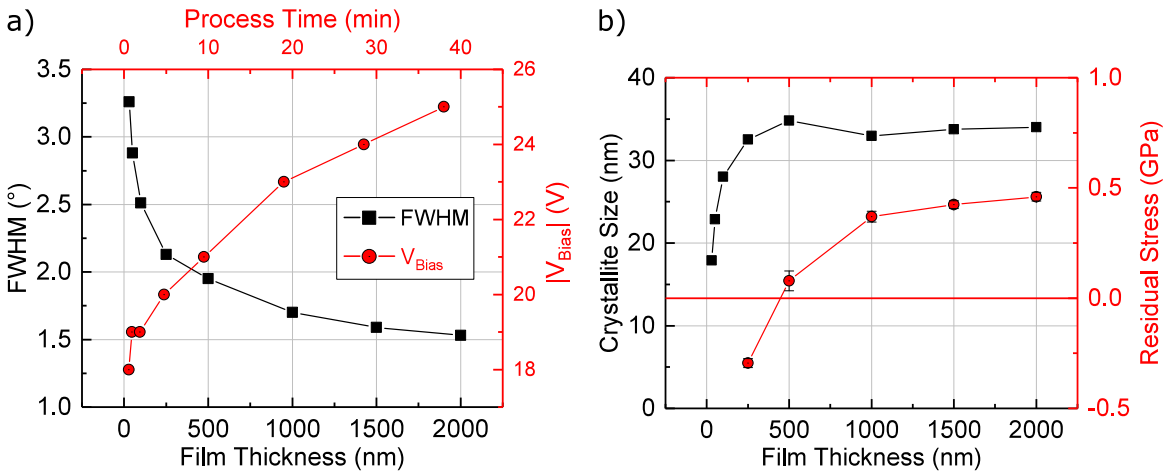


***Figure 4.12:*** *Relation between film thickness and texture quality. a) A continuous improvement of the FWHM with respect to increasing thickness is observed. Self-induced bias increases as the process continues longer. b) Longer processing leads to an increased surface temperature and diffusion. As a result, crystallite size increases until a saturation point is reached. Residual stress in AlN films undergo a transition from compressive to tensile stress mode as the thin film thickness increases.*

The mechanism can be explained as follows; once the sputtering process begins, <001> oriented AlN nucleates randomly on the Pt surface. Among numerous nuclei, only those that are above a certain critical size succeed nucleation and start to grow [137, p.147]. Some of the nuclei nucleate on the energetically favorable nucleation sites compared to the others. Grains nucleating at these sites grow much faster than the other grains, hence result in grain coarsening as the process continues. Normally, it is expected to see shadowing effects under these circumstances. However, the presence of a plasma treated Pt seed layer already establishes a preferentially oriented growth that is free of any secondary growth directions. Bombardment of the growing film surface with energetic particles, consequently, enhances the process by increasing the surface temperature and diffusion; i.e., adatom mobility. Maximum calculated grain coarsening is approximately 32 nm and is observed at 250 nm thickness. Further film deposition seems ineffective on the crystallite size.

***Residual Film Stress Properties***: Despite the apparent enhancement of the texture quality, increasing film thickness and energetic bombardment contributes to the residual thin film stress as well. Figure 4.12b depicts the evolution of AlN residual stress with respect to AlN film thickness. When sputtering begins and AlN molecules reach the Pt surface, the lattice at the interface strains in order to accommodate the difference in the lattice length of both materials. This results in the formation of a residual stress with opposing sign; i.e., compressive stress, in Pt surface. The influence of the mentioned stress can be observed both from the XRD and TEM investigations.

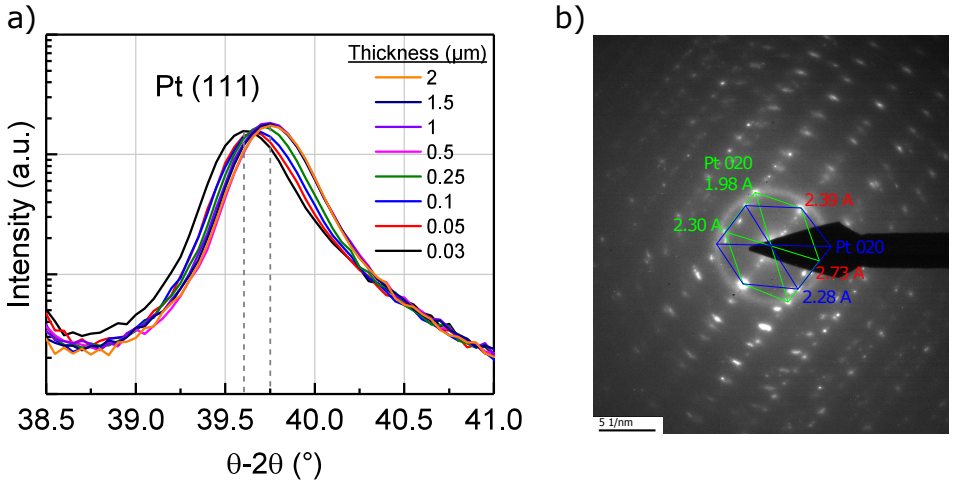


***Figure 4.13:*** *Influence of residual stress on Pt. a) Increase of the compressive stress acting on Pt and shift of the (111)-Pt peak to higher 2Θ values. Given thickness values belong to the deposited AlN films. b) TEM investigations of an 100 nm thick AlN deposited on Pt. Pt twins are shown in green and blue, AlN is given in red. Measured lattice parameters are noted.*

Figure 4.13a depicts a close-up of the (111)-Pt peak seen in Figure 4.11a. In the given plot, main Pt peak is found at $2\Theta = 39.6°$ for the thinnest sample. At the end of a 30 min long deposition process, however, it is shifted up to $2\Theta = 39.75°$. Note that the given thickness values belong to the overlaying AlN layer and Pt thickness is constant for all samples. Peak shifts observed in the XRD diffractograms are often due to different stoichiometry and film stress [44, p.309]. Since the former is not related here, it can be concluded that the observed peak shifts are due to the planar stresses acting at the Pt-AlN interface. A wider 2Θ value, as observed here, suggests an increasing compressive stress, which is also confirmed by the radius of curvature measurements. Furthermore, analysis of the Pt-AlN interface by TEM[1] and captured diffraction patterns[2] are shown in Figure 4.13b. The pattern contains diffraction spots from two twinned Pt domains[3] and AlN on top of that[4]. The diffraction spots belonging to (111)-Pt of both Pt domains coincide with (011)-AlN indicating co-oriented or even epitaxial growth of AlN on top of the Pt layer. However, it is not possible to definitively confirm this observation from a single 2-dimensional TEM investigation. The lattice parameters extracted from the diffraction pattern for AlN indicate that it is slightly stretched as is expected from a strained film[5].

[1] TEM investigation is completed by M.Sc. Julian Strobel from the chair for Synthesis and Real Structure (Prof. Dr. Lorenz Kienle) of the Kiel University.

[2] At 300 kV, field emission gun, $C_s = 1.2$ mm, taken with an aperture limiting the area of acquisition to 280 nm in diameter.

[3] Both zone axes 10-1, space group Fm-3m.

[4] Zone axis: 100, space group P63mc

[5] Experimental, 011: 2.39 Å, 010: 2.73 Å. Literature, 011: 2.3691 Å, 010: 2.6933 Å [231].

In summary, at very small AlN thickness, the large lattice difference between AlN and Pt results in a large compressive stress. This stress might be compensated via dislocations as the film grows thicker. As the AlN growing on Pt is no longer influenced by the initial lattice mismatch, the overall stress decreases. Continuous deposition of AlN is accompanied with sustained bombardment of the film and a greater adatom mobility. This results in the reversal of the stress sign as the texture quality of the deposited films improve. It is also important to consider the increasing crystallite size and consequent coarsening effects in accordance to increasing film thickness [157].

### 4.1.5 Piezoelectric and Dielectric Properties

Additional to the microstructural properties, it is imperative to obtain high sensor properties; e.g., high piezoelectric coefficient, low dielectric losses, etc.. For example, samples that are highly stressed would already bend their substrate and since the 4-point-bending method depends on the displacement at the middle point of a cantilever shaped sample, already bend samples would have lower charge generation. Considering samples fabricated at different process pressures, for instance, a cantilever sample with an AlN layer deposited at $0.9 \cdot 10^{-6}$ bar exhibits a maximum bending of approximately 6 µm. However, the bending reaches as high as 16 µm for the samples deposited at $3 \cdot 10^{-6}$ bar. Therefore, adjusting the pressure for stress tailoring can only be utilized as long as the piezoelectric and dielectric properties of the deposited films are in the desired levels, for instance.

As discussed in Section 2.1.4, the important piezoelectric effect of AlN lays along the *c*-axis, which is perpendicular to the substrate surface. Nevertheless, both longitudinal ($d_{33,f}$) and transversal piezoelectric coefficient ($e_{31,f}$) of the deposited films were determined using the DBLI (see Section 3.3.2) and the 4-point-bending (see Section 3.3.2) measurement methods, respectively. Additionally, fabricated samples were characterized in terms of the dielectric losses and capacitance measurements. As a result of these investigations, optimal AlN deposition parameters and film thickness are determined. Optimized films are then used as the piezoelectric constituent in the magnetoelectric composites.

***Process Pressure:*** First investigations focus on the influence of the process pressure. As seen in Figure 4.14a, there is an inversely proportional relationship between the $|e_{31,f}|$ and the process pressure. Recorded values increase from $\sim$1.36 C/m$^2$ to $\sim$1.51 C/m$^2$ as the pressure is decreased from $3 \cdot 10^{-6}$ bar to $0.9 \cdot 10^{-6}$ bar. This relationship is dependent both on the texture quality and the residual film stress. Samples deposited at lower pressures have

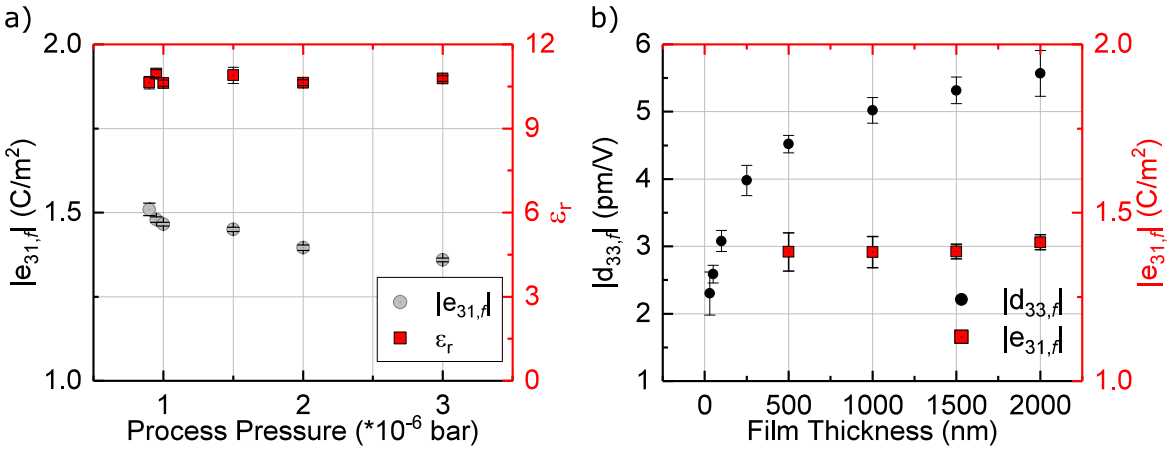


***Figure 4.14:*** *Influence of the process pressure and film thickness on piezoelectric and dielectric properties. a) Investigated sample stacks include Si (300 µm) / $SiO_2$ (1.5 µm) / Ta (15 nm) / Pt (150 nm) / AlN (1.5 µm). Lower process pressure improves the piezoelectric properties. Relative permittivity is kept constant for all samples. b) The evolution of the piezoelectric coefficients with respect to AlN film thickness. All AlN films are deposited at $2 \cdot 10^{-6}$ bar process pressure. Clamped longitudinal ($d_{33,f}$) and transversal ($e_{31,f}$) piezoelectric coefficients are given in absolute values. 500 nm film thickness marks the minimum thickness for a high piezoelectric coefficient. Number of investigated samples is 6 and 7 for each thickness and pressure value, respectively. Each sample is measured for a minimum of 3 times.*

better texture quality (see Figure 4.7b), hence they exhibit, in return, a higher piezoelectric coefficient [157]. Also, at lower pressure values the residual stress of the AlN thin films are much lower compared to the samples deposited at higher pressures (see Figure 4.8).

Figure 4.14a depicts the influence of the process pressure on the relative permittivity of the AlN films. A near constant relative permittivity is observed for all samples. An average permittivity of $10.75 \pm 0.15$ is found from the values calculated using capacitance measurements. Both the piezoelectric coefficient and the relative permittivity values are in good agreement with the values given in the literature [226][232][233]. This is a reassuring outcome, since it confirms the applicability of the attempted stress optimization via pressure adjustment. Control of the stress is achieved without worsening the piezoelectric/dielectric properties of the AlN films, which is crucial for the intended sensor applications.

***Film Thickness:*** Further investigations consider the thickness influence on the piezoelectric and dielectric properties. An improvement of the piezoelectric activity in response to increasing film thickness can be observed from Figure 4.14b. For instance, longitudinal piezoelectric coefficient ($d_{33,f}$) is measured as $2.30 \pm 0.32\,\mathrm{pm/V}$ for 30 nm thick samples. At 2 µm thickness, $d_{33,f}$ reaches an average value as high as $5.57 \pm 0.34\,\mathrm{pm/V}$. The improvement of the piezoelectric activity with respect to thickness is most pronounced at 500 nm thick sam-

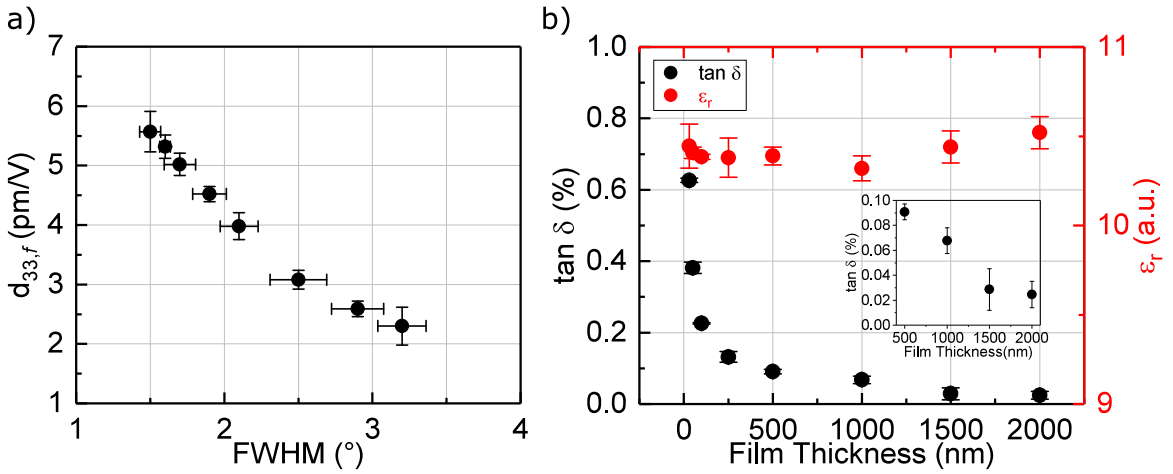


***Figure 4.15:*** *Influence of the texture quality on the piezoelectric behavior and the evolution of the dielectric properties with respect to AlN film thickness. a) A quasi linear relation is present between the texture quality of the deposited films and the piezoelectric activity. b) Dielectric loss (tan $\delta$) and the relative permittivity ($\varepsilon_r$) are presented with respect to AlN film thickness. The inset depicts a close-up to the samples which exhibit tan $\delta$ < 0.1%. Relative permittivity is almost constant independent of the film thickness. Number of investigated samples is 6 for each thickness value. Each sample is measured for a minimum of 3 times.*

ples. On the other hand, thickness does not improve the $e_{31,f}$, within the investigated range. Once again, the observed behavior can be related to the texture quality and the film stress.

For a better assessment, the texture quality is plotted against the $d_{33,f}$ coefficient as seen in Figure 4.15a. An obvious relationship between two parameters can be observed, where a quasi linear dependency is present. Clearly, a better crystal structure produces a better piezoelectric behavior. At this point it is also important to point out that DBLI measurements proved to be more reliable in comparison to 4-point-bending method. For instance, the determination of the $e_{31,f}$ coefficient was not successful for samples thinner than 500 nm due to short circuit problems.

The last important parameters to investigate are the dielectric properties of the deposited films. To that end, top electrodes with an area of $0.570 \pm 0.015\,\mathrm{mm}^2$ were sputtered and structured on the AlN films. Afterwards, AlN samples of various film thicknesses were characterized using a LCR meter, in a wide frequency range, in terms of capacitance and dielectric loss tangent. Respective relative permittivity values were calculated using the capacitance measurements as well. In a parallel plate capacitor setup, the capacitance and the relative permittivity of the material are related with each other according to the following formula;

$$C = \frac{A \cdot \varepsilon_0 \cdot \varepsilon_{33}}{t} \tag{4.4}$$

where $C$ is the capacitance, $A$ is the electrode area, $\varepsilon_0$ is the vacuum permittivity, $\varepsilon_{33}$ is the relative permittivity and $t$ is the distance between top and bottom electrodes; i.e., thickness of the piezoelectric film [137, p.490].

Normally, the dielectric loss tangent varies with respect to increasing frequency; i.e., as the polarization can not keep up with the fast switching field and lacks behind. Therefore the actual measurements are completed at frequencies as high as 10 kHz, since it is the standard measurement value. Figure 4.15b summarizes the decrease of the dielectric losses with respect to increasing film thickness. Thinnest samples yield a dielectric loss tangent values as high as $0.626\% \pm 0.006\%$. As the AlN thickness increases, dielectric losses decrease to a minimum average value of $0.025\% \pm 0.011\%$ at 2 µm film thickness. The decrease of the dielectric losses suggests a superior crystal quality since these losses mostly originate from structural defects. In fact, the shape of the slope depicts good correlation with the improvement of the texture quality previously observed in Figure 4.12a. Near constant relative permittivity values with small variations ($10.4 \pm 0.05$) are calculated from the capacitance measurements. Observed variation can be correlated with the non-uniform electrode areas originating from the metallic top electrode mask.

***Table 4.3:*** *Summary of the measured and derived piezoelectric and dielectric properties*

| Piezoelectric Coefficient and Unit | | AlN Film Thickness 30 nm | 50 nm | 100 nm | 250 nm | 500 nm | 1000 nm | 1500 nm | 2000 nm | PZT 2000 nm |
|---|---|---|---|---|---|---|---|---|---|---|
| $e_{31,f}$ | $C/m^2$ | – | – | – | – | *–1.38* | *–1.38* | *–1.38* | *–1.41* | *–15.5* |
| $d_{33,f}$ | pm/V | *2.30* | *2.59* | *2.68* | *3.98* | *4.52* | *5.02* | *5.32* | *5.57* | – |
| $\varepsilon_{r,33}$ | – | *11.5* | *10.5* | *10.1* | *10.4* | *10.4* | *10.3* | *10.4* | *10.5* | *1000* |
| $tan\delta$ (%) | $10^5$ V/m | *0.626* | *0.368* | *0.225* | *0.132* | *0.091* | *0.068* | *0.029* | *0.025* | *2.7* |
| $*e_{31,f}/\varepsilon_0 \cdot \varepsilon_{33}$ | GV/m | – | – | – | – | –15 | –15 | –15 | –15 | –1.8 |
| $*e_{31,f}/\sqrt{\varepsilon_0 \cdot \varepsilon_{33} \cdot tan\delta}$ | $10^5\,Pa^{1/2}$ | – | – | – | – | 48 | 56 | 85 | 94 | 10 |
| $e_{33}$ | $C/m^2$ | 0.91 | 1.02 | 1.06 | 1.57 | 1.79 | 1.98 | 2.10 | 2.20 | – |
| $d_{31}$ | pm/V | –1.61 | –1.81 | –1.88 | –2.79 | –3.16 | –3.51 | –3.72 | –3.90 | – |
| $d_{33}$ | pm/V | 3.22 | 3.62 | 3.75 | 5.57 | 6.33 | 7.03 | 7.44 | 7.80 | – |
| $e_{31}$ | $C/m^2$ | –0.49 | –0.55 | –0.57 | –0.85 | –0.96 | –1.07 | –1.13 | –1.19 | – |
| $e_{31,f}$ | $C/m^2$ | –0.77 | –0.86 | –0.89 | –1.33 | –1.51 | –1.67 | –1.77 | –1.86 | – |
| $**e_{31,f}/\varepsilon_0 \cdot \varepsilon_{33}$ | GV/m | –8 | –9 | –10 | –14 | –16 | –18 | –19 | –20 | – |
| $**e_{31,f}/\sqrt{\varepsilon_0 \cdot \varepsilon_{33} \cdot tan\delta}$ | $10^5\,Pa^{1/2}$ | 10 | 15 | 20 | 38 | 52 | 67 | 109 | 123 | – |

Given measurement values are the mean values of 10-20 measurements for each sample, with a minimum of 5 samples per investigated thickness. Standard deviations are not included. Italic: Measured data, Upright: Derived data.
*See Equation (2.12).
**Derived FOMs for comparative purposes.
PZT data belong to a 2 µm thick PZT sample with a parallel plate capacitor configuration. Data taken from [234].

Table 4.3 summarizes all piezoelectric and dielectric measurements completed for the samples with varied AlN film thickness. Furthermore unclamped longitudinal ($d_{31}$, $d_{33}$) and transversal ($e_{31}$, $e_{33}$) piezoelectric coefficients are estimated from Equation (2.8) and Equation (2.9)[1] using the measured clamped piezoelectric coefficient values. Note that, $e_{31,f}$ is also estimated due to previously discussed measurements unreliability of the measurement device. Accordingly, derived $e_{31,f}$ values are higher than the actual measured values. However, these derived values can only be considered as speculated figures since verification through 4-point-bending measurements on stress compensated samples are necessary.

Nevertheless, measured piezoelectric coefficients, dielectric loss tangent values and the figure of merits are superior to previously given state-of-the-art piezoelectric materials (see Table 2.2). Due to the very low dielectric losses, in particular, FOM of the deposited films are found to be twice as large as the state-of-the-art AlN thin films for comparable film thicknesses. Obtained FOM values are even better than PZT films, when comparing both materials in parallel-plate electrode configuration [34].

[1]Elastic compliances and stifness constants are taken from [235]. $d_{33} = -2d_{31}$ according to [236].

## 4.2 Properties of Magnetoelectric Sensors

Properties of the fabricated magnetoelectric sensors are summarized in the following section. Among all investigated sensors, inverse-bilayer sensors exhibit the highest sensitivity and the lowest LOD. Therefore, this chapter is structured in such a way that it fully characterizes an exemplary inverse-bilayer senso and addresses all of its relevant properties. These properties include not only magnetoelectric properties but also crystallographic and magnetostrictive properties of the constituent materials. Furthermore, additional investigations concerning the influence of the constituents' deposition order and the influence of the top electrode size are also discussed.

### 4.2.1 Inverse-Bilayer Magnetoelectric Sensors

***Microstructural Properties***: Inverse-bilayer magnetoelectric sensors are fabricated on Si substrates with a layer ordering of Ta/FeCoSiB/Ta/Pt/AlN/Cr/Au as described in Section 3.2. An exemplary XRD diffractogram of such a composite stack is given in Figure 4.16a. Presented plot depicts two scans; the blue curve shows the diffractogram of a single 3 µm thick FeCoSiB film. The red curve belongs to the same film after the sample is covered with 140 nm thick Pt, 1.6 µm thick AlN and after the magnetic annealing of the sample is completed.

When FeCoSiB is brought above its crystallization temperature, the first phase to appear is the $\alpha$-Fe phase found at $2\Theta = 44.8°$. Since both scans are free of $\alpha$-Fe peak, it can be said that the amorphous structure of FeCoSiB is kept intact during sensor fabrication process. Furthermore, a textured polycrystallinity of the deposited AlN is observed. Observed reflections are (002)-AlN found at $2\Theta = 36.1\,^\circ$ and its multiple (004)-AlN at $2\Theta = 76.5\,^\circ$. The main reflection from the bottom electrode material (111)-Pt is detected at $2\Theta = 39.7\,^\circ$ and its multiple (222)-Pt at $2\Theta = 85.7\,^\circ$. Additionally, the (004)-Si reflection from the substrate material is detected at $2\Theta = 68.9\,^\circ$. Note that the adhesion layer (Ta) is not observable in neither case, most probably due to its very low thickness. A sharp rocking curve of the main AlN peak is obtained from the rocking curve measurements as seen in Figure 4.16b. A FWHM of $1.3\,^\circ$ is calculated from the applied Gaussian fit. To summarize; the presence of a single preferential AlN growth direction, low FWHM and the absence of an $\alpha$-Fe peak confirm that the growth of highly textured AlN is succeeded without influencing the amorphous structure of FeCoSiB.

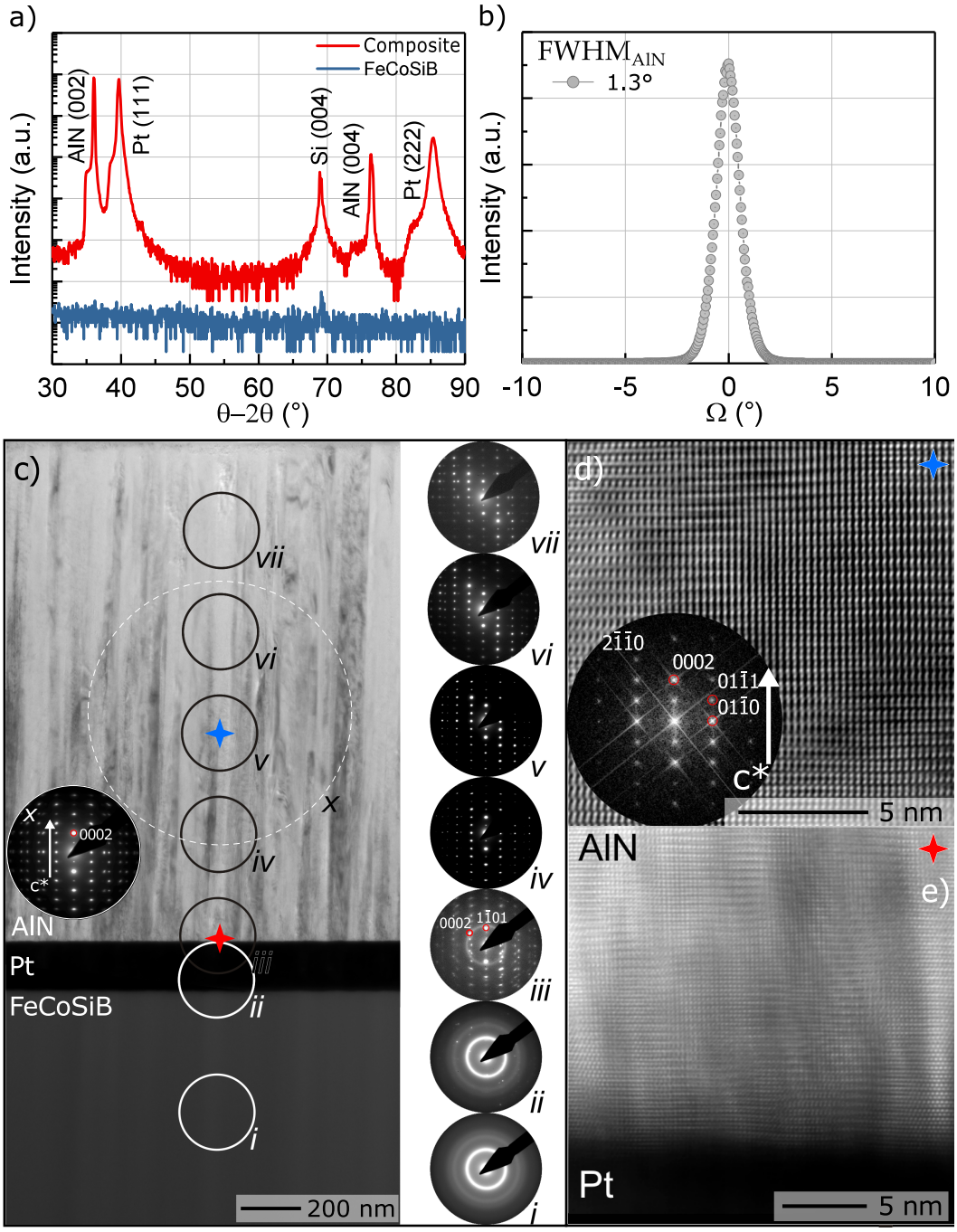


***Figure 4.16:*** *Microstructural properties of a magnetoelectric composite stack. a) XRD diffractogram of a magnetoelectric composite stack (red curve) consisting of Si (300 µm) / $SiO_2$ (1.5 µm) / Ta (10 nm) / FeCoSiB (3 µm) / Ta (10 nm) / Pt (140 nm) / AlN (1.6 µm). The diffractogram of a single 3 µm thick FeCoSiB layer is shown in blue. b) Rocking curve measurement at 2Θ = 36.1° and the calculated FWHM. c) TEM bright field image with a SAED pattern (illumination area: 850 nm) as inset. The white/black circles mark the positions of the SAEDs (illumination area: 250 nm). The red and blue crosses mark the positions of HRTEM studies. d) Top HRTEM micrograph is taken at the middle of the AlN layer and a corresponding FFT is included as inset where the white arrow marks the growing direction along c (or the corresponding reciprocal c*). e) Bottom HRTEM micrograph is taken at the AlN–Pt interface.*

Nevertheless, in order to obtain an in-depth structural analysis, which XRD can not provide, TEM investigations were performed as well[1]. Accordingly, a 2.6 µm thick cross sectional specimen[2] of the above described composite stack was prepared by FIB milling. The TEM bright field image of the investigated specimen is shown in Figure 4.16c. The large scale SAED pattern, recorded from the middle part of the specimen ($x$) reveals (0002)[3] texture as well as a superposition of azimuthally rotated single crystalline AlN patterns with the zone axes [$uvt$0]. The combination of the SAED patterns recorded along the thickness of the specimen (circles *i* to *vii*) and the supplementing HRTEM micrographs exhibit the growth texture for the entire length of the specimen. An amorphous structure is confirmed for FeCoSiB from the SAED taken at (*i*). Slight contributions of Pt are initially seen in the SAED taken at (*ii*). Starting from the Pt-AlN interface (*iii*), a textured growth along the common $c$-axis of all grains is observable in all the following SAEDs. A closer look into the nanostructure of the specimen (Figure 4.16d) was performed in a series of HRTEM micrographs. A local epitaxy between the surface of the <111> oriented Pt and the deposited AlN results in a <0001> oriented nucleation and growth at the common interface to Pt is confirmed (red cross). On the other hand, a slight elongation for the higher order AlN reflections is detected, indicating a non-perfect alignment for several adjacent columnar grains. Some planar defects, commonly observed in wurtzite type structures, are occasionally detected and can be observed at the (0001), $(01\bar{1}0)$, $(01\bar{1}1)$ and $(2\bar{1}\bar{1}0)$ planes.

In summary, the specimen depicts structural characteristics, which are in good agreement with the state-of-the-art AlN thin films deposited at higher temperatures [233]. As seen in the previous chapter, an epitaxial growth of AlN starting from the Pt-AlN interface is confirmed for a magnetoelectric composite stack as well. Furthermore, <001> direction is established as the single nucleation/growth direction of AlN without any transition zones.

***DC Magnetic Properties***: Once the microstructural integrity of FeCoSiB is confirmed, its magnetic behavior was characterized. The magnetic hysteresis curves of an exemplary square shaped sample[4] is given in Figure 4.17a. The plot includes two measurements; once when magnetizing along the hard (red curve) and once along the easy (blue curve) axis of the magnetization. Note that the $y$-axis of the plot magnetization is normalized with respect

[1] TEM investigations are completed by Dr.-Ing. Dipl. Phys. Viktor Hrkac from the chair for Synthesis and Real Structure (Prof. Dr. Lorenz Kienle) of the Kiel University.

[2] Starting from the top surface.

[3] Since AlN has an hexagonal crystal system, Bravais-Miller indices can be utilized instead of the more common Miller indices as the notation system. In the former, $h$, $k$ and $l$ are identical to the corresponding Miller indices and $i = -(h+k)$ [237, p.133].

[4] 5 mm · 5 mm, absent of AlN layer.

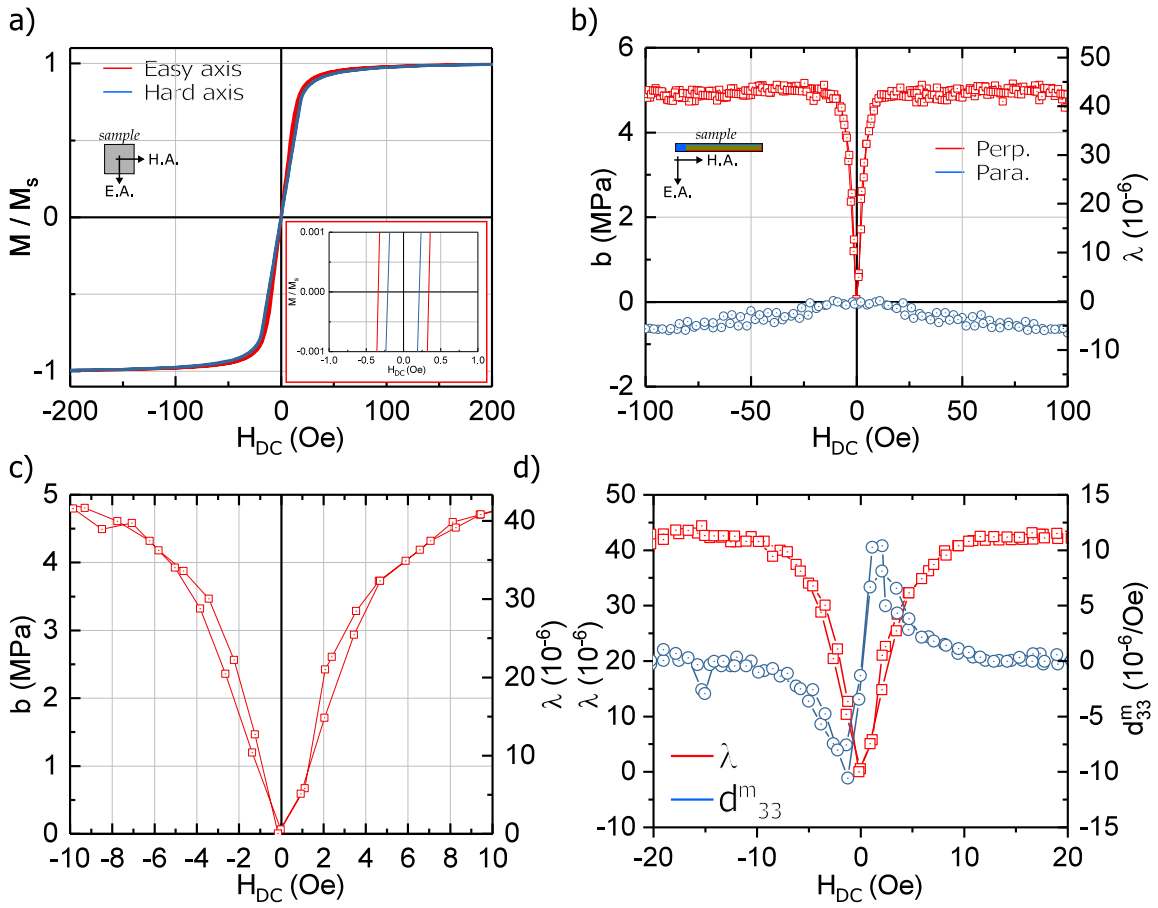


***Figure 4.17:*** *Magnetic characterization of an inverse-bilayer magnetoelectric composite stack after magnetic annealing. a) Magnetization properties of a square shaped, single layer and 3 µm thick FeCoSiB sample. Measurement curves along the magnetically easy and hard axis are plotted in red and blue, respectively. The inset shows the coercive magnetic field for both curves. b) Magnetoelastic coefficient (b) of a 3 µm thick FeCoSiB layer deposited on a Si cantilever with the dimensions of 2.2 mm · 25.2 mm · 0.3 mm. Measurements completed with an external magnetic field applied once parallel and once perpendicular to the sample's easy axis are plotted in blue and red, respectively. Secondary y-axis shows the calculated magnetostriction. c) Close-up to the highest slope region. d) Plot depicting the piezomagnetic coefficient, derived from the magnetostriction curve.*

to the saturation magnetization. Magnetization exhibits near hysteresis-free behavior along both directions. As seen from the inset, FeCoSiB layer has extremely small coercive fields that is as low as 0.2 Oe and 0.3 Oe along the hard and easy axis magnetization, respectively. The coercive field ($H_c$) is higher for the easy axis magnetization since in this configuration, every second domain is oriented opposite to the external magnetic field direction compared to the hard axis magnetization where all domains are approximately perpendicular. Hence in the former case, the energy necessary for the domain rotation is higher in comparison to the latter.

***Magnetostrictive Properties***: Figure 4.17b depicts the magnetoelastic coupling coefficient ($b$) of a 3 µm thick FeCoSiB layer deposited on a 300 µm thick Si cantilever with the dimensions of 2.2 mm · 25.2 mm. The hard and easy magnetization directions are along the length and the width of the cantilever, respectively. A positive magnetostriction is observed when the magnetic field is applied perpendicular to the magnetically easy axis of the sample (red curve). In this case, all dipoles rotate 90° in order to align with the external field and as a result FeCoSiB tries to expand. A maximum $b$ value of 5 MPa is recorded at the magnetic saturation. The direction of the magnetostriction is reversed when the magnetic field is applied along the magnetically easy axis of the sample (blue curve). Here, FeCoSiB layer tries to shrink and a negative $b$ value of approximately $-0.6$ MPa is measured. Note that in an ideal case, where the magnetic anisotropy is perfectly induced, the magnetostriction should be zero when measured along the easy direction. Since this is not the case here, it can be suggested that there is still room for improvement concerning the magnetic optimization of the deposited films (see Section 3.2.3).

The second $y$-axis in Figure 4.17b depicts the magnetostriction value of the FeCoSiB film derived using Equation (2.22). Accordingly, the saturation magnetostriction ($\lambda_s$) is obtained as

$$|\lambda_s| = (\frac{1+\nu_f}{E_f}) \cdot 5\,\text{MPa} = 43 \cdot 10^{-6} \tag{4.5}$$

where, the Young's modulus and the Poisson's ratio of FeCoSiB are assumed as $E_f = 150$ GPa[1] and $\vartheta_f = 0.3$, respectively.

Figure 4.17c shows a close-up to the highest slope region of the magnetostriction curve (at $H_{DC} \sim 2$ Oe). A very small hysteresis is observed reflecting the soft magnetic nature of the FeCoSiB.

Finally, the piezomagnetic coefficient is derived from the magnetostriction curve as seen in Figure 4.17d. The highest value reaches $d_{33}^m = 10.4 \cdot 10^{-6}/\text{Oe}$. This value exceeds previously given state-of-the-art magnetostrictive materials used in magnetoelastic composites (see Table 2.3). In particular, obtained piezomagnetic coefficient is approximately 40% higher than of FeGaB. However, since the Young's modulus of FeCoSiB is not experimentally confirmed, it is not possible to suggest a definite superiority at this point.

[1] Young's modulus of FeCoSiB is taken as an average value, since literature sources present different values; $E_f$ = 100 GPa in [72] and 176 GPa in [123].

***Magnetoelectric Properties***: All magnetoelectric properties described in Section 3.3.5 are presented in this section. A constant external bias field of $\mu_0 \cdot H_{DC} = \pm 1.6\,\text{Oe}$ and a driving AC field of $\mu_0 \cdot H_{AC} = 1 \cdot 10^{-3}\,\text{Oe}$ was used for the measurements. First of all, the frequency dependence of the measured magnetoelectric output voltage ($V_{ME}$) is characterized across a wide frequency range (see Figure 4.18a). The resonance frequency of the cantilever sensor is estimated as 837 Hz using Equation (2.38), where the dimensionless parameter $\lambda$ is taken as 1.875 for the first-bending vibrational mode [115]. Free-standing length of the cantilever is determined as 22 mm. Furthermore, the Young's modulus and the Poisson's ratio of Si are taken as $E_s = 169\,\text{GPa}$ and $\nu_s = 0.064$, respectively [207]. The material density and individual film thickness values are summarized in Table 4.4. The estimated value of 837 Hz is in good agreement with the measured value of ∼868 Hz, nevertheless there is a deviation as high as 3%. This deviation might originate from the non-perfect clamping of the cantilever via a bonding agent, as well as non-precise determination of the free-standing cantilever length. Note that a $\pm 0.1$ mm change of the latter, shifts the resonance frequency as much as $\pm 7.6$ Hz. Another possible reason for the observed deviation can be the substrate thickness, which might show variations for every single wafer.

***Table 4.4:*** *Material parameters used for the determination of the resonance frequency of a magnetoelectric cantilever sensor.*

| Material | Thickness (µm) | Density ($\text{g/cm}^3$) | Ref. |
|---|---|---|---|
| Si | 300 | 2.3 | [238] |
| $SiO_2$ | 1.5 | 2.2 | [239] |
| Ta | 0.03 | 15.6 | [240] |
| FeCoSiB | 3 | 7.25 | [72] |
| Pt | 0.14 | 21.44 | [238] |
| AlN | 1.6 | 3.2 | [241] |

In addition to the sensor output ($V_{ME}$) with respect to the AC magnetic field frequency, the secondary *y*-axis in Figure 4.18a depicts the sensor sensitivity ($\alpha_{ME}$) that is normalized with respect to the external field and the film thickness of the piezoelectric layer (see Equation (3.29)). Accordingly, $\alpha_{ME}$ is calculated as $3\,\text{V}/(\text{cm}\cdot\text{Oe})$ at 10 Hz. The drastic decrease of the voltage output at low frequencies (1 Hz – 100 Hz) was previously demonstrated [72]. When operating at the mechanical resonance frequency of the sensor, on the other hand, it is enhanced approximately 3 orders of magnitude and reaches $4.9\,\text{kV}/(\text{cm}\cdot\text{Oe})$ (see the inset). As discussed in Section 2.3.4, the magnitude response of a damped mechanical oscillator scales with the quality factor of the cantilever material. However, observed enhancement is 5 times higher than the expected value. Additional signal enhancing contributions, such as a superior coupling factor between the piezoelectric and magnetostrictive phases might

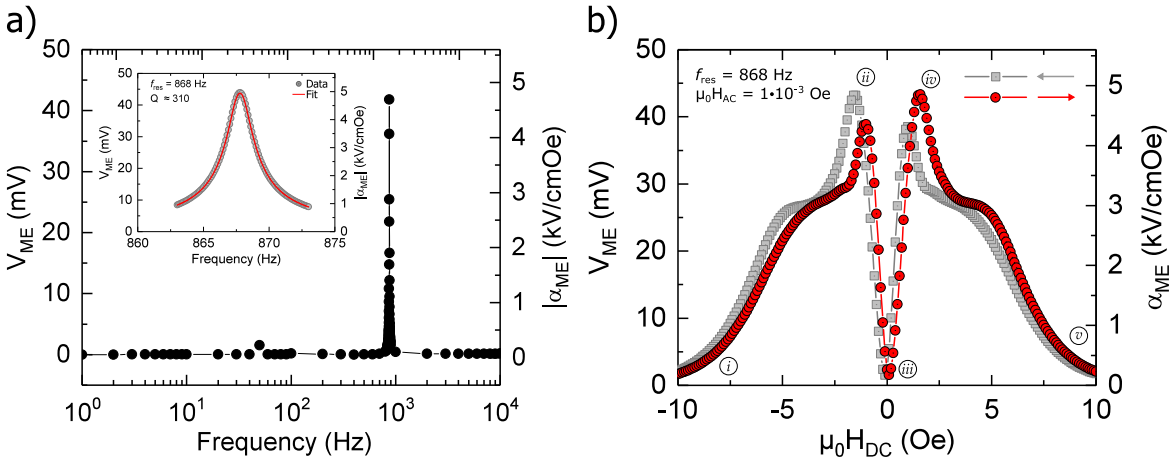


***Figure 4.18:*** *Magnetoelectric voltage output of an inverse-bilayer sensor a) in dependence of the mechanical resonance frequency. The inset depicts a close-up to the resonance frequency. The voltage output is measured at every +0.01 Hz between 863 Hz and 873 Hz. The resonance frequency is determined as 867.78 Hz, as exact value. Due to the very high number of data points, 10 data points are skipped between each plotted consecutive data points. b) Magnetoelectric voltage output at the resonance frequency and in dependence of the external bias field. External DC field is increased by 0.1 Oe between consecutive measurement points. Optimal working point is determined as* $\mu_0 \cdot H_{DC} = \pm$ *1.6 Oe.*

be responsible of the observed discrepancy. However it is not possible to give a definite explanation at this point, since no further investigations were conducted.

Figure 4.18b depicts the dependency of the sensor sensitivity on the external bias field $\mu_0 \cdot H_{DC}$. In this measurement, the external magnetic field direction is inverted by 180° between a negative and a positive maximum field magnitude. Accordingly, the red and grey curves are recorded along the measurement directions $-H_{max} \rightarrow H_{max}$ and $H_{max} \rightarrow -H_{max}$, respectively. The sensor sensitivity reaches to $4.9\,\mathrm{kV/(cm \cdot Oe)}$ at $\mu_0 \cdot H_{DC} = \pm 1.6\,\mathrm{Oe}$ and at the mechanical resonance frequency. This field magnitude coincides with the field magnitude at which the magnetostriction curve of FeCoSiB exhibits the highest slope.

Another important property of the magnetoelectric sensors is their hysteretic behavior in response to external magnetic field. Despite the extremely small hysteresis of the magnetostriction curve, magnetoelectric bias curve contains a much bigger hysteresis. Reducing the external magnetic field from its negative saturation ($-H_{max} \rightarrow H_{max}$) for instance, the curve first depicts a shoulder around $-3.5\,\mathrm{Oe}$ and reaches a maximum at $-1\,\mathrm{Oe}$. After reversing the magnetization direction, however, a secondary and even higher peak is observed at $1.6\,\mathrm{Oe}$. Further increase of the field results in a secondary shoulder at $4.5\,\mathrm{Oe}$, which is steeper than the initial one. Once the sample is saturated and the field is reversed, the same process is observed once again. First, a shoulder is seen at $3.5\,\mathrm{Oe}$ and then a maximum is

reached at 1 Oe. Upon crossing the zero field and the magnetization reversal occurs, the high peak at $-1.6$ Oe is reached. Further increase of the field produces the second shoulder at $-4.5$ Oe. The reason for the observed behavior during magnetization reversal was attributed to the presence of the so-called blocked and wide domain states [242].

***Discussion***

According to Figure 4.18b, reducing the magnetization below the saturation point (*i*) initially creates a difference in the domain structure of the sample; low angle domains form in the center but the edge regions stay at saturation. FeCoSiB exhibits a low permeability in these magnetic fields. Further decrease of the magnetic field only results in coarsening of the central domains but the edge regions continue to stay in the saturated state. This structure is defined as the blocked domain state. As the external field continues to decrease, there comes a point (*ii*) where the domains snap out of the blocked state in an instant and form the wide domain state. The edge areas stay magnetically saturated and the closure domains stretch along the center of the sample towards the edges. The transition area between the two magnetic regions depict continuously shrinking spike-shaped domains as the sample is brought to zero magnetic field conditions (*iii*). With the reversal of the magnetic field direction, the magnetization direction in the edge regions rotate by 180°. As the magnetic field increases, the spike-shaped domains start to grow and the highest magnetoelectric response is observed as a result of the high permeability of the wide domain state (*iv*). Finally, wide domains continuously shrink as the sample is brought closer to its saturated state (*v*). Note that the reason for the shoulder formation is unclear since initial measurements of the sample did not produce such curves. However after several hundreds of magnetization/demagnetization cycles these shoulders formed and remained. This behavior can be related to a temporary permeability drop in the FeCoSiB, however in-depth investigations were not conducted.

***Noise and LOD Properties***: Figure 4.19a depicts the noise characteristics of the investigated sensor under a bias field of $\mu_0 \cdot H_{DC} = 1.6$ Oe. The single measurement and the modeled noise[1] are plotted in blue and red, respectively. The grey curve represents the averaged noise obtained through repetitive measurements[2]. In addition to the increased noise at the resonance frequency, additional peaks originating from the parasitic power line contributions are observed at 50 Hz, 150 Hz and 250 Hz. The resonance frequency of the cantilever is within the frequency range, where the Johnson-Nyquist noise ($E_{ME}$) of the piezoelectric phase dominates. A close-up around the resonance frequency is shown in Figure 4.19b.

[1] According the the initial noise model.

[2] Measurement repeated 89 times, standard deviation is not represented here but in Figure 4.19b.

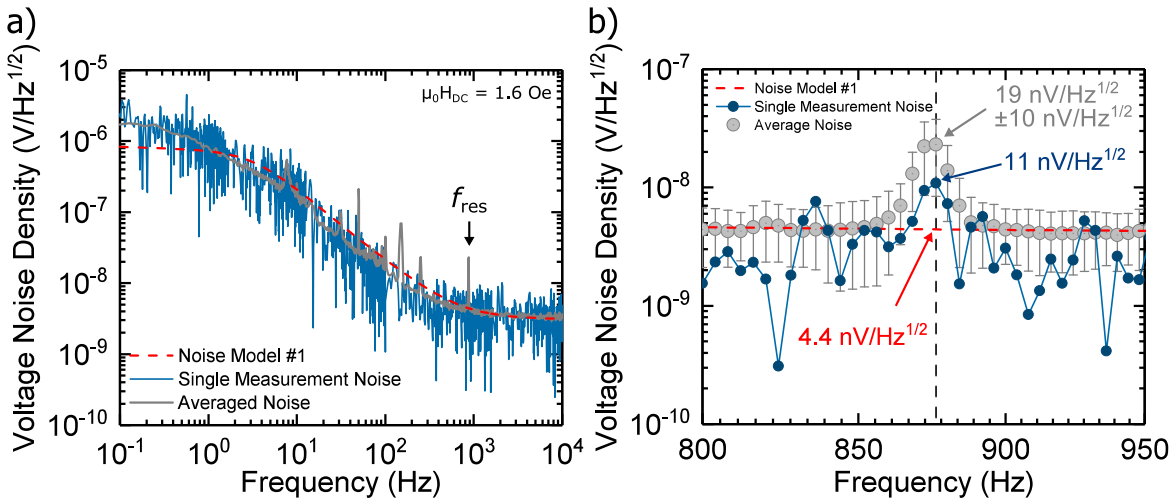


***Figure 4.19:*** *a) The dependency of the voltage noise density of an inverse-bilayer magnetoelectric sensor (blue curve) on the frequency. Modeled noise curve of the detection unit is shown in red. The black arrow shows the resonance peak. Grey curve represents the mean average of 89 measurements. b) A close-up to near the mechanical resonance frequency of the sensor. Consecutive data points are separated by 4 Hz. Voltage noise density at the resonance frequency is 4.4 nV/Hz$^{1/2}$ and 11 nV/Hz$^{1/2}$ for the noise model and the single measurement, respectively. Noise from the averaged curve is calculated as 19 nV/Hz$^{1/2}$ ± 10 nV/Hz$^{1/2}$.*

The modeled noise depicts a lower noise level than the actual measurement and averaged values. Accordingly, a noise voltage density ($E_{co}$) as low as $4.4\,\mathrm{nV/Hz^{1/2}}$ is predicted at $f_{res} = 868\,\mathrm{Hz}$[1]. The actual measurement value at the output of the charge amplifier, however, is 2.5 times higher reaching a minimum of $11\,\mathrm{nV/Hz^{1/2}}$ under the same conditions. Finally, the averaged noise is calculated as $19\,\mathrm{nV/Hz^{1/2}} \pm 10\,\mathrm{nV/Hz^{1/2}}$.

It is, at this point, possible to estimate the LOD of the investigated sensor by replacing the previously determined sensor sensitivity $\alpha_{ME} = 4.9\,\mathrm{kV/(cm \cdot Oe)}$ and the $E_{co}$ values in Equation (3.26). Accordingly, the LOD values are predicted as

$$LOD_{Modeled} = \frac{4.4\,\mathrm{nV/Hz^{1/2}}}{4.9\,\mathrm{kV/(cm \cdot Oe)} \cdot 1.6\,\mu\mathrm{m}} = 570\,\mathrm{fT/Hz^{1/2}} \tag{4.6}$$

$$LOD_{Measured} = \frac{11\,\mathrm{nV/Hz^{1/2}}}{4.9\,\mathrm{kV/(cm \cdot Oe)} \cdot 1.6\,\mu\mathrm{m}} = 1.4\,\mathrm{pT/Hz^{1/2}} \tag{4.7}$$

[1] After the gain factor is removed.

$$LOD_{Averaged} = \frac{19\,\mathrm{nV/Hz^{1/2}} \pm 10\,\mathrm{nV/Hz^{1/2}}}{4.9\,\mathrm{kV/(cm \cdot Oe)} \cdot 1.6\,\mu\mathrm{m}} = 2.4\,\mathrm{pT/Hz^{1/2}} \pm 1.3\,\mathrm{pT/Hz^{1/2}} \tag{4.8}$$

from the modeled, single measured and averaged noise densities, respectively.

Figure 4.20 depicts the LOD measurement of the inverse-bilayer sensor completed with a signal analyzer (*a*) and a lock-in amplifier (*b*), respectively. The red straight lines represent the linear fit applied to the output voltage in both cases. The dashed lines show the averaged noise level for the measurements. Finally, the minimum detectable AC magnetic field in each measurement can be determined at the intersection point of the averaged noise level and the linear fit. Note that below this point, where SNR = 1, observed output voltage values exhibit a random distribution and do no longer represent the actual sensor signal. Minimum detectable $\mu_0 \cdot H_{AC}$ values are determined as 1.4 pT and 670 fT for the the signal analyzer and the lock-in amplifier measurements, respectively. Here, even though identical output voltage values are obtained from both devices when operating at SNR $> 1$, the averaged noise differ when SNR $< 1$. It can be observed from Figure 4.20 that the averaged noise levels of the signal analyzer and the lock-in amplifier equal 27 nV and 13 nV, respectively. This difference originates from the different equivalent noise band width[1] of the measurements devices as discussed in Section 3.3.5. Therefore, this difference must be taken into consideration when

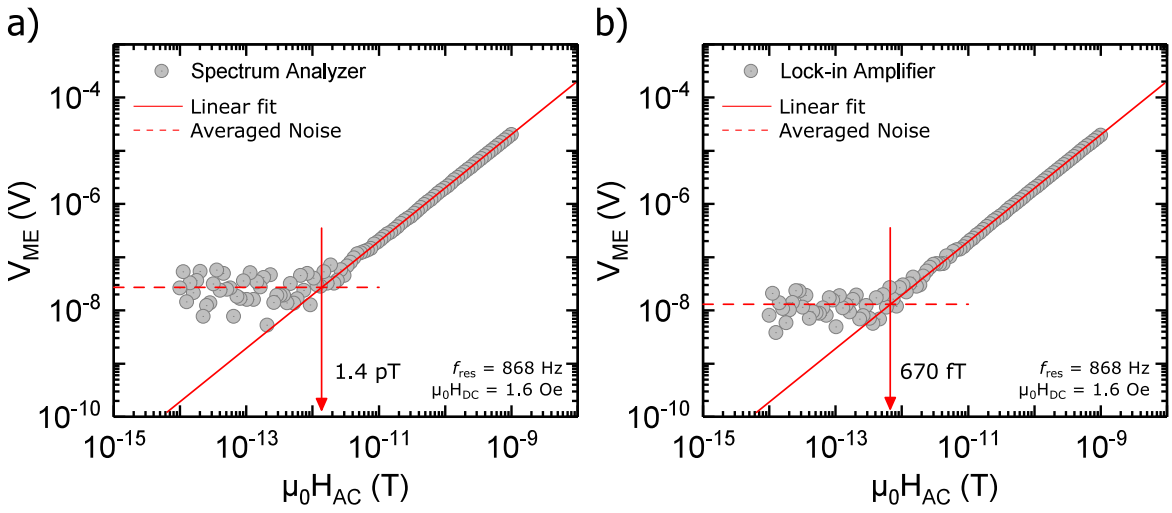


***Figure 4.20:*** *The minimum detectable magnetic field by an inverse-bilayer sensor when measuring with a) a spectrum analyzer and b) a lock-in amplifier. The red straight lines represent the linear fits applied to the output signal. The dashed lines represent the averaged noise. The arrows depict the minimum detectable field.*

[1] ENBW=1 Hz for the signal analyzer and 78 mHz for the lock-in amplifier.

comparing the results obtained through these two devices with each other.

Accordingly, the LOD of the measured sensors are determined as

$$LOD_{SA} = \frac{1.4\,\mathrm{pT}}{\sqrt{1\,\mathrm{Hz}}} = 1.4\,\mathrm{pT/Hz^{1/2}} \tag{4.9}$$

$$LOD_{LI} = \frac{670\,\mathrm{fT}}{\sqrt{78\,\mathrm{mHz}}} = 2.4\,\mathrm{pT/Hz^{1/2}} \tag{4.10}$$

from the spectrum analyzer and the lock-in amplifier measurements, respectively.

***Discussion***

Comparing the predicted and measured LOD values, it is clear that the utilized model fails at successfully predicting the LOD of a resonant sensor [196]. The noise model predicts a much lower LOD value than the actual measurements. This is due to the fact that the model does not include the resonant effects on the total noise such as the increased dielectric losses. Predictions based on the single and averaged noise voltage density values, however, are successful at estimating the LOD of the sensor.

An important factor to take into account is the reliability of the noise measurements. The large deviation of the averaged curve seen in Figure 4.19b suggests that the LOD prediction based on a single noise measurement might be misleading. In fact, the total noise of a sensor includes several components (see Equation (3.27)) and is susceptible to acoustic vibrations from environmental noise sources, as well. In order to confirm this influence, additional acoustic measurements were conducted[1].

Figure 4.21 depicts the noise characterization of an inverse-bilayer magnetoelectric sensor[2] completed alongside a piezoelectric (AlN) sensor[3]. The sensors are characterized when placed in a mu-metal box and in a shielded environment. The noise spectrum recorded in a silent environment is shown in Figure 4.21a. Parasitic contributions from the electric lines are observed at 50 Hz and its multiples. The noise increase at the respective resonance frequencies is clearly observed from the close up given in Figure 4.21b). Both sensors have a maximum noise density as high as $26\,\mathrm{nV/Hz^{1/2}}$. This value is in good agreement with the

[1] Noise characterization is completed by M.Sc. Jens Reermann from the chair for Digital Signal Processing and System Theory (Prof. Dr.-Ing. Gerhard Schmidt) of the Kiel University.

[2] $C_{ME} = 556\,\mathrm{pF}$, $H_{AC} = 1 \cdot 10^{-3}\,\mathrm{Oe}$ and $H_{DC} = 2.1\,\mathrm{Oe}$.

[3] $C_{ME} = 1.5\,\mathrm{nF}$.

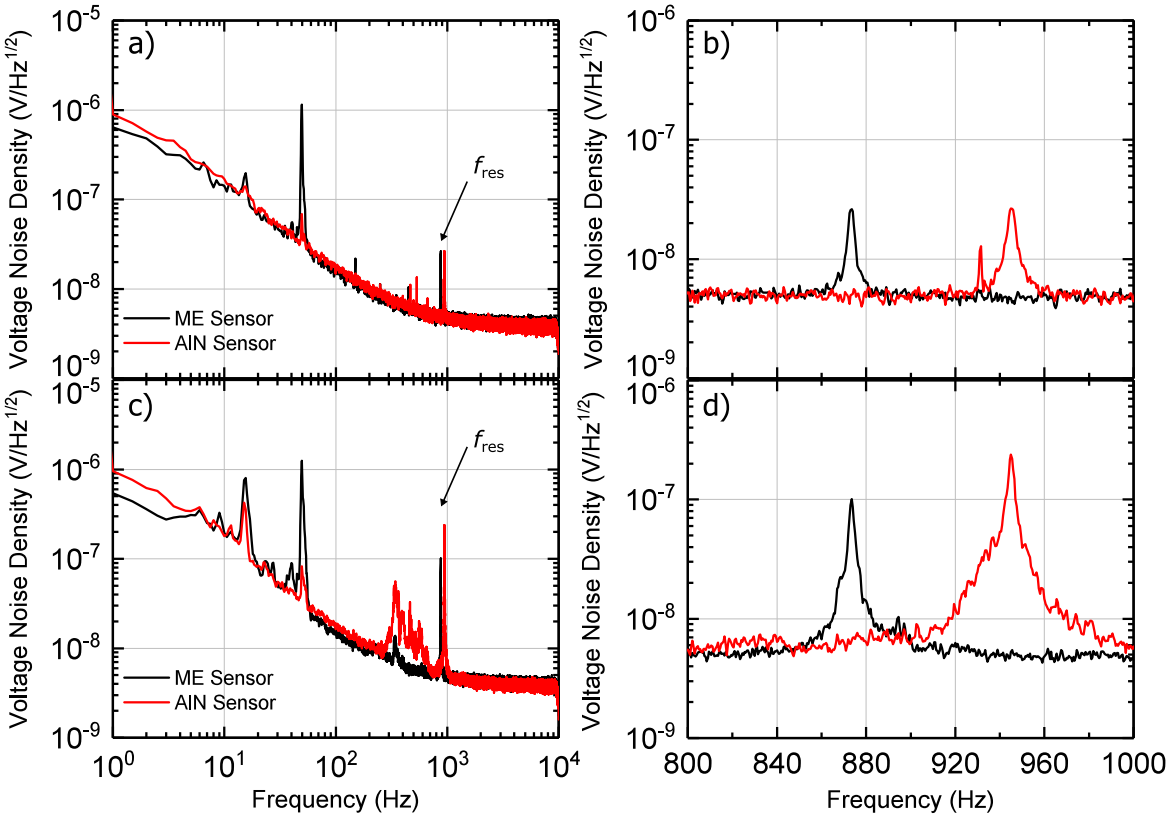


***Figure 4.21:*** *Influence of external noise sources on the magnetoelectric and piezoelectric sensor noise. a) Measurements completed at a silent environment. b) Close up near the sensors' resonance frequencies, which depict identical noise levels. c) Measurements completed at a noisy environment. d) Close up near the sensors' resonance frequencies, which depict increased noise levels.*

averaged magnetic noise measurement (see Figure 4.19). Coupling of the external vibrations increases the noise spectrum of the sensors, as can be seen from Figure 4.21c. Their influence can be better assessed from the close up plot of a noisy environment (see Figure 4.21d). Here, both the magnetoelectric and the piezoelectric noise increase up to $100\,\mathrm{nV/Hz^{1/2}}$ and $240\,\mathrm{nV/Hz^{1/2}}$, respectively. The increase of the noise density is as high as factor 4 and 9 for magnetoelectric and piezoelectric sensors, respectively. Such high increase of the noise density would diminish the SNR, hence deteriorate the sensor properties, especially when operating at low resonance frequencies.

Clearly, it is a high possibility that different noise levels are observed from a single sensor over numerous measurements depending on the environmental noise at the moment of sensor characterization. Despite the fact that the measurement setup is acoustically shielded, the level of shielding proves insufficient. Urban noise is almost always present to a some extent, depending on the time of the day. Therefore, it is more reasonable to adopt a statistical approach and repeat noise measurements in order to receive an average noise density

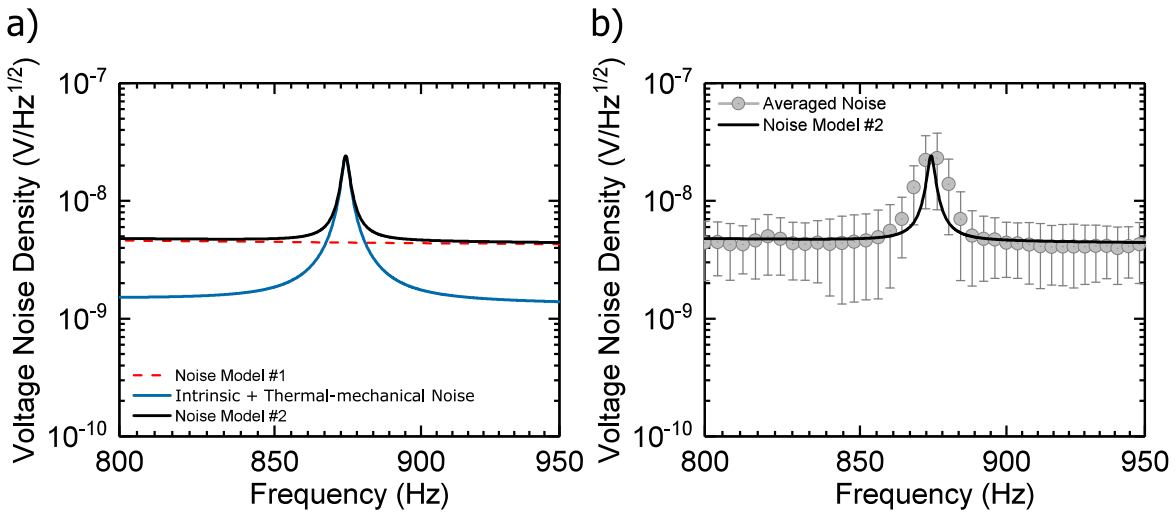


***Figure 4.22:*** *Comparison of noise models. a) Comparison of the initial noise model (dashed line) to the intrinsic sensor noise, which includes the thermal-mechanical noise at the resonance (blue) and the total noise at the amplifier's output. Base noise increases half-an-order of magnitude due to the extra noise of the amplifier. At the resonance frequency, dielectric losses dominate and increase the voltage noise density approximately an order of magnitude. b) Comparison between the model noise and average noise voltage density measurement previously presented in Figure 4.19b. The model succesfully predicts the mean value of the averaged noise but fails at the estimation of the deviation.*

rather than a single measurement value. To that end, the second model, which takes the thermal-mechanical noise into consideration, was utilized. Accordingly, Figure 4.22a depicts the noise density modeled for the above discussed sensor. Here, the piezoelectric noise of AlN in addition to the thermal-mechanical noise and the total noise, which represents the behavior of the whole detection unit[1], are shown in blue and black curves, respectively. Furthermore, the first noise model is plotted (red curve) for comparison purposes, as well. Note that the difference in the noise density between the out-of-resonance values of the piezoelectric layer ($1-2\,\mathrm{nV/Hz^{1/2}}$) and the total noise ($5\,\mathrm{nV/Hz^{1/2}}$) is due to the charge amplifier's influence. Figure 4.22b compares the secondary noise model (black line) to the averaged noise of the sensor. Here the noise model predicts the mean value of the averaged noise curve in a consistent manner, but fails at predicting the deviation. Nevertheless, it is a more accurate estimation of the sensor noise in comparison to the previous model and was henceforth utilized in the remainder of the characterizations/calculations presented in this work.

A similar approach is beneficial for the determination of the minimum detectable field as well. Figure 4.23 compares a single LOD measurement to an averaged one[2]. Given single measurement belongs to the same sample as seen in Figure 4.20b. It depicts a linear rela-

[1]Note that the total noise includes the first amplifier input from the AD 745 charge amplifier.
[2]Measurement repeated 16 times, standard deviation is represented by the error bar.

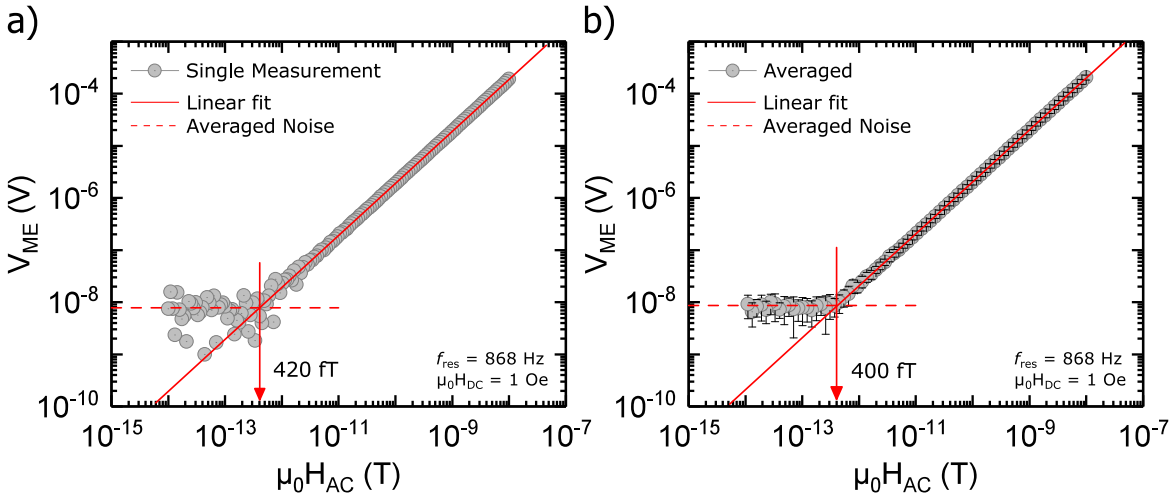


***Figure 4.23:*** *Comparison between a) singular and b) averaged LOD measurements of a single sensor obtained with the lock-in amplifier and a ENBW of 78 mHz.*

tionship between the output signal and the decreasing AC field until 7 pT. The data points begin to deviate from the applied linear fit for lower AC fields, as the SNR approaches to 1. Consecutive data point recorded at 780 fT and 710 fT, for instance, show $V_{ME}$ values of 27 nV and 42 nV, respectively. Especially below SNR = 1, the recorded output voltage values exhibit complete randomness. When numerous measurements are averaged, however, a much consistent plot is obtained. Even though the minimum detectable field is almost identical for both curves; i.e., 420 fT and 400 fT, the averaged plot shown in Figure 4.23b depicts a very clear separation between the linear region and the noise floor. The minimum detectable field is precisely observed and the LOD of the sensor can be calculated as

$$LOD_{Averaged} = \frac{400\,\mathrm{fT}}{\sqrt{78\,\mathrm{mHz}}} = 1.4\,\mathrm{pT/Hz^{1/2}} \tag{4.11}$$

from the averaged measurements. This value is well within the LOD range that is estimated using the averaged noise voltage density.

### *Application Range*

Full application range and the sensor performance is summarized in Figure 4.24. Here, individual LOD measurements[1] at certain frequencies are shown in order to emphasize the change in the signal and noise contributors. In the second and third plots, additional to the sensor's averaged voltage noise density (red curve) and sensitivity (black curve), its resolu-

[1]Measurements done using a lock-in amplifier with ENBW = 78 mHz.

tion (blue curve) is summarized over a wide frequency range as well. The summarized plot contains 40 individual LOD measurements completed at various frequencies (blue circles) in order to assess the usable frequency range of the sensor.

Dominant noise regimes over a large frequency range were previously defined by *Jahns et al.* [117]. It is possible to observe these noise regimes and how they affect the sensor from the averaged noise curve seen in Figure 4.24b.

- Accordingly, in the low frequency range ($f = 1\,\mathrm{Hz} - 100\,\mathrm{Hz}$) the current noise dominates the total noise behavior of the sensor and scales with respect to the reciprocal of the frequency ($1/f$). Due to the non-resonant operation, a limited charge generation is achieved and an $\alpha_{ME}$ value of $1.5\,\mathrm{V/(cm \cdot Oe)}$ and a minimum detectable field of $55\,\mathrm{nT}$ is obtained at $f = 1\,\mathrm{Hz}$. When operating at $f = 10\,\mathrm{Hz}$, $\alpha_{ME}$ improves up to $3\,\mathrm{V/(cm \cdot Oe)}$ and the minimum detectable field decreases down to $7\,\mathrm{nT}$.

- In the medium frequency range ($f = 100\,\mathrm{Hz} - 1000\,\mathrm{Hz}$), the piezoelectric noise of the sensor dominates. In this region, AlN benefits greatly from its much lower dielectric losses compared to other piezoelectric materials. $\alpha_{ME}$ values range from $10\,\mathrm{V/(cm \cdot Oe)}$ at $200\,\mathrm{Hz}$ up to $50\,\mathrm{V/(cm \cdot Oe)}$ at $1\,\mathrm{kHz}$. The minimum detectable field by the sensor ranges between $\mathrm{nT} - \mathrm{pT}$ range. At the resonance frequency (see Figure 4.24c), all sensor properties are enhanced; $\alpha_{ME}$ reaches $\sim 5\,\mathrm{kV/(cm \cdot Oe)}$ and the minimum detectable field goes down to $400\,\mathrm{fT}$ despite the increase of the total noise. Note that the observed resonance behavior is in good agreement with Equation (3.26) and Equation (3.28).

- At higher frequencies ($f > 1\,\mathrm{kHz}$), the voltage noise of the amplifier dominates the total noise behavior and a constant noise varying between $3\,\mathrm{nV/Hz^{1/2}} - 4\,\mathrm{nV/Hz^{1/2}}$ is observed. With $\alpha_{ME}$ values ranging between $10\,\mathrm{V/(cm \cdot Oe)} - 20\,\mathrm{V/(cm \cdot Oe)}$, this restricts the minimum detectable field to a minimum of $1\,\mathrm{pT} - 2\,\mathrm{pT}$.

In summary, it was observed that single noise density and LOD measurements are susceptible to external noise sources and contain a wide deviation range. Both measurements produce different results when repeated at different times of the day. Therefore it is misleading to utilize single measurements for the characterization of the fabricated sensors. In order to address this problem, numerous measurements shall be completed for each investigated sensor and statistical results shall be derived.

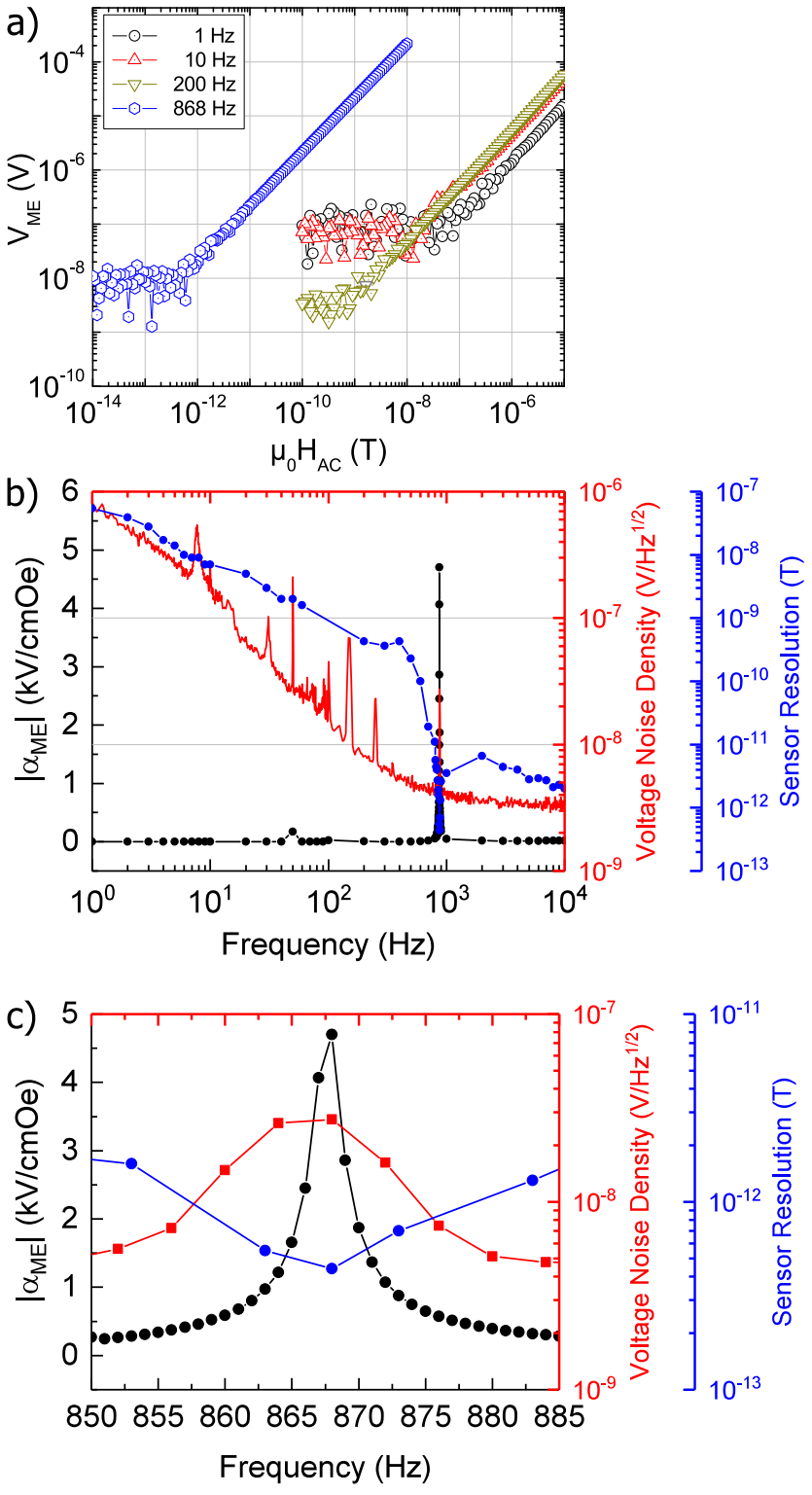


***Figure 4.24:*** *a) The evolution of LOD with respect to the measurement frequency. b) Full application range and the performance of inverse-bilayer sensor. Sensor sensitivity, resolution and averaged noise voltage density is depicted with respect to the frequency. c) A close-up around the resonance frequency of the sensor and consequent improvement of sensor properties when operating at the mechanical resonance frequency.*

Accordingly, the full application range of an inverse-bilayer resonant sensor was investigated. It was observed that the detection limit of the sensor scales in accordance with the sensor sensitivity ($\alpha_{ME}$) and the total noise at the output of the detection unit ($E_{CO}$). At $f = \pm 10\% \cdot f_{res}$, the output signal ($V_{ME}$) was greatly reduced and the noise levels were high.

At the actual resonance frequency, resonant bilayer sensor was able to detect AC magnetic fields as low as 400 fT at room temperature and by using a lock-in amplifier. This value corresponds to the lowest detected magnetic field ever reported for a thin film resonant magnetoelectric sensor. Furthermore, the sensor successfully detected magnetic fields ranging between nT and pT when operating out-of-resonance. Note that the latter was only confirmed for frequencies between 800 Hz and 10 kHz.

### 4.2.2 Influence of the Top Electrode Dimensions

Previously discussed properties of the inverse-bilayer sensors result from the combination of several factors. These include not only an improved piezoelectric contribution due to AlN but also the use of an optimized top electrode area, which allows the concentration of optimal charge generating areas within the electrode area rather than spreading it along the full length of the top electrode. In this section, the influence of the top electrode dimensions are discussed, results of the FEM model and actual sensor measurements are compared.

Figure 4.25a depicts the relationship between calculated $\alpha_{ME_{SC}}$ coefficients and the electrode length. As shown in the red curve, $\alpha_{ME_{SC}}$ increases linearly as the electrode length diminishes, reaching a maximum as the electrode length reaches a minimum. This behavior can be explained by the cantilever displacement along $x$– and $z$– axes as seen in Figure 4.25b. Here, the magnetic field applied onto the sample is considered as a force, which is acting on the tip of the cantilever and bending/displacing it along the $z$–axis. Starting from the clamping point of the cantilever up to a 5 mm, a very high bending of the cantilever is observed. The remaining length of the cantilever does not bend at all but simply displaces, hence can not contribute to the charge generation. Hence a much higher voltage generation can be expected from this area [118].

In order to estimate the LOD of the magnetoelectric sensors, intrinsic noise sources and the noise related to the AD 745 charge amplifier are taken into consideration (see Equation (3.27)) [196]. For the calculations, a dissipation factor of $\tan\delta = 0.082\%$ and AlN permittivity of $\varepsilon = 9$ is taken. The resistance, capacitance and the dissipation factor of the

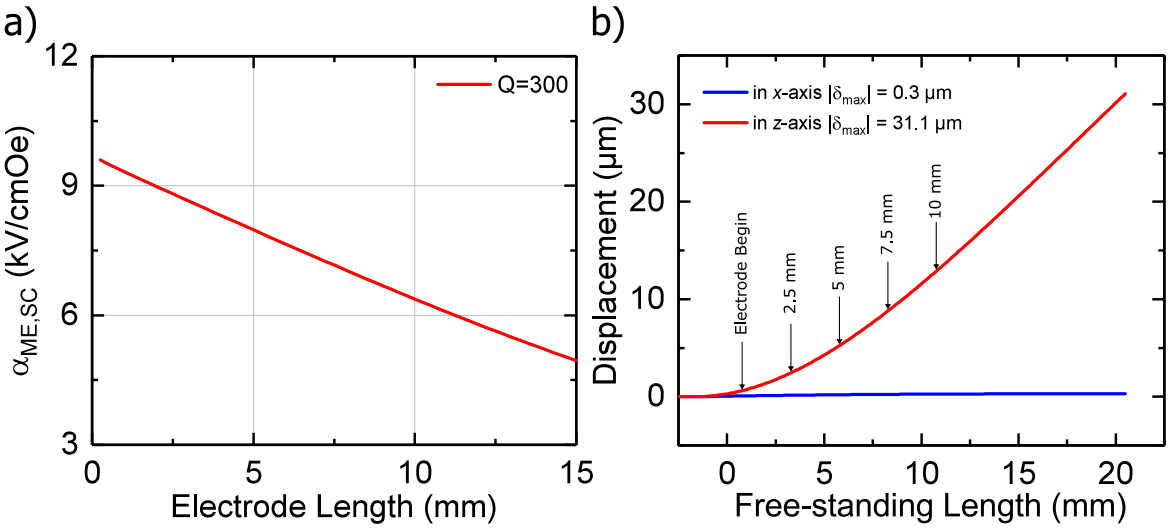


***Figure 4.25:*** *a) Modeled $\alpha_{ME_{SC}}$ as a function of the electrode length and b) the bending of a one-end-fixed cantilever sensor. Arrows mark the extend of individual electrode lengths with respect to the free-standing length of the cantilever. $\delta$ is the bending. For all modeling, $Q$ = 300.*

wiring are considered as $R_c = 100\,\mathrm{M\Omega}$, $C_c = 14\,\mathrm{pF}$ and $\tan\delta = 0.05\%$, respectively. Influence of the individual noise contributors and the evolution of the total noise with respect to the electrode length are summarized in Figure 4.26a. Here, $E_{OC,ME}$ is the sensor's intrinsic noise, $E_{OC,Ek}$ is the dielectric cable losses, $E_{OC,EN}$ is the amplifier's voltage noise, $E_{OC,IN}$ is the amplifier's current noise and $E_{OC,Ef}$ is the noise form the amplifier's feedback network and finally $E_{OC}$ is the total voltage noise density at the amplifier's output. The latter is dominated by the amplifier's current and voltage noise for decreasing and increasing electrode lengths, respectively. Accordingly, the estimated total noise density of an inverse-bilayer sensor increases as the electrode length of the sensor increases. However, the effect is not as large as it is for $\alpha_{ME_{SC}}$ (see Figure 4.25a).

Finally, it is possible to estimate the LOD of the sensors from magnetoelectric coefficient and the total noise voltage density calculations with respect to

$$LOD = \frac{G \cdot E_{OC}}{t_{PE} \cdot \alpha_{ME_{SC}}} \tag{4.12}$$

where, $G$ is the gain factor ($G = {}^{C_{ME}}/_{C_f}$) and scales with the sensor's capacitance, which is proportional to the top electrode area.

The resulting LOD is depicted in Figure 4.26b. Estimated LOD values show a distinct behavior unlike the other modeled parameters. The minimized signal gain at very small electrode

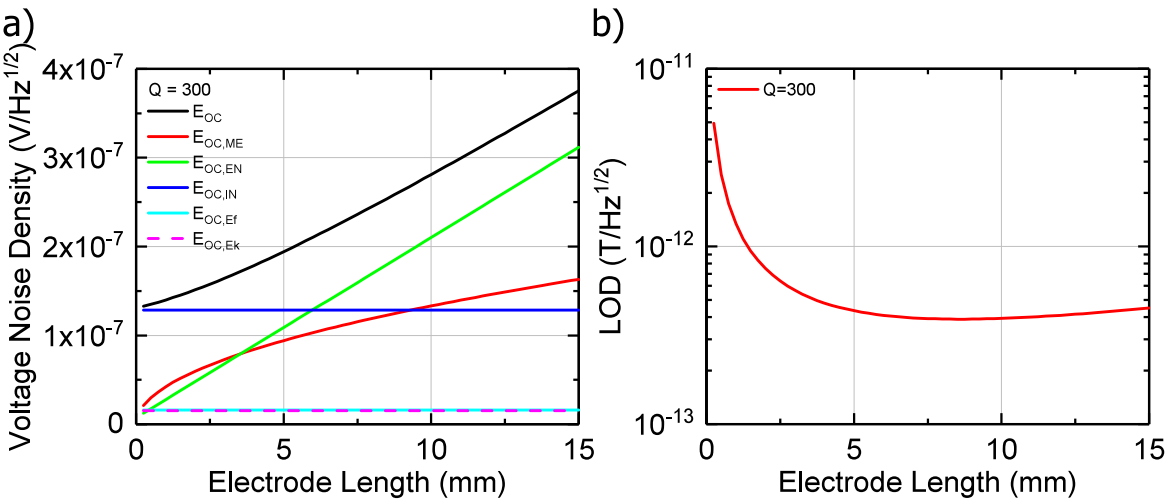


***Figure 4.26:*** *a) Calculated contributions of various noise sources on the total voltage noise density ($E_{OC}$) with respect to top electrode length. Gain factor is not extracted. b) Estimated LOD of the magnetoelectric sensor with respect to top electrode length.*

lengths greatly hinders the LOD of the sensor. On the other hand increased electrode length results in a much larger gain factor and a better LOD until a saturation point is reached. Accordingly, the sensor LOD reaches a minimum of $390\,\mathrm{fT/Hz^{1/2}}$ at 8 mm electrode length and then slightly deteriorates as the electrode length further increases.

### Sensor Characterization

Inverse-bilayer sensors are fabricated following the process flow described in Section 3.2. The deposited film stacks consist of 3 µm FeCoSiB, 140 nm Pt, 1.6 µm AlN and 100 nm Au on 300 µm thick Si substrates. The top electrode dimensions of the sensors are scaled using dedicated photolithography masks (see Appendix, Figure A.1). Accordingly, the electrode length is varied between 2.5 mm and 10 mm while keeping a constant width at 1.2 mm. At the end of the processing, cantilever sensors with $2.2\,\mu\mathrm{m} \cdot 25.2\,\mu\mathrm{m}$ dimensions are mounted on carrier PCBs and are characterized.

Table 4.5 summarizes the properties of fabricated inverse-bilayer sensors with varied electrode length. Here, measured $\alpha_{ME}$ values range between $4\,\mathrm{kV/(cm \cdot Oe)} - 5\,\mathrm{kV/(cm \cdot Oe)}$ with a maximum for the 7.5 mm sample, showing an incompatibility with the modeled $\alpha_{ME_{SC}}$ depicted in Figure 4.25a. All sensors have identical dielectric losses and the same working point, which is an indication of structural uniformity concerning AlN and FeCoSiB films, as well as similar magnetic properties for the latter. Therefore the inconsistency is attributed to the non-optimal bonding of the sensors on the PCBs. In fact, observed difference of the

***Table 4.5:*** *Overview of electrode length influence on the inverse-bilayer magnetoelectric sensor properties. Sample sensors are 2.2 µm · 25.2 µm sized cantilevers fabricated on 300 µm thick Si substrates with the following constituent thickness values; 3 µm FeCoSiB, 140 nm Pt, 1.6 µm AlN and 100 nm Au.*

| Property / Magnitude | Sample 1 | Sample 2 | Sample 3 | Sample 4 |
|---|---|---|---|---|
| Electrode length (mm) | 2.5 | 5 | 7.5 | 10 |
| $C_{ME}$ (pF) | 168 | 342 | 518 | 667 |
| $tan\delta$ (%) | 0.05 | 0.05 | 0.05 | 0.05 |
| $f_{res}$ (Hz) | 844 | 837 | 877 | 844 |
| Q-factor | 248 | 219 | 338 | 279 |
| Bias field (Oe) | -2.4 | -2.4 | -2.4 | -2.4 |
| $\alpha_{ME}@f_{res}$ (kV/(cm · Oe)) | 5.4 | 4.4 | 6.9 | 4.4 |
| Sensor resolution (pT) | 1.9 | 1.5 | 1.1 | 1.5 |
| LOD (pT/Hz$^{1/2}$) | 6.8 | 5.4 | 3.9 | 5.4 |

Capacitance and tan $\delta$ measurements are completed at 10 kHz. Noise measurements are repeated 100 times and averaged values are given in the table. For all measurements $\mu_0 \cdot H_{AC} = 1 \cdot 10^{-3}$ Oe, t = 1 s and the bandwidth = 1 Hz. Sensor resolution is measured by a lock-in amplifier and the LOD is estimated from the conducted measurements according to Equation (3.26).

sensor resonance frequencies suggest possible variations in the free-standing sensor length. Furthermore, a misalignment between the sensor and the PCB during mounting ($\neq 90°$) can be a potential reason for the different Q-factor magnitudes. This, in turn, might be a potential reason for different sensitivity values.

Figure 4.27 depicts the minimum detectable fields with respect to the decreasing AC magnetic field. Obtained values range between $1\,\text{pT} - 2\,\text{pT}$ and follow a similar behavior as the estimated model (see Figure 4.26b). It was shown in the previous chapter, that the noise voltage density of the sensors was dominated by the resonance effects. Hence it is not surprising to see very similar noise levels for all samples when operating at the resonance frequency. According to Equation (3.26), LOD of a given sensor improves with increasing $\alpha_{ME}$ and piezoelectric film thickness, as well as decreasing noise density. Since both the thickness and the noise density values are constant for all sensors, the improvement observed in the sensor resolution must be related to a higher $\alpha_{ME}$. However, all properties, which have an influence on $\alpha_{ME}$ (see Equation (3.30)) are kept constant as well. In fact, investigated sensors are always fabricated simultaneously, hence can not differ greatly from one and other in terms of piezoelectric, piezomagnetic and coupling coefficients. Here, the only difference among the compared sensors is the electrode length hence it can be suggested that the observed difference in the magnetoelectric properties originate directly from the electrode

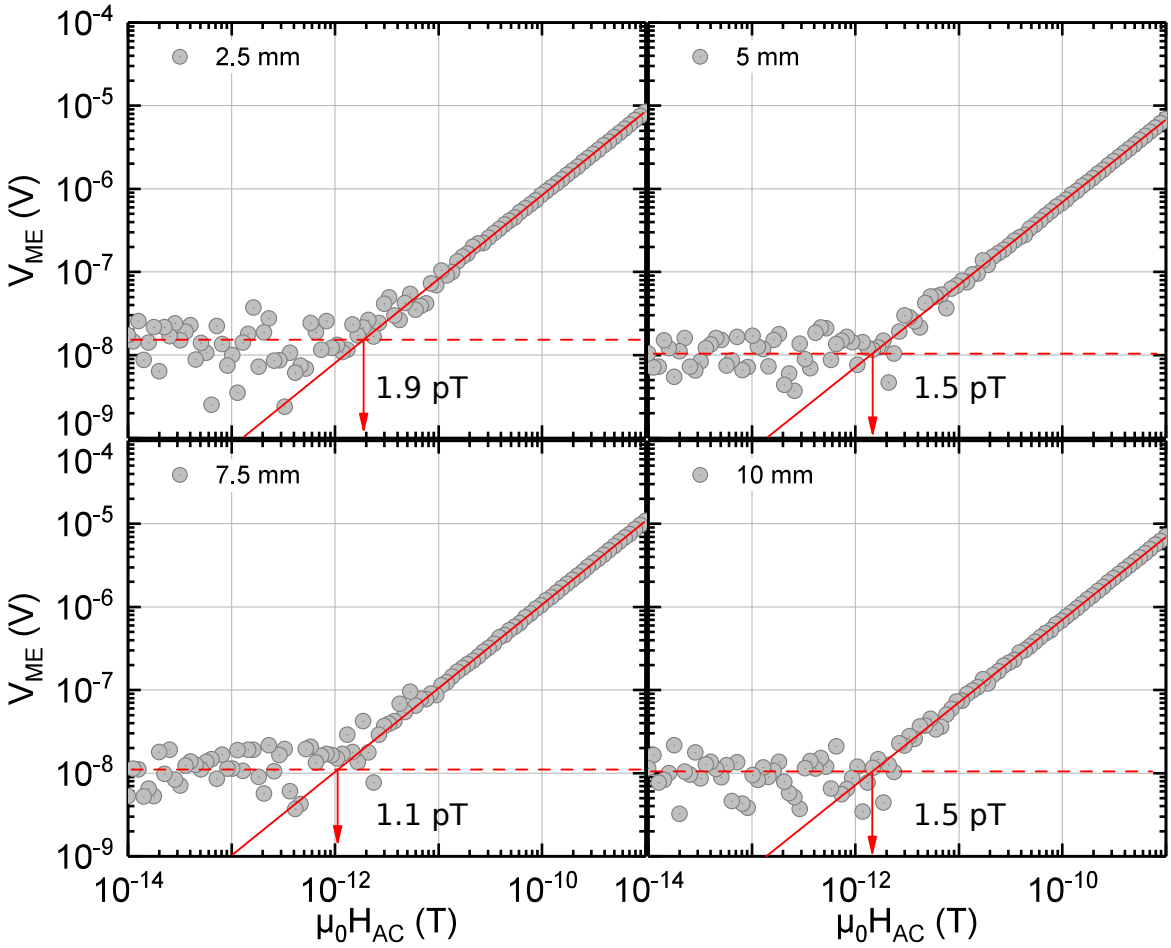


***Figure 4.27:*** *Influence of the top electrode length on the magnetic detection properties. Respective electrode lengths are marked on each plot. Minimum detectable field is determined where the SNR = 1. Increasing the electrode length improves sensor resolution up to a minimum at 7.5 mm length. Further increase proves counter-productive due to the coverage of low-strain areas within the electrode area.*

dimensions.

The strain and the displacement of an exemplary cantilever was previously shown in Figure 4.25b. Here the second half of the cantilever's length depicts a linear behavior; i.e., does not bend at all. Hence the electrode length, which would cover most of the bending area of a one-end fixed cantilever is expected to cover half of the top surface area, at maximum. Accordingly, obtained results depict that maximizing the electrode area does not necessarily improve the $\alpha_{ME}$ probably due to the increasing coverage of low-strain areas. Therefore, $\alpha_{ME}$ shows a decrease at 10 mm length compared to 7.5 mm. Even though the optimal electrode length definitely lays between the two, 7.5 mm was considered as the optimal electrode length and no further investigation was made concerning the electrode lengths for the rest of this work. It was also noted that the modeling of the sensor LOD must be revisited, so that

it includes the thermal-mechanical noise since the latter dominates the noise behavior at the resonance frequency.

### 4.2.3 Influence of the Surface Roughness

Previous sections demonstrated good sensor properties of the inverse-bilayer magnetoelectric sensors. However during this research, it was observed that magnetoelectric sensors fabricated at different times did not always perform comparably. It is, therefore, important to emphasize that fabricated sensor properties are not only dependent on the constituent properties but also on various factors such as the magnetic annealing temperature [14], roughness of the growth surface [34] and residual film stress [243].

According to *Piorra et al.*[34], the deposition of FeCoSiB on a polished surface of a silicon substrate improved the soft magnetic properties of FeCoSiB and consequently the piezomagnetic coefficient. Therefore, a similar approach was attempted and a comparative investigation between conventional and inverse-bilayer sensors was prepared following the process flows described in Section 3.2. The deposited film stacks consist of 1.7 µm FeCoSiB, 140 nm Pt, 1.6 µm AlN and 100 nm Au on 300 µm thick Si substrates. In both cases, the top electrodes of the sensors stretched along the whole length of the cantilever. At the end of the processing, cantilever sensors with $2.2\,\mu m \cdot 25.2\,\mu m$ dimensions were mounted on carrier PCBs and characterized. Results of the completed investigations are summarized in Table 4.6.

Unlike the aforementioned work, both sensor types exhibit similar magnetoelectric results in the current case. Considering the dielectric losses, conventional-bilayer sensors depict slightly higher values. This can be related to the much thicker top electrode thickness. Given the fact that the FeCoSiB and AlN layers have almost equal thickness, the top electrode thickness is doubled for conventional-bilayer sensors. Here, the whole thickness of the FeCoSiB must be traversed by the charge carriers in addition to Cr/Au. Therefore the probability of structural defects, which might be resulting in higher dielectric losses, increases as well. This is in good agreement with the voltage noise density values, where conventional-bilayer sensors produce slightly higher noise compared to inverse-bilayer sensors. Despite the fact that both sensor types have similar $\alpha_{ME}$ coefficients, the increased noise of the conventional sensors deteriorate the sensor's LOD. Nevertheless, it can be said that almost all parameters are identical despite the fact that in one case FeCoSiB is grown directly on the polished surface of a Si substrate and in the other on AlN.

***Table 4.6:*** *Properties of conventional and inverse-bilayer sensors with full-size top electrodes.*

| Property / Magnitude | Average and St. Dev. | |
|---|---|---|
| Sensor Type | *Conventional* | *Inverse* |
| Electrode length (mm) | 22 | 22 |
| $C_{ME}$ (pF) | $2872 \pm 2$ | $2061 \pm 12$ |
| $tan\delta$ (%) | $0.111 \pm 0.017$ | $0.083 \pm 0.006$ |
| $f_{res}$ (Hz) | $759 \pm 7$ | $758 \pm 14$ |
| Q-factor | $241 \pm 44$ | $258 \pm 12$ |
| Open circuit voltage (mV/Oe) | $115 \pm 32$ | $97 \pm 19$ |
| $\alpha_{ME}$ @ $f_{res}$ (kV/(cm·Oe)) | $0.7 \pm 0.2$ | $0.6 \pm 0.1$ |
| Voltage noise density @ $f_{res}$ (nV/Hz$^{1/2}$) | $16 \pm 5$ | $13 \pm 2$ |
| Sensor resolution (pT) | $16 \pm 9$ | $14 \pm 5$ |
| LOD (pT/Hz$^{1/2}$) | $58 \pm 33$ | $52 \pm 17$ |

8 sensors are investigated for each sensor type. Capacitance and tan $\delta$ measurements are completed at 10 kHz. Noise measurements are repeated 100 times and averaged values are given in the table. For all measurements $\mu_0 \cdot H_{AC} = 1 \cdot 10^{-3}$ Oe, t = 1 s and the bandwidth = 1 Hz. Sensor resolution is estimated from the conducted measurements according to Equation (3.26).

Observed similarity of the sensor properties suggests that the magnetostrictive layers have similar properties for both sensor type. In other words, both growth surfaces provide similar conditions. Accordingly, AlN films fabricated in this work have very low surface roughness. In the given literature example, peak-to-valley height difference of the piezoelectric layer on which FeCoSiB is deposited amounts to 74 nm in comparison to the polished surface 23 nm. Therefore, magnetostrictive films deposited on the polished Si surface exhibit much superior properties compared to the films deposited on the rougher surface. In the current work, on the other hand, peak-to-valley height difference is as low as 11 nm (see Figure 4.6). Clearly, this is an extremely smooth surface and FeCoSiB grown on this surface has comparable properties to the FeCoSiB grown on a commercially available Si substrate. It is important to emphasize that even though conventional and inverse-bilayer sensors exhibit similar properties in the current investigation, the top electrode dimensions of the conventional-bilayer sensors can not be optimized. Therefore it is preferable to utilize an inverse-bilayer stack order.

### 4.2.4 Influence of the Residual Film Stress

Residual film stress, in particular, appears as a crucial factor due to the fact that it can influence the magnetic anisotropy of FeCoSiB. Amorphous FeCoSiB is absent of magne-

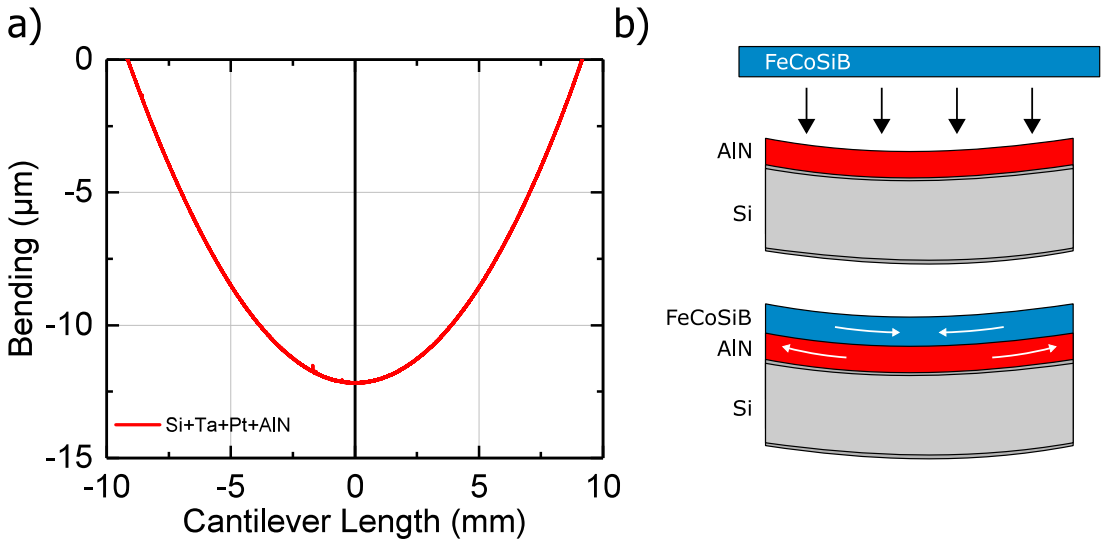


***Figure 4.28:*** *Deposition of FeCoSiB on prestressed substrates. a) Stress profile of an exemplary substrate. The y-axis is adjusted in such a way that the maximum bending point of the cantilever coincides with zero. b) Schematic depiction of stress accommodation upon film deposition. At the AlN/FeCoSiB interface, individual films are subject to tensile and compressive stresses, respectively. White arrows depict how individual films behave in order to accommodate stress.*

tocrystalline anisotropy and it must be deliberately induced via magnetic field annealing as explained in Section 3.2.3. However, it is observed that the induced anisotropy hence the magnetic properties are easily influenced by stress-related effects which deteriorate the overall sensor properties. Therefore in this section, the influence of the residual film stress on the magnetoelectric properties is discussed.

To that end, conventional magnetoelectric sensors[1] were fabricated following the process flow described in Section 3.2. In this investigation, the residual stress of the composite stacks were not compensated so that the influence of stress could be easily observed. The deposited film stacks consisted of 10 nm Ta, 140 nm Pt, 1.6 µm AlN and 1.7 µm FeCoSiB on 300 µm thick Si substrates. FeCoSiB film was sandwiched between two 10 nm thick Ta layers. Pt/AlN layers deposited prior to FeCoSiB were intentionally kept in a tensile stress state of ∼400 MPa with a large substrate bending as seen in Figure 4.28a. Upon FeCoSiB deposition on the concave substrate (AlN) surface and magnetic annealing, the final composite stack had a residual tensile stress of ∼200 MPa. As a result, FeCoSiB was subject to compressive stresses at the AlN/FeCoSiB interface (see Figure 4.28b). The top electrode size of all sensors were kept spread along the whole top surface length of the cantilevers. Cantilever sensors were finally cut into 2.2 mm · 25.2 mm dimensions and were mounted on carrier PCBs. The results of the magnetic characterizations completed on an

[1] Inverse-bilayer sensors can not be investigated with MOKE due to the thickness of the overlaying film.

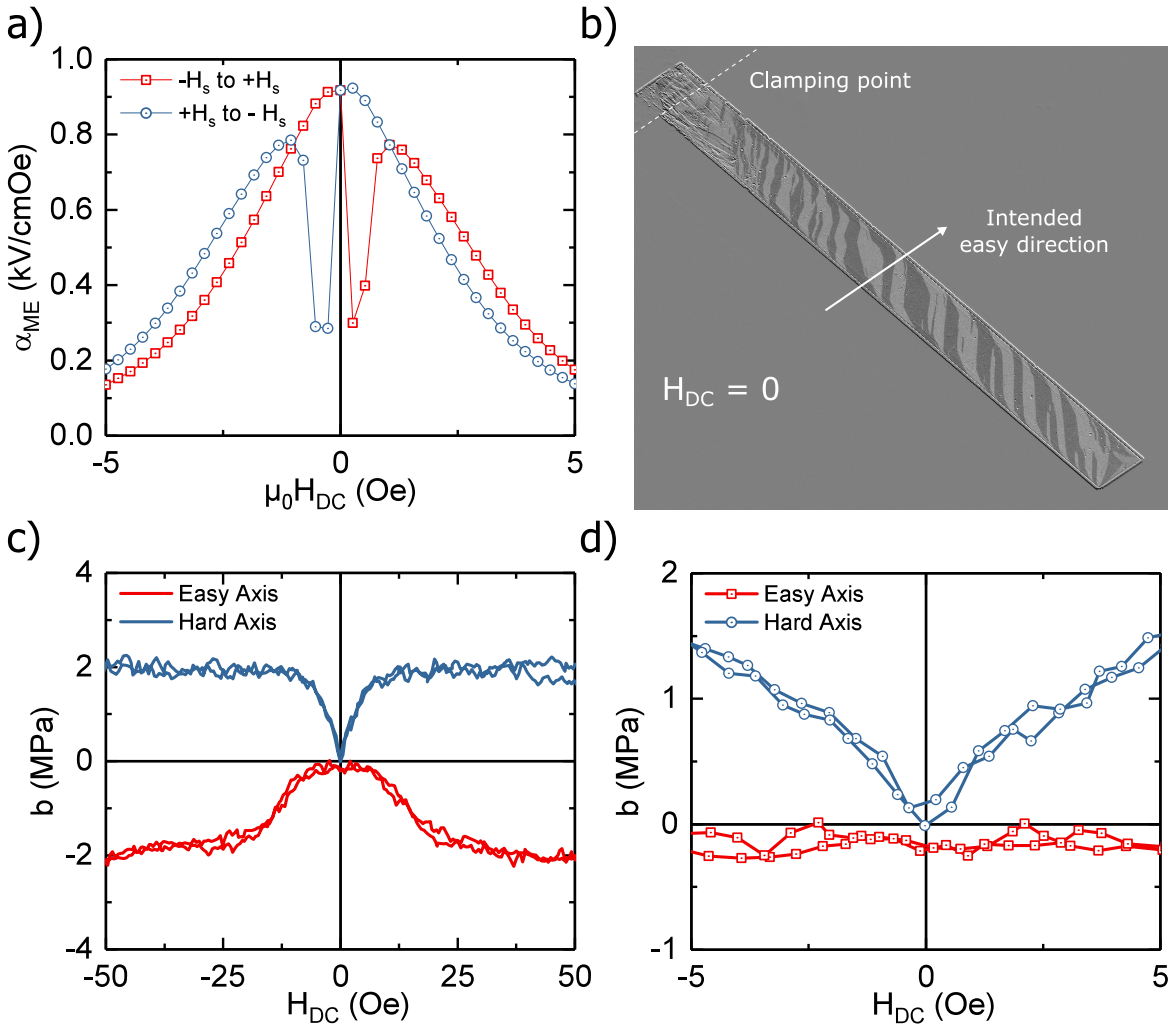


***Figure 4.29:*** *Magnetic characterization and MOKE investigation of a magnetoelectric sensor under residual film stress. a) Magnetic field directions are given with respective color codes. Samples are saturated prior to the measurements, but only near zero field regions are shown. b) MOKE investigation of a magnetoelectric sensor at the decayed state. Investigated sensor depicts a deterioration of the induced anisotropy starting from the clamping point of the cantilever. c) Magnetostriction curve depicting an imperfect induced anisotropy. Easy and hard axis refer to the intended directions; i.e., along the short and long cantilever axis, respectively. d) Close-up to small magnetic field regions.*

exemplary sensor are plotted in Figure 4.29.

First of all, soft magnetic properties of FeCoSiB are not influenced by the residual film stress. However, overall magnetoelectric response to the external DC field is different in comparison to non-stressed samples. Reducing the external magnetic field from its negative saturation (red curve), for instance, the curve first depicts a maximum at $-0.25\,\mathrm{Oe}$, stays highly magnetized at zero field and after reversing the magnetization direction depicts another, but smaller, peak at $1\,\mathrm{Oe}$. Once the sample is saturated and the field is reversed, the same behavior repeats itself. First, a maximum is seen at $0.25\,\mathrm{Oe}$ and the secondary peak is

reached at $-1$ Oe. Once more, the sample retains most of its magnetization at zero field.

Observed behavior differ from the previously investigated stress-compensated sensors. As seen from Figure 4.18, the latter requires a magnetization direction reversal before reaching the optimum working point. However, magnetoelectric voltage output ($\alpha_{ME}$) of the currently investigated sensor reaches a maximum at the same field direction as the saturation direction. Furthermore, it does retain most of its magnetization at zero field rather than reaching a minimum. This suggests the presence of an imperfect induced anisotropy. Hence complementary magneto-optic Kerr microscopy (MOKE) investigations were done in order to better understand the observed effects.

As seen from Figure 4.29b, investigated sample depicts a tilt of the induced anisotropy from the intended direction. When induced perfectly, the magnetic anisotropy lays parallel to the short axis of the cantilever sensor as a result of the magnetic annealing process. However here, the magnetic domains are rotated starting form the clamping point of the cantilever. If such a behavior would be observed in stress-compensated sensors, then one could consider it to be the influence of the seed layer laying under FeCoSiB. As was previously stated, FeCoSiB is deposited on the AlN surface (with a thin Ta layer in between) in case of the conventional-sensors. Therefore one could argue that the deposition of FeCoSiB on a rough surface could be the reason for the nucleation of magnetically harder grains [14]. Even though these grains are in small concentrations (in comparison to the whole volume of the material), they might still affect the demagnetization of the material when they are present. However, this argument can not be valid here. Previous investigations proved that AlN films utilized in this work are smooth enough and do not deteriorate the soft magnetic properties of FeCoSiB. Therefore, the only possible reason for the observed anisotropy tilting can be the residual stress of the composite structure acting on the properties of FeCoSiB.

Figure 4.29c and d depict the results of the magnetostriction measurements completed on the investigated sensor. It can be seen that the intended anisotropy is missing from the sample. There is almost no distinction between magnetically easy-hard axes and a comparable magnetostriction is present along both of them. One could argue that the magnetoelectric voltage coefficient and the magnetostriction curves are contradicting, since the latter exhibits zero magnetostriction at zero field (see close-up) despite the retained magnetization seen in Figure 4.29a. That can probably be due to an artifact during the magnetostriction measurement, or an inaccuracy resulting from the curved sample geometry. In any case, the influence of the stress can be clearly observed from the magnetostriction curves. The fact that the magnetostriction is equal along both directions is well-matched with the MOKE investigation,

***Table 4.7:*** *Properties of conventional-bilayer sensors under the effects of residual stress.*

| Property / Magnitude | Sample 1 | Sample 2 | Sample 3 | Sample 4 |
|---|---|---|---|---|
| $C_{ME}$ (pF) | 2873 | 2873 | 2870 | 2874 |
| $tan\delta$ (%) | 0.124 | 0.124 | 0.077 | 0.110 |
| $f_{res}$ (Hz) | 762 | 755 | 768 | 764 |
| Q-factor | 177 | 228 | 256 | 293 |
| Bias field (Oe) | 0 | 0.3 | 0 | 0 |
| $\alpha_{ME}@f_{res}$ (kV/(cm·Oe)) | 0.4 | 0.7 | 0.9 | 0.9 |
| Voltage noise density $@f_{res}$ (nV/Hz$^{1/2}$) | 13 | 14 | 12 | 23 |
| Sensor resolution (pT) | 18 | 12 | 8 | 16 |
| LOD (pT/Hz$^{1/2}$) | 64 | 43 | 29 | 56 |

Capacitance and tan $\delta$ measurements are completed at 10 kHz. Noise measurements are repeated 100 times and averaged values are given in the table. For all measurements $\mu_0 \cdot H_{AC} = 1 \cdot 10^{-3}$ Oe, t = 1 s and the bandwidth = 1 Hz. Sensor resolution is estimated from the conducted measurements according to Equation (3.26).

which reveals that the rotation of the domains is as high as $45 - 50°$ across the length of the sample. Considering the overall magnetoelectric characterization, all investigated sensor properties are summarized in Table 4.7. Despite the fact that the $\alpha_{ME}$ and the LOD values are similar to previously investigated conventional sensors, the working point of the sensors are shifted near zero field magnitudes.

In summary, influence of the residual film stress was observed both from magnetic measurements and MOKE investigations. Clearly, residual film stress alters the magnetic properties of the fabricated sensors, overcomes the initially induced magnetic anisotropy and worsens the sensor properties. Measured $\alpha_{ME}$ coefficient was in the range of previously published conventional-bilayer magnetoelectric sensors [72], but much lower than the sensors fabricated in the current work. Therefore, it is crucial that a stress-optimization step is implemented into the fabrication process of the magnetoelectric sensors.

# 5 Summary and Conclusion

The aim of this work was the development of magnetoelectric sensors for the detection of sub-pT magnetic fields at room temperature and in atmospheric pressure. To that end resonant cantilever sensors based on AlN/FeCoSiB composite structures were developed. Starting from the individual constituent layers; at first a reactive magnetron sputtering process was established for the deposition of AlN. In order to preserve the soft magnetic properties of the amorphous FeCoSiB, a low temperature deposition process where substrate heating is avoided, was developed. Influences of the power source, various process parameters; i.e., gas composition, pressure, power, pulsing parameters, etc., seed layer material and film thickness on the microstructural, piezoelectric, dielectric as well as residual stress properties of the fabricated films were thoroughly investigated. After optimizing the AlN deposition process, a process flow, which allows the fabrication of magnetoelectric sensors without breaking vacuum between consecutive film depositions, was implemented. Fabricated composites were structured using a combination of photolithography techniques and wet/dry etching processes. The residual stress of the composite sensors were compensated by adjusting AlN deposition parameters, and the top electrode dimensions were confined to a region where the cantilever bending was maximum. Additionally, composites of AlN/FeCoSiB with various deposition orders and sensor geometries were realized. The most important results of this work are summarized in the following chapter.

**Aluminum Nitride Deposition**

It was shown that various parameters influence the properties of the fabricated films;

1. *Substrate heating* is not a requirement for the fabrication of highly textured AlN thin

films with high piezoelectric coefficients. Enhanced adatom mobility and the necessary energy for preferential *c*-axis growth can be provided by adjusting other deposition parameters.

2. *Gas composition (Al/$N_2$ ratio)* is found to influence the deposited film stoichiometry via an enhanced nitrification of the target material. An increasing reactive gas concentration improved the deposited film quality and resulted in a smoother surface. Substitution of the Ar gas, in return, decreased the sputtering rate approximately 20%. Complete removal of Ar resulted in a higher texture quality of the deposited films, shown by an improvement of the FWHM by 30%.

3. *Seed layer* on which AlN is deposited is influential on the crystal orientation and the texture quality of the deposited films. It was observed that improving the texture quality of the Pt seed layer, in turn, improved the texture quality of AlN. Furthermore, modifying the Pt surface via plasma etching (prior to AlN deposition) increased the nucleation sites that favored the nucleation of *c*-axis oriented AlN grains. Through TEM investigations, a heteroepitaxial growth of AlN on top of Pt was confirmed. AlN films deposited on plasma treated Pt surface exhibit approximately 50% narrower FWHM. Additionally, fabricated AlN films exhibit an extremely smooth surface with an average RMS roughness as low as 1.1 nm.

4. *Gas pressure* is arguably the most influential sputtering parameter. Low gas pressure favored the *c*-axis orientation, improved the texture quality and produced dense, circular as well as small grains. It was concluded that at low pressures, ions present in the plasma would retain most of their energy as they reach the growing film surface due to a higher MFP. Despite its influence on the texture quality, gas pressure exhibits only a limited effect on the piezoelectric/dielectric properties. Furthermore, a transition from tensile to compressive film stress was observed with decreasing pressure.

5. *Pulsing parameters*; e.g., the pulsing frequency and the duty cycle proved crucial for the prevention of arc formation and minimizing the target poisoning around the erosion trench. In particular, the latter strongly influences the film deposition rate and the fabricated film stoichiometry. Stoichiometry, in return, influences all microstructural, piezoelectric and dielectric properties. It was observed that keeping the on-part of the duty cycle above 60% resulted in fast nitrification of the target surface and eventual plasma failure unless a high pulsing frequency is adopted (e.g., 250 kHz).

It was also observed that increased sputtering power and self-bias improved the texture qual-

ity, due to a higher kinetic energy of the deposited particles. However, these parameters shall be chosen in such a way that they do not damage the growing film surface and deteriorate the texture quality.

Film thickness is not a sputtering parameter, nevertheless it is an influential factor on the AlN properties. In principal, thin and thick films demonstrated comparable nucleation/growth characteristics, however increased film thickness improved the texture quality as well as the piezoelectric properties.

It was observed that starting from 500 nm film thickness, deposited samples exhibit high piezoelectric properties ($d_{33,f} = 4.5\,\mathrm{pm/V}$) and low dielectric losses ($< 0.1\%$). These values improved to $d_{33,f} = 5.6\,\mathrm{pm/V}$ and $\tan\delta = 0.025\%$ for the thickest films at 2000 nm. It was also observed that the residual film stress of AlN transitioned from compressive to tensile with increasing film thickness.

**Magnetoelectric Sensors**

Developed AlN fabrication process provided a very reliable and repeatable method, which enabled the deposition of highly textured films even at sub-µm film thicknesses. These films provided a high quality piezoelectric constituent for the fabrication of magnetoelectric sensors. By utilizing AlN films, highly sensitive AC magnetic field sensors with various deposition orders were fabricated while retaining the soft magnetic properties and high piezomagnetic coefficient of the magnetostrictive constituent. Among them, inverse-bilayer sensors exhibit superior properties; i.e., highest sensitivity and lowest LOD, in comparison to other sensors when driven at the mechanical resonance frequency. These properties originated from the combination of constituent material properties; i.e., good piezoelectric and magnetostrictive properties, as well as the mechanical and electrical optimization of the sensors; i.e., residual stress and top electrode confinement. Most sensitive sensors exhibit magnetoelectric coefficients ($\alpha_{ME}$) as high as $7.5\,\mathrm{kV/(cm\cdot Oe)}$ when operating The bandwidth was determined as 2 Hz, and a linear response over a wide magnitude range ($10^{-6}\,\mathrm{T} - 10^{-12}\,\mathrm{T}$) was observed. Using a lock-in amplifier, detection of magnetic fields as low as 400 fT[1] was achieved at room temperature and atmospheric pressure. This corresponds to an improvement as high as factor 5 in comparison to the previously published conventional-bilayer sensors of AlN/FeCoSiB [117]. Best sensors exhibit LOD values as low as $1\,\mathrm{pT/Hz^{1/2}}$, which is within the range of MEG signals (see Figure 5.1). Additionally, magnetic frequency conversion was applied to the sensors in an attempt to compensate the loss of resonance en-

[1] This value is equivalent to $1.4\,\mathrm{pT/Hz^{1/2}}$.

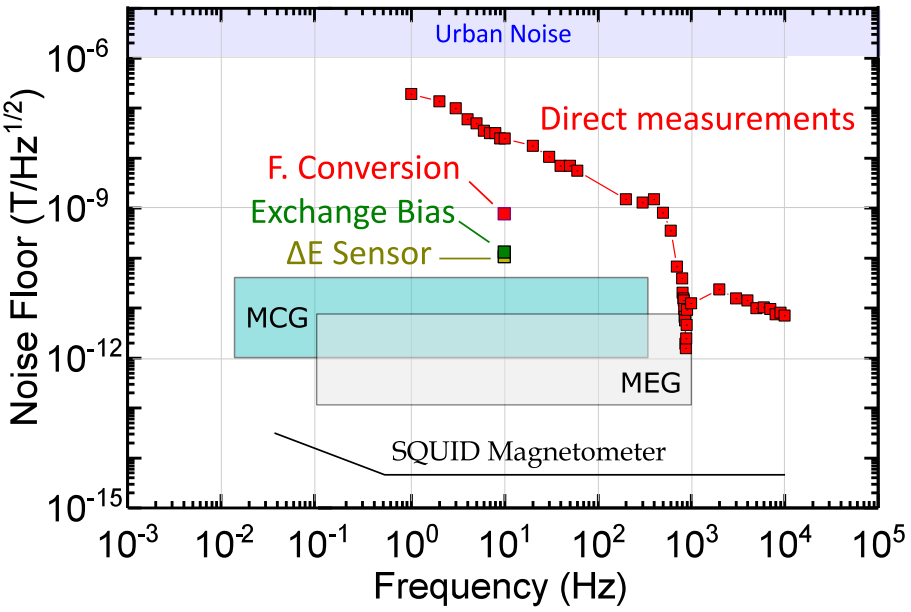


***Figure 5.1:*** *Overview of the magnetoelectric sensor performance. The range of the MCG and MEG signals are given. LOD of the inverse-bilayer, as well as magnetoelectric exchange-biased and delta-E effect sensors, which utilize low temperature AlN as the piezoelectric coefficient, are shown.*

hancement when operating at out-of-resonance conditions. Accordingly, a LOD as low as $10\,\mathrm{nT/Hz^{1/2}}$ was achieved due to an increased noise level originating from abrupt magnetization changes in the magnetostrictive layer [125].

Furthermore, AlN fabrication process was integrated within the process flow of different magnetoelectric sensors investigated at the collaborative research center CRC 855 and PAK 902 as well. Through direct collaborations and/or via technology transfer to the members of the collaborative research center, low temperature AlN was utilized as the piezoelectric constituent in magnetoelectric exchange-biased [125] and delta-E effect [180] sensors. These sensors exhibit LOD values as low as $180\,\mathrm{pT/Hz^{1/2}}$ and $100\,\mathrm{pT/Hz^{1/2}}$ at 10 Hz, respectively.

Considering both the low temperature deposition of AlN and the detection of sub-pT magnetic fields at room temperature as well as technology transfer within the CRC, it can be said that the entirety of the set goals for this doctoral thesis were achieved and fulfilled. It is also important to emphasize that magnetoelectric sensors have potential for further improvement. Despite currently not being the most sensitive among magnetometers, they already present a good alternative to the state-of-the-art magnetic field detection devices in terms of both measurement range and LOD. Additionally, they are small, passive, economical and easily fabricated using MEMS technology. Finally, through the development of novel piezoelectric and magnetostrictive materials, magnetoelectric sensors can surpass state-of-the-art sensors and detect biomagnetic fields at fT range.

# 6 Outlook

In this chapter, the possibilities of improving the LOD of the magnetoelectric sensors are discussed as an outlook of the current work. To that end, previously presented most sensitive sensor results (see Figure 4.23) are considered as reference.

The minimum magnetic field that a sensor can detect is basically a question of the SNR; when SNR equals 1, the linear relation between the external AC field and the sensor output is no longer preserved. Figure 6.1 summarizes this relationship; meaningful signals (gray circles) can not be distinguished from the total noise (blue circles) below the point where SNR equals 1. Hence higher SNR is a prerequisite for the detection of the intended magnetic fields. This can be achieved by improving either (or both) contributor.

Considering the LOD of the currently best sensor, approximately 3 orders of magnitude noise reduction is necessary in order to detect 1 fT AC magnetic field, given that the same signal level is preserved (see Figure 6.1a). Following the applied linear fit onto the sensor signal (purple dashed line), it can be speculated that fT resolution (*II*) can be reached if the average sensor noise (*III*) is decreased approximately 2.5 orders of magnitude (*IV*). As discussed within the results part (see Figure 4.22a), the total noise density of the sensor is higher than the intrinsic piezoelectric noise due to the thermal-mechanical contributions at the resonant drive. Replacing the piezoelectric material (AlN) is not a viable option, since other alternatives; e.g., PZT, ZnO, have much higher noise contributions in comparison to AlN[1]. Utilized AlN readily depicts extremely low dielectric losses in comparison to other piezoelectric materials, therefore they would not improve the total noise (see Table 2.2).

[1] AlScN, a new piezoelectric material with improved piezoelectric properties can offer SNR improvement, however there are no reports concerning its use within the magnetoelectric composite sensor structures as of yet.

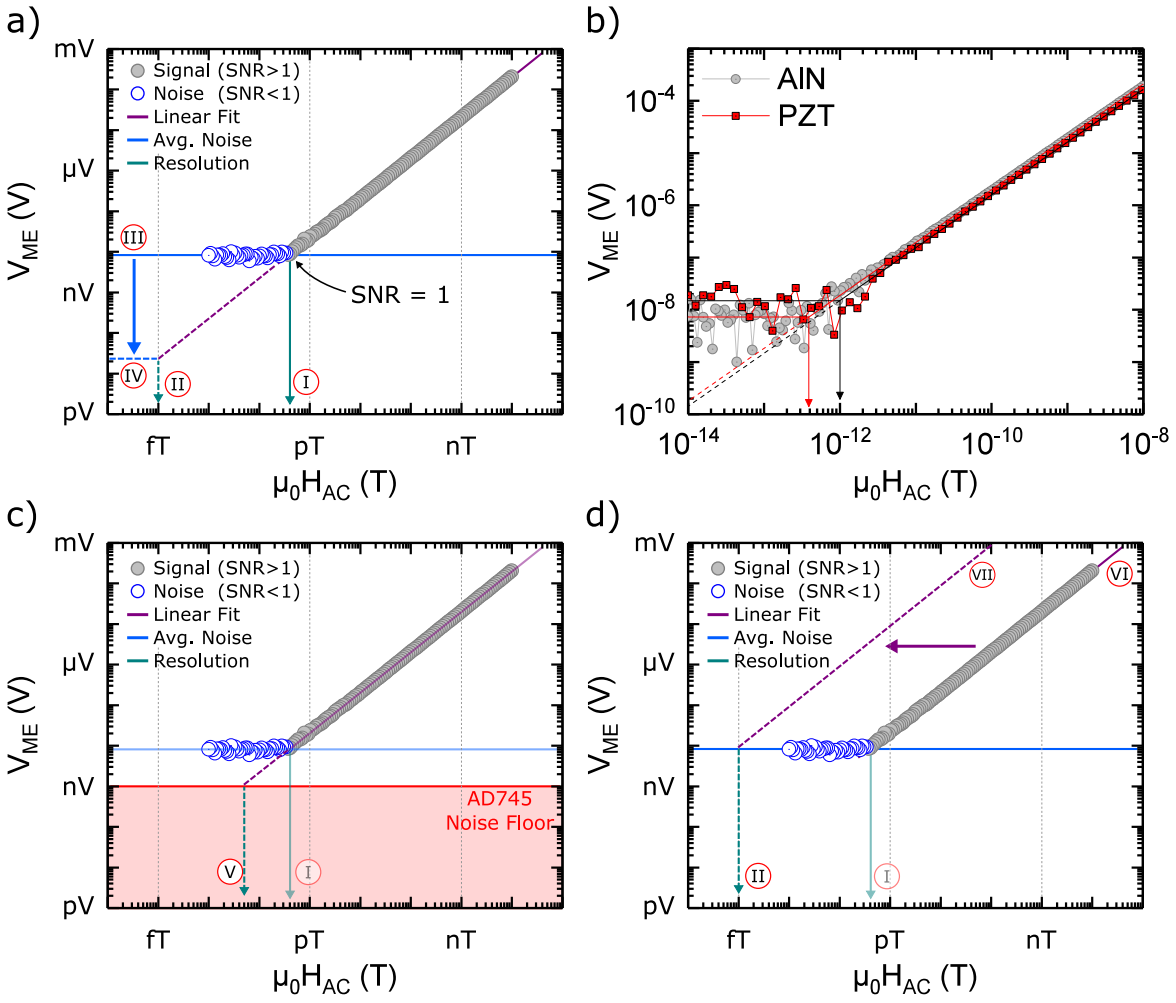


***Figure 6.1:*** *Simplified LOD measurement of the best magnetoelectric sensor and outlook. a) Definition of the SNR, and the prospect sensor LOD under different conditions. b) Comparison between the LOD values of magnetoelectric sensors with AlN and PZT as the piezoelectric constituent. c) Noise floor of the utilized charge amplifier. d) Necessary output improvement for the detection of fT-range AC magnetic fields.*

This can also be seen from Figure 6.1b, which compares the LOD obtained via AlN and PZT-based magnetoelectric sensors. In resonance[1], PZT-based sensor has 2 times higher noise in comparison to AlN-based sensor. Note that, both sensors almost have an identical output signal despite the fact that the PZT-based sensor has IDT-electrodes. It can be argued that an alternative piezoelectric material, with lower dielectric losses, could decrease the overall noise however such thin film piezoelectric material is not within the knowledge of the author. The only thin film material that might achieve the proposed improvement is AlScN, however, current state-of-the-art AlScN did not produce such results yet.

Even if such a novel material is found, it is still debatable whether it would be of use due to

[1]Both sensors have comparable resonance frequencies of 868 Hz and 885 Hz, respectively.

the increased noise at the resonance frequency. Utilized charge amplifier readily produces more noise than the investigated sensor's intrinsic piezoelectric noise (see Figure 4.22a). The input voltage noise of the amplifier provided by the manufacturer equals $3.2\,\mathrm{nV/Hz^{1/2}}$ at 1 kHz [214]. Considering the different time constant of the lock-in amplifier device, an equivalent voltage noise density as low as

$$3.2\,\mathrm{nV} \cdot \sqrt{78\,\mathrm{mHz}} \approx 1\,\mathrm{nV/Hz^{1/2}} \tag{6.1}$$

can be estimated.

In this case, the minimum detectable magnetic field ($V$) can reach approximately 50 fT, given the fact that the same sensor output is preserved (see Figure 6.1c). In other words, available electronics are already at their technological limit and generate way too much noise considering how small the signals to be measured are. Therefore even if the thermal-mechanical noise could be suppressed and the sensor noise could be decreased, it can be expected that the current hardware would increase the total noise and prevent the detection of biomagnetic signals. Clearly, a certain technological breakthrough is necessary for the fabrication of charge amplifiers, which would generate several orders of magnitude lower noise.

To that end, an alternative aim to pursue can be the improvement of the sensor output itself (see Figure 6.1d) rather than to decrease the noise. If the currently achieved sensor output (*VI*) can be increased up to 3 orders of magnitude (*VII*), it can then be possible to detect fT magnetic fields given that the current noise level is preserved. Hence one shall focus on maximizing individual piezoelectric and piezomagnetic contributions of the constituent materials, as well as the coupling between them, in accordance to Equation (3.30). Magnetostrictive alternatives will not be discussed here, since the only thin film alternative is FeGaB (Table 2.3) and FeCoSiB readily exhibits better performance. However the optimization of the substrate material rather than the magnetostrictive material; e.g., use of thinner substrates and/or with higher Q-factor, can be an alternative method of increasing the piezomagnetic coefficient and consequently the magnetoelectric sensor output. Considering the piezoelectric materials, there is an increasing interest in $Al_{1-x}Sc_xN$ for both sensor and energy harvesting applications [244]. Since the substitution of Al with Sc increases the piezoelectric coefficients ($d_{33,f}$ and $e_{31,f}$) more than the dielectric constant ($\varepsilon_{33,f}$), both the energy and voltage FOMs of $Al_{1-x}Sc_xN$ increase in comparison to AlN [245]. However, material properties are strongly dependent on the growth temperature and is not yet compatible to be used with amorphous magnetostricitive materials such as FeCoSiB.

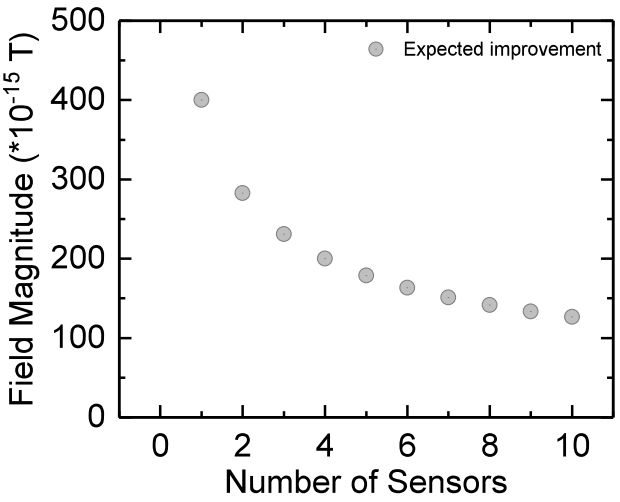


***Figure 6.2:*** *Estimated improvement of the detection capabilities via sensor-arrays.*

Another alternative for improving the SNR can be the use of substrate/AlN/FeCoSiB sensors in an array setup. Previous research defines the magnetic noise as the biggest challenge to overcome and arguments that it is relatively harder to bring down the noise level of singular sensors in comparison to sensor arrays utilized in serial and parallel modes [246]. In this manner, an improvement of the magnetic field sensitivity that scales approximately with the square root of the number of sensors ($\sqrt{N}$) can be realized [99].

Figure 6.2 depicts the expected improvement with respect to the number of sensors, considering that the previously discussed most sensitive sensor is replicated. That is, however, not a straightforward approach. Arrays of macroscopic sensors and all the necessary electronic components would increase the unit size, hence, would result in bulky devices. Therefore, development of on-chip sensor arrays via miniaturization can be a better option. In this case, on the other hand, sensor performance of individual sensors might deteriorate due to the decreased magnetic material volume per sensor.

In summary, it can be speculated that putting effort into noise suppression might not be the optimal goal to pursue in the first place. Focusing on the sensor output, either via the use of novel piezoelectric materials or array structures, can improve the current sensing capabilities remarkably.

# A Appendix

## A.1 Photolithography Masks

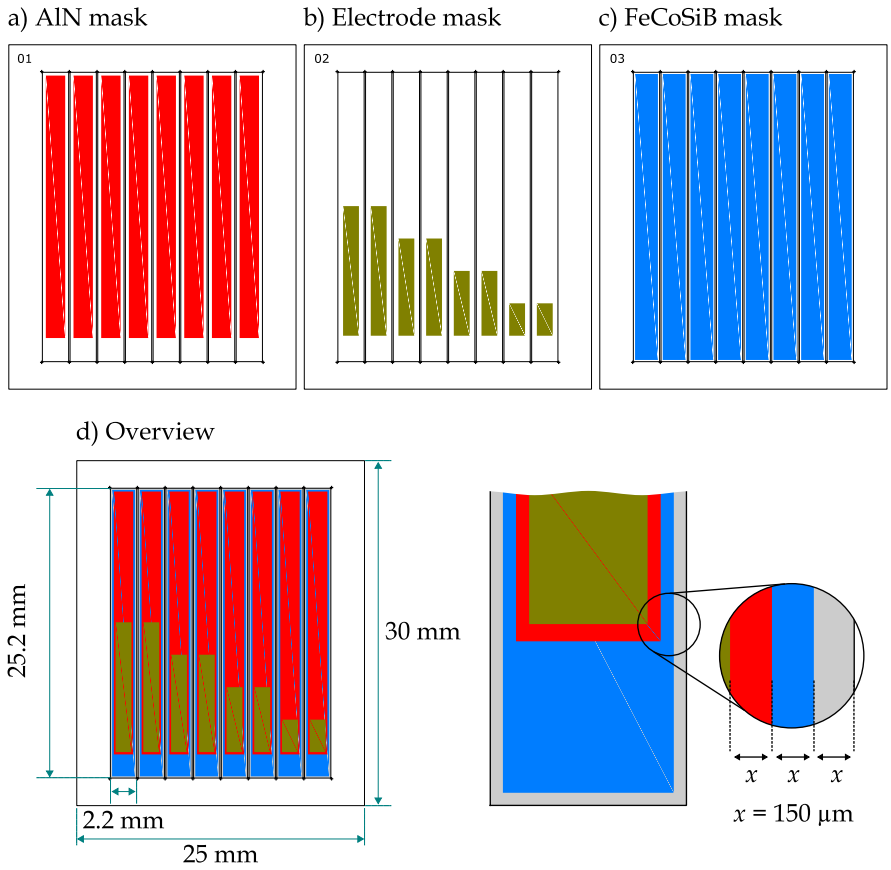


***Figure A.1:*** *Schematic overview of the photolithography masks utilized in the fabrication of bilayer sensors and an exemplary sensor chip geometry. Masks are made of plastic and have a spatial density of 25000 dpi.*

## A.2 Modeling of the Power Losses

A model to predict power losses at a given frequency with respect to dielectric loss tangent ($\tan\delta$) and capacitance values.

### Parameters

$C = 2.87 \cdot 10^{-11}\,\mathrm{F}$
$\tan\delta = 0.00025 \cdot 10^{5}\,\mathrm{V/m}$
$I_{rms} = 3.1 \cdot 10^{-9}\,\mathrm{A}$
$f = 10\,\mathrm{kHz}$
$t = 100\,\mu\mathrm{s}$

### Calculations

$\varphi = \pi/2 - \delta$
$I_{peak} = I_{rms} \cdot \sqrt{2}$
$R_{series} = \frac{1}{\omega \cdot C \cdot \tan\varphi}$
$R_{parallel} = \frac{1}{\omega \cdot C \cdot \tan\delta}$
$I(t) = I_{peak} \cdot \cos(\omega \cdot t)$
$V(t) = I_{peak} \cdot [R \cdot \cos(\omega \cdot t) + (\frac{1}{\omega \cdot C}) \cdot \sin(\omega \cdot t)]$
$P_{avg} = I_{rms} \cdot V_{rms}$

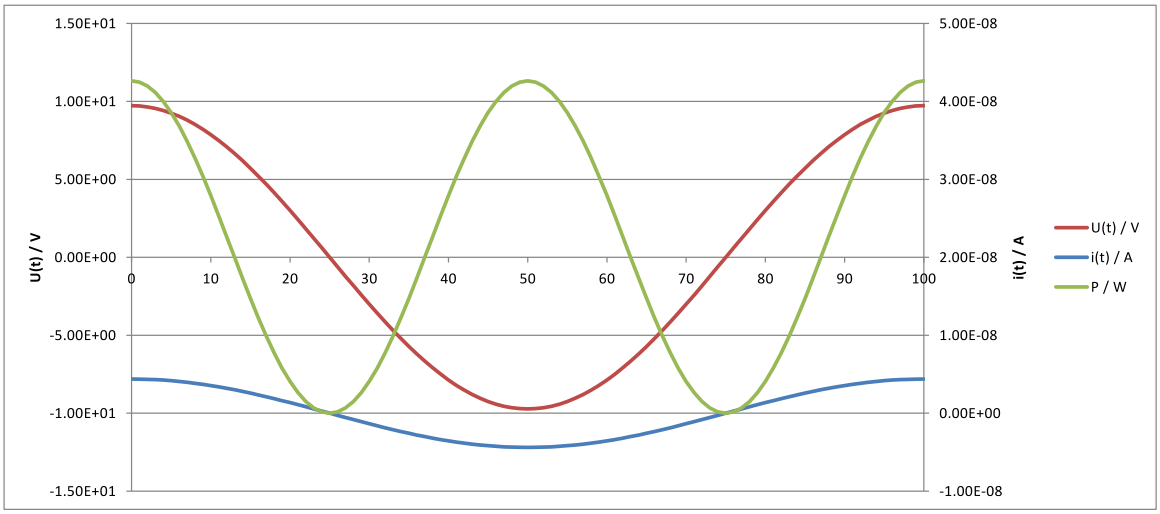


***Figure A.2:*** *Modeled power losses of a piezoelectric AlN thin film.*

## A.3 Diffraction Lines of AlN

Diffraction lines of a uniaxially hot-pressed (in vacuum at 2100 °C) AlN solid solution [219]. Specimen dimensions are; $\varnothing = 2.5\,\text{cm}$ and $t \approx 1\,\text{cm}$

***Table A.1:*** *Computed diffraction lines of AlN.*

| 2Θ (°) | Intensity | h | k | l | 2Θ (°) | Intensity | h | k | l |
|---|---|---|---|---|---|---|---|---|---|
| 33.15 | 1000.0 | 1 | 0 | 0 | 71.55 | 457.6 | 1 | 1 | 2 |
| **36.15** | **664.5** | **0** | **0** | **2** | 72.75 | 152.1 | 2 | 0 | 1 |
| 37.95 | 905.2 | 1 | 0 | 1 | 76.35 | 23.5 | 0 | 0 | 4 |
| 49.95 | 364.7 | 1 | 0 | 2 | 81.15 | 79.2 | 2 | 0 | 2 |
| 59.55 | 618.4 | 1 | 1 | 0 | 85.95 | 26.8 | 1 | 0 | 4 |
| 66.15 | 522.4 | 1 | 0 | 3 | 94.95 | 198.8 | 2 | 0 | 3 |
| 69.75 | 90.7 | 2 | 0 | 0 | 98.55 | 77.5 | 2 | 1 | 0 |

# Bibliography


[1] *Global Smart Sensors Market - Growth, Trends and Forecast (2014-2020), Access Date: 18.07.2017*. URL: https://www.researchandmarkets.com/research/h2gkfw/global_smart.

[2] S. H. Sheen, A. C. Raptis, and M. J. Moscynski. *Automotive vehicle sensors*. 1995.

[3] Organisation Internationale Constructeurs Des d'Automobiles. *World Motor Vehicle Production by Country and Type, Access date: 15.06.2017*. URL: http://www.oica.net/wp-content/uploads//Total-2015-Q4-March-16.xls.

[4] W. Andrä and H. Nowak. *Magnetism in Medicine*. 2nd ed. Weinheim, 2006. ISBN: 3527405585.

[5] A. Grosz, M. J.. Haji-Sheikh, and S. C. Mukhopadhyay, eds. *High Sensitivity Magnetometers*. Vol. 19. Smart Sensors, Measurement and Instrumentation. Springer International Publishing, 2017. ISBN: 9783319340685.

[6] S. Macintyre. "Magnetic Field Measurement." In: *The measurement, instrumentation, and sensors handbook*. Ed. by John G. Webster. The electrical engineering handbook series. Boca Raton Fla.: CRC Press published in cooperation with IEEE Press, 1999. ISBN: 978-0-8493-8347-2.

[7] M. Schmelz, R. Stolz, V. Zakosarenko, T. Schönau, S. Anders, L. Fritzsch, M. Mück, M. Meyer, and H.-G. Meyer. "Sub-fT/Hz1/2 resolution and field-stable SQUID magnetometer based on low parasitic capacitance sub-micrometer cross-type Josephson tunnel junctions." In: *Physica C: Superconductivity and its Applications* 482 (2012), pp. 27–32. ISSN: 09214534.

[8] D. Drung. "High-performance DC SQUID read-out electronics." In: *Physica C: Superconductivity and its Applications* 368.1-4 (2002), pp. 134–140. ISSN: 09214534.

[9] *Advanced Brain Investigations Can Become Better and Cheaper, Access date: 16.06.2017*. URL: http://www.chalmers.se/en/news/Pages/Advanced-brain-investigations.aspx.

[10] S. Braeutigam. "Magnetoencephalography: fundamentals and established and emerging clinical applications in radiology." In: *ISRN radiology* 2013 (2013), p. 529463. ISSN: 2314-4084.

[11] A. Walia. *Not Just Brain to Body: Researchers Discover That The Heart Sends Signals to the Brain, Access Date: 01.03.2017*. 2017. URL: http://www.collective-evolution.com/2015/10/30/not-just-brain-to-body-researchers-discover-that-the-heart-sends-signals-to-the-brain/.

[12] F. Ludwig, S. Mäuselein, E. Heim, and M. Schilling. "Magnetorelaxometry of magnetic nanoparticles in magnetically unshielded environment utilizing a differential fluxgate arrangement." In: *Review of Scientific Instruments* 76.10 (2005), p. 106102. ISSN: 0034-6748.

[13] J. P. Valadeiro, J. Amaral, D. C. Leitao, R. Ferreira, Freitas C. S., and P. J. P. Freitas. "Strategies for pTesla field detection using magnetoresistive sensors with a soft pinned sensing layer." In: *IEEE Transactions on Magnetics* 51.1 (2015), pp. 1–4. ISSN: 0018-9464.

[14] V. Hrkac, E. Lage, G. Köppel, J. Strobel, J. McCord, E. Quandt, D. Meyners, and L. Kienle. "Amorphous FeCoSiB for exchange bias coupled and decoupled magnetoelectric multilayer systems: Real-structure and magnetic properties." In: *Journal of Applied Physics* 116.13 (2014), p. 134302. ISSN: 0021-8979.

[15] H. Suharyadi. "Thin Film Deposition and Optimization of Piezoelectric Aluminum Nitride for Magnetoelectric Sensors." Master Thesis. Germany: Christian-Albrechts-Universität zu Kiel, 2015.

[16] S. Marauska. "Hochempfindliche mikromechanische magnetoelektrische Magnetfeldsensoren." PhD thesis. Christian-Albrechts-Universitaet zu Kiel, 1.01.2013.

[17] A. Kittmann. "Development and Characterization of Metglas Based Substrate-free Magnetoelectric Sensors." Master Thesis. Germany: Christian-Albrechts-Universität zu Kiel, 2015.

[18] K. Uchino. *Ferroelectric Devices*. 2nd ed. Boca Raton, Fla.: CRC, 2010. ISBN: 1439803757.

[19] W. Voigt. *Lehrbuch der Kristallphysik: Mit Ausschluß der Kristalloptik*. Wiesbaden: Vieweg +Teubner Verlag and Imprint, 1966. ISBN: 978-3-663-15884-4.

[20] W. D. Hackmann. "Underwater acoustics and the Royal Navy, 1893-1930." In: *Annals of Science* 36.3 (1979), pp. 255–278. ISSN: 0003-3790.

[21] H. Bhugra and G. Piazza. *Piezoelectric MEMS Resonators*. Microsystems and nanosystems. Cham, Switzerland: Springer Nature, 2017. ISBN: 3319286889.

[22] A. J. Moulson. *Electroceramics (Second Edition): Materials, Properties, Applications*. 2nd ed. Chichester: John Wiley Sons, 2003. ISBN: 9780470867969.

[23] J. F. Nye. *Physical properties of crystals: Their representation by tensors and matrices*. New ed. Oxford: Clarendon, 1985. ISBN: 0198511655.

[24] A. Safari and E. K. Akdoğan. *Piezoelectric and Acoustic Materials for Transducer Applications*. New York: Springer Science + Business Media, op. 2010. ISBN: 0387765409.

[25] A. Meitzler, H. F. Tiersten, A. W. Warner, D. Berlincourt, G. A. Couqin, and F. S. Welsh III. *IEEE Standard on Piezoelectricity*. IEEE / Institute of Electrical and Electronics Engineers Incorporated, 1988.

[26] T. L. Jordan and Zoubeida Ounaies. *Piezoelectric ceramics characterization*. National Aeronautics and Space Administration (NASA).

[27] P. Muralt. "PZT thin films for microsensors and actuators: Where do we stand?" In: *IEEE transactions on ultrasonics, ferroelectrics, and frequency control* 47.4 (2000), pp. 903–915. ISSN: 0885-3010.

[28] P. Muralt, J. Conde, A. Artieda, F. Martin, and M. Cantoni. "Piezoelectric materials parameters for piezoelectric thin films in GHz applications." In: *International Journal of Microwave and Wireless Technologies* 1.01 (2009), pp. 19–27. ISSN: 1759-0795.

[29] P. Muralt. "Piezoelectric Thin Films for MEMS." In: *Integrated Ferroelectrics* 17.1-4 (1997), pp. 297–307.

[30] S. Trolier-McKinstry and P. Muralt. "Thin Film Piezoelectrics for MEMS." In: *Journal of Electroceramics* 12.1-2 (2004), pp. 7–17. ISSN: 1385-3449.

[31] C.-B Eom and S. Trolier-McKinstry. "Thin-film piezoelectric MEMS." In: *MRS Bulletin* 37.11 (2012), pp. 1007–1017. ISSN: 1938-1425.

[32] X.-H. Du, J. Zheng, U. Belegundu, and K. Uchino. "Crystal orientation dependence of piezoelectric properties of lead zirconate titanate near the morphotropic phase boundary." In: *Applied Physics Letters* 72.19 (1998), pp. 2421–2423. ISSN: 0003-6951.

[33] B. Noheda, D. E. Cox, G. Shirane, R. Guo, B. Jones, and L. E. Cross. "Stability of the monoclinic phase in the ferroelectric perovskite PbZr1−xTixO3." In: *Physical Review B* 63.1 (2000).

[34] A. Piorra, R. Jahns, I. Teliban, J. L. Gugat, M. Gerken, R. Knöchel, and E. Quandt. "Magnetoelectric thin film composites with interdigital electrodes." In: *Applied Physics Letters* 103.3 (2013). ISSN: 0003-6951.

[35] S. Marauska, V. Hrkac, T. Dankwort, R. Jahns, H. J. Quenzer, R. Knöchel, L. Kienle, and B. Wagner. "Sputtered thin film piezoelectric aluminum nitride as a functional MEMS material." In: *Microsystem Technologies* 18.6 (2012), pp. 787–795. ISSN: 0946-7076.

[36] B. Jaffe, W. R. Cook, and H. Jaffe. *Piezoelectric Ceramics*. Vol. 3. Non-metallic solids. London: Academic Press, 1971. ISBN: 0123795508.

[37] S. K. Pandey, A. R. James, R. Raman, S. N. Chatterjee, A. Goyal, C. Prakash, and T. C. Goel. "Structural, ferroelectric and optical properties of PZT thin films." In: *Physica B: Condensed Matter* 369.1-4 (2005), pp. 135–142. ISSN: 09214526.

[38] N. Sama, C. Soyer, D. Remiens, C. Verrue, and R. Bouregba. "Bottom and top electrodes nature and PZT film thickness influence on electrical properties." In: *Sensors and Actuators A: Physical* 158.1 (2010), pp. 99–105. ISSN: 0924-4247.

[39] N. Ledermann, P. Muralt, J. Baborowski, S. Gentil, K. Mukati, M. Cantoni, A. Seifert, and N. Setter. "1 0 0-Textured, piezoelectric Pb(Zrx, Ti1−x)O3 thin films for MEMS: Integration, deposition and properties." In: *Sensors and Actuators A: Physical* 105.2 (2003), pp. 162–170. ISSN: 0924-4247.

[40] J. E. Northrup, R. Di Felice, and J. Neugebauer. "Atomic structure and stability of AlN(0001) and (000-1) surfaces." In: *Physical Review B* 55.20 (1997), pp. 13878–13883.

[41] E. Milyutin, S. Harada, D. Martin, J. F. Carlin, N. Grandjean, V. Savu, O. Vaszquez-Mena, J. Brugger, and P. Muralt. "Sputtering of (001)AlN thin films: Control of polarity by a seed layer." In: *Journal of Vacuum Science & Technology B* 28.6 (2010), pp. L61–L63.

[42] F. Bernardini, V. Fiorentini, and D. Vanderbilt. "Spontaneous polarization and piezoelectric constants of III-V nitrides." In: *Physical Review B* 56.16 (1997), R10024–R10027.

[43] J. Cervenka, D. W. M. Lau, N. Dontschuk, O. Shimoni, L. Silvestri, F. Ladouceur, S. G. Duvall, and S. Prawer. "Nucleation and Chemical Vapor Deposition Growth of Polycrystalline Diamond on Aluminum Nitride: Role of Surface Termination and Polarity." In: *Crystal Growth & Design* 13.8 (2013), pp. 3490–3497. ISSN: 1528-7483.

[44] B. D. Cullity and C. D. Graham. *Introduction to Magnetic Materials*. 2nd ed. Somerset: Wiley, 2011. ISBN: 978-1-118-21149-6.

[45] S. Chikazumi and C. D. Graham. *Physics of Ferromagnetism*. 2nd ed. Vol. 94. International series of monographs on physics. Oxford: Clarendon Press, 1997. ISBN: 0198517769.

[46] C. Kittel. *Introduction to Solid State Physics*. 8th ed. Hoboken, N.J.: John Wiley, 2005. ISBN: 0-471-41526-X.

[47] Metglas2714a. *Magnetic Alloy Used in Distribution and Power Transformers, Access Date: 01.03.2017*. URL: `http://www.metglas.com/products/magnetic_materials/2714a.asp`.

[48] L. Landau and E. Lifshitz. "On the theory of the dispersion of magnetic permeability in ferromagnetic bodies." In: *Physikalische Zeitschrift der Sowjetunion* 8.153 (1935), pp. 101–114.

[49] J. P. Joule. "XVII. On the effects of magnetism upon the dimensions of iron and steel bars." In: *Philosophical Magazine Series 3* 30.199 (2009), pp. 76–87. ISSN: 1941-5966.

[50] R. D. James and M. Wuttig. “Magnetostriction of martensite.” In: *Philosophical Magazine A* 77.5 (2009), pp. 1273–1299. ISSN: 0141-8610.

[51] E. Villari. “Uber die Anderungen des magnetischen Moments, welche der Zug und das Hindurchleiten eines galvanischen Stroms in einem Stabe von Stahl oder Eisen hervorbringen.” In: *Annalen der Physik* 202.9 (1865), pp. 87–122. ISSN: 00033804.

[52] R. Boll and K. J. Overshott. *Sensors*. Vol. 5. Weinheim, Germany: Wiley-VCH Verlag GmbH, 1989. ISBN: 9783527620166.

[53] Du Trémolet de Lacheisserie, E. *Magnetostriction: Theory and Applications of Magnetoelasticity*. Boca Raton, FL: CRC Press, 1993. ISBN: 0849369347.

[54] L. Sandlund, M. Fahlander, T. Cedell, A. E. Clark, J. B. Restorff, and M. Wun-Fogle. “Magnetostriction, elastic moduli, and coupling factors of composite Terfenol-D.” In: *Journal of Applied Physics* 75.10 (1994), pp. 5656–5658. ISSN: 0021-8979.

[55] “IEEE Standard on Magnetostrictive Materials: Piezomagnetic Nomenclature.” In: *IEEE Std 319-1990* (1991).

[56] J. Zhai, Z. Xing, Dong, S. Li, J., and D. Viehland. “Thermal noise cancellation in symmetric magnetoelectric bimorph laminates.” In: *Applied Physics Letters* 93.7 (2008), p. 072906. ISSN: 0003-6951.

[57] G. Srinivasan, E. T. Rasmussen, J. Gallegos, R. Srinivasan, Yu. I. Bokhan, and V. M. Laletin. “Magnetoelectric bilayer and multilayer structures of magnetostrictive and piezoelectric oxides.” In: *Physical Review B* 64.21 (2001), p. 214408.

[58] A. E. Clark and H. S. Belson. “Giant Room-Temperature Magnetostrictions in TbFe2 and DyFe2.” In: *Physical Review B* 5.9 (1972), pp. 3642–3644.

[59] E. Quandt and A. Ludwig. “Giant magnetostrictive multilayers.” In: *Journal of Applied Physics* 85.8 (1999), pp. 6232–6237. ISSN: 0021-8979.

[60] A. Ludwig and E. Quandt. “Giant magnetostrictive thin films for applications in microelectromechanical systems.” In: *Journal of Applied Physics* 87.9 (2000), pp. 4691–4695. ISSN: 0021-8979.

[61] S. Dong, J. Zhai, N. Wang, F. Bai, J. Li, D. Viehland, and T. A. Lograsso. “Fe–Ga-Pb(Mg1-3Nb2-3)O3–PbTiO3 magnetoelectric laminate composites.” In: *Applied Physics Letters* 87.22 (2005), p. 222504. ISSN: 0003-6951.

[62] S. Priya, R. Islam, S. Dong, and D. Viehland. “Recent advancements in magnetoelectric particulate and laminate composites.” In: *Journal of Electroceramics* 19.1 (2007), pp. 149–166. ISSN: 1385-3449.

[63] M. C. Zhang, H. L. Jiang, X. X. Gao, J. Zhu, and S. Z. Zhou. “Magnetostriction and microstructure of the melt-spun Fe83Ga17 alloy.” In: *Journal of Applied Physics* 99.2 (2006), p. 023903. ISSN: 0021-8979.

[64] A. E. Clark, M. Wun-Fogle, J. B. Restorff, T. A. Lograsso, and J. R. Cullen. “Effect of quenching on the magnetostriction on Fe1-xGax (0.13x lt;0.21).” In: *IEEE Transactions on Magnetics* 37.4 (2001), pp. 2678–2680. ISSN: 0018-9464.

[65] J. Lou, M. Liu, D. Reed, Y. Ren, and N. X. Sun. “Giant electric field tuning of magnetism in novel multiferroic FeGaB/Lead Zinc Niobate-Lead Titanate (PZN-PT) heterostructures.” In: *Advanced Materials* 21.46 (2009), pp. 4711–4715. ISSN: 09359648.

[66] J. Lou, R. E. Insignares, Z. Cai, K. S. Ziemer, M. Liu, and N. X. Sun. “Soft magnetism, magnetostriction, and microwave properties of FeGaB thin films.” In: *Applied Physics Letters* 91.18 (2007), p. 182504. ISSN: 0003-6951.

[67] Metglas2605SA1. *Magnetic Alloy Used in Amorphous Metal Transformers, Access Date: 01.03.2017*. URL: `http://metglas.com/products/magnetic_materials/2605SA1.asp`.

[68] H. Palneedi, V. Annapureddy, S. Priya, and J. Ryu. “Status and perspectives of multiferroic magnetoelectric composite materials and applications.” In: *Actuators* 5.1 (2016), p. 9. ISSN: 2076-0825.

[69] S. Dong, J. Zhai, F. Bai, J.-F. Li, and D. Viehland. “Push-pull mode magnetostrictive / piezoelectric laminate composite with an enhanced magnetoelectric voltage coefficient.” In: *Applied Physics Letters* 87.6 (2005), p. 062502. ISSN: 0003-6951.

[70] R. W. Cahn and P. Haasen. *Physical Metallurgy*. 4th, revised and enhanced edition. Amsterdam: North-Holland, 1996. ISBN: 9780444898753.

[71] D. C. Hofmann. “Bulk metallic glasses and their composites: A brief history of diverging fields.” In: *Journal of Materials* 2013.12 (2013), pp. 1–8. ISSN: 2314-4866.

[72] H. Greve, E. Woltermann, H.-J. Quenzer, B. Wagner, and E. Quandt. “Giant magnetoelectric coefficients in (Fe90Co10)78Si12B10-AlN thin film composites.” In: *Applied Physics Letters* 96.18 (2010). ISSN: 0003-6951.

[73] E. Yarar, S. Salzer, V. Hrkac, A. Piorra, M. Höft, R. Knöchel, L. Kienle, and E. Quandt. “Inverse bilayer magnetoelectric thin film sensor.” In: *Applied Physics Letters* 109.2 (2016), p. 022901. ISSN: 0003-6951.

[74] Du Trémolet de Lacheisserie, E. and J. C. Peuzin. “Magnetostriction and internal stresses in thin films: The cantilever method revisited.” In: *Journal of Magnetism and Magnetic Materials* 136.1–2 (1994), pp. 189–196. ISSN: 0304-8853.

[75] N. A. Spaldin and M. Fiebig. “The renaissance of magnetoelectric multiferroics.” In: *Science (New York, N.Y.)* 309.5733 (2005), pp. 391–392. ISSN: 0036-8075.

[76] P. Curie. “Sur la symétrie dans les phénomènes physiques, symétrie d’un champ électrique et d’un champ magnétique.” In: *Journal de Physique Théorique et Appliquée* 3.1 (1894), pp. 393–415. ISSN: 0368-3893.

[77] I. E. Dzyaloshinskii. “On the magneto-electrical effect in antiferromagnets.” In: *Soviet Physics JETP* 10.3 (1960), pp. 628–629.

[78] D. N. Astrov. “Magnetoelectric effect in chromium oxide.” In: *Soviet Physics JETP* 13.4 (1961), pp. 729–733.

[79] M. Fiebig. “Revival of the magnetoelectric effect.” In: *Journal of Physics D: Applied Physics* 38.8 (2005), R123–R152.

[80] T. H. O’Dell. “The field invariants in a magneto-electric medium.” In: *Philosophical Magazine* 8.87 (1963), pp. 411–418. ISSN: 0031-8086.

[81] J. Wang, J. B. Neaton, H. Zheng, V. Nagarajan, S. B. Ogale, B. Liu, D. Viehland, D. G. Schlom, U. V. Waghmare, V. Vaithyanathan, N. A. Spaldin, K. M. Rabe, M. Wuttig, and R. Ramesh. “Epitaxial BiFeO3 multiferroic thin film heterostructures.” In: *Science (New York)* 299.5613 (2003), pp. 1719–1722.

[82] J. van Suchtelen. “Product Properties: A New Application of Composite Materials.” In: *Philips Research Reports* 27.1 (1972), pp. 28–37.

[83] J. van den Boomgaard, D. R. Terrell, R. A. J. Born, and H. F. J. I. Giller. “An in situ grown eutectic magnetoelectric composite material.” In: *Journal of Materials Science* 9.10 (1974), pp. 1705–1709. ISSN: 0022-2461.

[84] H. Schmid. “Multi-ferroic magnetoelectrics.” In: *Ferroelectrics* 162.1 (1994), pp. 317–338. ISSN: 0015-0193.

[85] W. Eerenstein, N. D. Mathur, and James F. Scott. “Multiferroic and magnetoelectric materials.” In: *Nature* 442.7104 (2006), pp. 759–765.

[86] L. W. Martin, S. P. Crane, Y-H Chu, M. B. Holcomb, M. Gajek, M. Huijben, C-H Yang, N. Balke, and R. Ramesh. “Multiferroics and magnetoelectrics: Thin films and nanostructures.” In: *Journal of Physics: Condensed Matter* 20.43 (2008), p. 434220.

[87] W. F. Brown, R. M. Hornreich, and S. Shtrikman. “Upper bound on the magnetoelectric susceptibility.” In: *Physical Review* 168.2 (1968), pp. 574–577.

[88] J. P. Velev, S. S. Jaswal, and E. Y. Tsymbal. “Multi-ferroic and magnetoelectric materials and interfaces.” In: *Philosophical Transactions of the Royal Society of London A: Mathematical, Physical and Engineering Sciences* 369.1948 (2011), pp. 3069–3097.

[89] Y. Wang, J. Hu, Y. Lin, and C.-W. Nan. “Multiferroic magnetoelectric composite nanostructures.” In: *NPG Asia Materials* 2.2 (2010), pp. 61–68.

[90] S. Dong, J.-M. Liu, S.-W. Cheong, and Z. Ren. “Multiferroic materials and magnetoelectric physics: Symmetry, entanglement, excitation, and topology.” In: *Advances in Physics* 64.5-6 (2015), pp. 519–626. ISSN: 0001-8732.

[91] H. Das, A. L. Wysocki, Y. Geng, W. Wu, and C. J. Fennie. “Bulk magnetoelectricity in the hexagonal manganites and ferrites.” In: *Nature communications* 5 (2014), p. 2998. ISSN: 2041-1723.

[92] C.-W. Nan. “Magnetoelectric effect in composites of piezoelectric and piezomagnetic phases.” In: *Physical Review B* 50.9 (1994), pp. 6082–6088.

[93] MatWeb Material Property. *Terfenol-D Magnetostrictive Smart Material (Tb0.3Dy0.7Fe1.92), Access Date: 01.03.2017*. 2017. URL: http://www.matweb.com/search/datasheet.aspx?matguid=aa68cad05c7c4d39932834d68e669a5d&ckck=1.

[94] C.-W. Nan, M. I. Bichurin, S. Dong, D. Viehland, and G. Srinivasan. “Multiferroic magnetoelectric composites: Historical perspective, status, and future directions.” In: *Journal of Applied Physics* 103.3 (2008). ISSN: 0021-8979.

[95] R. E. Newnham, D. P. Skinner, and L. E. Cross. “Connectivity and piezoelectric-pyroelectric composites.” In: *Materials Research Bulletin* 13.5 (1978), pp. 525–536. ISSN: 0025-5408.

[96] J. Ryu, S. Priya, A. V. Carazo, K. Uchino, and H.-E. Kim. “Effect of the magnetostrictive layer on magnetoelectric properties in Lead Zirconate Titanate / Terfenol-D laminate composites.” In: *Journal of the American Ceramic Society* 84.12 (2001), pp. 2905–2908. ISSN: 0002-7820.

[97] J. Ryu, S. Priya, K. Uchino, and H.-E. Kim. “Magnetoelectric effect in composites of magnetostrictive and piezoelectric materials.” In: *Journal of Electroceramics* 8.2 (2002), pp. 107–119. ISSN: 1385-3449.

[98] S. Dong, J. Zhai, J. Li, and D. Viehland. “Near-ideal magnetoelectricity in high-permeability magnetostrictive/piezofiber laminates with a (2-1) connectivity.” In: *Applied Physics Letters* 89.25 (2006), p. 252904. ISSN: 0003-6951.

[99] M. Li, Y. Wang, J. Gao, J. Li, and D. Viehland. “Enhanced magnetoelectric effect in self-stressed multi-push-pull mode Metglas/Pb(Zr,Ti)O3/Metglas laminates.” In: *Applied Physics Letters* 101.2 (2012). ISSN: 0003-6951.

[100] J. Zhai, S. Dong, Z. Xing, J. Li, and D. Viehland. “Giant magnetoelectric effect in Metglas / polyvinylidene fluoride laminates.” In: *Applied Physics Letters* 89.8 (2006). ISSN: 0003-6951.

[101] G. Srinivasan, I. V. Zavislyak, and A. S. Tatarenko. “Millimeter-wave magnetoelectric effects in bilayers of barium hexaferrite and lead zirconate titanate.” In: *Applied Physics Letters* 89.15 (2006), p. 152508. ISSN: 0003-6951.

[102] Z. Wang, L. Yan, Y. Yang, J.-F. Li, J. Das, A. L. Geiler, A. Yang, Y. Chen, V. G. Harris, and D. Viehland. "Magnetoelectric effect in crystallographically textured BaTiO3 films deposited on ferromagnetic metallic glass foils." In: *Journal of Applied Physics* 109.3 (2011). ISSN: 0021-8979.

[103] P. Zhao, Z. Zhao, D. Hunter, R. Suchoski, C. Gao, S. Mathews, M. Wuttig, and I. Takeuchi. "Fabrication and characterization of all-thin-film magnetoelectric sensors." In: *Applied Physics Letters* 94.24 (2009). ISSN: 0003-6951.

[104] E. Quandt, S. Stein, and M. Wuttig. "Magnetic vector field sensor using magnetoelectric thin-film composites." In: *IEEE Transactions on Magnetics* 41.10 (2005), pp. 3667–3669. ISSN: 0018-9464.

[105] H. Zheng, J. Wang, S. E. Lofland, Z. Ma, L. Mohaddes-Ardabili, T. Zhao, L. Salamanca-Riba, S. R. Shinde, S. B. Ogale, F. Bai, D. Viehland, Y. Jia, D. G. Schlom, M. Wuttig, A. Roytburd, and R. Ramesh. "Multiferroic BaTiO3-CoFe2O4 Nanostructures." In: *Science (New York)* 303.5658 (2004), pp. 661–663.

[106] H. Greve, E. Woltermann, R. Jahns, S. Marauska, B. Wagner, R. Knöchel, M. Wuttig, and E. Quandt. "Low damping resonant magnetoelectric sensors." In: *Applied Physics Letters* 97.15 (2010). ISSN: 0003-6951.

[107] S. Cho. "Effect of nitrogen flow ratio on the structural and optical properties of aluminum nitride thin films." In: *Journal of Crystal Growth* 326.1 (2011), pp. 179–182. ISSN: 0022-0248.

[108] D. R. Tilley and J. F. Scott. "Frequency dependence of magnetoelectric phenomena in BaMn F4." In: *Physical Review B* 25.5 (1982), pp. 3251–3260. ISSN: 0163-1829.

[109] M. I. Bichurin, V. M. Petrov, and G. Srinivasan. "Theory of low-frequency magnetoelectric coupling in magnetostrictive-piezoelectric bilayers." In: *Physical Review B* 68.5 (2003), p. 054402.

[110] J. G. Wan, Z. Y. Li, Y. Wang, M. Zeng, G. H. Wang, and J.-M. Liu. "Strong flexural resonant magnetoelectric effect in Terfenol-D-epoxy-Pb(Zr,Ti)O3 bilayer." In: *Applied Physics Letters* 86.20 (2005), p. 202504. ISSN: 0003-6951.

[111] Z. Xing, S. Dong, J. Zhai, L. Yan, J. Li, and D. Viehland. "Resonant bending mode of Terfenol-D-steel-Pb(Zr,Ti)O3 magnetoelectric laminate composites." In: *Applied Physics Letters* 89.11 (2006), p. 112911. ISSN: 0003-6951.

[112] F. R. Blom. "Dependence of the quality factor of micromachined silicon beam resonators on pressure and geometry." In: *Journal of Vacuum Science & Technology B: Microelectronics and Nanometer Structures* 10.1 (1992), p. 19.

[113] I. Petrov, P. B. Barna, L. Hultman, and J. E. Greene. “Microstructural evolution during film growth.” In: *Journal of Vacuum Science & Technology A* 21.5 (2003), S117–S128.

[114] C. Kirchhof, M. Krantz, I. Teliban, R. Jahns, S. Marauska, B. Wagner, R. Knöchel, M. Gerken, D. Meyners, and E. Quandt. “Giant magnetoelectric effect in vacuum.” In: *Applied Physics Letters* 102.23 (2013). ISSN: 0003-6951.

[115] F. Lochon, I. Dufour, and D. Rebière. “An alternative solution to improve sensitivity of resonant microcantilever chemical sensors: Comparison between using high-order modes and reducing dimensions.” In: *Sensors and Actuators B: Chemical* 108.1–2 (2005), pp. 979–985. ISSN: 0925-4005.

[116] T. B. Gabrielson. “Mechanical-thermal noise in micromachined acoustic and vibration sensors.” In: *IEEE Transactions on Electron Devices* 40.5 (1993), pp. 903–909. ISSN: 0018-9383.

[117] R. Jahns, R. Knöchel, H. Greve, E. Woltermann, E. Lage, and E. Quandt. “Magnetoelectric sensors for biomagnetic measurements.” In: *Medical Measurements and Applications Proceedings (MeMeA), 2011 IEEE International Workshop on*. 2011, pp. 107–110.

[118] U. B. Bala, M. C. Krantz, and M. Gerken. “Electrode position optimization in magnetoelectric sensors based on magnetostrictive-piezoelectric bilayers on cantilever substrates.” In: *IEEE transactions on ultrasonics, ferroelectrics, and frequency control* 61.3 (2014), pp. 392–398. ISSN: 0885-3010.

[119] G. Srinivasan, S. Priya, and Nian X. Sun. *Composite Magnetoelectrics: Materials, Structures, and Applications*. Vol. 62. Woodhead Publishing series in electronic and optical materials. ISBN: 9781782422549.

[120] S. Dong, J.-F. Li, and D. Viehland. “Ultra high magnetic field sensitivity in laminates of Terfenol-D and Pb(Mg1/3Nb2/3)O3–PbTiO3 crystals.” In: *Applied Physics Letters* 83.11 (2003), pp. 2265–2267. ISSN: 0003-6951.

[121] N. Tiercelin, A. Talbi, V. Preobrazhensky, P. Pernod, V. Mortet, K. Haenen, and A. Soltani. “Magnetoelectric effect near spin reorientation transition in giant magnetostrictive-aluminum nitride thin film structure.” In: *Applied Physics Letters* 93.16 (2008). ISSN: 0003-6951.

[122] M. Li, Z. Wang, Y. Wang, J. Li, and D. Viehland. “Giant magnetoelectric effect in self-biased laminates under zero magnetic field.” In: *Applied Physics Letters* 102.8 (2013), p. 082404. ISSN: 0003-6951.

[123] S. Marauska, R. Jahns, C. Kirchhof, M. Claus, E. Quandt, R. Knöchel, and B. Wagner. “Highly sensitive wafer-level packaged MEMS magnetic field sensor based on magnetoelectric composites.” In: *Sensors and Actuators A: Physical* 189 (2013), pp. 321–327. ISSN: 0924-4247.

[124] E. Lage, C. Kirchhof, V. Hrkac, L. Kienle, R. Jahns, R. Knochel, E. Quandt, and D. Meyners. “Exchange biasing of magnetoelectric composites.” In: *Nature materials* 11.6 (2012), pp. 523–529. ISSN: 1476-1122.

[125] V. Röbisch, E. Yarar, N. O. Urs, I. Teliban, R. Knöchel, J. McCord, E. Quandt, and D. Meyners. “Exchange biased magnetoelectric composites for magnetic field sensor application by frequency conversion.” In: *Journal of Applied Physics* 117.17 (2015). ISSN: 0021-8979.

[126] S. Salzer, R. Jahns, A. Piorra, I. Teliban, J. Reermann, M. Höft, E. Quandt, and R. Knöchel. “Tuning fork for noise suppression in magnetoelectric sensors.” In: *Sensors and Actuators A: Physical* 237 (2016), pp. 91–95. ISSN: 0924-4247.

[127] M. J. Madou. *Fundamentals of Microfabrication*. CRC Press, 1997. ISBN: 0849394511.

[128] L. E. Scriven. “Physics and applications of dipcoating and spin coating.” In: *MRS Proceedings* 121 (1988), p. 244.

[129] G. Yi, Z. Wu, and M. Sayer. “Preparation of Pb(Zr,Ti)O3 thin films by sol gel processing: Electrical, optical, and electro-optic properties.” In: *Journal of Applied Physics* 64.5 (1988), pp. 2717–2724. ISSN: 0021-8979.

[130] H. M. Manasevit. “Recollections and reflections of MO-CVD.” In: *Journal of Crystal Growth* 55.1 (1981), pp. 1–9. ISSN: 0022-0248.

[131] M. R. Hilton, L. R. Narasimhan, S. Nakamura, M. Salmeron, and G. A. Somorjai. “Composition, morphology and mechanical properties of plasma-assisted chemically vapor-deposited TiN films on M2 tool steel.” In: *Thin Solid Films* 139.3 (1986), pp. 247–260. ISSN: 0040-6090.

[132] R. W. Johnson, A. Hultqvist, and S. F. Bent. “A brief review of atomic layer deposition: From fundamentals to applications.” In: *Materials Today* 17.5 (2014), pp. 236–246. ISSN: 13697021.

[133] R. Behrisch, ed. *Sputtering by Particle Bombardment I: Physical Sputtering of Single-Element Solids*. Vol. 47. Topics in Applied Physics. Berlin and Heidelberg: Springer, 1981. ISBN: 9783540105213.

[134] R. Eason, ed. *Pulsed Laser Deposition of Thin Films: Applications-led Growth of Functional Materials*. Hoboken, N.J.: Wiley-Interscience, 2007. ISBN: 0471447099.

[135] A. Y. Cho and J. R. Arthur. “Molecular beam epitaxy.” In: *Progress in Solid State Chemistry* 10 (1975), pp. 157–191. ISSN: 00796786.

[136] K. Seshan, ed. *Handbook of Thin Film Deposition: Techniques, Processes, and Technologies*. 3rd ed. Amsterdam and Boston: Elsevier, 2012. ISBN: 1437778739.

[137] D. L. Smith. *Thin-film Deposition: Principles and Practice*. New York and London: McGraw-Hill, 1995. ISBN: 0071139133.

[138] M. Ohring. *The Materials Science of Thin Films: Deposition and Structure*. Beijing: World Pub. Corp, 2006. ISBN: 9787506282079.

[139] M. A. Lieberman and A. J. Lichtenberg. *Principles of plasma discharges and materials processing*. 2nd ed. Hoboken, N.J. and Chichester: Wiley-Interscience, 2005. ISBN: 0471720011.

[140] S. Berg and T. Nyberg. "Fundamental understanding and modeling of reactive sputtering processes." In: *Thin Solid Films* 476.2 (2005), pp. 215–230. ISSN: 0040-6090.

[141] D. Depla and R. de Gryse. "Target poisoning during reactive magnetron sputtering: Part I: the influence of ion implantation." In: *Surface and Coatings Technology* 183.2-3 (2004), pp. 184–189. ISSN: 0257-8972.

[142] L. B. Jonsson, T. Nyberg, and S. Berg. "Target compound layer formation during reactive sputtering." In: *Journal of Vacuum Science & Technology A: Vacuum, Surfaces, and Films* 17.4 (1999), pp. 1827–1831. ISSN: 0734-2101.

[143] J. W. Bradley and T. Welzel. "Physics and phenomena in pulsed magnetrons: An overview." In: *Journal of Physics D: Applied Physics* 42.9 (2009), p. 093001.

[144] W. D. Sproul, D. J. Christie, and D. C. Carter. "Control of reactive sputtering processes." In: *Thin Solid Films* 491.1–2 (2005), pp. 1–17. ISSN: 0040-6090.

[145] J. Sellers. "Asymmetric bipolar pulsed DC: The enabling technology for reactive PVD." In: *Surface and Coatings Technology* 98.13 (1998), pp. 1245–1250. ISSN: 0257-8972.

[146] K. Reichelt. "Nucleation and growth of thin films." In: *Vacuum* 38.12 (1988), pp. 1083–1099.

[147] J. A. Thornton. "High rate thick film growth." In: *Annual review of materials science* 7.1 (1977), pp. 239–260.

[148] J. A. Thornton. "The microstructure of sputter deposited coatings." In: *Journal of Vacuum Science & Technology A* 4.6 (1986), pp. 3059–3065.

[149] P. B. Barna and M. Adamik. "Fundamental structure forming phenomena of polycrystalline films and the structure zone models." In: *Thin Solid Films* 317.1-2 (1998), pp. 27–33. ISSN: 0040-6090.

[150] R. Messier, A. P. Giri, and R. A. Roy. "Revised structure zone model for thin film physical structure." In: *Journal of Vacuum Science & Technology A* 2.2 (1984), pp. 500–503.

[151] D. Liufu and K. C. Kao. "Piezoelectric, dielectric, and interfacial properties of aluminum nitride films." In: *Journal of Vacuum Science & Technology A* 16.4 (1998), pp. 2360–2366.

[152] M. Tabbal, P. Mérel, M. Chaker, and H. Pépin. "Pulsed laser deposition of c-axis oriented aluminum nitride thin films on silicon." In: *The European Physical Journal Applied Physics* 14.2 (2001), pp. 115–119. ISSN: 1286-0042.

[153] T. L. Hu, S. W. Mao, C. P. Chao, M. F. Wu, H. L. Huang, and D. Gan. “Deposition characteristics of AlN thin film prepared by the dual ion beam sputtering system.” In: *Journal of Electronic Materials* 36.1 (2007), pp. 81–87.

[154] G. Kipshidze, S. Nikishin, V. Kuryatkov, K. Choi, Iu. Gherasoiu, T. Prokofyeva, M. Holtz, H. Temkin, K. D. Hobart, F. J. Kub, and M. Fatemi. “High quality AIN and GaN grown on compliant Si/SiC substrates by gas source molecular beam epitaxy.” In: *Journal of Electronic Materials* 30.7 (2001), pp. 825–828. ISSN: 0361-5235.

[155] G. Meng, X. Liu, S. Xie, and D. Peng. “<0001>-oriented growth of AlN films on Si (111) by microwave plasma CVD with AlBr3-NH3-N2 system.” In: *Journal of Crystal Growth* 163.3 (1996), pp. 232–237. ISSN: 0022-0248.

[156] K. Tonisch, V. Cimalla, Ch. Foerster, D. Dontsov, and O. Ambacher. “Piezoelectric properties of thin AlN layers for MEMS application determined by piezoresponse force microscopy.” In: *physica status solidi (c)* 3.6 (2006), pp. 2274–2277. ISSN: 1610-1634.

[157] F. Martin, P. Muralt, M. Cantoni, and M. A. Dubois. “Re-growth of c-axis oriented AlN thin films.” In: *Ultrasonics Symposium, 2004 IEEE*. Vol. 1. 2004, pp. 169–172.

[158] Farotex Limited. *A brief explanation of how magnetron sputtering works, Access Date: 01.03.2017*. URL: `http://farotex.com/technology.html`.

[159] Z.-X. Lin, S. Wu, R. Ro, and M.-S. Lee. “Surface acoustic wave properties of (100) AlN films on diamond with different IDT positions.” In: *IEEE transactions on ultrasonics, ferroelectrics, and frequency control* 56.6 (2009), pp. 1246–1251. ISSN: 0885-3010.

[160] G. F. Iriarte, F. Engelmark, and I. V. Katardjiev. “Reactive sputter deposition of highly oriented AlN films at room temperature.” In: *Journal of Materials Research* 17.06 (2002), pp. 1469–1475.

[161] W.-J. Liu, S.-J. Wu, C.-M. Chen, Y.-C. Lai, and C.-H. Chuang. “Microstructural evolution and formation of highly c-axis-oriented aluminum nitride films by reactively magnetron sputtering deposition.” In: *Journal of Crystal Growth* 276.3-4 (2005), pp. 525–533. ISSN: 0022-0248.

[162] M. Clement, E. Iborra, J. Sangrador, A. Sanz-Hervas, L. Vergara, and M. Aguilar. “Influence of sputtering mechanisms on the preferred orientation of aluminum nitride thin films.” In: *Journal of Applied Physics* 94.3 (2003), pp. 1495–1500. ISSN: 0021-8979.

[163] R. D. Gould and S. A. Awan. “Dielectric properties of AlNx thin films prepared by RF magnetron sputtering of Al using a N2/Ar sputtering gas mixture.” In: *Thin Solid Films* 469-470 (2004), pp. 184–189. ISSN: 0040-6090.

[164] J. P. Kar, G. Bose, and S. Tuli. “Correlation of electrical and morphological properties of sputtered aluminum nitride films with deposition temperature.” In: *Current Applied Physics* 6.5 (2006), pp. 873–876. ISSN: 1567-1739.

[165] F. Engelmark, G. F. Iriarte, I. V. Katardjiev, M. Ottosson, P. Muralt, and S. Berg. “Structural and electroacoustic studies of AlN thin films during low temperature radio frequency sputter deposition.” In: *Journal of Vacuum Science & Technology A* 19.5 (2001), pp. 2664–2669.

[166] M. Akiyama, K. Nagao, N. Ueno, H. Tateyama, and T. Yamada. “Influence of metal electrodes on crystal orientation of aluminum nitride thin films.” In: *Vacuum* 74.3 (2004), pp. 699–703.

[167] G. F. Iriarte, J. G. Rodríguez, and F. Calle. “Synthesis of c-axis oriented AlN thin films on different substrates: A review.” In: *Materials Research Bulletin* 45.9 (2010), pp. 1039–1045. ISSN: 0025-5408.

[168] H.-C. Lee, G.-H. Kim, S.-K. Hong, K.-Y. Lee, Y.-J. Yong, C.-H. Chun, and J.-Y. Lee. “Influence of sputtering pressure on the microstructure evolution of AlN thin films prepared by reactive sputtering.” In: *Thin Solid Films* 261.1-2 (1995), pp. 148–153. ISSN: 0040-6090.

[169] G. F. Iriarte, J. G. Rodriguez, and F. Calle. “Effect of substrate–target distance and sputtering pressure in the synthesis of AlN thin films.” In: *Microsystem Technologies* 17.3 (2011), pp. 381–386. ISSN: 0946-7076.

[170] F. Medjani, R. Sanjines, G. Allidi, and A. Karimi. “Effect of substrate temperature and bias voltage on the crystallite orientation in RF magnetron sputtered AlN thin films.” In: *Thin Solid Films* 515.1 (2006), pp. 260–265. ISSN: 0040-6090.

[171] M. Schneider, A. Bittner, and U. Schmid. “Impact of film thickness on the temperature-activated leakage current behavior of sputtered aluminum nitride thin films.” In: *Sensors and Actuators A: Physical* 224 (2015), pp. 177–184. ISSN: 0924-4247.

[172] M. Dubois and P. Muralt. “Stress and piezoelectric properties of aluminum nitride thin films deposited onto metal electrodes by pulsed direct current reactive sputtering.” In: *Journal of Applied Physics* 89.11 (2001), pp. 6389–6395. ISSN: 0021-8979.

[173] T. P. Drüsedau and J. Bläsing. “Optical and structural properties of highly c-axis oriented aluminum nitride prepared by sputter-deposition in pure nitrogen.” In: *Thin Solid Films* 377–378 (2000), pp. 27–31. ISSN: 0040-6090.

[174] H. L. Kao, P. J. Shih, and C.-H. Lai. “The study of preferred orientation growth of aluminum nitride thin films on ceramic and glass substrates.” In: *Japanese Journal of Applied Physics* 38.Part 1, No. 3A (1999), pp. 1526–1529. ISSN: 0021-4922.

[175] X.-H. Xu, H.-S. Wu, C.-J. Zhang, and Z.-H. Jin. “Morphological properties of AlN piezoelectric thin films deposited by DC reactive magnetron sputtering.” In: *Thin Solid Films* 388.1–2 (2001), pp. 62–67. ISSN: 0040-6090.

[176] V. Dumitru, C. Morosanu, V. Sandu, and A. Stoica. “Optical and structural differences between RF and DC AlxNy magnetron sputtered films.” In: *Thin Solid Films* 359.1 (2000), pp. 17–20. ISSN: 0040-6090.

[177] M. Fujiki, M. Takahashi, S. Kikkawa, and F. Kanamaru. “Microstructure and preferred orientation in rf sputter deposited AlN thin film.” In: *Journal of Materials Science Letters* 19.18 (2000), pp. 1625–1627. ISSN: 02618028.

[178] H. Cheng, Y. Sun, and P. Hing. “The influence of deposition conditions on structure and morphology of aluminum nitride films deposited by radio frequency reactive sputtering.” In: *Thin Solid Films* 434.1–2 (2003), pp. 112–120. ISSN: 0040-6090.

[179] P. E. Walker and W. H. Tarn. *CRC Handbook of Metal Etchants*. 1991. ISBN: 0849336236.

[180] S. Zabel, C. Kirchhof, E. Yarar, D. Meyners, E. Quandt, and F. Faupel. “Phase modulated magnetoelectric delta-E effect sensor for sub-nano tesla magnetic fields.” In: *Applied Physics Letters* 107.15 (2015), p. 152402. ISSN: 0003-6951.

[181] Advanced Energy. *Pinnacle Series DC Magnetron Power Supplies - Access date: 01.03.2017*. URL: http://www.advanced-energy.com/upload/File/DC/SL-PNCL-210-04.pdf.

[182] F. Martin, P. Muralt, M.-A. Dubois, and A. Pezous. “Thickness dependence of the properties of highly c-axis textured AlN thin films.” In: *Journal of Vacuum Science & Technology A* 22.2 (2004), pp. 361–365.

[183] Oxford Instruments. *Ionfab300 Ion Beam Etching (IBE) - Access date 01.03.2017*. URL: https://www.oxford-instruments.com/products/etching-deposition-and-growth/tools/ionfab/ion-beam-system-ionfab-300plus.

[184] P. Williams. “Secondary ion mass spectrometry.” In: *Annual review of materials science* 15.1 (1985), pp. 517–548.

[185] R. Jahns, A. Piorra, E. Lage, C. Kirchhof, D. Meyners, J. L. Gugat, M. Krantz, M. Gerken, R. Knöchel, and E. Quandt. “Giant magnetoelectric effect in thin-film composites.” In: *Journal of the American Ceramic Society* 96.6 (2013), pp. 1673–1681. ISSN: 0002-7820.

[186] National Institute of Standards and Technology. *X-ray Transition Energies Database, Access Date: 01.03.2017*. URL: http://physics.nist.gov/PhysRefData/XrayTrans/Html/search.html.

[187] W. H. Bragg and W. L. Bragg. “The reflection of X-rays by crystals.” In: *Proceedings of the Royal Society A: Mathematical, Physical and Engineering Sciences* 88.605 (1913), pp. 428–438. ISSN: 1364-5021.

[188] A. Monshi, M. R. Foroughi, and M. R. Monshi. “Modified Scherrer equation to estimate more accurately nano-crystallite size using XRD.” In: *World Journal of Nano Science and Engineering* 02.03 (2012), pp. 154–160. ISSN: 2161-4954.

[189] R. Kilaas. “Optimal and near-optimal filters in high-resolution electron microscopy.” In: *Journal of Microscopy* 190.1-2 (1998), pp. 45–51.

[190] J. C. Russ, M. A. Frs, R. Kiessling, and J. Charles. *Fundamentals of Energy Dispersive X-ray Analysis: Butterworths Monographs in Materials*. Burlington: Elsevier Science, 1984. ISBN: 9780408110310.

[191] G. Binnig, C. F. Quate, and Ch. Gerber. “Atomic force microscope.” In: *Physical Review Letters* 56.9 (1986), pp. 930–933.

[192] T. von Hofe, N. O. Urs, B. Mozooni, T. Jansen, C. Kirchhof, D. E. Bürgler, E. Quandt, and J. McCord. “Dual wavelength magneto-optical imaging of magnetic thin films.” In: *Applied Physics Letters* 103.14 (2013), p. 142410. ISSN: 0003-6951.

[193] aixACCT Systems. *aixDBLI - 8 inch wafer Double Beam Laser Interferometer, Access Date: 01.03.2017*. URL: http://www.aixacct.com/pdfs/Mems-8inchDBLI.pdf.

[194] aixACCT Systems. *aix4PB - Piezoelectric thin film characterization system for MEMS, Access Date: 01.03.2017*. URL: http://www.aixacct.com/pdfs/Mems-4PB.pdf.

[195] K. Prume, P. Muralt, F. Calame, T. Schmitz-Kempen, and S. Tiedke. “Extensive electromechanical characterization of PZT thin films for MEMS applications by electrical and mechanical excitation signals.” In: *Journal of Electroceramics* 19.4 (2007), pp. 407–411. ISSN: 1385-3449.

[196] R. Jahns, H. Greve, E. Woltermann, E. Quandt, and R. H. Knochel. “Noise performance of magnetometers with resonant thin-film magnetoelectric sensors.” In: *IEEE Transactions on Instrumentation and Measurement* 60.8 (2011), pp. 2995–3001. ISSN: 0018-9456.

[197] Sourcetronic. *ST2819A Precision LCR Meter, Access Date: 01.03.2017*. URL: https://www.sourcetronic.com/wp-content/uploads/2014/02/ST2819A_LCR_Meter_manual.pdf.

[198] G. Gottstein. *Physical Foundations of Materials Science*. Berlin, Heidelberg and s.l.: Springer, 2004. ISBN: 9783642072710.

[199] K.-S. Chen and K.-S. Ou. “Modification of curvature-based thin-film residual stress measurement for MEMS applications.” In: *Journal of Micromechanics and Microengineering* 12.6 (2002), pp. 917–924. ISSN: 0960-1317.

[200] HTSKorea. *Ambios Technology XP-2 Profilometer, Access Date: 01.03.2017*. URL: http://www.htskorea.com/product/ambios/XP-Plus%20Brochure%2010-2007.pdf.

[201] G. G. Stoney. “The tension of metallic films deposited by electrolysis.” In: *Proceedings of the Royal Society of London: Series A, Containing Papers of a Mathematical and Physical Character* 553 (1909), pp. 172–175.

[202] Lakeshore Cryotronics. *7400 Series VSM System, Access Date: 01.03.2017*. URL: http://www.lakeshore.com/products/Vibrating-Sample-Magnetometer/7400-Series-VSM/Pages/Overview.aspx.

[203] S. Foner. "Versatile and sensitive vibrating–sample magnetometer." In: *Review of Scientific Instruments* 30.7 (1959), pp. 548–557. ISSN: 0034-6748.

[204] Lakeshore Cryotronics. *Application Note, Nickel Sphere Calibration Sample, Model 730908, Access Date: 01.03.2017*. URL: http://www.lakeshore.com/Documents/F045-00-00.pdf.

[205] E. Klokholm. "The measurement of magnetostriction in ferromagnetic thin films." In: *IEEE Transactions on Magnetics* 12.6 (1976), pp. 819–821. ISSN: 0018-9464.

[206] Melles Griot. *Helium Neon laser, Access Date: 01.03.2017*. URL: https://www.idex-hs.com/optics/laser-light-sources/helium-neon-lasers/random-polarization.html.

[207] M. Hopcroft, W. D. Nix, and T. W. Kenny. "What is the Young's Modulus of Silicon?" In: *Journal of Microelectromechanical Systems* 19.2 (2010), pp. 229–238.

[208] Kepco Inc. *Bipolar power supply, Model BOP 100-4M, Access Date: 01.03.2017*. URL: http://www.kepcopower.com/1461971.pdf.

[209] Keithley Instruments Inc. *Model 6221 AC and DC Current Source, Access Date: 01.03.2017*. URL: http://www.imperial.ac.uk/media/imperial-college/research-centres-and-groups/centre-for-bio-inspired-technology/7293202.PDF.

[210] Aaronia AG. *Earth magnetic field free environment Zero-Gauss-Chamber (ZG1), Access Date: 01.03.2017*. URL: http://www.aaronia.com/products/shielding-screening/Zero-Gauss-Chamber/.

[211] P. Durdaut, S. Salzer, J. Reermann, V. Robisch, P. Hayes, A. Piorra, D. Meyners, E. Quandt, G. Schmidt, R. Knochel, and M. Hoft. "Thermal-mechanical noise in resonant thin-film magnetoelectric sensors." In: *IEEE Sensors Journal* (2017), p. 1.

[212] J. B. Johnson. "Thermal agitation of electricity in conductors." In: *Physical Review* 32.1 (1928), pp. 97–109.

[213] H. Nyquist. "Thermal agitation of electric charge in conductors." In: *Physical Review* 32.1 (1928), pp. 110–113.

[214] Analog Devices. *Ultralow Noise Amplifier AD745, High Speed, BiFET Op Amp, Access Date: 01.03.2017*. URL: http://www.analog.com/media/en/technical-documentation/data-sheets/AD745.pdf.

[215] Stanford Research Systems. *Model SR785 Dynamic Signal Analyzer, Access Date: 01.03.2017*. URL: http://www.thinksrs.com/downloads/PDFs/Manuals/SR785m.pdf.

[216] Stanford Research Systems. *Model SR830 DSP Lock-in Amplifier, Access Date: 01.03.2017*. URL: http://www.thinksrs.com/downloads/PDFs/Manuals/SR830m.pdf.

[217] P. A. Temple. "An introduction to phase–sensitive amplifiers: An inexpensive student instrument." In: *American Journal of Physics* 43.9 (1975), pp. 801–807. ISSN: 0002-9505.

[218] J. L. Gugat, M. C. Krantz, and M. Gerken. "Two-Dimensional Versus Three-Dimensional Finite-Element Method Simulations of Cantilever Magnetoelectric Sensors." In: *IEEE Transactions on Magnetics* 49.10 (2013), pp. 5287–5293. ISSN: 0018-9464.

[219] R. Ruh and A. Zangvil. "Composition and properties of hot-pressed SiC-AIN solid solutions." In: *Journal of the American Ceramic Society* 65.5 (1982), pp. 260–265. ISSN: 0002-7820.

[220] H.-C. Lee and J.-Y. Lee. "Effect of negative bias voltage on the microstructures of AlN thin films fabricated by reactive r.f. magnetron sputtering." In: *Journal of Materials Science Materials in Electronics* 8.6 (1997), pp. 385–390. ISSN: 09574522.

[221] Commission on Isotopic Abundances and Atomic Weights. *Standard Atomic Weights, Access Date: 22.03.2017*. URL: http://www.ciaaw.org/atomic-weights.htm.

[222] W. Eckstein and J. P. Biersack. "Reflection of heavy ions." In: *Zeitschrift für Physik B: Condensed Matter* 63.4 (1986), pp. 471–478.

[223] A. F. Ismail, Chandra K. K., and T. Matsuura. *Gas Separation Membranes: Polymeric and Inorganic*. Cham: Springer International Publishing, 2015. ISBN: 978-3-319-01095-3.

[224] F. Martin, P. Muralt, and M.-A. Dubois. "Process optimization for the sputter deposition of molybdenum thin films as electrode for AlN thin films." In: *Journal of Vacuum Science & Technology A* 24.4 (2006), pp. 946–952.

[225] J. Xiong, H.-S. Gu, K. Hu, and M.-Z. Hu. "Influence of substrate metals on the crystal growth of AlN films." In: *International Journal of Minerals, Metallurgy, and Materials* 17.1 (2010), pp. 98–103. ISSN: 1674-4799.

[226] R. Lanz, C. Lambert, L. Senn, L. Gabathuler, and G. J. Reynolds. "Aluminum-nitride manufacturing solution for BAW and other MEMS applications using a novel, high-uniformity PVD source." In: *Ultrasonics Symposium, 2006. IEEE* 15 (2006), pp. 1481–1485.

[227] W. P. Davey. "Precision measurements of the lattice constants of twelve common metals." In: *Physical Review* 25.6 (1925), pp. 753–761.

[228] A. Artieda, M. Barbieri, C. S. Sandu, and P. Muralt. "Effect of substrate roughness on c-oriented AlN thin films." In: *Journal of Applied Physics* 105.2 (2009). ISSN: 0021-8979.

[229] J. A. Thornton and D. W. Hoffman. "Stress-related effects in thin films." In: *Thin Solid Films* 171.1 (1989), pp. 5–31. ISSN: 0040-6090.

[230] M. Akiyama, T. Kamohara, K. Kano, A. Teshigahara, and N. Kawahara. “Influence of oxygen concentration in sputtering gas on piezoelectric response of aluminum nitride thin films.” In: *Applied Physics Letters* 93.2 (2008). ISSN: 0003-6951.

[231] A. F. Wright. “Elastic properties of zinc-blende and wurtzite AlN, GaN, and InN.” In: *Journal of Applied Physics* 82.6 (1997), pp. 2833–2839. ISSN: 0021-8979.

[232] P. Muralt, J. Antifakos, M. Cantoni, R. Lanz, and F. Martin. “Is there a better material for thin film BAW applications than AlN?” In: *Ultrasonics Symposium, 2005 IEEE*. Vol. 1. 2005, pp. 315–320.

[233] S. Tadigadapa and K. Mateti. “Piezoelectric MEMS sensors: State-of-the-art and perspectives.” In: *Measurement Science and Technology* 20.9 (2009), p. 092001.

[234] A. Piorra. “Ferroelektrische Schichten fur magnetoelektrische Komposite.” PhD thesis. Christian-Albrechts-Universitaet zu Kiel, 1.01.2014.

[235] K. Tsubouchi and N. Mikoshiba. “Zero-temperature-coefficients SAW devices on AlN epitaxial films.” In: *IEEE Transactions on Sonics and Ultrasonics* 32.5 (1985), pp. 634–644.

[236] D. Berlincourt, H. Jaffe, and L. R. Shiozawa. “Electroelastic properties of the sulfides, selenides, and tellurides of zinc and cadmium.” In: *Physical Review* 129.3 (1963), pp. 1009–1017.

[237] W. Borchardt-Ott. *Crystallography*. Berlin, Heidelberg: Springer Berlin Heidelberg, 1995. ISBN: 978-3-540-59478-9.

[238] J. J. Hall. “Electronic effects in the elastic constants of n-type silicon.” In: *Physical Review* 161.3 (1967), pp. 756–761.

[239] E. Bassous. “Fabrication of novel three-dimensional microstructures by the anisotropic etching of (100) and (110) silicon.” In: *IEEE Transactions on Electron Devices* 25.10 (1978), pp. 1178–1185. ISSN: 0018-9383.

[240] M. H. Read and C. Altman. “A new structure in tantalum thin films.” In: *Applied Physics Letters* 7.3 (1965), pp. 51–52. ISSN: 0003-6951.

[241] Q. Chen, L. Qin, and Q.-M. Wang. “Property characterization of AlN thin films in composite resonator structure.” In: *Journal of Applied Physics* 101.8 (2007), p. 084103. ISSN: 0021-8979.

[242] N. O. Urs, I. Teliban, A. Piorra, R. Knöchel, E. Quandt, and J. McCord. “Origin of hysteretic magnetoelastic behavior in magnetoelectric 2-2 composites.” In: *Applied Physics Letters* 105.20 (2014), p. 202406. ISSN: 0003-6951.

[243] P. Zou, W. Yu, and J. A. Bain. “Influence of stress and texture on soft magnetic properties of thin films.” In: *IEEE Transactions on Magnetics* 38.5 (2002), pp. 3501–3520. ISSN: 0018-9464.

[244] M. Akiyama, T. Kamohara, K. Kano, A. Teshigahara, Y. Takeuchi, and N. Kawahara. “Enhancement of piezoelectric response in scandium aluminum nitride alloy thin films prepared by dual reactive cosputtering.” In: *Advanced Materials* 21.5 (2009), pp. 593–596. ISSN: 09359648.

[245] R. Matloub, M. Hadad, A. Mazzalai, N. Chidambaram, G. Moulard, C. S. Sandu, Th . Metzger, and P. Muralt. “Piezoelectric Al(1−x)Sc(x) N thin films: A semiconductor compatible solution for mechanical energy harvesting and sensors.” In: *Applied Physics Letters* 102.15 (2013), p. 152903. ISSN: 0003-6951.

[246] Y. Wang, J. Li, and D. Viehland. “Magnetoelectrics for magnetic sensor applications: Status, challenges and perspectives.” In: *Materials Today* 17.6 (2014), pp. 269–275. ISSN: 13697021.

# Publications and Conferences

The publications' list is given in order of authorship appearance and chronology

- V. Röbisch, S. Salzer, N. O. Urs, J. Reermann, E. Yarar, A. Piorra, C. Kirchhof, E. Lage, M. Höft, G. U. Schmidt, R. Knöchel, J. McCord, E. Quandt, and D. Meyners. "Pushing the detection limit of thin film magnetoelectric heterostructures." *Journal of Materials Research*, 32(6), 1009-1019, (2017).

- E. Yarar, S. Salzer, V. Hrkac, A. Piorra, M. Höft, R. Knöchel, L. Kienle and E. Quandt. "Inverse bilayer magnetoelectric thin film sensor." *Applied Physics Letters* 109, 022901, (2016).

- E. Yarar, V. Hrkac, C. Zamponi, A. Piorra, L. Kienle, and E. Quandt. "Low temperature aluminum nitride thin films for sensory applications." *AIP Advances* 6, 075115, (2016).

- P. Hayes, S. Salzer, J. Reermann, E. Yarar, V. Röbisch, A. Piorra, D. Meyners, M. Höft, R. Knöchel, G. U. Schmidt, and E. Quandt. "Electrically modulated magnetoelectric sensors." *Applied Physics Letters* 108, 182902, (2016).

- S. Zabel, C. Kirchhof, E. Yarar, D. Meyners, E. Quandt, and F. Faupel. "Phase modulated magnetoelectric delta-E effect sensor for sub-nano tesla magnetic fields". *Applied Physics Letters* 107, 152402, (2015)

- V. Röbisch, E. Yarar, N. O. Urs, I. Teliban, R. Knöchel, J. McCord, E. Quandt, and D. Meyners. "Exchange biased magnetoelectric composites for magnetic field sen-

sor application by frequency conversion". *Journal of Applied Physics* 117, 17B513, (2015).

- S. Salzer, P. Hayes, E. Yarar, A. Piorra, E. Quandt, R. Knöchel, and M. Höft. "Comparison of frequency conversion techniques for magnetoelectric sensors". *Procedia Engineering* 120, 940-943, (2015).

- E. Lage, A. Piorra, C. Kirchhof, E. Yarar, D. Meyners, and E. Quandt. "Giant magnetoelectric effect in thin film composites". *ECS Transactions* 50 (10), 231-234, (2013).

Personally presented conference contributions are listed in order of authorship appearance and chronology

- Oral presentation; E. Yarar, S. Salzer, V. Hrkac, A. Piorra, M. Höft, L. Kienle and E. Quandt. "Inverse-bilayer magnetoelectric thin film sensors." *Euro Intelligent Materials 2017*, 7 - 9 June 2017. Kiel, Germany.

- Oral presentation; E. Yarar, S. Salzer, V. Hrkac, A. Kittmann, A. Piorra, M. Höft, L. Kienle and E. Quandt. "Inverse-bilayer and sandwich-type magnetoelectric thin film sensors." *Materials Research Society Fall Meeting 2015*, 29 November - 4 December 2015. Boston, United States of America.

- Oral presentation; E. Yarar, A. Piorra and E. Quandt. "Inverse-bilayer and sandwich-type magnetoelectric thin film sensors." *Euro Intelligent Materials 2015*, 10 - 12 June 2015. Kiel, Germany.

- Poster presentation; E. Yarar, I. Teliban, V. Hrkac, L. Kienle, R. Knöchel and E. Quandt. "Detection of pT magnetic fields at room temperature: Inverse-bilayer and sandwich-type magnetoelectric thin film sensors." *Materials Science Engineering 2014*, 23 - 25 September 2014. Darmstadt, Kiel.

- Poster presentation; E. Yarar and E. Quandt. "Sandwich type AlN-FeCoSiB thin film magnetoelectric composites." *Euro Intelligent Materials 2013*, 25 - 27 September 2013. Kiel, Germany.

- Poster presentation; E. Yarar A. Piorra, D. Meyners and E. Quandt. "Magnetoelectric 2-2 Thin Film Composites." *Materials Science Engineering 2012*, 25 - 27 September 2012. Darmstadt, Germany.

# Acknowledgements

At the end of my work, I'd like to take this opportunity and present my gratitude to all my colleagues, friends and family for their trust and support which made the presented work possible.

I would like to begin with expressing my sincerest gratitude to Prof. Dr.-Ing. Eckhard Quandt who gave me the priceless opportunity to join his research group. I am thankful to be part of such a great group which combines diverse research topics, brilliant scientists and state-of-the-art laboratory facilities. I enjoyed being in this inspiring environment and the opportunity to mature as a scientist under his supervision and guidance. I am especially thankful for the freedom which allowed me to follow a research path according to my personal interests. I particularly consider myself lucky that I had the opportunity to carry out my doctoral research within the projects CRC 855 "Magnetoelectric Composites – Future Biomagnetic Interfaces" and PAK 902 "Magnetoelectric Sensors for Medicine". I kindly acknowledge the funding by the German Research Foundation (DFG). It was a great privilege and I appreciate that I had the chance to experience it.

I would like to thank Dr.-Ing. André Piorra for his support during the writing of my thesis and his contributions to my overall research. I would also like to thank him for the guidance he provided me concerning numerous laboratory equipment and measurements.

I would like to thank Dr. rer. nat. Christiane Zamponi for her contributions on various topics, especially on my published work. Numerous discussions with her gave me valuable insight and helped me solve the questions at hand.

I would like to thank Dr. rer. nat. Dirk Meyners and Dr.-Ing. Claas Thede, who in many occasions gave me their time and insight concerning both theoretical and practical problems. These talks helped me have a much deeper understanding of several physical phenomena.

I also would like to thank Dr. rer. nat. Antonio Malavé for his patience and guidance concerning clean room operations. I appreciate his collaboration and support in solving technical questions, which contributed to my work.

I especially would like to thank my colleagues and office mates M.Sc. Till Jurgeleit and M.Sc. Patrick Hayes for their contributions and support. I acknowledge that our several discussions on numerous topics strengthened my understanding of many aspects and greatly improved my work. I would also like to thank my classmate and colleague Dr.-Ing. Ali Tavassolizadeh for always being supportive and understanding.

I am very thankful to my colleagues M. Sc. Sebastian Salzer, Dr.-Ing. Dipl. Phys. Viktor Hrkac, M.Sc. Julian Strobel, Dr.-Ing. Jascha Lukas Gugat, M.Sc. Jens Reermann, M. Sc. Volker Röbisch, M. Sc. Christine Kirchhof, M. Sc. Phillip Durdaut, Dr.-Ing. Alexander Teplyuk, Dipl.-Phys. Sebastian Zabel and Dr.-Ing. Enno Lage for various collaborations and laboratory support.

I would like to thank M. Sc. Anne Kittmann and M. Sc. Hafid Suharyadi for their great contributions to my research during their master theses. I would like to express my special thanks to Gislinde Schroeder, who countless times, helped me with the complicated world of bureaucracy. Additionally, I would like to thank Berndt Neumann and the workshop of the Faculty of Engineering for their great work and collaboration in numerous occasions.

I would like to thank my wife for her support and encouragement that helped me see the end of this long journey, especially when things got though.

Finally, I would like to thank my great family for their selfless efforts throughout the years, both materially and morally, in shaping a scientist out of me. I am well aware that it was not the easiest of the tasks and that the outcome is a reflection of your unwavering resolution. I appreciate your confidence in me and love you for it.

Erdem Yarar
Kiel, 2017